Proceedings ICSBM 2019 Volume 5 - Biogenic and functionalized materials

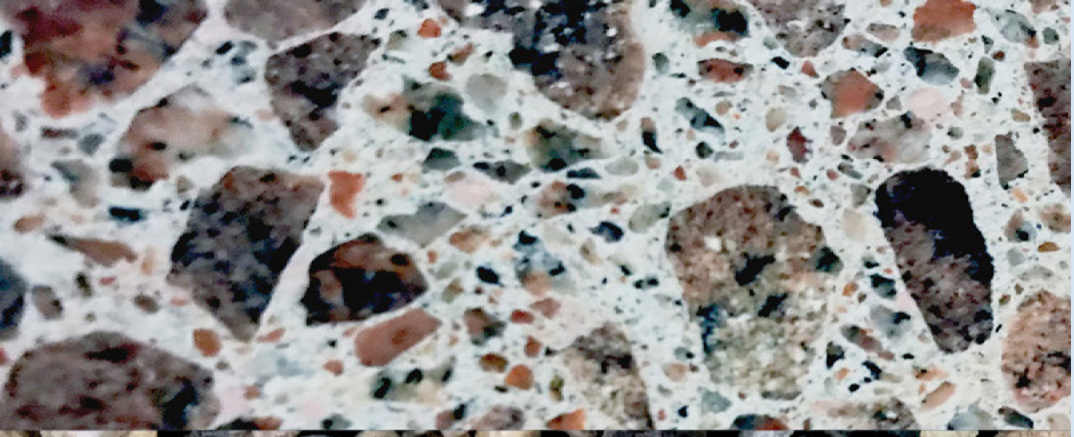

Organized by
Eindhoven University of Technology

In cooperation with
Wuhan University of Technology

PROCEEDINGS ICSBM 2019
VOLUME 5 - Biogenic and functionalized materials

2nd International Conference on Sustainable Building Materials

August 12-15, 2019 - Eindhoven, The Netherlands

Editors: V. Caprai and H.J.H. Brouwers

and supported by

ICSBM 2019, Conference proceedings

A catalogue record is available from the Eindhoven University of Technology Library

ISBN of the volumes set: 978-90-386-4898-9

ISBN of Volume 5: 978-90-386-4914-6

Sponsored by: CRH, Eltomation - Wood cement board plant, Tata Steel Europe (Gold sponsors), VDZ, PCA (Bronze Sponsors).

Front page image: V. Caprai

Editors: V. Caprai and H.J.H. Brouwers

Organizing committee:

Table of Contents

Volume 5

Biogenic and functionalized materials

Bio-based admixtures

W. Schmidt

Bundesanstalt für Materialforschung und -prüfung, Division: Technology of Construction Materials.

Abstract

Due to the high carbon emissions linked to concrete production and a rapidly increasing demand for cementitious materials, particularly in the global South, it is inevitable to use cement in concrete more efficiently. This can be achieved best by minimising the Portland cement content in the binder and by developing concrete mixtures with low water to cement ratios. For both approaches, chemical admixtures are required to cope with the negative rheological influences of supplementary cementitious materials that are often observed, and the higher solid volume fraction, respectively.

However, particularly in the growing economies of the Southern hemisphere, where a massive part of the future construction activities will take place, the supply chains are often poor with regard to performance enhancing chemical admixtures, and local production facilities are lacking today.

This paper presents case studies of polysaccharide based alternative admixtures such as acacia gum, cassava starch and the gum of the bark of Triumfetta pendrata A. Rich, which can be used effectively as superplasticizer, robustness enhancer, and thixotropy incorporating agent, respectively. Their modes of operation are discussed based on their zeta potentials and hydrodynamic diameters in the presence of calcium ions. Eventually, local value chains are discussed for bio-based by products on the example of cassava peels wastes.

Keywords: admixtures, concrete, cassava, acacia gum, Triumfetta pendrata A. Rich.

1. Introduction

Cement production consumes a high amount of raw materials, required high energy and involved chemical processing. Thus, it contributes significantly to global CO_2 emission. Global cement production is estimated at 4.6 Gt/a [1] in 2015 and will rise to values between 6 and 13.5 Gt/a in 2050 [2, 3]. However, since cement is urgently required to build structures and infrastructures with concrete, and concrete is the only material in the world that can meet the global demand for construction materials, the situation is aggravated as the world's population increases from today 7.3 to 9.7 billion in 2050 [4]. The production of cement creates high carbon emissions from fuelling, but even more from decarbonation of calcium carbonate from the limestone to convert it to calcium oxide, resulting in assumedly more than 8% of all the greenhouse gases released by human activity and carbon emission estimates for concrete in the order of magnitude of 10% of all global carbon emissions [5]. Yet, other materials have even higher carbon footprints and energy demands [6, 7], which makes concrete inevitable as mass construction material.

Consequently, the only way to make the construction industry more environmentally friendly means making concrete technology greener and using cement in concrete more efficiently. This means that the water cement ratios in concrete have to be reduced by using chemical admixtures that help to control the rheology despite the lower water content [23]. In Africa, the efficient usage of cement is even more important, since the cement prices are significantly higher than in other parts of the world, when expressed in local

purchasing power (Fig. 1). The efficient use of chemical admixtures for higher performance materials, thus, can have a tremendous leverage towards a better global climate.

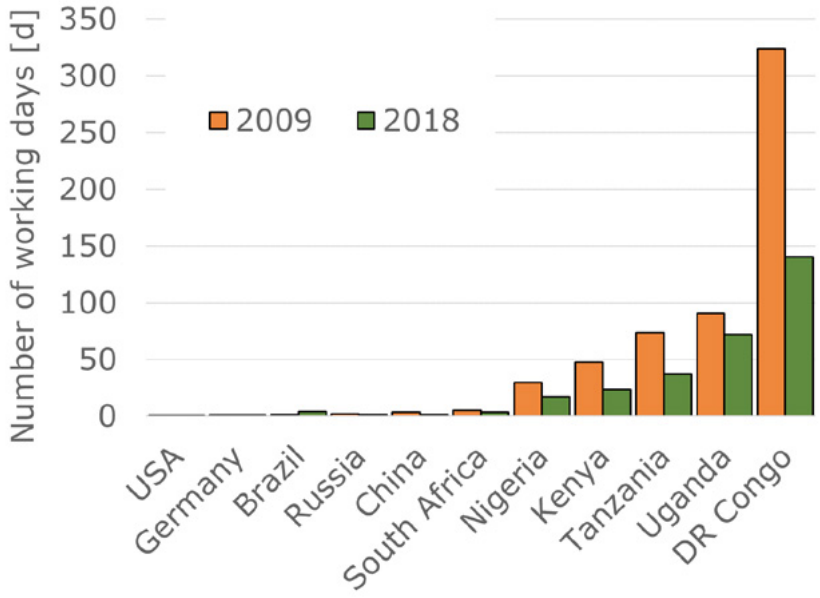

Figure 1: cement price differences in different countries in the world expressed in number of working days for an average income earner to purchase a ton of cement for the years 2009 and 2018. Price information obtained from local inhabitants.

Furthermore, this inevitably calls for blending cement with more sustainable supplementary cementitious materials [8]. In most developing countries in sub-Saharan Africa, the established materials such as ground granulated blast furnace slag or fly ash are hardly available, but agricultural wastes are available in large quantities with a growing potential for the agricultural industry on the continent [9, 10]. Thus, using bio materials as pozzolanic materials is getting more important in research, globally, but particularly in Africa. Some notable studies that demonstrate the use of ashes of rice husk, sugar cane straw and groundnut husk as pozzolanic components in concrete are presented in [11-20]. They have shown that mechanical and durability properties can be enhanced, depending upon the amorphous silica content. Africa provides 60% of the global unused arable land [21]. Thus, the continent has a tremendous potential for further development of the agricultural harvest. Hence, vegetable ashes are a real potential for many African countries to make concrete technology greener and more economically viable by creating local value chains.

Nevertheless, the use of agricultural by-products as cementitious materials often comes along with new challenges for the workability, since the rough and fissured surfaces absorb more water than cement, which demands for chemical admixtures again to control the rheology.

Hence, chemical admixtures help to use cement in concrete more efficiently by reducing the required water and helping to cope with the challenges arising from the use of supplementary cementitious materials used to reduce the amount of Portland cement clinker in the binder. However, many regions in the world, particularly in the Southern hemisphere lack supply of chemical admixtures, that often have to be imported from Europe, North America or Asia. As a result, they are available only in limited variability and at high costs [22]. This limits the applicability of sustainable and high performance applications in regions of the Southern hemisphere, particularly on the African continent, which is a real obstacle for Africa's enormous innovation potential and rapid economic upswing [9].

Feasible alternatives to traditional synthetic polymers are innovative and efficient admixtures based on locally available plant-based bio-materials. It has already been shown that high performance concrete can be

developed [23], and complex rheological properties can be achieved [24-26] with bio-based polysaccharides. In addition, new markets can be created [27].

This paper shows a review of some potentially viable bio-polymers that can be used for high performance applications in concrete technology.

2. Case studies

2.1 Acacia gum as superplasticizer

Acacia gum can be found in various modifications all over the African continent. The most important global exporters are Senegal and Sudan, while there is hardly a real market in other countries. Acacia gum has shown to be an excellent superplasticizer, though, its effect depends strongly on the solid volume fraction. Fig. 2 shows the torque change of cement pastes with different polymer dosages of two qualities of acacia gum from Sudan and South Africa in comparison to two polycarboxylates (PCE) and a lignosulfonate.

At low dosage, the acacia gum acts as a stabilising agent, which can be seen from the increasing torque. However, upon addition of higher amount the torque decreases indicating a reduced viscosity. Both acacia gums show this liquefying effect. The gum from Sudan shows even higher efficiency than the pre-cast PCE, while the South African gums has similar effect to the ready-mix PCE and the lignosulfonate.

The effect of acacia gums depends strongly on the solid volume fraction. A liquefying effect can only be observed, when the w/c is moderately low. At extremely low w/c no liquefying effect can be observed.

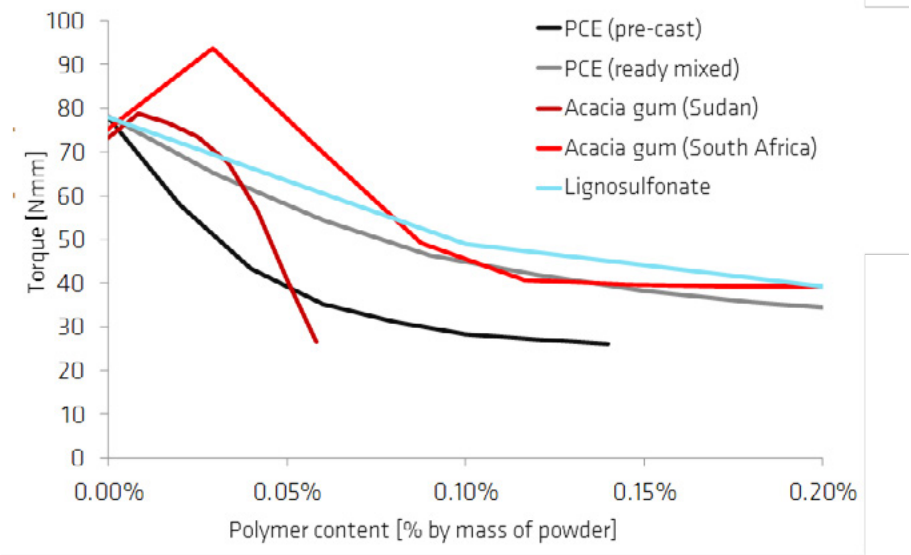

Figure 2: effect of different polymer dosages on the torque at rotational speed of 240 rpm in cement pastes with a solid volume fraction of 0.40.

2.2 Cassava starch as stabilising and plasticizing admixture

Cassava is the third most important source of starch in the world after rice and maize. It feeds about half a billion people in the Southern hemisphere. Major cassava producers can be found in East Asia, Africa, and South America (Fig. 3), the most important of which is Nigeria where about 20% of the global cassava is being produced.

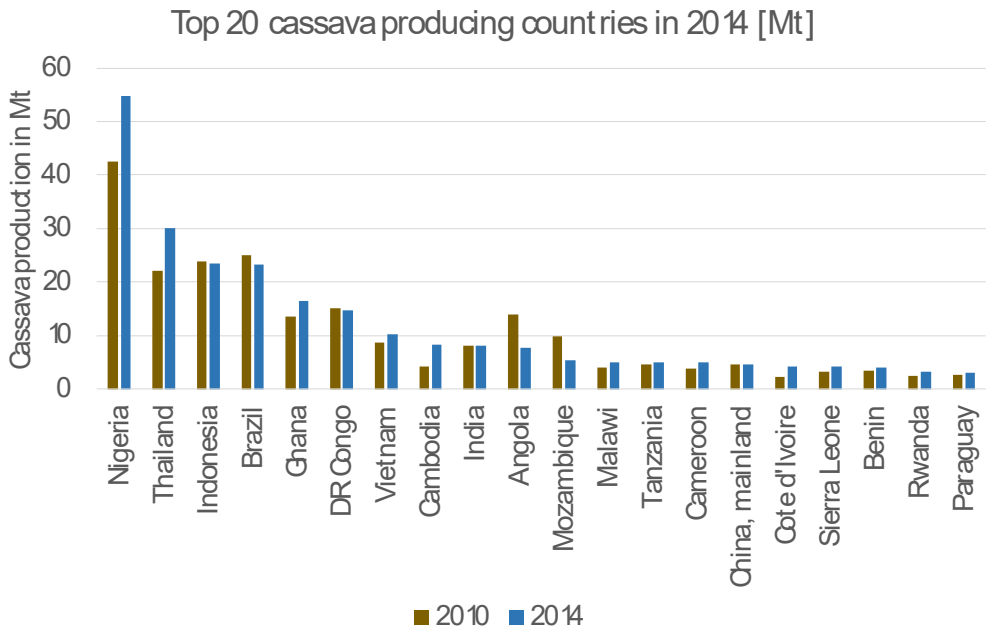

Figure 3: top 20 cassava producing countries in 2010 and 2014.

Cassava tubers are rich in starch, and like potato starch it contains around 80% amylopectin and 20% amylose. Nevertheless, potato starch is typically used to increase the stability of cementitious systems by increasing the viscosity, while cassava starch can incorporate plasticizing effects as well (Fig. 3). Depending on dosage and solid volume fraction, cassava can thus help to generate a softer consistency, while, due to the viscosity enhancing properties of the starch, the coherence of the cementitious system is increased, which creates higher robustness.

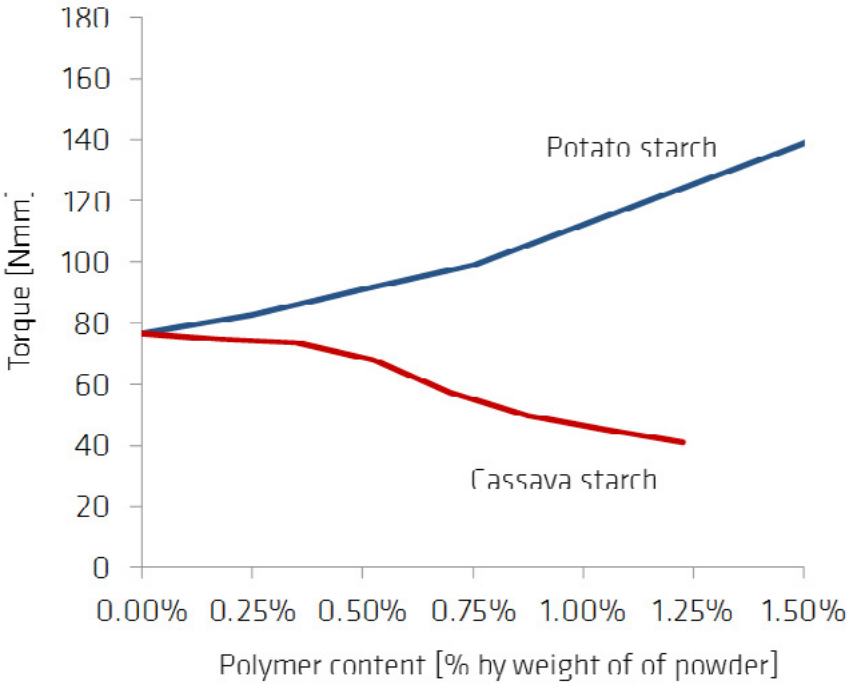

Figure 4: Torque change in cement pastes at a solid volume fraction of 0.4 and a rotational speed of 240 rpm due to the addition of potato starch and cassava starch.

2.3 Triumfetta pendrata A. Rich to enhance thixotropy

The gum of the malvaceous plant Triumfetta pendrata A. Rich is typically used as food consistency regulating agent for a typical Cameroonian dish called 'nkui'. The easily water-soluble polymers incorporate a very cohesive consistency to the soup. Mixed with concrete, the polymers have little effect in cement pastes only, but in the presence of superplasticizers they bear the capacity to totally reverse the liquefying effect by dramatically increasing the yield stress without significantly affecting the plastic viscosity. Flowable systems, thus, build up a thixotropic structure within short period of time.

The effect is shown in Fig. 5. The red curves show the flow values on the Haegermann table without strokes. The blue curves show the results of the respective samples after 15 strokes. The strokes significantly increase the flow values for both systems, with and without the addition of nkui gum.

The effect of the gum becomes most obvious at a w/c of 0.4. While the system without gum spreads wide without strokes, the system with gum nearly shows no flow, but after 15 strokes, the flowability with and without gum are nearly identical. The strong thixotropic effect of the gum can be used beneficially, e.g. in all kinds of additive processing such as 3D-printing.

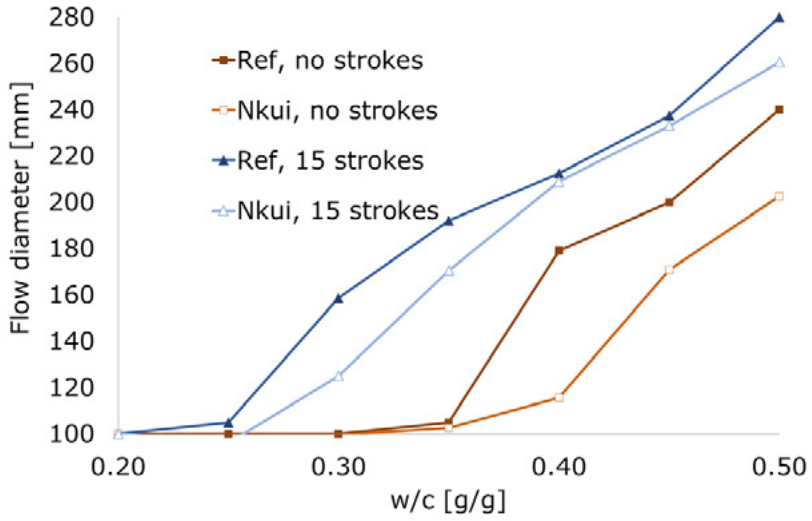

Figure 5: flow values (Haegermann cone) of cement pastes with 0.35% PCE (bwoc) in the presence of 0.08% Nkui gum (bwoc) and without the gum. Blue curves show results after 15 strokes, red curves show results without strokes.

3. Discussion of results

The results of some rheological experiments in the presence of different bio-gums were presented. In the case of the present polymers the following conclusions can be made:

- Acacia gum can be used as superplasticizer. However, at low dosages they act as stiffening agents.
- Cassava starch can be used as slight plasticizer and consistency regulator.
- The gum of the bark of Triumfetta pendrata A. Rich incorporates strong thixotropy.

Zeta potential measurements and measurements of the hydrodynamic radii provide some indicators for the different behaviours of the gums. Although their zeta potentials vary greatly in water, in the presence of calcium ions, their zeta potentials are all negative in the same order of magnitude between -7.4 and -13.2 mV. Thus, all polymers can be assumed to adsorb on cementitious particles, which alone cannot explain their effect. Their major difference lies in their polymer sizes and agglomeration tendency.

The acacia gum polymers tend to agglomerate to form a large variety of polymer sizes. The range goes from 20 nm to 1 µm. Thus, it can be assumed that polymers are packed densely in the liquid phase, which explains, why at low dosages they have a stiffening tendency. Only, when the water between the particles is sufficiently high, the polymers become more mobile, and thus may create a kind of a ball bearing effect in the liquid phase, while the adsorbed polymers sterically keep the cement particles in distance, thus, causing the excellent flow properties.

The cassava starch also adsorbs on particles in the cementitious system. The present cassava starch polymers are significantly smaller in size (~150 nm] than what is reported in literature for potato starch (amylopectin > 500 nm) [28], which explains the different effects shown in Fig. 4. While potato starch polymers are particle sized and, thus, hinder particles from movements [25], the investigated cassava starch polymers are much smaller, so that the particle stabilising effect becomes much smaller, and steric effects become more prominent.

The Triumfetta pendrata A. Rich polymers seem to significantly form huge agglomerates in the presence of calcium ions. The agglomerates being formed show sizes up to 5 µm, which is particle size. This agglomeration explains the strong thixotropic structural build up. Since the calcium linking is not stable, the structure easily breaks down under shear forces, giving the material good flow under forces.

The present figures and the table show the clear difference between the use of synthetic polymers and biopolymers. While synthetic polymers can be modified according to the requirements, bio-gums have to be taken as they are. This means, the polymers' effects have to be understood at first, and then their best use can be determined. However, despite their different effects all polymers can be applied in different high-performance applications. Thus, they provide enormous potentials for greener concrete admixtures.

Table 1: Zeta potentials and hydrodynamic radii of the present polymers in different ionic media, measured with dynamic light scatter.

	Acacia gum		Cassava starch		Bark gum of Triumfetta pendrata A. Rich	
	Water	Saturated limewater	Water	Saturated limewater	Water	Saturated limewater
Zeta potential [mV]	-16.3	-7.7	0.6	-7.4	-25.3	-13.2
D_{hyd} [nm]	Distinct peaks at ~10 nm and ~100 nm	Broad range between ~20 nm and ~1 µm	Distinct peak at ~150 nm	Distinct peak at ~120 nm	Distinct peak at ~250 nm	Distinct peaks at ~700 nm and 5 µm

4. Local value chain potentials

Considering the scarcity of chemical admixtures in many countries of the Southern hemisphere, bio-based solutions can become a viable option, particularly since plants containing promising polysaccharides grow all over the African and South American continents. This easy availability creates potentials for local value chains that support the local markets as well.

Cassava is one most promising example. The peels of cassava have limited use in livestock feeding as they cannot be digested by most animals. Thus, the peels are typically dumped away. They require large spaces, where the waste rots away, creates malodour and attracts insects. Sometimes the wastes are burnt to save the space for dumping, but the ashes are not further used any more.

However, instead of dumping, the organic starch content that is still adhered to the peels can easily be

obtained to become a precursor for a concrete chemical admixture to enhance the performance and save cement in concrete. After obtaining the starch, the residual peels can still be burnt, thus, create energy for example for brick production. After burning, the ashes were shown to have pozzolanic properties, thus, help reducing the Portland cement content in the binder for concrete. The concept is shown in Fig. 6.

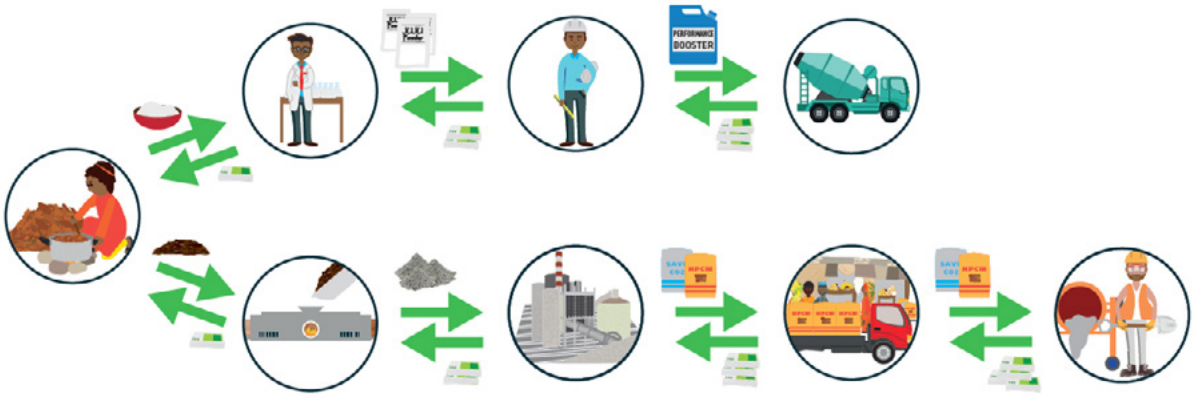

Figure 6: possible new value chains based on today simply dumped cassava peels. An organic and an inorganic value chain can be created from the same residues in parallel. Both value chains help making concrete more sustainable, by enhancing the concrete properties and reducing the Portland cement content in the binder, respectively.

5. Conclusions

The present results and interpretation have shown some remarkable properties of bio-gums obtained from acacia gum, cassava starch and the gum of the bark of Triumfetta pendrata A. Rich. The mode of operation of the different gums in the cementitious system is complex and requires further understanding. Much of the effects can be explained by the polymer sizes and size distributions as well as their interactions with particle surfaces and calcium ions in the aqueous phase of cement paste.

6. Acknowledgment

Some of the present result were obtained within the framework of the German African Innovation Incentive Award provided by the Federal Ministry of Education and Research. The author gratefully acknowledges the financial support for this research

7. References

[1] K. Carstensen and O. Rapf, "A blueprint for a climate friendly cement industry," WWF, Nürnberg, Germany2008.

[2] CEMBUREAU, "Cement & concrete: key facts & figures," t. E. c. association, Ed., ed, 2015.

[3] P. Edwards. (2016). *The Rise and Potential Peak of Cement Demand in the Urbanized World.* Available: http://cornerstonemag.net/the-rise-and-potential-peak-of-cement-demand-in-the-urbanized-world/

[4] UN. (2015). *World Population Prospects: The 2015 Revision.* Available: http://www.un.org/en/development/desa/news/population/2015-report.html

[5] "Concrete CO2 Fact Sheet," 2008, Available: http://www.nrmca.org/greenconcrete/concrete%20co2%20fact%20sheet%20june%202008.pdf.

[6] K. Scrivener, V. M. John, and E. M. Gartner, "Eco-effcient cements: Potential, economically viable solutions for a low-CO2, cement-based materials industry," United Nations Environment Programme2016.

[7] L. Barcelo, J. Kline, G. Walenta, and E. Gartner, "Cement and carbon emissions," *Materials and Structures,* journal article vol. 47, no. 6, pp. 1055-1065, 2014.

[8] J. W. Wilson and Y. C. Ding, "A Comprehensive Report on Pozzolanic Admixtures, the Cement Industry, Market and Economic Trends and Major Companies Operating in the Far East, with Reference to Pagan Island," 2007.

[9] W. Schmidt, "Potentials for sustainable cement and concrete technologies – comparison between Africa and Europe," presented at the Proceedings of the 1st International Conference on Construction Materials for a Sustainable Future, Zadar, Croatia, 19 - 21 April 2017, 2017.

[10] W. Schmidt, "Why Africa can spearhead innovative and sustainable cement and concrete technologies globally," in *KEYS Knowledge Exchange for Young Scientists: Valorisation of Industrial By-products for Sustainable Cement and Concrete Construction – Improvement of Solid Waste Management*, N. S. Msinjili and W. Schmidt, Eds. Accra, Ghana: BAM, 2016, pp. 7-19.

[11] K. Olonade, A. M. Olajumoke, A. O. Omotosho, and F. A. Oyekunle, "Effects of sulphuric acid on the compressive strength of blended cement-cassava peel ash concrete," (in English), *Construction Materials and Structures,* pp. 764-771, 2014.

[12] M. A. Salau and K. A. Olonade, "Pozzolanic Potentials of Cassava Peel Ash," *Journal of Engineering Research,* vol. 16, no. 1, pp. 10-21, 2011.

[13] W. Schmidt, N. S. Msinjili, S. Pirskawetz, and H. C. Kühne, "Efficiency of high performance concrete types incorporating bio-materials like rice husk ashes, cassava starch, lignosulfonate, and sisal fibres," in *First International Conference on Bio-based Building Materials*, Clermont-Ferrand, France, 2015, vol. 208-2014: RILEM.

[14] N. van Tuan, Y. Guang, and B. D. Dai, "Study the Hydration Process of Cement Blended with Rice Husk Ash by Means of Isothermal Calorimetry," in *13th International Congress on the Chemistry of Cement*, Madrid, Spain, 2011.

[15] B. Chatveera and P. Lertwattanaruk, "Evaluation of sulfate resistance of cement mortars containing black rice husk ash," *Journal of Environmental Management,* vol. 90, no. 3, pp. 1435-1441, Mar 2009.

[16] T. S. Ketkukah and E. E. Ndububa, "Groundnut Husk Ash (GHA) as a Pozzolana Material in Mortar," *International Journal of Science and Technological Research,* vol. 3, no. 2, pp. 209-214, 2006.

[17] I. C. Mayowa, "Making Durable Concrete Through Inhibition of Chloride Ion Penetration by Pozzolanic Reaction," in *1st Symposium on Knowledge Exchange for Young Scientists (KEYS) - Sub-Saharan African Standards for Cement and Concrete Research and Raw Materials, Quality Control and Maintenance of Cementitious Products*, Dar es Salaam, Tanzania, 2015, pp. 145-150: BAM.

[18] N. S. Msinjili, W. Schmidt, A. Rogge, and H. C. Kühne, "Optimising available resources for production of good concrete properties," in *Advances in Cement and Concrete Technology in Africa*, Dar es Salaam, Tanzania, 2016, pp. 323-332: BAM.

[19] M. Frias, E. Villar Cocina, and E. Valencia-Morales, "Characterisation of sugar cane straw waste as pozzolanic material for construction: Calcining temperature and kinetic parameters," *Journal of Waste Management,* vol. 27, pp. 533-538, 2007.

[20] O. Cizer, K. Van Balen, J. Elsen, and D. Van Gemert, "Carbonation and hydration of calcium hydroxide and Calcium silicate binders with Rice Husk Ash," in *2nd International Symposium on Advances in*

Concrete through Science and Engineering, Quebec City, Canada, 2006.

[21] A. Perry, *The Rift: A New Africa Breaks Free*. Little, Brown and Company 2015.

[22] W. Schmidt, N. S. Msinjili, and H.-C. Kühne, "Materials and technology solutions to tackle the challenges in daily concrete construction for housing and infrastructure in sub-Saharan Africa," *African Journal of Science, Technology, Innovation and Development,* pp. 1-15, 2018.

[23] W. Schmidt, N. S. Msinjili, H. C. Uzoegbo, and J. K. Makunza, "Admixture Concepts for the Sub-Saharan African Environment with Indigenous Raw Materials," in *SP-302 Eleventh International Conference on Superplasticizers and Other Chemical Admixtures in Concrete*, V. M. Malhotra, Ed., 2015, pp. 491-505.

[24] W. Schmidt, I. L. Tchetgnia Ngassam, R. Mbugua, and K. A. Olonade, *Natural rheology modifying admixtures for concrete* (Rheologische Messungen an Baustoffen). tredition GmbH, 2017.

[25] W. Schmidt, H. J. H. Brouwers, H.-C. Kühne, and B. Meng, "Interactions of polysaccharide stabilising agents with early cement hydration without and in the presence of superplasticizers," *Construction and Building Materials,* vol. 139, pp. 584-593, 2017.

[26] W. Schmidt, I. Tchetgnia Ngassam, K. Olonade, Mbugua, R, and H.-C. Kühne, "Plant based chemical admixtures – potentials and effects on the performance of cementitious materials," *RILEM Technical Letters,,* vol. 3, pp. 124-128, 2019.

[27] W. Schmidt and M. J. Barucker-Sturzenbecher, "Bio-based concrete (https://vimeo.com/310549146)," ed. Berlin, 2019, p. 7:51.

[28] W. Schmidt, H. J. H. Brouwers, H.-C. Kühne, and B. Meng, "The working mechanism of starch and diutan gum in cementitious and limestone dispersions in presence of polycarboxylate ether superplasticizers," *Applied Rheology,* vol. 23, no. 5, p. 12, 2013.

Parallel session contributions

Functionalization of fibres for cement-based materials – selected test methods

J. von Werder[1], A. Gardei[1], B. Meng[1]

[1]*Bundesanstalt für Materialforschung und -prüfung, Unter den Eichen 87, 12205 Berlin, Germany, julia.von-werder@bam.de*

Abstract

The low tensile strength of cement-based materials can be improved by the addition of fibres. In a joint research project, an industrial partner designed special coatings for polymer and carbon fibres by integrating surfactants and hydrophilic compounds. Aim of the developed functionalization was to ensure an even coverage of the fibre surfaces and to anchor them chemically in the cement-based matrix. Task of the BAM was to quantify the effect of the improved bond. In a first step a workable mortar adjusted to the strength of the tested fibres was developed and the fibre distribution assessed by light microscopy and computed tomography. To test the new coating for its efficiency to prevent cracking during hardening and to improve the loadbearing behaviour new test setups were developed or existing methods were adjusted. The experiments showed that the functionalization leads to a reduction of the crack area measured after the exposure of the wet mortar to strong drying conditions in the wind channel. Regarding the efficiency to mitigate shrinkage cracks the functionalisation turned out to be more efficient for fibres made from polyacrylonitrile (PAN) than for carbon fibres. An improvement of the tensile strength after cracking of the cementitious matrix could only be documented for the coated carbon fibres. It could be quantified, however, only in the three-point bending tests because the fibres turned out to be too brittle for the applied single fibre pull-through test.

Keywords: fibres, functionalization, mortar, computed tomography, shrinkage

1. Introduction

Cement based materials play a decisive role in the building materials sector because of their economic and technical benefits. To further improve their applicability and durability regarding special applications, they are more and more frequently equipped with fibres made from different types of material like for example steel, carbon or polymers. Due to their superior mechanical performance, even carbon nano tubes are used [1]. Fibres are added because of different reasons. Within renders as part of external thermal insulation composite systems (ETICS) for example their purpose is to permanently absorb the tensile and flexural stress resulting from thermal and hygric loads [2]. In other cases, their primary aim is to reduce shrinkage cracking during the hardening process [3,5] or to prevent explosive spalling in case of fire [6].

The effectiveness of fibres is based on the dissipation of the fracture energy due to the adhesive friction between the fibres which are in most cases hydrophobic and the hydrophilic hardened cement paste. This pure physical interaction between fibres and matrix requires a certain amount and length of fibres [2] for a specific load case which can lead to technical restrictions in terms of workability especially for slender components with high requirements regarding mechanical strength (ultra-high-performance concrete).

Aim of a joint research project with an industrial partner was therefore, to improve the fibre performance

by the integration of surfactants and hydrophilic compounds into a new polymeric coating. The functionalization was designed to allow an even coating and to make the surface of the fibres hydrophilic so that a chemical bond between the fibres and the hardened cement paste is established [7,9]. The preparation process of the fibres was developed and continuously refined by the project industrial partner. Task of the BAM was to quantify the improved chemical bond between the fibres and the cementitious matrix due to the new functionalization. To evaluate the effect on the mechanical performance and the shrinkage cracking in comparison to uncoated reference fibres existing tests had to be adjusted and new test set-ups had to be developed

2. Methodology

2.1 Materials

To analyse the performance of the functionalization a mortar with a good workability allowing a homogeneous distribution of the fibres had to be designed. Furthermore, the strength of the mortar had to be carefully adjusted so that a differentiation between the performance of the standard untreated fibres (reference) and the chemically functionalized fibres was feasible. To achieve a significant number of evaluable cracks in the wind tunnel test, the formulation was impoverished by adding a substantial proportion of limestone powder (Table 1).

Table 1: Formulation of the cement mortar to evaluate the effectiveness of the functionalization

Component	Weight
	g
CEM I 32,5 R	270
limestone powder	1145
standard sand	1350
water	550

Fibres for test were selected from different material types: polyacrylonitrile (PAN), polypropylene (PP) and carbon (Table 2). The carbon fibres were covered by an epoxy-coating. In the course of the research project two different batches of the same carbon fibres were ordered.

For mixing the fibres into the mortar two different modes were tested: in the first case they were added in a wet state immediately after the treatment with the agent and in the other case they were put in after the treatment agent had dried on their surface.

1a) 1b) 1c)

Figure 1: PAN fibres (1a), PP fibres (1b) and carbon fibres (1c).

Table 2: Physical properties of the fibres used in the study.

Sample	Length	Diameter	Young's Modulus	Tensile strength	Raw density	Fibre surface (dry)
	mm	µm	kN/mm²	N/mm²	g/cm³	cm²/g
PAN	4;6;8;12	15	15-20	330-530	1,18	2250
PP	4,6; 6	15,4	4-18	320-560	0,9	
Carbon	6	7	240	4.000		

2.2 Methods

The workability of the mortar, depending on the amount of fibres added, was quantified by the flow spread according to DIN EN 1015-3 [10].

Because of their fluorescent properties, the distribution of the PAN-fibres within the cementitious matrix was analysed in a first step two dimensionally by optical microscopy employing ultraviolet light. For this microscopic analysis polished cross sections of standard prims (40 x 40 x 160 mm³) were used. The three-dimensional analysis of the fibre distribution was performed by x-ray computer tomography (3D-CT) using small cores with a maximum diameter of 10 mm and a minimum length of 20 mm. These samples were drilled out of solidified standard mortar prisms, which were impregnated with epoxy resin for stabilization. The measuring principle of the 3D-CT is based on the radiography of a sample from different angles during the stepwise rotation around 360°. By specific reconstruction algorithms the spatial distribution of the X-ray absorptivity coefficient α is calculated from the individual images and visualized three-dimensionally by the allocation of greyscales (Figure 2).

The distribution of the carbon fibres could only be examined under the light microscope. Due to the small difference in x-ray absorptivity to the mortar matrix a three-dimensional analysis by CT was not possible.

The flexural strength after the incipient crack was quantified by calculating the energy of deformation from the area under the load-deflection-curve resulting from a three-point bending tests of mortar prisms (mean value of a set of three mortar prisms 40 x 40 x 160 mm³).

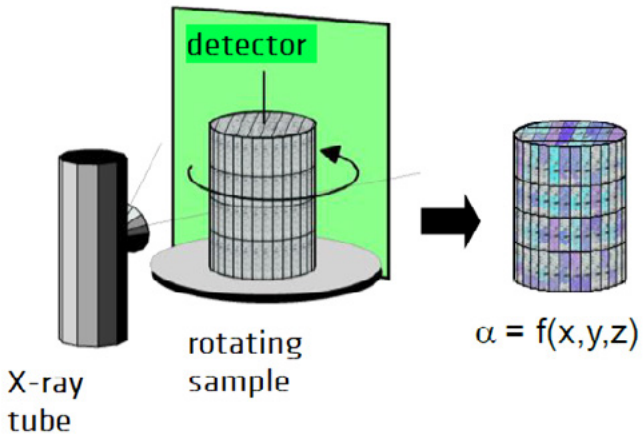

Figure 2: Measuring principle of the 3D-CT.

To exclude effects due to the distribution and orientation of the fibres, the improvement of the bond between the fibres and the matrix was additionally quantified by a fibre pull-through test. For the test set-up individual fibres with a larger diameter (PAN: 80 µm and PP: 72 µm) and a length of 2 cm were embedded into the fresh mortar of small specimens with a thickness of 2, 3 and 4 mm (Figure 3).

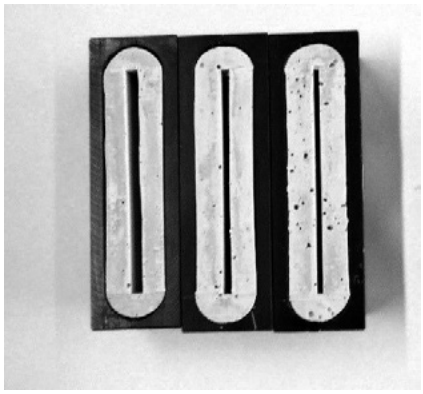

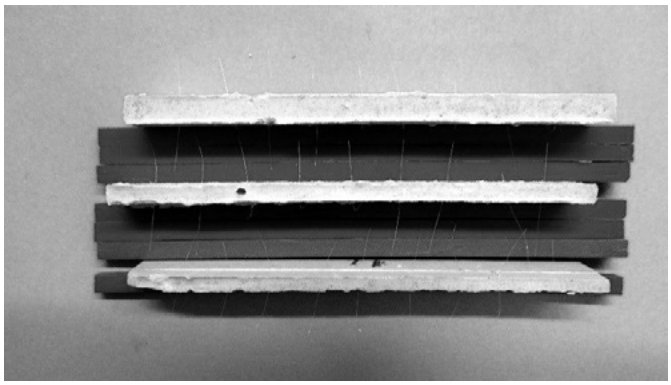

3a) 3b)

Figure 3a: Form work of the samples made for the individual fibre pull-through test
Figure 3b: Specimens in the thickness of 2,3 and 4 mm with embedded fibres

The shrinkage behaviour was evaluated according to the test procedure of the German Institute for Building Technology (DIBt) for the entrance examination for the approval of polymer fibres to be used in concrete [11,13]. To provoke shrinkage cracks, paving slabs of the size 30 x 30 cm² were plastered with the different fibre-mortar mixes and afterwards rapidly dried in a wind channel at 30 °C and 50 % relative humidity at a wind speed of 5 m/s (Figure 4).

For the analysing procedure after rapid drying three areas (16 x 16 cm²) were selected, and digitized (with a resolution of 50 µm/pixel). From these images the length and the width of all cracks above 100 µm were measured and the crack opening area was calculated.

Figure 4: Wind channel with four previously plastered paving slabs (30 x 30 cm) in a climate chamber operated at 30° C and 50 % relative humidity

3. Results and discussion

As expected, the addition of fibres had a significant impact on the properties of the freshly mixed mortar. Figure 5 shows the correlation between increasing fibre content and increasing stiffness of the mortar, which is reflected by a decreasing flow spread and confirms the observations by [14]. The decreasing flow spread with increasing volume content of fibres is most prominent for the carbon fibres (Figure 5) and least pronounced for the PP fibres. The mode of addition of the functionalized fibres (in the wet or dry state) as well as the length of the fibres seems to have no or rather a minor impact on the flow spread in such tests.

The analysis of the two-dimensional fibre distribution revealed that an increasing fibre content favours

the agglomeration of fibres (Figure 6). The three-dimensional analysis further illustrates that the spatial distribution is not homogeneous in terms of amount and preferred orientation (Figure 7). The smaller amount of untreated PP fibres in the reference sample (Figure 7a) indicates that the functionalization improves their even distribution (Figure 7b). As already confirmed for the mortar with 0,5 Vol.-% of PAN fibres by optical microscopy (Figure 6a) the 3D-CT images show that also the mortar with 0,5 Vol.-% of PP fibres does not agglomerate. It could be demonstrated that the orientation distribution function derived from the 3D-CT results can be used for calculation of the effective elastic properties of polymer fibre reinforced concrete [15, 16].

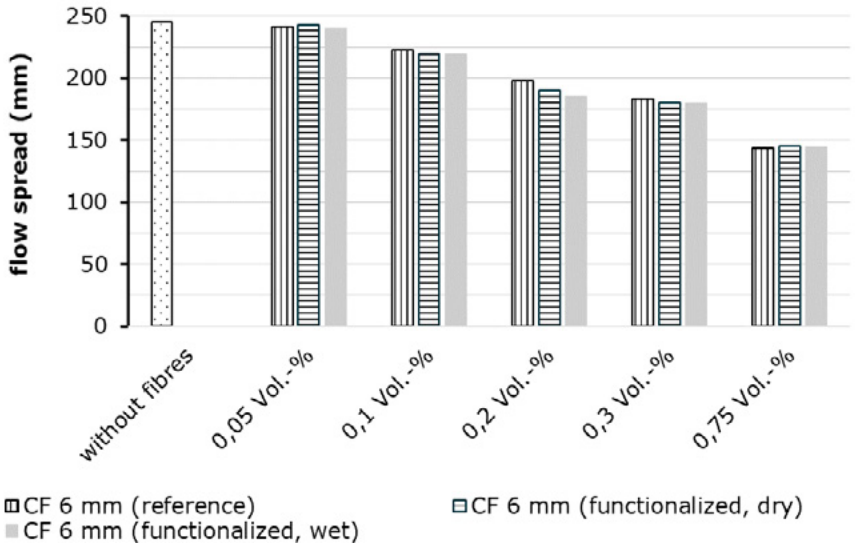

Figure 5: Flow spread fibres according to the fibre content and the mode of addition (mean of two measurements with a maximum standard deviation of 6 mm)

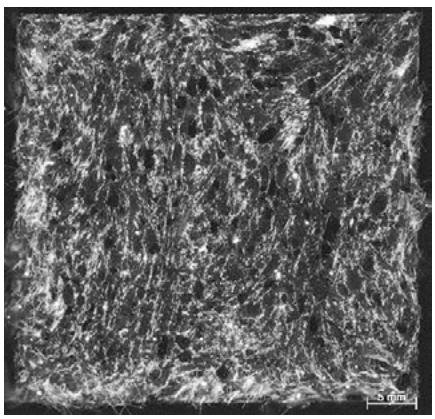

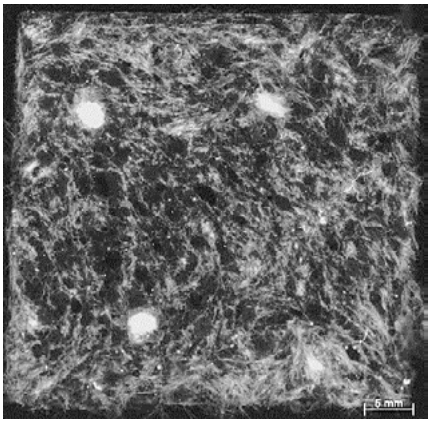

6a) 6b)

Figure 6: Sections of mortar prisms with PAN fibres (length = 4 mm) under UV-light

6a) 0,5 Vol.% 6b) 1,0 Vol.-%

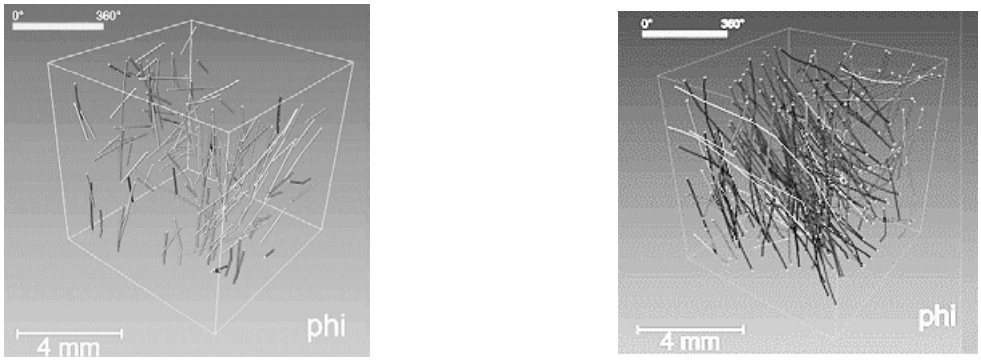

7a) 7b)

Figure 7: Three-dimensional distribution of PP in the cement mortar (fibre-content: 0.5 Vol.-%, fibre length: 4,6 mm) analysed by CT with colour code attributed to the fibre orientation
7a) reference 7b) functionalized, wet

The load deflection curves from the three-point bending test, shown in Figure 8, illustrate if maximum load has been reached the matrix breaks and the load is transferred to the fibres. The higher the load related to the deformation, the more efficient is the transfer of loads due to adhesion and friction. To compare the mechanical performance of the mortars the energy of deformation is calculated which is represented by the area below the load-deflection curve. For the addition of 0.05 Vol.-% of carbon fibres the energy of deformation increases up to 50 %, when the functionalized carbon fibres are compared to the hydrophobic reference (Figure 9). To provide reliable statistics, however, numerous retries were performed in which it turned out that the magnitude of improvement also depends on the batch of fibres. Whereas one batch of carbon fibres exhibited a comparable low energy of deformation in the not treated reference state, the next order was characterized by a high level already for the reference so that the potential for improvement decreased. Using scanning electron microscopy, no differences could be distinguished regarding the surface structure of the fibres, so that chemical differences of the epoxy coating might be an explanation.

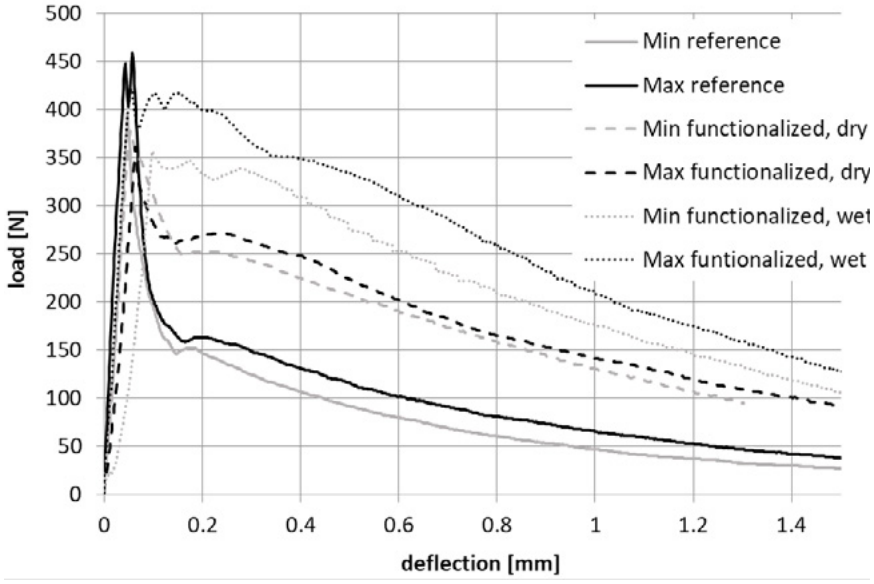

Figure 8: Envelope curves of the minimum and maximum values for load and deflection of three mortar prisms with 0,05 Vol.-% carbon fibres, not treated versus functionalized, added in the wet and in the dry state

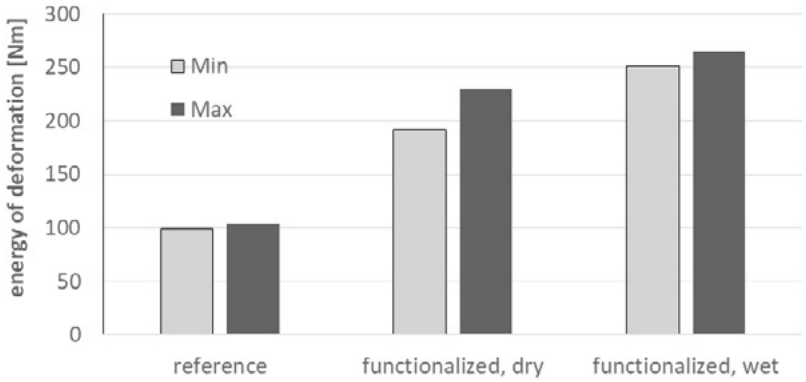

Figure 9: Energy of deformation calculated from the area under the envelope curves from Figure 8 until a deflection of 1 mm

As expected, optimum fibre contents can be defined regarding the optimization of the post-cracking behaviour. While for mortars containing the not treated fibres (reference) the energy of deformation increases up to a fibre content of 0.3 Vol.-% (Figure 10), the maximum is already reached at 0.1 Vol.-% for the functionalized fibres.

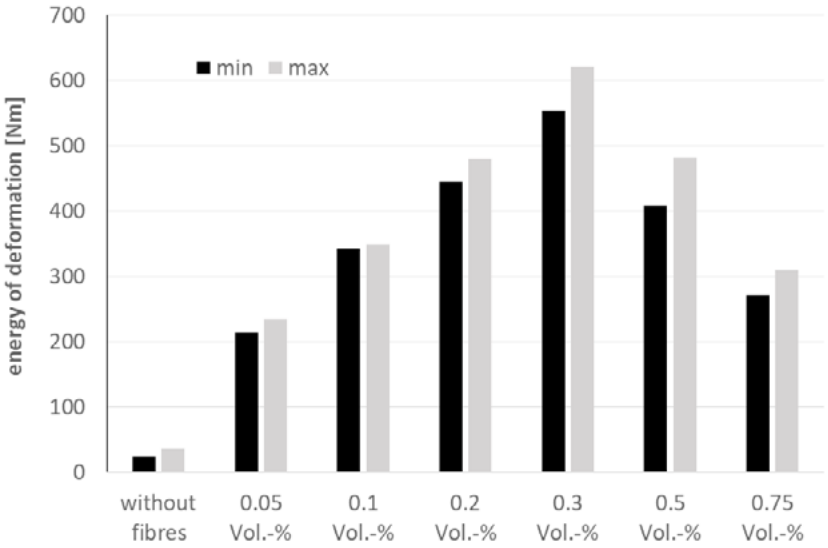

Figure 10: Minimum and maximum values (3 prisms) of the energy of deformation of mortars with increasing contents of not treated carbon fibres (reference)

Whereas the addition of fibres increases the energy of deformation for all types of materials, only for the much stiffer carbon fibres a further improvement by the functionalization of the fibres could be measured. The reason for the inefficiency of the functionalization applied to the elastic PAN and PP fibres could be the lateral contraction under load, which might lead to a delamination of the chemical bond between the hydrophilic fibre surface and the cementitious matrix. The results gained for the elastic fibres in the three-point bending test are confirmed by the individual fibre pull-through test. The load-displacement curve illustrates that after reaching the maximum load the bond between the fibre and the cementitious matrix breaks abrupt and subsequently the fibre is pulled out through the sample (Figure 11a). The PAN fibres exhibited in general higher maximum pull-out loads as the PP fibres. Both types of fibres however show no increase in the maximum load for the functionalized fibres compared to the reference, as shown in Figure 11b for the PAN fibres. The improvement of the mechanical performance by the functionalization of the carbon fibres quantified by the energy of deformation could unfortunately not be verified by the pull-through test. The brittle fibres broke while imbedding them into the mortar specimens so that the actual

test could not be performed.

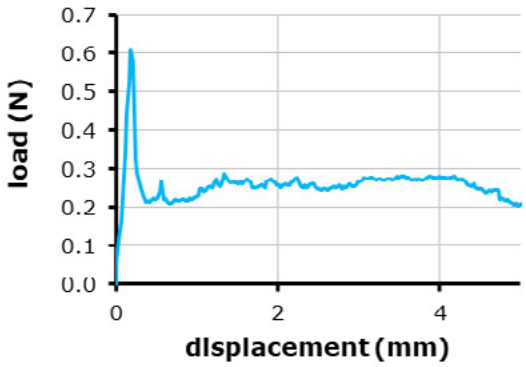

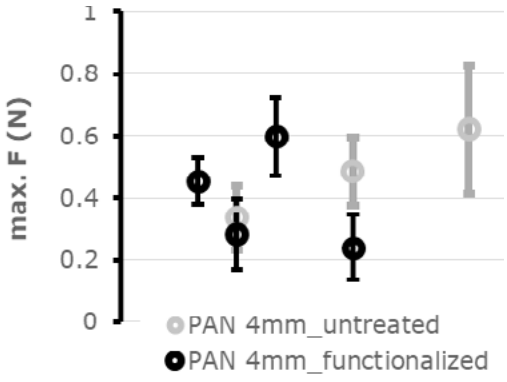

11a) 11b)

Figure 11a): load displacement curve of an untreated PAN fibre with an embedment depth of 4 mm
Figure 11b): Median values of the maximum loads (n=9) for the reference fibres and the functionalized PAN fibres with an embedment depth of 4 mm

The analysis of the crack formation due to shrinkage promoted by the wind tunnel test turned out to be very sensitive to slightest changes in the test conditions. The simultaneous test of several specimens positioned one after another (Figure 4) or in different heights did not generate consistent results. Also, specimens which were positioned in the wind channel with a delay of 10 minutes were not comparable to specimens moved immediately after manufacture. A further challenge was to define the content of untreated reference fibres. The volume had to be adjusted to allow enough crack formation so that a reduction due to the functionalization could be measured. After many preliminary tests and retries it could be proved that a fibre amount of 0,05 Vol.-% is suitable to evaluate the functionalization of the PAN fibres and for the carbon fibres an even smaller amount of 0,025 Vol.-% is enough. For the PAN-fibres the addition of untreated fibres did not decrease the formation of shrinkage cracks whereas the addition of functionalized fibres reduced the average crack opening area by about 50 %. The samples containing standard carbon fibres exhibited a reduction of about 10 % compared to the samples without fibres and the functionalization of the fibres further reduced the average crack opening area further by about 30 % (Figure 12).

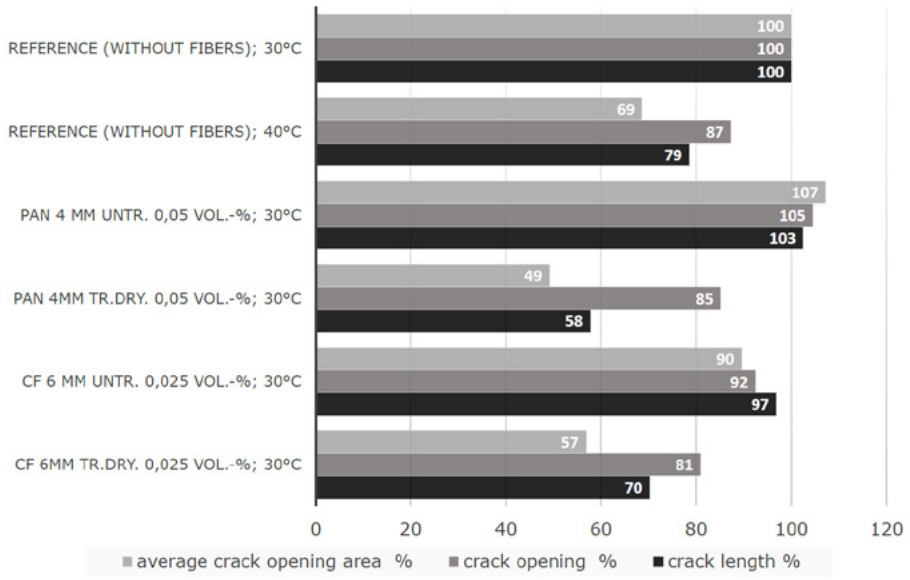

Figure 12: Geometrical parameters of the shrinkage cracks analysed after the wind tunnel test

ICSBM 2019
ID 002

normalized to 100 % of the specimen without fibres

4. Conclusions

- The tests performed confirm that the special functionalization developed by the project partner is efficient in improving the bond behaviour between the fibres and the cementitious matrix.
- To assess the efficiency of the functionalization in reducing shrinkage cracking a very lean mortar had to be formulated. Only after diluting the mortar with a high amount of limestone powder and strongly reducing the amount of fibres enough cracks were formed in the wind tunnel test.
- The test set-up to evaluate the crack formation during accelerated shrinkage in the wind tunnel proved to be very sensitive to slightest changes in the test conditions and therefore requires adequate statistics.
- For the mortar selected it could be demonstrated that the functionalization effectively reduced the average crack opening area for the elastic PAN fibres as well as for the brittle carbon fibres. Due to their worse performance in the individual pull-through test the analysis of the PP fibres regarding shrinkage cracking was deferred.
- The potential increase in ductility of the functionalization was evaluated by calculation of the energy of deformation derived from three-point bending tests. An improved mechanical behaviour could only be measured for the functionalized carbon fibres. The degree of improvement further proofed to depend on the batch of fibres. The maximum amount of functionalized fibres for achieving effectiveness was specified as 0,1 Vol.-%
- The results derived from the individual pull-through test confirmed that the functionalization of the polymer fibres does not affect the load transfer after incipient crack and are therefore in accordance with the results from the bending test. Because of their brittleness the pull-through test could not be performed with the carbon fibres.
- The analysis of the three-dimensional fibre distribution by CT revealed that the polymer fibres added in small amounts do not agglomerate but are not homogeneously distributed and oriented. The calculation of the effective elastic properties based on the derived orientation distribution function requires therefore adequate statistics.

5. Acknowledgment

This work was supported by the Bundesministerium für Bildung und Forschung (BMBF) grant 13N13306. The authors wish to express their gratitude to Natalia Rachmatulin for her comprehensive contribution to the achievements.

6. References

[1] A. Sobolkina, V. Mechtcherine, C. Bellmann, A. Leonhardt, 2013, Investigation of the surface propertiesof carbon nanotubes, 1st International Conference on the Chemistry of Construction Materials, Berlin, 157-160

[2] T. Schrepfer: Faserbewehrte Putze auf hochdämmenden Untergründen. Bauphysik 30 (2008), Heft 2, S. 117-122.

[3] P. Balaguru: Contribution of Fibers to Crack Reduction of Cement Composites During the Initial and Final Setting Period, ACI Materials Journal 91 (3) (1994), 280-288.

[4] N. Banthia, R. Gupta, Influence of polypropylene fiber geometry on plastic shrinkage cracking in concrete, Cement and Concrete Research 36 (2006), 1263-1267.

[5] C. Qi, J. Weiss, J. Olek: Characterization of plastic shrinkage cracking in fiber reinforced concrete slabs using image analysis and a modified Weibull function, Materials and Structures 36 (2003), 386-395.

[6] K. Pistol, F. Weise, B. Meng, U. Diederichs: Polypropylene fibres and micro cracking in fire exposed concrete. Advanced materials research 897 (2014), 284-289; Trans Tech Publ.

[7] Patent DE 4316 667 C1 (13.5.1993) "Hydrophile synthetische Armierungs- und Prozessfasern mit silikataffinen Eigenschaften"

[8] Patent WO 94/26969 (24.11.1994) "Variable liquid surface finishing medium"

[9] J. Peschel, H. Seibt, D. Ballschuh, R. Ohme: Sulfobetaine, Teil 5: Anwendung von Sulfobetainen als neue Zusatzstoffe für Chemiefaserpräparationen. Tenside Surf. Det. 30 (1993) 321

[10] DIN EN 1015-3: Methods of test for mortar for masonry - Part 3: Determination of consistence of fresh mortar (by flow table); German version EN 1015-3:1999+A1:2004+A2:2006

[11] Prüfplan für die Zulassungsprüfung von Polymerfasern zur Verwendung in Beton nach DIN EN 206-1 in Verbindung mit DIN 1045-2 mit nachgewiesener Wirksamkeit. Deutsches Institut für Bautechnik, Mai 2012.

[12] DIN EN 206-1: Beton – Teil 1: Festlegung, Eigenschaften, Herstellung und Konformität. Beuth Verlag GmbH, Berlin Juli 2001.

[13] DIN 1045-2: Tragwerke aus Beton, Stahlbeton und Spannbeton – Teil 2: Beton – Festlegung, Eigenschaften. Herstellung und Konformität. Beuth Verlag GmbH, Berlin August 2008.

[14] H. Hähne: Eigenschaften von mit Polyacrylnitril-Fasern verstärktem Beton. Beton und Stahlbetonbau 88 (1993), H. 1, S. 5-9

[15] T. Mishurova, N. Rachmatulin, P. Fontana, T. Oesch, G. Bruno, E. Radi und Igor Sevostianov: Evaluation of the probability density of inhomogeneous fiber orientations by computed tomography and its application to the calculation of the effective properties of a fiber-reinforced composite in International Journal of Engineering Science 122 (2018) pp 14-29, Elsevier, 2018

[16] T. Mishurova, F. Léonard, T. Oesch, D. Meinel, G. Bruno, N. Rachmatulin, P. Fontana und Igor Sevostianov: Evaluation of fiber orientation in a composite and its effect on material behavior, 7th Conference on Industrial Computed Tomography, Leuven, Belgium (iCT 2017) lecture and contribution in the conference proceedings

Reduced graphene oxide-coated copper foam composite cathode for the microbial electrosynthesis of acetate from carbon dioxide

P. Tremblay[1,2,3], T. Zhang[1,2,3]

[1]State Key Laboratory of Silicate Materials for Architectures, Wuhan University of Technology, Wuhan 430070, PR China

2School of Chemistry, Chemical Engineering and Life Science, Wuhan University of Technology, Wuhan 430070, PR China

[3]International School of Materials Science and Engineering, Wuhan University of Technology, Wuhan 430070, P. R. China

Abstract

5% of all man-made emissions of the greenhouse gas carbon dioxide in the world is generated by the cement industry. The bioconversion of CO2 into multicarbon products of interest such as biofuels is a particularly efficient and versatile strategy to create value from greenhouse gas and to reduce their footprint on the environment. Chemical or biological CO2 reduction requires an energy source, which ideally should be renewable and inexpensive. One promising and novel technology for biological CO2 reduction is microbial electrosynthesis (MES) where a biocatalyst uses electrons from the cathode of an electrochemical system to reduce inorganic carbon into useful organic carbon molecules.

In essence, MES makes it possible to plug biocatalysts into the power grid and tap energy for biological CO2 conversion. Electrochemical systems for MES are usually powered by renewable sources of electricity such as wind or solar. Additionally, MES reactions can also be partly driven by useful biological oxidation reaction at the anode such as organic carbon removal from municipal, commercial or industrial wastewater. Here, we describe the development of a novel high-performance cathode for MES made of a copper foam core and coated with reduced graphene oxide (rGO). Copper is a highly conductive and inexpensive cathode material widely employed in electrochemical apparatuses. However, the antimicrobial properties of copper limit its usage in bioelectrochemical systems.

Thus, we coated biocompatible and conductive rGO on copper foam and tested the resulting electrode in a MES system where the acetogenic bacterium Sporomusa ovata was catalyzing the conversion of electricity and CO2 into acetate. The novel composite cathode combines the outstanding physicochemcial and electrical properties of copper with the biocompatibility of rGO to enable the fast MES of acetate at a rate of 1697.6 mmol m-2 d-1. A current density of -21.6 A m-2 and a Coulombic efficiency of 70.2 % were also observed. Acetate production rate by MES with the rGO-coated copper foam cathode was 21.3 times and 7.6 times faster than uncoated copper foam and pure rGO foam cathodes, respectively.

The results demonstrated the potential of copper in bioelectrosynthesis systems and led to the conclusion that rGO-copper foam composite is a promising cathode material for the scaling up of MES and the reduction of CO2 emitted by industries such as cement.

Keywords: Carbon dioxide emission, Bioproduction, Microbial electrosynthesis, Bioelectrochemistry, Acetate

Prewashed wood ash for utilization in cement-based materials

N.M. Sigvardsen[1], J. Pedersen[1] and L.M. Ottosen[1]

[1]Department of Civil Engineering, Technical University of Denmark, Kgs. Lyngby, Denmark

Email of the corresponding author: nimasi@byg.dtu.dk

ICSBM 2019
ID 047

Abstract

In the transition towards a more sustainable energy system, renewable energy sources, e.g. wood, are of significant importance in the withdrawal of the coal-fired power plants. This leads to a decrease in the availability of the by-product coal fly ash, which is traditionally used in the concrete production, and to an increase in the residual waste, wood ash. The performance of wood ash in cementitious materials varies markedly throughout the literature depending on the physicochemical characteristics, determined by, e.g. the wood product, temperature, combustion method, and on pretreatment of the wood ash before utilization. This aim of this study was to determine the influence from the physicochemical characteristics of wood ash from grate combustion of wood pellets and the properties of cementitious materials. The work includes both with partial cement replacements with the untreated (marked WA) and prewashed WA (marked WA-W).

The WA was divided into two portions. One portion was subjected to a washing treatment as follows: WA and distilled water were mixed to an L/S (liquid-to-solid) ratio 5 and shaken for 1 min. After settling, the water was decanted. This procedure was repeated three times and the suspension was vacuum-filtered. The morphology of the particles for cement, WA and WA-W was evaluated with SEM. Cementitious materials with 10 wt% cement replacement with WA and WA-W, respectively, were investigated. The w/b-ratio for all mixes was kept at 0.55. The workability was determined according to EN 196-3, the setting time according to EN 196-3 and the compressive strength at 7, 14, 28, 60 and 90 days according to EN 196-1. Development of phases were measured on cement paste with 10 wt% cement replacement with WA and WA-W, respectively, by XRD and TGA at 7, 14, 28, 60 and 90 days. Reference tests were conducted for all test with 100 wt% cement.

Use of WA and WA-W in the mortar mix resulted in a decrease in the workability due to the water absorption of the WA and WA-W and a delay in the setting time compared to reference mixtures. A more distinctive decrease in the compressive strength was seen for WA compared to WA-W. The delayed setting time and the decrease in compressive strength can both be attributed to the clinker dilution effect for both ashes. The rounded particles (filler effect) determined by SEM and the increase in portlandite content determined by TGA for WA-W can explain the higher compressive strength when WA-W is utilized compared to WA. The phase development showed a decrease for portlandite and the ettringite content for pastes containing WA and WA-W, more profound for WA. Thus, the washing treatment of wood ash from grate combustion of wood pellets facilitates a wood ash more suitable for utilization in cement-based materials.

Utilization of wood ash in cementitious materials presents new challenges. However, due to the possibility for hydraulic activity and the particles to function as a filler, the potential for wood ash as a partial cement replacement should be taken into consideration for new and sustainable cementitious materials.

Keywords: wood ash, prewashing, cementitious materials

Investigating the efficiency of "in-house" produced hydrogels as internal curing agents in cement pastes

J.R. Tenório Filho[1,2], E. Mannekens[3], D. Snoeck[1], N. De Belie[1]

[1]Magnel Laboratory for Concrete Research, Department of Structural Engineering, Faculty of Engineering and Architecture, Ghent University, Tech Lane Ghent Science Park, Campus Ardoyen, Technologiepark Zwijnaarde 60, B-9052 Gent, Belgium.

[2]SIM vzw, Technologiepark 48, Zwijnaarde B-9052 Ghent, Belgium.

[3]Chemstream bvba, Drie Eikenstraat 661, 2650 Edegem, Belgium.

ICSBM 2019
ID 049

Abstract

Appropriate curing is of utmost importance to guarantee that a concrete structure (or any cementitious material) achieves proper hydration and can provide the user with the best of its desired properties. For most of conventional concrete compositions external curing has proven to be effective, but the advent of the (ultra) high performance showed a different reality. Given its finer microstructure, the water from external curing methods cannot always penetrate the whole depth of the structure. External curing thus is not efficient in preventing problems such as cracking due to autogenous shrinkage, but a solution could be to include an internal curing system. Alternative inclusions such as lightweight aggregates and shrinkage-reducing admixture (SRA) have been studied and used as internal curing agents. Recently, researchers have been investigating the use of hydrogels or superabsorbent polymers for internal curing purposes and the results are promising. In this paper three different "in-house" produced polymers are studied as internal curing agents in cement pastes. The polymers differ in chemical composition leading to different properties. Initially they were tested for the water uptake in artificial cement pore solution by means of a filtration test and further tested in cement pastes with a range of w/c ratios from 0.30 to 0.40. Their efficiency as internal curing agents was assessed by means of autogenous shrinkage measurements with corrugated tubes for a period of seven days. All three polymers showed promising results in the mitigation of the autogenous shrinkage but two of them with the pitfall of requiring a higher amount of additional water. To summarize, the hydrogels are indeed interesting as internal curing agents but attention should be given to their chemical composition and physical aspects since for each application different properties are required.

Keywords: hydrogels, autogenous shrinkage, cement, superabsorbent polymers.

1. Introduction

Most of the deteriorating mechanisms acting on concrete structures are related to the ingress of aggressive agents inside structures. Even before reaching its hardened state, a cement-based material is subjected to crack formation especially due to the effects of shrinkage during the early age. The formed porosity of the material can become the perfect path for the ingress of those aggressive agents. After the formation the water intrusion causes a drop in pH of the concrete that can lead to steel corrosion; the ingress of

chlorides causes the de-passivation of the protective film, the intrusion of CO_2 can cause carbonation and both processes can accelerate the corrosion.

The shrinkage phenomena, especially when referring to autogenous and plastic shrinkage, are inherent to the hydration process of the cementitious material and (among other factors) are a function of the water-to-cement ratio and curing conditions (temperature and humidity). The autogenous shrinkage is related to the self-desiccation initiated in the pores of the material due to the hydration process [1].

Appropriate curing is of utmost importance to guarantee that a concrete structure (or any cementitious material) achieves proper hydration and can provide the user with the best of its desired properties. For most of conventional concrete compositions external curing has proven to be quite effective, but the advent of the (ultra) high performance showed a different reality. Given its finer microstructure, the water from external curing methods cannot always penetrate the whole depth of the structure. External curing thus is not efficient in preventing problems such as cracking due to autogenous shrinkage, but a solution could be to include an internal curing system. Alternative inclusions such as lightweight aggregates and shrinkage-reducing admixture (SRA) have been studied and used as internal curing agents. Recently, researchers have been investigating the use of hydrogels or superabsorbent polymers (SAPs) for internal curing purposes and the results are promising [2-4].

Superabsorbent polymers (or hydrogels) are a natural or synthetic water-insoluble 3D network of polymeric chains cross-linked by chemical or physical bonding. They possess the ability to take up a significant amount of fluids from the environment (in amounts up to 500 times their own weight). The swelling and posterior water release are of great interest in the study of smart self-healing materials but can also be explored to promote self-sealing [2-5]. In this paper, three different in-house produced SAPs are presented as alternative for promoting internal curing in cement pastes.

All SAPs are produced with different co-monomers (Figure 1), each of them being designed to have different swelling capacities. The required properties of the SAPs were based on the properties found in literature for commercially available SAPs aiming at a proper internal curing of cementitious materials.

The internal curing efficiency of the SAPs was evaluated by means of an autogenous shrinkage test. A filtration test and slump flow test were also performed to assess the water uptake by the SAPs and their influence in the workability of the mixtures.

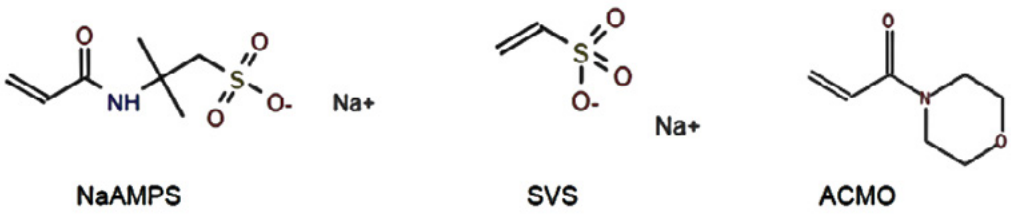

Figure 1: Co-monomers that were used in the SAPs from ChemStream.

2. Methodology

2.1 Materials

All tests were performed on cement pastes produced with cement type CEM III-B 42.5N – LH/SR; a polycarboxylate superplasticizer (at a constant dosage of 0.3 m% in relation to the cement mass; Glenium 51, 35% conc.); an effective water to cement ratio of 0.3; three different hydrogels (all in-house produced) with a dosage in the range of 0.023 m% to 0.4 m%. The composition of the studied mixtures can be found

in Table 1.

Table 1: Composition of the mixtures studied.

Mixture	Cement [kg/m³]	Mixing water [kg/m³]	Superplasticizer [kg/m³]	SAP [kg/m³] (m%)	Additional water [kg/m³]	w/c	
						Effective	Total
REF1	1620	486	4.86	0	0	0.3	0.3
REF2	1490	447	4.47	0	0	0.354	0.354
SAP1.1	1490	447	4.47	0.34 (0.023%)	80.46	0.3	0.354
SAP1.2	1198	359.4	3.59	1.31 (0.11%)	259.96	0.3	0.517
SAP2.1	1490	447	4.47	2.01 (0.135%)	80.46	0.3	0.354
SAP2.2	1393	417.9	4.17	2.78 (0.2%)	139.3	0.3	0.4
SAP3	1490	447	4.47	5.96 (0.4%)	80.46	0.3	0.354

All SAPs were produced by ChemStream and have been tested specifically for use in cementitious materials.

SAP type 1 is a SAP composed of 2 co-monomers NaAMPS (2-acrylamido-2-methyl-1-propanesulfonic acid sodium salt) and SVS (sodium vinyl sulfonate) that are lightly cross-linked. Both co-monomers contain the sodium salt form of a sulphonic acid group, which leads to a very densely charged hydrogel with great osmotic power for absorbing water. This type of SAP-composition is based on ChemStream's prior art EP2835385.

SAP type 2 is a SAP that is similar to SAP type 1, since it mainly consists of co-monomer NaAMPS, but it is 'diluted' with a non-charged or neutral monomer ACMO (acryloyl morpholino acrylate) (20% mol).

SAP type 3 is also very similar to SAP type 1, because it is solely composed of monomer NaAMPS but with a lower absorption capacity.

More information on the properties of the SAPs can be found in Table 2.

Table 2: Properties of the SAPs.

SAP	Mean particle size D_{50} [µm]	Absorption capacity* [g/g]	Soluble materials [%]
SAP1	100	275	36
SAP2	100	261	9
SAP3	100	54	8

*For absorption in demineralized water after 24 hours

2.2 Methods

The absorption capacity of the SAPs was evaluated by means of a filtration test using cement filtrate (1 kg of cement CEM III-B 42.5N – LH/SR and 5 l of demineralized water) at 10 min and 24h after the first contact of the dry hydrogels with water.

Afterwards the absorption capacity in real cement pore fluid was assessed by means of slump flow test with the cement pastes mentioned in Table 1. The principle of this test is to add a certain amount of SAPs to a cement paste with w/c of 0.354 (theoretical value for a complete hydration of the system according to [6, 7]) until the slump flow measured equals the value of the reference cement paste REF1. By doing so, it is assumed that the difference in water content of both reference mixtures (w/c of 0.054) is totally absorbed

by the SAPs. The average slump of the reference mixture REF1 was 300 ± 15 mm. The measurements were performed after 10 min counted from the moment the water was added to the mixture.

The internal curing effect of the SAPs was evaluated by means of a shrinkage test, performed with corrugated tubes, in compliance with ASTM C1698-09. The measurements of deformation were performed automatically with linear variable differential transducers (LVDT) with a range of 5 mm (Figure 2). From the total deformation curve, the autogenous shrinkage strain was calculated zeroing the deformations at the knee-points of the original curves [8] (Figure 3).

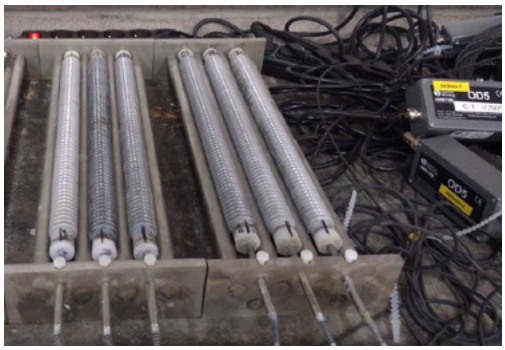

Figure 2: Set up for the autogenous shrinkage measurement.

In some cases, the amount of SAP determined to absorb the additional amount of water corresponding to the additional 0.054 in the w/c ratio was not enough to completely mitigate the autogenous shrinkage of the mixture. For those cases, the amount of SAP was increased and the additional water inserted in the system was corrected to achieve a fully mitigation of the autogenous shrinkage. This justifies the existence of mixtures SAP1.2 and SAP2.2 (shown in Table 1) for which results will be presented in the following section.

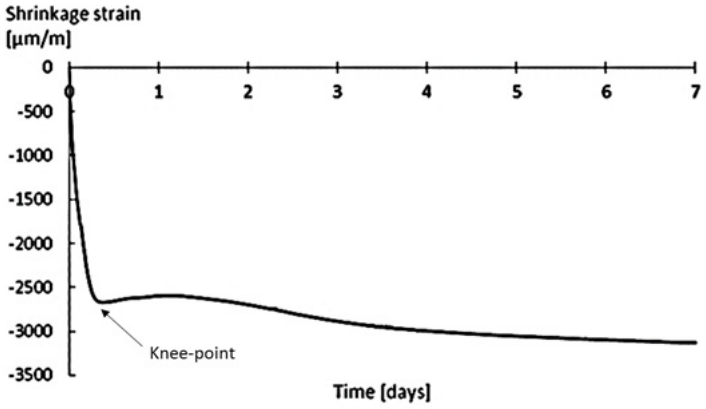

Figure 3: Illustration of the knee-point in the shrinkage strain curve over time for a cement paste.

3. Results and discussion

The absorption capacity of the SAPs in the different media shows different trends in behavior for the studied hydrogels (Figure 4).

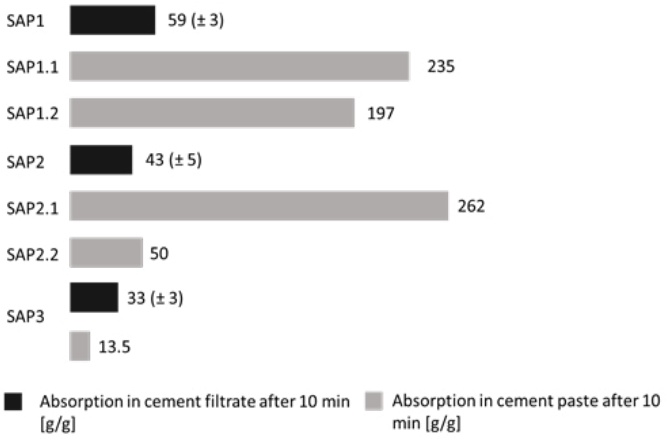

Figure 4: SAP1 and SAP2 present a higher absorption capacity in cement paste in comparison with cement filtrate. SAP3 shows the opposite.

SAP1 and SAP2 both present a higher absorption capacity in the cement paste in comparison to the cement filtrate solution. The opposite was noticed with SAP3, which is in accordance to the behavior of commercially available hydrogels reported in other studies [9]. By increasing the amount of SAPs in the system (mixtures SAP 1.2, and SAP 2.2) the increase in the required additional water did not show a linear behavior. This is also mentioned by [10] and can be explained by the change in the concentration of ions in the system that occurs when more water is added and its influence on the sorption/desorption kinetics of SAPs.

In terms of chemical composition, SAP1 is more densely charged in comparison to SAP2 and SAP3 which theoretically would lead to a higher absorption capacity. The fact the this absorption is higher in the cement paste in comparison to the cement filtrate shows evidence that more variables are influencing the kinetics of the SAPs once they are in contact with the paste (the presence of superplasticizer, for example).

The results for autogenous shrinkage of the mixtures are show in Figure 5.

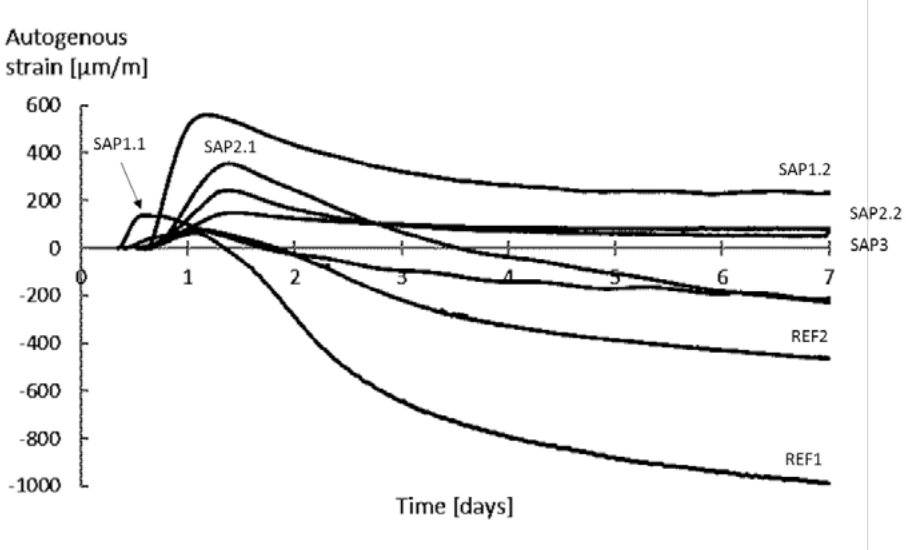

Figure 5: All SAPs promote a reduction in the autogenous strain of the cement paste in comparison to the references without SAPs. SAP3 shows the most promising result in terms of additional water and effective internal curing.

All SAPs promote a reduction in the autogenous strain in comparison to the both references. Considering only the mixtures SAP1.1, SAP2.1 and SAP3 in comparison with the REF2 (all of them with the same total

w/c ratio) only SAP3 is able to completely mitigate the autogenous shrinkage. Still, both mixtures SAP1.1 and SAP2.1 show a shrinkage strain lower than the reference.

In both mixtures SAP1.2 and SAP2.2 there is complete mitigation of the autogenous shrinkage during the complete period of testing (seven days). However, the total w/c ratio of both mixtures is higher in comparison to the references (0.517 and 0.4). In that case, in order to verify the real efficiency of the SAPs in those mixtures, new references should be mixed with the same w/c ratios (0.517 and 0.4) to assess till what extent the mitigation of shrinkage is due to the controlled released of water promoted by the SAPs or due to the higher amount of free water in the system. Also for clarification of that matter, the water release of the SAPs in the mixtures should be investigated, especially for SAP1 and SAP2. This should reveal why SAP3 showed a completely mitigation of the autogenous shrinkage with the same w/c ratio as REF2 while the other SAPs needed to be added in a dosage higher than initially defined.

4. Conclusions

Despite the differences in chemical composition and properties, all SAPs showed promising results. In the range of 0.2-0.4 m% a complete mitigation of autogenous shrinkage was obtained with a very small increase in the total w/c of the mixtures and an amount of 0.1% led to a reduction of around 80% in the shrinkage strain.

SAP1 and SAP2 showed a different behavior depending on the amount of SAP and water in the system, in comparison with SAP3. Further study is needed to investigate the kinetics of water release by the SAPs in the different situations presented in this paper.

The addition of SAPs and water in the system might also have effects (not only positive) on other aspects of the cementitious materials such as mechanical strength, setting time, microstructure and so on. All these influences should be taken into account when deciding to use a specific type of SAP and a balance should be made between its positive and negative influences in order to choose the SAP that best suits a certain application.

5. Acknowledgment

The work has been financed by SIM program SHE (Engineered Self-Healing Materials) within the ICON project iSAP (Innovative SuperAbsorbent Polymers for crack mitigation and increased service life of concrete structures).

6. References

[1] Sahinagic-Isovic, M., Markovski, G., Cecez, Marko. Shrinkage strain of concrete – causes and types. Journal of the Croatian Association of Civil Engineers, GRADEVINAR 64 9, 727-734. 2012.

[2] Snoeck, D. Self-Healing and Microstructure of Cementitious Materials with Microfibres and Superabsorbent Polymers. Doctorate thesis – Faculty of Architecture and Engineering/Ghent University. Belgium, 2015.

[3] Mechtcherine, V., Dudziak, L., & Hempel, S. Mitigating early age shrinkage of Ultra-High-Performance Concrete by using Super Absorbent Polymers (SAP). Paper presented at the Creep, Shrinkage and Durability Mechanics of Concrete and Concrete Structures, Ise-Shima, Taylor & Francis, 847-853. 2009.

[4] Jensen, O.M. Use of superabsorbent polymers in construction materials. Paper presented at the International Conference on Microstructure Related Durability of Cementitious Composites, Nanjing, RILEM Publications S.A.R.L., 757-764. 2008.

[5] Mignon, A., Snoeck, D., Dubruel, P., Van Vlierberghe, S., De Belie, N. Crack mitigation in concrete : superabsorbent polymers as key to success? Materials, 10(3), 237. 2017.

[6] Powers, T.C., & Brownyard, T.L. Studies of the physical properties of hardened Portland cement paste (Vol. 22). Cornell: Portland Cement Association, Research Laboratories, pp. 892. 1948.

[7] Jensen, O.M., & Hansen, P.F. Water-entrained cement-based materials I. Principles and theoretical background. Cement and Concrete Research, 31(4), 647-654. 2001.

[8] Lyu, Y. Autogenous Shrinkage of Cement-Based Materials: From the Fundamental Role of Self-Desiccation to Mitigation Strategies Based on Alternative Materials. Doctorate thesis – Faculty of Architecture and Engineering/Ghent University. Belgium, 2017.

[9] Tenório Filho, José Roberto; Snoeck, D. ; Belie, N. . The effect of superabsorbent polymers on the cracking behavior due to autogenous shrinkage of cement-based materials. In: 60 Congresso Brasileiro do Concreto, 2018, Foz do Iguaçu. Anais do 60 Congresso Brasileiro do Concreto, 2018.

[10] Ma, X., Yuan, Q., Liu, J., Shi, C. Effect of water absorption of SAP on the rheological properties of cement-based materials with ultra-low w/b ratio. Construction and Building Materials, 195, 66-74. 2019.

The course of water absorption and desorption from superabsorbent polymers (SAP) in cementitious environment

M. Kalinowski[1], P. Woyciechowski[1]

[1]Warsaw University of Technology, Department of Civil Engineering.

Abstract

Superabsorbent polymers (SAP) are compounds that are able to absorb water increasing their mass and volume, resulting in mass exceeding the staring value by hundreds times or more. Their absorption capacity depends on the water absorption environment – the higher alkali content, the worse is the capacity. In terms of concrete technology, the laboratory tests results indicate that the SAP absorption capacity in tap water is about ten times higher than in the environment of liquid solution of alkali content which is to simulate the cement paste environment. Taking into consideration the potential function of SAP in hardening process of cement binder as an. internal curing agent, the course of desorption of water from SAP particles should be taken into consideration while designing composites. The paper investigates the course of SAP water absorption/desorption in the environment of cement pastes of water/cement ratio ranging from 50 to 0.5, by means of a teabag tests. In regards to absorption tests results it was found that the absorption capacity of SAP decreases along with the decrease of the water/cement ratio. To evaluate the dynamics of course of water absorption of SAP, the time of reaching the 95% of the maximal absorption was analysed. Depending on the water/cement ratio of the absorption environment, it occurred within 2-40 minutes from the preparation of cement paste. The methodology of tests of water desorption from SAP included obtaining full saturation of SAP in the tap water and placing it in the cement paste solutions of water/cement ratios varying from 50 to 0.5. and determining the course of SAP mass change in time. It was found that in cementitious environment the process of water desorption from SAP was much slower than in case of water absorption. Desorption tests lasted approx. 24 h depending on the water/cement ratio. Obtained results show strong impact of paste characteristics on the course of SAP water absorption and desorption in various cementitious composites.

Keywords: superabsorbent polymers, absorption, desorption, water migration, cement composites.

1. Introduction

Superabsorbent polymers (SAP) could be described as a group of cross-linked polyelectrolyte polymers capable of absorbing high amounts of water while maintaining a three-dimensional structure [1-2]. Due to high osmotic pressure caused by accumulation of ions in SAPs structure, when exposed to water environment superabsorbent polymers swell, i.e. absorb water, in order to reduce aforementioned pressure [3]. With such a model of SAPs interaction with water solutions in mind, its absorption capacity depend not only on the chemical composition of any given SAP but is also influenced by external pressures resulting from SAPs change in volume in the process of absorbing water [4]. Additionally, the alkalinity of the environment in which the absorption takes place has an influence on the overall absorption capacity [5].

In concrete technology SAP is used as an internal curing agent – if the balance between osmotic pressure

within SAP saturated with water and the internal stresses in cementitious composite is lost, SAP is able to reduce its volume, i.e. desorb water [6]. By using this effect, the kinetics of water migration within the capillary network can be altered and wide range of composite properties can be affected as a result, including modification of the degree of hydration [7], autogenous shrinkage [8], compressive strength [9] or changes in pore network distribution itself [10]. With such an impact on properties of cementitious composites, in order to fully predict and control the influence of SAP only on the properties that one wants to alter, as much information on properties of SAP in cementitious environment as possible should be gathered, including SAPs granulation and its properties concerning course of water absorption and desorption in the cement paste environment. Those properties would be crucial to predict SAPs capabilities to modify the capillary network and alter the water migration within the cementitious composite.

In order to evaluate water absorption properties of SAP, several testing methods have been developed, including teabag method test and others [11]. Usually, these tests are performed in liquid solutions that are to simulate the pH and alkali content of cement paste. However, those variables are not the only ones that have the influence on SAP properties in a cement paste. Another property of cement pastes that cannot be taken into account in an absorption tests performed in a liquid environment is that cement paste environment could be described as a porous fluid consisting of several phases. Those contribute to changes in the kinetics of water migration compared to tests performed in liquid water solutions, i.e. by taking into account the impact of solid particles of cement in the absorption/desorption environment on the SAP properties and the capillary pressures resulting from presence of several phases in the cement paste . By studying and experimenting with SAP behaviour in the environment most similar to the one of cementitious composite, ambiguous SAP influence may be easier to quantify.

The aim of the study was to investigate the course of water absorption and desorption from SAP in cementitious environment and identify variables that have the biggest impact on SAP properties. By modifying the content of cement particles in tested solutions, i.e. by performing water absorption/desorption tests in cement pastes of different water-cement ratios, an environment most close to the actual SAP activation environment in concrete technology was created. SAP is most usually used in concrete technology as an internal curing agent. It would suggest that the desorption mechanics of those polymers should have the biggest significance when designing cement composites modified with that kind of modifier. The role of internal curing agents in composite is to maintain the internal humidity within the pore/capillary network at as high level for as long as possible. Without understanding SAPs properties concerning course of water desorption and focusing only on the water absorption properties, full potential of SAP may be yet not fully achieved in concrete technology. By focusing only on SAP absorption properties, a misinterpretation of its properties is indicated by assumption that the course of water desorption from SAP is directed in the same way as course of water absorption but with negative coefficients.

The information about SAP absorption potential in activation environments characterized by different water-cement ratios may also ensure an useful approximation of the change in SAP properties dependent on water-cement ratio and help to improve its effectiveness in concrete technology. Others articles on the subject of SAP absorption characteristics in different environments suggest that absorption potential in liquid environments with high alkali content is of a level of magnitude lower then in the environment of water. By confirming this hypothesis, simplification of SAP properties could be formed and the design process of cement composites incorporating SAP could be developed.

ICSBM 2019
ID 060

2. Methodology

2.1 Materials

Cement CEM I 42,5 N was used as a binder in all of the tested cement pastes. Its properties were in accordance with EN 196 standard. In order to obtain cement pastes with various water-binder ratios, water with properties in accordance with EN 1008 standard was used. Prepared cement pastes that served as water absorption/desorption environment for SAP were characterized by different water-binder ratios (Tab. 1). The water-cement ratios of the tested cement pastes were designed between 0.5 and 500. While it's unreasonable to think that water-cement ratios above 0.5 have any use in concrete technology, especially concerning UHPC or other high performance cement composites, the range of properties of tested cement pastes was designed in order to track the change in SAP properties dependant on the change from liquid environment of absorption to the one of porous liquid. As the properties of porous liquid in cement pastes start to present themselves in a solution of water-cement ratio approx.. 1-2, those values had to be included in the research program. Furthermore, this experiment was conducted in order to track the properties of SAP that could be used in concrete, not in order to design new types of cement pastes with extremely high water-cement ratios. The cement paste with water-cement ratio of 500 was to simulate water activation environment with pH level of 12.3.

Table 1: Water-binder ratios of cement pastes which served as water absorption/desorption environment.

Cement paste ID	Water-cement ratio [g/g]
CP05	0,5
CP1	1,0
CP2	2,0
CP5	5,0
CP50	50,0
CP500	500,0

Superabsorbent polymer which properties were tested during experiments was characterized by granulation measured using HORIBA Compact Laser Diffraction Particle Size Analyzer (Fig. 1) ranging from 175 to 595 [μm] and was of properties presented in Tab. 2.

Table 2: Material characterization of the superabsorbent polymer used in research program.

Characteristic	SAP S
Chemical characterization	Potassium acrylate and acrylic acid polymer
Solubility in water	Insoluble
Polymerization process	Invert suspention polimerisation

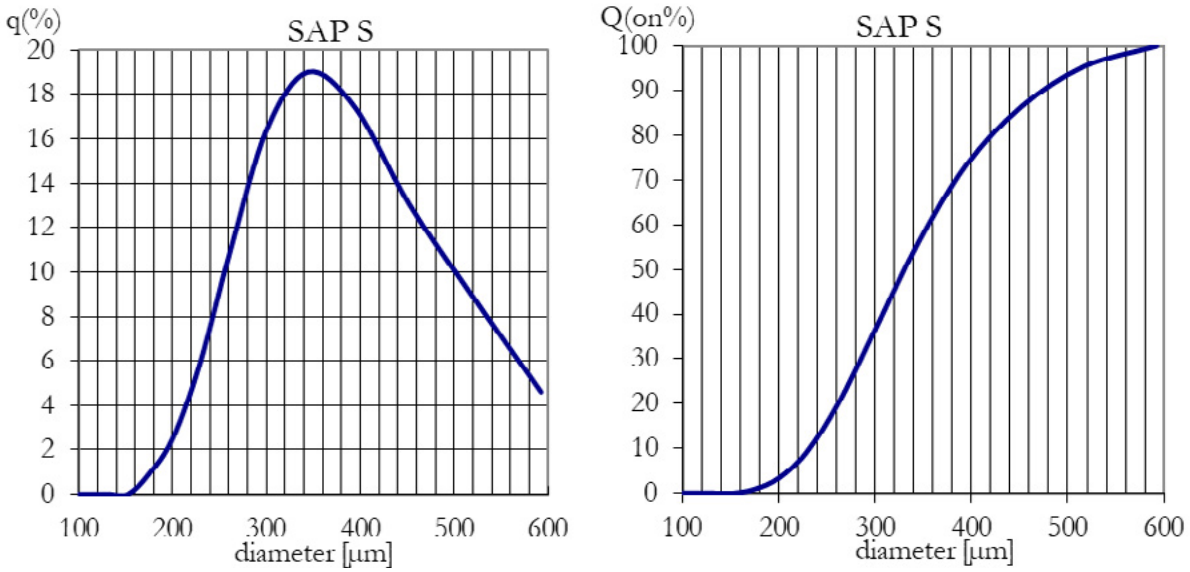

Figure 1: SAP S granulation measured by means of Laser Diffraction.

ICSBM 2019
ID 060

2.2 Methods

In order to estimate the influence of water-binder ratio of the cement paste on the absorption properties of SAP, a regular teabag method test was conducted. It included sealing a known mass of SAP in a teabag of a known mass and measuring the increase in mass dependent on a time spend in the absorption environment. In order to mitigate the influence of cement paste mass gathering on the outer side of the teabag, a reference sample with no sealed SAP was prepared and put into cement paste of the same water-binder ratio. The increase of mass on the reference sample was then subtracted from the sample with sealed SAP at every measurement point. The test lasted for 60 minutes as it proved sufficient to reach maximal water absorption capacity of SAP in each of the tested cement pastes.

A slightly modified methodology was adopted in a case of desorption tests in order to determine SAPs water desorption parameters. It involved preparing fully saturated SAP teabag sample in tap water environment which was then inserted into cement paste of a given water-binder ratio. Unlike the absorption test, desorption tests lasted approx. 24 hours. The reduction in mass of the teabag sample was then considered as the amount of water that was released from SAP into the cement paste. As in the absorption tests, a reference sample was prepared for each of the tests in order to mitigate the effect of mass increase on the outer side of the teabag exposed to cement paste environment which would have significant impact on the results if left unchecked.

3. Results and discussion

The absorption tests results (Fig. 2) suggest a decrease in SAP water absorption capacity along with a decrease of water-binder ratio of the cement paste which served as an absorption environment. Obtained results were in accordance with other experiments on the subject [12], however the change from liquid absorption environment to gel cement paste could suggest an additional explanation for the reduced absorption capacity in cement pastes with lower water-cement ratios. The SAP water absorption capacity in any given absorption environment was defined as an asymptote value of the hyperbolic trend line that estimated the course of SAP water absorption (Tab 3). The time of SAP activation was defined as the time required for tested SAP to reach the level of 95% of the asymptote value (Tab 3). The influence of alkali content of the solution on the properties of SAP is undeniable – however additional effect reducing the SAP water absorption capacity in certain environments, in form of solid particles in the absorption

environment is present in cement pastes. The aforementioned influence presents itself in form of different times required by SAP to achieve its maximal saturation in any of the tested absorption environments (Tab. 3).

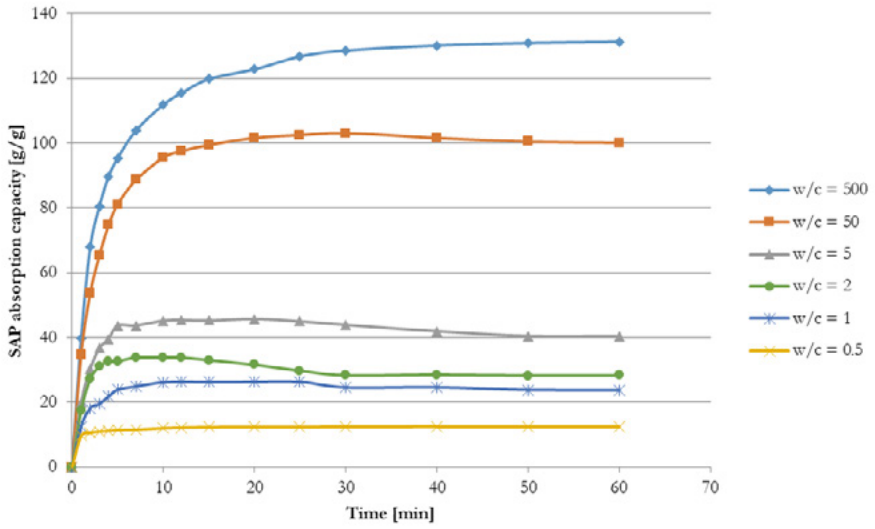

Figure 2: SAP water absorption capacity vs time for cement pastes of different water-binder ratios serving as water absorption environments.

Table 3: Asymptote values for hyperbolic trend lines that estimated the course of SAP water absorption and the time required for SAP to reach 95% of its maximal water absorption capacity.

Cement paste ID	Asymptote value [g/g]	95% of the asymptote value [g/g]	Time required by SAP to reach 95% of water absorption capacity [min]
CP500	135,3	128,5	40,1
CP50	105,8	100,5	24,1
CP5	44,1	41,9	5,4
CP2	31,2	29,6	2,5
CP1	25,5	24,2	6,4
CP05	12,2	11,6	3,4

This phenomena could be explained by shortage of water in the close distance from the teabag containing SAP. As the water is removed from between cement particles, an increasing in strength capillary pressure reduces the water migration within the capillary network towards the area of SAP absorption. Also, as the cement grains have high surface areas, there's a limited volume of water that can overcome combined effect of the surface tension of the cement grains, the capillary forces of the porous liquid and the influence of the ions present in the cement paste. The influence of all those variables was combined and resulted in a decrease in SAP water absorption capacity as the water-cement ratio of the cement paste that served as water absorption environment.

The course of SAP water absorption capacity in a function of water-binder ratio of tested cement pastes (Fig. 4) shows a logarithmic dependence between absorption capacity achieved at any time by SAP and the water-binder ratio of the cement paste which served as an absorption environment.

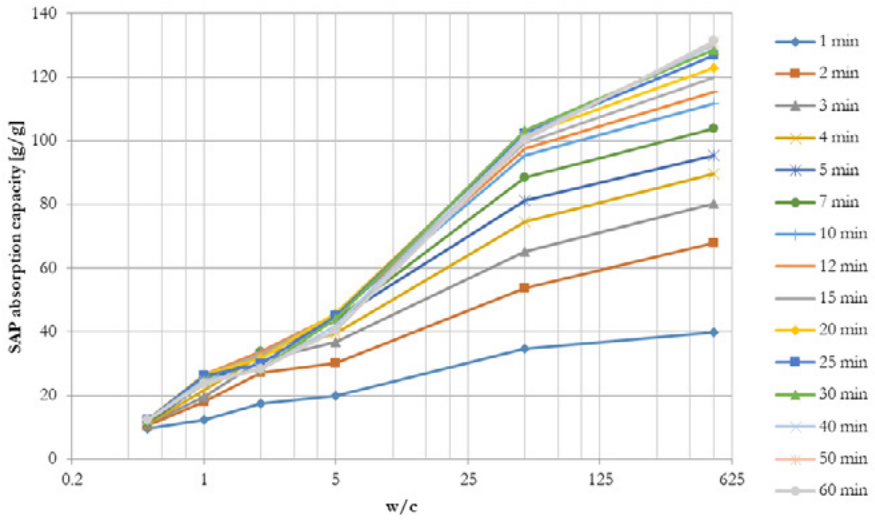

Figure 4: SAP water absorption capacity vs w/c ratio, for different measurement points.

With small differences in the coefficients of the logarithmic trend lines between different time of measurements, one can observe that the hypothetical water-binder ratio of the cement paste environment in which the SAP water absorption capacity would be zero, presented itself between 0.2-0.3, the amount of water that is usually used in full for hydration purposes [13]. Unfortunately, water absorption tests in cement pastes characterized by such low water-binder ratios would be extremely inaccurate, hence this hypothesis would be difficult, if not impossible, to confirm experimentally.

Between tested cement paste a severe difference in SAP water absorption capacities were observed. The cement paste with water-binder ratio at 500 illustrates the maximal SAP water absorption capacity. The absorption in cement paste characterized by water-binder ratio of 0.5 was approx. 10 times lower than the SAP maximal water absorption capacity. It's reasonable to assume that in absorption environments characterized by even lower water-cement ratios, SAPs water absorption capacity would be further limited, although this motion would need to be verified experimentally. However, the assumption that SAP water absorption potential in cement pastes of water-cement ratio of 0.5 is approx. 10 times lower that the one of SAP activated in water presents itself as an reasonable starting point for designing cement composites modified with SAP. As the water desorption from SAP tests were performed in cementitious environments, the duration of those test was dependant on the properties of cement pastes and the course of hydration – the last measurement was performed after 24 hours from placing the teabag containing SAP in the test solution. The desorption tests results (Tab 4 and Fig 6) suggest even stronger influence of an additional variable except the ion content in the water desorption environment on the course of water migration from SAP.

Table 4: Initial and final results of SAP absorption capacities in different desorption environments.

Cement paste that served as SAP water desorption environment	Initial SAP water absorption capacity [g/g]	Final SAP water absorption capacity after 24 h [g/g]	105 % of SAP water absorption capacity in cement paste that served as water desorption environment [g/g]
CP50	132.1	110.5	111.1
CP5	132.1	36.8	46.3
CP2	130.3	11.4	32.8
CP1	131.9	14.4	26.8
CP05	130.4	30.3	12.8

As cement paste with low water-cement ratio cannot be treated as a fluid, presence of alkali in cement pastes allows to explain the logarithmic dependant desorption in a function of water-binder of the cement paste which served as a desorption environment only to a certain w/c, below which the properties of a porous liquid start to control the course of water desorption from SAP. Below that w/c ratio, other phenomena block the movement of water from SAP to cement paste, mostly the change in the parameters of a capillary network. When exposed to high capillary pressure resulting for local presence of additional water (desorbed from SAP under the influence of alkali originating from cement paste), the network loses its homogeneity, preventing continuous rapid desorption from SAP. That was the case with unusual course of water desorption from SAP in cement paste of a 0.5 water-cement ratio.

Results of the SAP water desorption test in this environment suggest, that in order for SAP to reduce its water absorption capacity to the level achieved in SAP water absorption tests, much more time would be required, i.e. that the water desorption process in cementitious environments characterized by low water-cement ratios lasts longer than 24 hours. The process of hydration and the properties of porous fluid such as cement paste limit the intensivity of the water desorption process from SAP. It indicates that much more time would be required for SAP to desorb its water to the water absorption level SAP achieved in absorption tests in a cement paste of a water-cement ratio of 0.5.

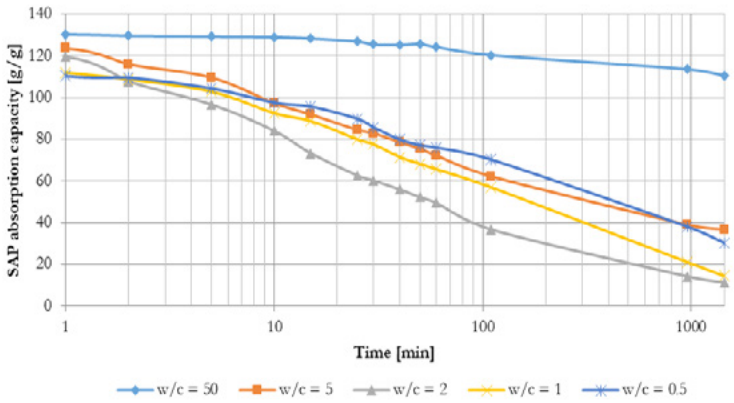

Figure 6: SAP water absorption capacity over time in cement pastes of different water-binder ratios serving as water desorption environments.

Several variables have the influence on water migration from SAP. In water desorption environments that could be described as fluids (characterized by water-cement ratio higher than 2), the ion content of the desorption environment is probable to have the biggest impact on SAP desorption (Fig 7). SAP water desorption process in all of the tested cement pastes that served as a SAP water desorption environment was characterized by logarithmic dependence. With time, in cement pastes with water-cement ratios lower then 2, the influence of other variables started to impact the course of water desorption from SAP, i.e. slowing the water desorption process. It is possibly prone to change in the properties of the desorption environment with a reduction of water-cement ratio.

Water migration in cement pastes does not occur in the entire volume of the desorption environment but is limited to migration through capillary/pore network. By adding additional restrictions on the water movement throughout the desorption environment, an increase in internal pressures further limit the rate of water desorption from SAP. It leads to conclusion, that the course of water desorption from SAP depends not only on the chemical properties of the SAP or the desorption environment, but also on the physical properties of the desorption environment.

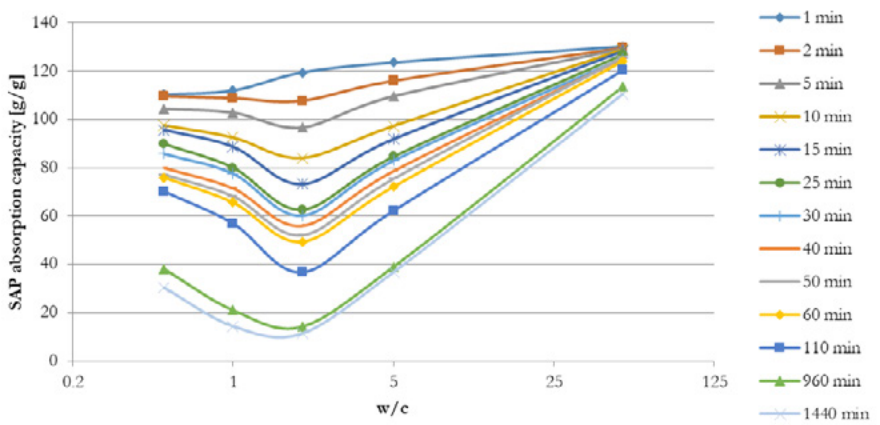

Figure 7: SAP water absorption capacity over specific measurement times in cement pastes characterized by different water-binder ratios serving as water desorption environments.

Research on the topic of SAP influence on the internal humidity in cementitious composites suggest that SAP contributes to the maintenance of internal humidity within concrete volume at the high level for a longer time than in reference mixes [14]. Most of experiments carried out suggest a certain SAP dosing method to the rest of the mix components – by introducing it as a non-saturated powder [15]. After its introduction into the mix, SAP is to absorb water from the mix and then, under the influence of internal pressures (hydrostatic, capillary etc.) is to desorb water and by doing so, maintain the internal humidity at a high level [16].

Research presented in this article suggest different approach to the phenomenon of water desorption from SAP. By adding SAP as a gel saturated with water to the rest of the components of the cement mix, the water migration is to occur only in a form of water desorption from SAP. As presented in the article, the rate of water desorption from SAP to an environment of a low water-cement ratio is much slower than in the case of SAP water absorption. This property of SAP introduces an additional period of intense water desorption from SAP into a cement composite. It occurs within first days after the preparation of the mix – in the time when intensive hydration occurs. The influence of this change in the properties in water migration within composites structure and its influence on the properties of concrete should be investigated further but it is safe to assume that this change would have an effect on the pore network distribution and consecutively, on other properties of the composite.

4. Conclusions

On the basis of conducted research following conclusions were made:

- SAP absorption capacity in environments characterized by low water-cement ratios could be approximated as one tenth of SAP absorption capacity in water environment.
- The rate of SAP water absorption process increases along with a decrease of water-cement ratio of the absorption environment.
- The influence of porous liquid properties on the course of SAP water desorption is observed in paste with low water-cement ratios.
- The time required for SAP saturated with water to reduce its water content due to the desorption in paste to the level of absorption capacity in paste prolongs as the water-cement ratio of the environment decreases.
- The process of water desorption from SAP has a slower rate than the process of SAP water absorption

in the same environment.

5. References

1. Mignon, A.; Snoeck, D.; Dubruel, P.; Van Vlierberghe, S.; De Belie, N., 2017, Crack Mitigation in Concrete: Superabsorbent Polymers as Key to Success? *Materials*, 10, 237, DOI: 10.3390/ma10030237.

2. Ghobashy M.,M. Superabsorbent, Hydrogels, S. Haider and A. Haider, IntechOpen **2018**, DOI: 10.5772/intechopen.74698.

3. Snoeck, L.F.; Velasco, P.; Mignon, A.; Van Vlierberghe, S.; Dubruel, P.; Lodewyckx, P.; De Belie, N., 2015, The effect of superabsorbent polymers on the microstructure of cementitious materials studied by sorption experiments. *Cem. Concr. Res.*, 77, 26-35, DOI: 10.1016/j.cemconres.2015.06.013.

4. Yu, Y.; Liu, L.; Kong, Y.; Zhang, E.; Liu, Y., 2011, Synthesis and properties of N-maleyl chitosan-cross-linked poly (acrylic acid-co-acrylamide) superabsorbents. *J. Polym. Environ.*, 19, 926–934, DOI: 10.1007/s10924-011-0340-2.

5. Lee, H.X.D.; Wong, H.S.; Buenfeld, N.R., 2018, Effect of alkalinity and calcium concentration of pore solution on the swelling and ionic exchange of superabsorbent polymers in cement paste. Cem. Concr. Compos., 88, 158–164, DOI: 10.1016/j.cemconcomp.2018.02.005.

6. Farzanian, K.; Ghahremaninezhad, A., 2018, Desorption of superabsorbent hydrogels with varied chemical compositions in cementitious materials. Mat. Struct., 51, 3, DOI: 10.1617/s11527-017-1128-11.

7. Hasholt, M.T.; Jensen, O.M.; Kovler, K.; Zhutovsky, S., 2012, Can superabsorbent polymers mitigate autogenous shrinkage of internally cured concrete without compromising the strength? Constr. Build. Mater., 31, 226–230, DOI: 10.1016/j.conbuildmat.2011.12.062.

8. Schrofl, C.; Mechtcherine, V.; Gorges, M., 2012, Relation between the molecular structure and the efficiency of superabsorbent polymers (SAP) as concrete admixture to mitigate autogenous shrinkage. Cem. Concr. Res., 42, 865–873, DOI: 10.1016/j.cemconres.2012.03.011

9. Pourjavadi, A.; Fakoorpoor, S.M.; Hosseini, P.; Khaloo, A., 2013, Interactions between superabsorbent polymers and cement-based composites incorporating colloidal silica nanoparticles. Cem. Concr. Compos., 37, 196–204, DOI: 10.1016/j.cemconcomp.2012.10.005

10. Snoeck, D.; Schaubroeck, D.; Dubruel, P.; De Belie, N., 2014, Effect of high amounts of superabsorbent polymer and additional water on the workability, microstructure and strength of mortars with water-to-cement ration of 0.50. Constr. Build. Mater., 72, 148–157, DOI: 10.1016/j.conbuildmat.2014.09.012

11. Mechtcherine V., Reinhardt, H.-W., 2012 Application of Superabsorbent Polymers (SAP) in Concrete Construction, State-of-the-Art Report Prepared by Technical Committee 225-SAP; Springer Science & Business Media: Berlin, Germany.

12. Lee, H.X.D.; Wong, H.S.; Buenfeld, N.R., 2018, Effect of alkalinity and calcium concentration of pore solution on the swelling and ionic exchange of superabsorbent polymers in cement paste. Cem. Concr. Compos., 88, 158–164, DOI: 10.1016/j.cemconcomp.2018.02.005

13. Powers, T.C.; Brownyard, T.L., 1946, Studies of the physical properties of hardened Portland cement paste. J. Am. Concrete Inst., 43, 101–132.

14. Chiwon Song,Young Cheol Choi, Seongcheol Choi, 2016, Effect of internal curing by

superabsorbent polymers – Internal relative humidity and autogenous shrinkage of alkali-activated slag mortars, Constr and Build Mat, 123, 198-206, DOI: 10.1016/j.conbuildmat.2016.07.007

15. Justs, J.; Wyrzykowski, M.; Bajare, D.; Lura, P., 2015, Internal curing by superabsorbent polymers in ultra-high performace concrete. Cem. Concr. Res., 76, 82–90, DOI: doi.org/10.1016/j.cemconres.2015.05.005

16. Woyciechowski, P.; Kalinowski, M., 2018, The Influence of Dosing Method and Material Characteristics of Superabsorbent Polymers (SAP) on the Effectiveness of the Concrete Internal Curing, Materials, 11(9), 1600, DOI: 10.3390/ma11091600

Study on Self-healing Cementitious Materials with Hydrogels Encapsulating Phosphate

X. Liu[2], Y. Tang[2], Z. Liu[2], W.Chen[1], Q. Li[1], W. Chen[1]*

[1] State Key Laboratory of Silicate Materials for Architectures, Wuhan University of Technology, 430070 Wuhan, Hubei, PR China

[2] School of Materials Science and Engineering, Wuhan University of Technology, 430070 Wuhan, Hubei, PR China

Abstract

At present, commonly-used self-healing methods include capsule encapsulation healing agents, hollow fiber encapsulation healing agents, or direct addition of microbial bacteria. Some methods heal cracks by producing minerals such as calcium carbonate. In this study, a novel self-healing cementitious material is developed by using a hydrogel impregnated with phosphate as the healing agent. Hydrogel has a sensitive response mechanism to changes in the external environment compared to other healing agent. The aim is to form a hydroxyapatite-type mineral as healing products in the crack during the self-healing process by controlling the release of phosphate.Hydrogels were used as a carrier to encapsulate phosphate and added to cement paste to manufacture self-healing cementitious materials. The self-healing mechanism of this material is mainly when the crack is induced in the cementitious material, and the phosphate in the hydrogel is released into the pore solution in the crack due to the change of the osmotic pressure. Water and carbon dioxide penetrate into the fracture and form bicarbonate ion (HCO_3^-), and the Ca^{2+} and OH^- ions released from the cement matrix react with the phosphate ions and HCO_3^- to form hydroxyapatite-type mineral which can heal the crack.The self-healing efficiency was evaluated by the water permeability test. The results show that the hydrogels successfully preserved the phosphate in the paste and the self-healing agent produced dense hydroxyapatite on the sample in the simulated pore solution. The self-healing efficiencies is more than 60% on the water permeability. The self-healing products were carbonated and calcium deficient hydroxyapatite (CCDHA) according to XRD and FTIR analysis.

Keywords: Self-healing cementitious materials, Hydrogel, Hydroxyapatite, Self-healing efficiency

1. Introduction

The self-healing technology has been widely used in concrete because it can fill external cracks and internal cracks in time when the concrete structure is destroyed, which greatly reduces the maintenance cost and prolongs the service life of the concrete structure [1-3]. Self-healing in concrete is mainly divided into the following two types: autogenous healing and autonomous healing. Autogenous healing is the natural process of crack repair occurring in concrete in the presence of moisture, the healing mechanism is based on the continued hydration of unhydrated cement particles and the formation of calcium carbonate at the crack edge. Its maximum healing width can reach 300μm [4]; Self-healing is a self-healing ability of an artificially designed cementitious material. At present, commonly-used self-healing methods include capsule encapsulation healing agents [1], hollow fiber encapsulation healing agents [5], or direct addition of microbial bacteria [6]. Its maximum healing width can reach 970μm [7, 8]. Most of the healing products

are C-S-H, ettringite, CaCO3, polymer binder [9, 10], etc., and there are few self-healing materials using hydroxyapatite as a healing product.

Varieties of self-healing materials are generally encapsulated by a polymer or glass to release the healing component of the cementitious material when cracks occur. Some studies have used hydrogels as carriers to carry and protect bacteria to healing cracks and achieve excellent healing results [6, 11]. Hydrogels have a hydrophilic three-dimensional network structure that is chemically cross-linked or physically cross-linked, and is often used as a drug delivery vehicle due to its adjustable physical properties, controlled degradability, and ability to protect unstable drugs from degradation. The release rate of the drug in the hydrogel is significantly related to the difference between the internal and external ion osmotic pressure and the pore size of the hydrogel surface. The smaller the ion osmotic pressure difference inside and outside, the slower the rate of release [12]. As an important component of bone tissue, hydroxyapatite (HA) plays an important role in the self-healing phenomenon of bone tissue, the solubility of hydroxyapatite is much less than the solubility of calcium carbonate, so hydroxyapatite-type minerals were formed and healed the cracks through the reaction between phosphate released from hydrogels and Ca^{2+} from the paste According to the encapsulated and sustained release characteristics of hydrogels, it is proposed to use hydrogel encapsulated phosphate as a cementitious material healing component. After the hydrogel encapsulates the phosphate, most of the water in the gel is bound by the hydrophilic hydrogel, leaving only a small amount of free water and phosphate, and the internal osmotic pressure of the hydrogel is larger. Then, the internal healing agent has a lower outward permeation rate with the same ions concentration in the cement slurry, which can effectively protect the healing agent.

In this study, a novel self-healing cementitious materials is developed by using a hydrogel impregnated with phosphate as the healing agent. The self-healing mechanism of this materials is mainly when the crack is induced in the cementitious material, and the phosphate in the hydrogel is released into the pore solution in the crack due to the change of the osmotic pressure. Water and carbon dioxide penetrate into the fracture and form HCO_3^-, and the Ca^{2+} and OH^- ions released from the cement matrix react with the phosphate ions and HCO_3^- to form hydroxyapatite-type mineral which can heal the crack. A variety of analytical testing methods were used to analyse and evaluate the phosphate release process, the characteristics of healing products in the crack and the healing effect.

2. Methodology

2.1 Materials

An ordinary Portland cement complying with the Chinese standard GB 175-2016 classified as P.O. 42.5 (Huaxin Cement Co, Ltd). The oxide compositions of cement are listed in Table 1.

Table 1: Chemical composition of cement (wt%)

Oxide	Al_2O_3	SiO_2	Fe_2O_3	CaO	K_2O	SO_3	Na_2O	MgO	LOI
OPC	5.86	21.50	2.85	59.81	0.67	2.06	0.20	2.23	3.70

LOI: Loss on ignition at 1000°C

Disodium hydrogen phosphate (Na_2HPO_4), sodium dihydrogen phosphate (NaH_2PO_4), acrylic acid (AA), N,N-methylene BIS acrylamide (BIS), sodium hydroxide (NaOH), sodium dodecyl sulfate (SDS)□ N_2 gas with purity of 99.99% and sodium carbonate (Na_2CO_3) are used. All chemicals are AR grade.

The mix design of self-healing cementitious materials in this experiment is shown in Table 2. The hydrogel used in the experiment is divided into two types. Where H is a blank hydrogel without phosphate, HP is a self-healing hydrogel containing phosphate, and the hydrogel is added in 3% by mass of cement.

Table 2: the mix design of self-healing cementitious materials (kg/m^3)

Type	Cement	Water	Hydrogel
HP	1875	656.25	Hydrogels encapsulated phosphate56.25
H	1875	656.25	Blank Hydrogels 56.25

2.2 Methods

The method of synthesizing hydrogel is as follows: 2 grams of Na_2HPO_4 and 2 grams of NaH_2PO_4 are simultaneously dissolved in 10 grams water and stirred until the PH value of the buffer solution is 7. 2 grams of AA and 0.1 grams of BIS are added into the solution, bubbled with N_2 gas for 10 min. then 0.1 grams of APS is added into solution followed by consistently stirred after which a clear solution is obtained. The solution was sealed and placed at 60 ° C for 4 h to form a PAA hydrogel with acrylic acid as a monomer, N,N-methylene BIS acrylamide as a crosslinking agent and sodium dodecyl sulfate as an initiator [13]. If no phosphate is added to the solution, the hydrogel H can be synthesize. The obtained gel is dried under Vacuum freeze dryer and grinded with a ball mill, the particle size of the HP is about 300μm.

The hydrogel swelling performance and the test of phosphate release performance are as follows prepare 200ml deionized water and 0.01mol/L NaOH solution as simulated pore solution respectively. The simulated pore solution was prepared by adding 200 grams of water to 20 grams of cement, filtering after half an hour, adding 0.3 g of Na_2CO_3 to remove Ca^{2+} in the solution, and filtering to obtain a clear simulated pore solution. Since the release of the hydrogel in the cement slurry is mainly in the initial stage of the cement hydration reaction, this method is used in order to simulate the pore solution in the initial stage of the hydration reaction. In order to avoid affecting the kinetics of phosphate release in the hydrogel caused by the reaction of $PO4^{3-}$ in the hydrogel and the Ca^{2+} reaction in the simulated pore solution, the same concentration of sodium carbonate was used to remove the Ca^{2+} but the total ion concentration in the solution remained unchanged.

2 g of hydrogel powder was placed in a dialysis bag (RC membrane, 6.16 ml/cm, protein molecular weight cutoff 3500) suspended in deionized water, 0.01 mol/L calcium hydroxide solution and simulated pore solution, 5ml of supernatant was taken from the solution at different time to test the phosphorus concentration, and the quality of the hydrogel in the dialysis bag was measured. The mass of hydrogel powder is referred to as m_0, the mass of hydrogel absorbed solution at different time periods is referred as m_t. Calculating the degree of swelling (Q_t)according to the following equation:

$$Q_t = (m_t - m_0)/m_0 \quad (1)$$

The preparation method of the hydrogel immersed in the simulated pore solution contain the hardened cement slurry to produce the healing product is as follows: 2 grams of hydrogel powder encapsulated phosphate is added into 200 grams of deionized water, placing a cement paste block curing 28 days with a fresh section after cutting in deionized water and sealed with plastic wrap. After placing for three days, a white substance will form on the surface of the fresh section of the cement. The white substance on the surface was separated from the cement by an ultrasonic disperser, dried by a vacuum freeze dryer, and then the phase and microscopic morphology of the white substance were tested by XRD and SEM.

The research method of the release of hydrogel phosphate in the cement matrix is as follows: Plain cement paste without HP is casted into the cubic mould with a layer thickness of 20 mm. 1 gram of HP powder are then dispersed on top of the fresh paste layer followed by slightly tapping the mould. The cubic mould is then filled with plain cement paste without HP again. The specimens are splitted along the HP powder layer after being cured for 1, 7, 14 and 28 days and use a fine brush to collect the hydrogel from the middle of the interlayer faces. The collected hydrogel was placed in a muffle furnace and calcined at 700 °C for two hours.

The weighing was taken out, and the weight of the ashes after the burning of the hydrogel was compared with that of the original hydrogel. The mass percentage of phosphate out of hydrogel was calculated by comparing the hydrogel masses of each curing age.

Each set of self-healing cementitious materials is made into a cylindrical specimen of Φ50mm×50mm, and all specimens were demoulded after 1 day of curing and transferred to the curing chamber at 20°C and 95%RH for 28 days. After the cylindrical sample is fixed with five layers of scotch tape along the side, place the side of the sample on the compressive testing machine and the ramp speed was adjusted into 0.1 KN/S. When the sample cracks, stop the compressive testing machine and record the width of the crack by using the crack width observation instrument. After cracking, all specimens were return in the curing chamber

The water permeability is performed on three vacuum saturated specimens in each batch according to Chinese standard GB/T 25993-2010. The specimens are loading with a compressive testing machine to generate crack after curing 28 days and record the width of the crack, then the total weight of the permeated water of the crack was tested for 5 minutes to calculate the amount of water permeating the sample and the water permeability. The water permeability is calculated as the average of three specimens, according to the following equation

$$E = \frac{G_s}{G_b} \quad (2)$$

In the equation, E is the self-healing efficiency of properties, G_s is the water permeability after curing, G_b is the water permeability after cracking.

3. Results and discussion

3.1 The morphology of hydrogel

The morphology of synthetic hydrogels H and HP is shown in Figure 1. Figure 1(a) is an SEM image of a hydrogel that is not encapsulated with phosphate, it can be seen from the figure that the hydrogel exhibits a fibrous network formed by cross-linking between monomers. The SEM image of hydrogel encapsulated phosphate is shown in Figure 1(b), unlike hydrogels that not encapsulated phosphate, the hydrogels encapsulated phosphate have no obvious fibrous network structure. The addition of phosphate causes wrinkles in the network inside the hydrogels. There are small pore structures on the surface of both hydrogels.

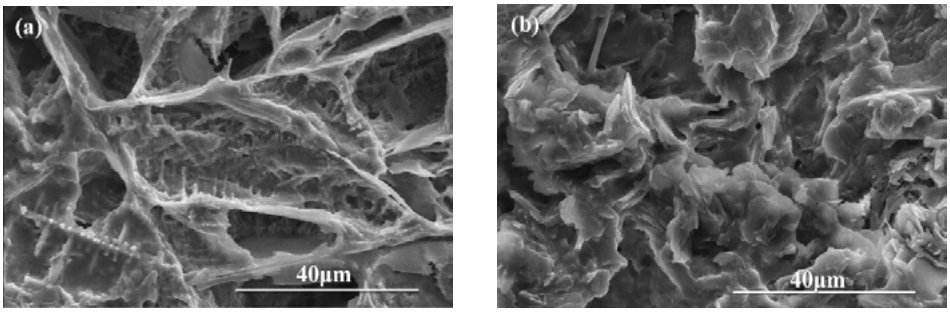

Figure 1: The SEM pattern of the hydrogels, (a) blank hydrogels, (b) hydrogel encapsulated phosphate

3.2 The hydrogel swelling performance and the diffusion of phosphate

The diffusion of phosphate in hydrogel encapsulated phosphate into various solutions are shown in Figure 2(a). It can be seen from the figure that the phosphate in hydrogel diffuse rapidly into deionized water and sodium hydroxide solution in the first 7 hours, but the diffuse rate is significantly reduced in the simulated pore solution. The highest diffusion rate is found in the deionized water, followed by NaOH solution and

pore solution. The release of phosphate ions from hydrogels in different solutions can be resulted from the difference in the osmotic pressure due to the different ions strength of different solutions [14]. The great the internal and external osmotic pressure difference, the faster the exchange speed. The ion concentration in the hydrogel is similar to that in the simulated pore solution, and the internal ion concentration of the hydrogel is larger than that in the simulated pore solution, and the diffusion rate is slower in the cement slurry solution. The hydrogel swelling performance in various solutions are shown in Figure 2(b). The swelling rate of the hydrogel in various solutions is the same as the tendency of the phosphate diffusion curve, the consistent tendency in deionized water and NaOH solution. A obvious different between deionized water and pore solution could be resulted from the difference in the osmotic pressure due to the different ions strength of different solutions.

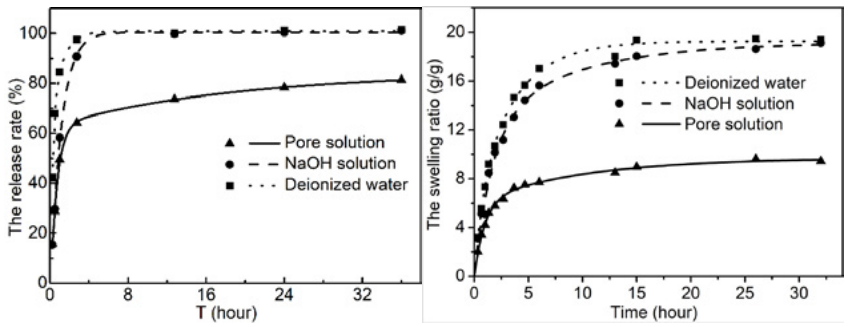

2a) 2b)

Figure 2: 2a) Diffusion curves of phosphate ion and 2b) the swelling properties of hydrogel immersing in different solutions

3.3 Diffusion of phosphate out of hydrogel in cement paste

A major feature of self-healing cementitious materials is the ability of materials to respond the formation cracks spontaneously. It means the self-healing cementitious materials can release the healing agent to form the healing product, and should not release the healing agent when the matrix not broken. The diffusion of phosphate out of hydrogel in cement paste is shown in Figure 3.

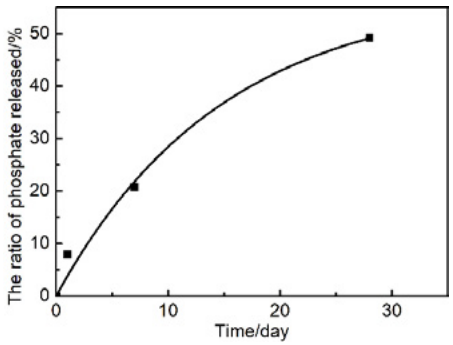

Figure 3: The release ratio of phosphate from hydrogels

It can be seen from the figure that the diffusion of phosphate out of hydrogel in cement paste is rapidly decrease after curing 7 days, but the diffuse rate is slowly reduced after curing 28 days, the phosphate in the hydrogel released a total of about 50% in the cement paste during curing 28 days. The main reason for this phenomenon is that the ion concentration of the cement pore solution is low in the initial stage of cement hydration, resulting in rapid exchange of ions in the cement slurry and hydrogel. The ions concentration of the pore solution increases with the hydration time in the later stage of cement hydration, then the ions exchange between the cement matrix and hydrogel decreases, which reduces the diffusion rate of phosphate. These results indicated that the hydrogel can prevent the unfavourable release of phosphate

without crack formation in the cement paste and is suitable for the self-healing cementitious materials.

3.4 The healing product in pore solution

The XRD pattern and SEM image of healing product created by putting the hydrogel into the simulated pore solution contain the hardened cement slurry are shown in Figure 4. Calcium deficient hydroxyapatite (CDHA, PDF-09-0432) is identified in the precipitated products, the formation of CDHA is due to the lack of calcium ions on the surface of the cement paste. It can be seen from the Figure 4(a) (b)that a large number of spherical substance appear around the cement hydration product, A large amount of needle-shaped substances are scattered around the surface of the spherical substance. The broad peak width of XRD pattern indicated the low crystallinity nature of healing products, this is also consistent with the CDHA morphology in the SEM. This is mainly due to the fact that hydroxyapatite will priority generated as amorphous calcium phosphate during crystallization, and then amorphous calcium phosphate is gradually converted to hydroxyapatite. The low crystallinity nature of CDHA is generated due to the difference in the ratio of calcium to phosphorus, The CDHA form a relatively stable packing structure, indicating good bonding between the hydroxyapatite and the cement matrix.

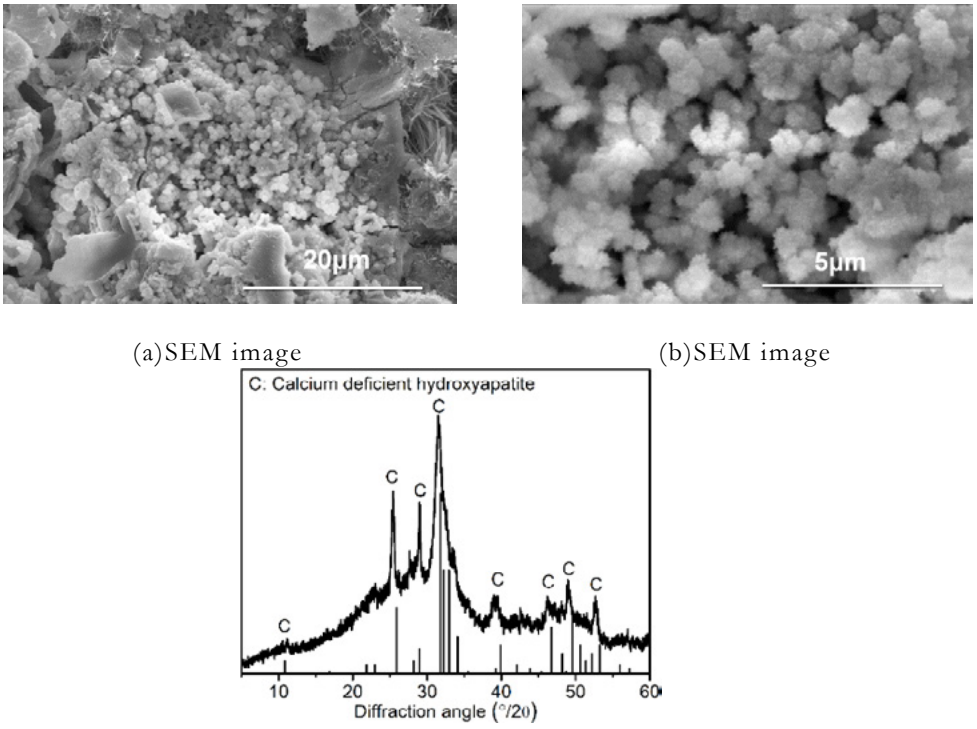

(a)SEM image (b)SEM image

(c)XRD pattern

Figure 4: the XRD pattern and SEM image of simulated products

3.5 Self-healing efficiency of HP

The crack healing area of the specimens after self-healing at different ages are shown in Figure 5(a). It can be seen from the figure that the hydrogels encapsulated phosphate is more than hydrogels not encapsulated phosphate for the crack healing area. The healing area ratio can reach 90% for the addition of HP after healing 28 days, and the healing area ratio of H is merely about 40% after healing 28 days. It indicated that the phosphate of hydrogels can fill the crack by producing the healing products. The water permeability of specimens after self-healing at different ages are shown in Figure 5(b). The water permeability is gradually decreased with the increase of time of self-healing. The water permeability of HP is dramatically by 60% after self-healing for 28 days by standard condition, but the water permeability of H is merely 40% after self-healing for 28 days. The results suggest that the phosphate of hydrogels is essential for the crack

healing, the self-healing cementitious materials with hydrogels encapsulated phosphate has an efficiency in the properties restoration in 28 days of self-healing.

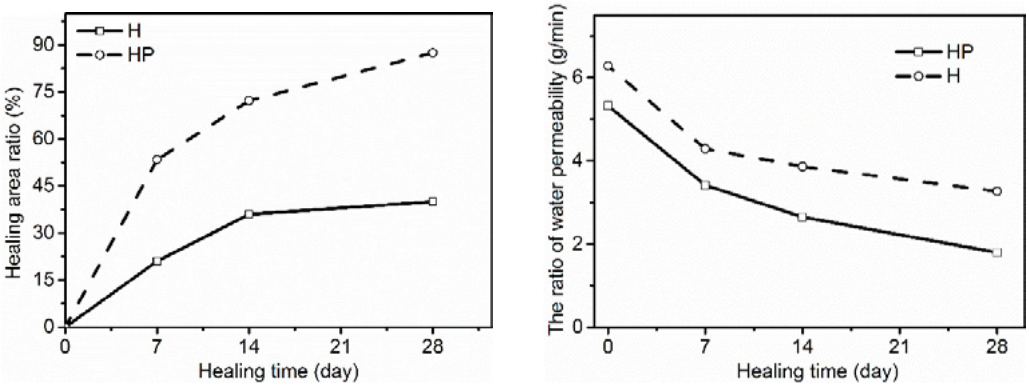

(a) (b)

Figure 5: the self-healing efficiency (a) Healing area after self-healing for different ages (b) Water permeability of specimens after self-healing for different ages

3.6 Self-healing products in cement paste after cracking

The morphology of self-healing products in the crack of cement paste after healing 14 days is shown in Figure 6. The edge of the crack is filled with a pleated spherical morphology of hydroxyapatite, and the particle size is approximately 40μm, which is very similar to the healing product in the simulated solutions. Figure 6(a) shows that the close accumulation of healing product particles indicates that the mechanical properties are better. Figure 6(b) the crack section is filled with cubic calcium carbonate and spherical hydroxyapatite.

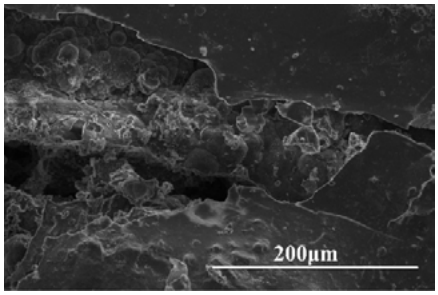

6a) 6b)

Figure 6: 6a) CDHA grew from both sides to the center of a crack 6b) a close look of morphology of CDHA and calcite

The particle size is about 40μm, which is also a wrinkled sphere. It can be seen from the figure that there are more hydroxyapatite and less calcium carbonate, which is because the solubility product of hydroxyapatite is much lower than that of calcite, which leads to its superiority in calcium ion competition [15].

The XRD pattern and FT-IR spectra of products of healing products formed in the cracks are shown in Figure 7. According to the XRD pattern of the healing products, the products consisted of hydroxyapatite and calcite, the XRD spectrum of hydroxyapatite is extremely different from calcium-deficient hydroxyapatite [16]. In the FT-IR spectra of products of healing products formed in the crack, the peaks at 3431 and 1648 cm^{-1}, which are represented to the adsorbed water in hydroxyapatite, the peaks at 1038, 960, 557, 607 cm^{-1}, which are assigned to PO_4^{3-}; The peak at 1460 cm^{-1} arises from the CO_3^{2-}, This also corresponds to the phenomenon of coexistence of hydroxyapatite and calcite in SEM image and indicates the healing products

is CCDHA.

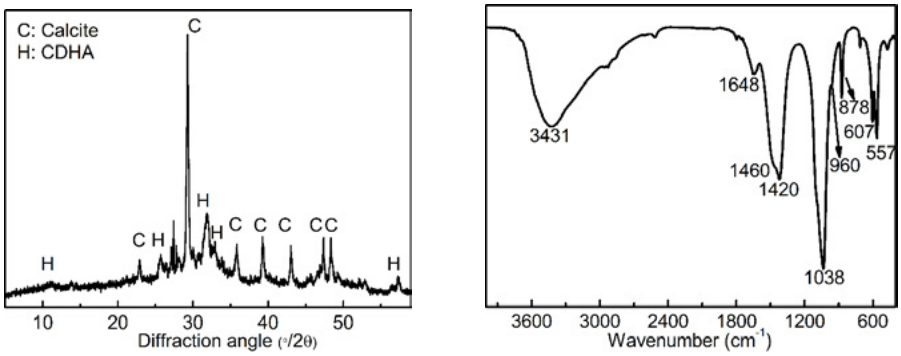

7a) 7b)

Figure 7: (a) The XRD pattern and (b) The FT-IR spectra of healing products formed in the crack

4. Conclusions

In this study, a novel self-healing cementitious materials is developed by using a hydrogel impregnated with phosphate as the healing agent. According to the results obtained, the following conclusions can be drawn.

(1) The self-healing cementitious materials were prepared by encapsulating phosphate with hydrogels and adding it to cement paste. The hydrogels is an excellent self-healing carrier by effectively encapsulated phosphate and not release the phosphate into the cement paste during the mixing or curing.

(2) Calcium deficient hydroxyapatite (CDHA) is identified on the surface of harden cement slurry with presence of simulated pore solution and hydrogels encapsulated phosphate.

(3) The crack healing area ratio of the specimens with the addition of HP after self-healing at 28 days can reach 90%, the water permeability of the specimens with the addition of HP is dramatically by 60% after self-healing for 28 days by standard condition

(3) The phosphate in the hydrogel can form the carbonated calcium deficient hydroxyapatite and healing the cracks by mixing the calcium ions in the cement matrix when the crack is generated, and the healing products are mainly carbonated calcium deficient hydroxyapatite and calcite.

5. Acknowledgment

This research has been financially supported by the National Natural Science Foundation of China (grant numbers 51672199); the Fundamental Research Funds for the Central Universities (grant number WUT: 2017-YB-008□ 2019III018GX); and the 111 Project (No. B18038)

6. Reference

[1] Kanellopoulos A, Qureshi T, Al-Tabbaa A. Glass encapsulated minerals for self-healing in cement based composites [J]. Construction and Building Materials, 2015, 98:780–791.

[2] Wu M, Johannesson B, Geiker M. A review: Self-healing in cementitious materials and engineered cementitious composite as a self-healing material [J]. Construction and Building Materials, 2012, 28(1): 571-583.

[3] Ramm W, Biscoping M. Autogenous healing and reinforcement corrosion of water-penetrated separation cracks in reinforced concrete [J]. Nuclear Engineering and Design, 1998, 179(2):191-200.

[4] Aldea C M, Song W J, Popovics J S, Shah S P. Extent of healing of cracked normal strength concrete [J].

Journal of materials in civil engineering, 2000, 12(1): 92-96.

[5] Di Shengkui L H. Self-Monitoring and Repairing Based on Crack of Concrete Beam Embededded with SMA [J]. Journal of Building Materials, 2009, 12(1): 27-31.

[6] Wang J, Mignon A, Snoeck D, et al. Application of modified-alginate encapsulated carbonate producing bacteria in concrete: a promising strategy for crack self-healing [J]. Frontiers in microbiology, 2015, 6: 1088.

[7] Tang W, Kardani O, Cui H. Robust evaluation of self-healing efficiency in cementitious materials – A review [J]. Construction and Building Materials, 2015, 81:233-247.

[8] Wang J Y, Soens H, Verstraete W. Self-healing concrete by use of microencapsulated bacterial spores[J]. Cement & Concrete Research, 2014, 56(2):139-152.

[9] B. Yuan, Y. Yang, Y. Wang, and K. Zhang, Self-healing efficiency of EVA-modified cement for hydraulic fracturing wells [J]. Constr. Build. Mater, 2017. 146:563–570.

[10] Sisomphon K, Copuroglu O, Koenders E A B. Self-healing of surface cracks in mortars with expansive additive and crystalline additive [J]. Cement and Concrete Composites, 2012, 34(4):566-574.

[11] Wang J Y, Snoeck D, Vlierberghe S V, et al. Application of hydrogel encapsulated carbonate precipitating bacteria for approaching a realistic self-healing in concrete [J]. Construction & Building Materials, 2014, 68(68):110-119.

[12] Li J, Mooney D J. Designing hydrogels for controlled drug delivery [J]. Nature Reviews Materials, 2016, 1(12): 16071.

[13] Chen Q, Liu C, Jiang G, Liu X, Yang M, Liu F. Studies on swelling behavior of poly (acrylic acid-co-octadecyl methacrylate) hydrophobic association hydrogels with high mechanical properties [J]. Acta Polymerica Sinica, 2010, 6: 797.

[14] Mignon A, Graulus G J, Snoeck D, et al. pH-sensitive superabsorbent polymers: a potential candidate material for self-healing concrete [J]. Journal of materials science, 2015, 50(2): 970-979.

[15] Mostafa N Y. Characterization, thermal stability and sintering of hydroxyapatite powders prepared by different routes [J]. Materials Chemistry and Physics, 2005, 94(2-3):333-341.

[16] A. Siddharthan, S.K. Seshadri, T.S. Sampath Kumar, Microwave accelerated synthesis of nanosized calcium deficient hydroxyapatite [J]. J.Mater. Sci. Mater. Med. 15 (2004) 1279–1284.

Biosorption of heavy metal ions of lead and zinc by Trichoderma reesei based on response surface method

Y. Sun[1,2], R. Yu1[*], Z. Shui[1], D. Qian[1,2], B. Rao[2], J. Huang[2]

[1] State Key Laboratory of Silicate Materials for Architectures, Wuhan University of Technology, Wuhan 430070, China

[2] School of Materials Science and Engineering, Wuhan University of Technology, Wuhan 430070, China

Abstract

Biosorption is a method of heavy metal removal. In the study, Response Surface Method (RSM) is utilized to get the optimal concentration of lead and zinc solution, and the inoculation amount of *Trichoderma reesei* (CCTCC AF 2015005 QM6a). Accordingly, the obtained results showed that the optimum condition is 0.8mg/L, 0.83mg/L of lead and zinc solution respectively and the inoculation amount of fungi is 300 uL. In this condition, Pb and Zn are best removed from the liquid media of *Trichoderma reesei* (CCTCC AF 2015005 QM6a) fungi, with an average of 27% and 56%, respectively. Value of correlation coeffificient (R2=0.9977 and 0.9734, respectively) and signifificant value for model $p < 0.0001$ indicated validity of model fifitness and adequate for optimization.

Keywords: Biosorption, Response Surface Method, *Trichoderma reesei*, lead, zinc

ICSBM 2019
ID 072

1. Introduction

The presence of heavy metal ions in the environment causes serious threat to human, animals and the environment. Heavy metal ions in the environment usually come from many sources, i.e. mining, electroplating, metal processing, automobile manufacturing, dyeing, textile, fertilizer and petroleum industries, which is harmful for the environment.[1,2] To solve the problem and reduce harm of heavy metal accumulation on human body, some of physical or chemical treatment ways such as chemical oxidation and reduction, precipitation, adsorption, solidification, electrolytic recovery and ion exchange are used for heavy metal removal in some study.[3,4] However, application of such processes is sometimes restricted due to economical or technical constraints and secondary pollution because of the addition of chemical reagents. Therefore, there is a need for an innovative method with low cost and advanced security that metal ions can be removed economically and safely.Microorganisms, i.e. bacteria, fungi and yeasts, as the most usually used organisms in biotechnology, are frequently studied over many years. And biosorption technology is considered to be one of the most effective and environmentally friendly technologies of heavy metal removal from waste water.[5-10] Especially, using fungi to remove heavy metal ions from waste water has drawn more and more attention in recent years as well as a very broad application prospect, among which, *Trichoderma reesei* is one of the most popular commercial cellulases. And the adsorption of *Trichoderma reesei* on heavy metal Cr(VI) has been studied.[11] However, the adsorption of *Trichoderma reesei* on other heavy metals such as lead and zinc have drawn few researchers' attention. Thus, it is necessary to study the biosorption of *Trichoderma reesei* on lead and zinc.Plenty of studies in heavy metal absorption by using fungi have shown good results in heavy metal removal, but almost all have used shake flask cultures

along with Sabouraud Dextrose Broth[12,13], which is more expensive compared to PDB thus increasing the cost of experiments. PDB can easily be made in the laboratory and cheap and accessible. By using PDB as nutrients can easily reduce the experimental cost.

In this study, response surface methodology (RSM) has been developed as an effective tool for optimization of reaction conditions, i.e. concentration of lead and zinc and inoculation amount for fully utilization of biosorption of *Trichoderma reesei* (CCTCC AF 2015005 QM6a).

2. Materials and methods

2.1 Microorganism

In the study, *Trichoderma reesei* (CCTCC AF 2015005 QM6a) from China Center for Type Culture Collection (CCTCC) is used as adsorbent material. A spore suspension was obtained by growing on potato dextrose agar (PDA) for two days and then cultured in the potato dextrose broth (PDB) for 72 hours in the condition of 20 ℃, illuminating and 150 r/min in the table concentrator. The strains used in this experiment are kept in the refrigerator (4℃), and the remaining strains are kept in the refrigerator (-80℃).

2.2 Preparation of heavy metal solution

Before operating the experiments, the media and deionized water useful for the next step were sterilized in autoclave for 121 ℃, 30 min in the autoclave. The preparation of heavy metal ion solution is obtained by fully mixed dissolution of deionized water and $Pb(NO)_3$ and $Zn(NO)_3$. The ranges of concentrations varied according to the design of part 2.4. After weighing the chemicals, place them in deionized water and use a magnetic mixer to fully promote dissolution.

2.3 Inoculation of Trichoderma reesei

The inoculation amount of *Trichoderma reesei* is determined by the design of response surface method. Before inoculation, firstly, the mycelium of the strain is evenly dispersed to make it distributed in the culture medium uniformly, so as to ensure that the amount of the strain in each culture medium is approximately the same. The liquid volume of the inoculated fungi solution was calculated into the volume of the heavy metal solution.

2.4 Measurement of heavy metal ion concentration

The concentration of heavy metal ion solutions with the fungal medium was determined by using full spectrum direct reading plasma emission spectrometer (Inductively Coupled Plasma-Optical Emission Spectr, Prodigy 7/Prodigy 7, USA). Select 5 ml of the uniform solution after the reaction (avoiding the fungi), and compare with the concentration of the solution before reaction. The removal rate of the strain is calculated by the following equation:

Removal rate (R%)=[Concentration before reaction (counting strain volume)-Concentration after reaction]/ Concentration before reaction (counting strain volume) *100% (1)

2.5 Response surface methodology

The central composite design (CCD) of response surface methodology (RSM) is utilized to determine the optimum operational conditions for the biosorption process. Every numeric factor is varied over 5 levels: plus and minus alpha, plus and minus 1(factorial points) and the center point.[14]. Three factors, i.e., concentration of lead, concentration of zinc and inoculation amount of *Trichoderma reesei*, and varies from 0.5 mg/L~2mg/L, 0.5mg/L~1.5mg/L, 300 uL~1000uL, respectively. And the range of variation is shown in Table 1.

Table 1: Range of variation

Factors	Variables	Low actual	High actual	Low Coded	High coded
X1	Concentration of lead (mg/L)	0.8	1.7	-1.000	1.000
X2	Concentration of zinc (mg/L)	0.7	1.3	-1.000	1.000
X3	Inoculation amount (uL)	300	1000	-1.000	1.000

Table 2: Central composite design and experimental responses.

Run	X1	X2	X3	Response 1	Response 2
1	1.25	1	61.37	0.860658	0.413809
2	0.5	1	650	0.369979	0.44457
3	1.25	1	1238.63	0.901682	0.508715
4	0.8	0.7	300	0.595091	0.311385
5	0.8	1.3	1000	0.632161	0.566632
6	1.7	0.7	300	1.28242	0.321636
7	0.8	1.3	300	0.616915	0.547159
8	1.25	1.5	650	1.00219	0.725871
9	1.25	0.5	650	1.02338	0.271081
10	0.8	0.7	1000	0.675207	0.308048
11	1.25	1	650	0.955306	0.473142
12	1.7	1.3	300	1.30144	0.597697
13	1.7	0.7	1000	1.36635	0.351149
14	1.7	1.3	1000	1.34437	0.596442
15	2	1	650	1.52814	0.477513
16	1.25	1	650	0.939204	0.465596

Total 16 experimental groups were designed by the central composite design (CCD) model and performed as shown in Table 2. As shown in Table 1, the X1, X2 and X3 represents concentration of lead , zinc, and inoculation amount of fungi, respectively. And response 1, 2 are the concentration of lead and zinc after

reaction, respectively.

3. Results and discussions

3.1 Effect of variables on the removal of lead

As shown in Table 3, the variance of the removal of lead is analyzed. The present model is not only the defifine optimum conditions for lead removal but also showed combined effect of variables i.e. concentration of lead and zinc and inoculation amount of fungi. The Model F-value of 295.29 implies the model is significant. There is only a 0.01% chance that a "Model F-Value" this large could occur due to noise. The "Lack of Fit F-value" of 5.58 implies the Lack of Fit is not significant relative to the pure error. There is a 31.04% chance that a "Lack of Fit F-value" this large could occur due to noise. Non-significant lack of fit is good.

The concentration of Pb after biosorption of *Trichoderma reesei* is shown in equation 2.

Concentration of Pb after biosorption of fungi (mg/L)

$$=0.94+0.35*A-4.380E-003*B+0.021*C+2.283E-003*A*B+3.936E-003*A*C-0.013*B*C+7.404E-003*A^2+0.030*B^2-0.017*C^2 \quad (2)$$

Table 3: Analysis of variance (ANOVA) for response surface quadratic model

Sources	Sum of squares	DF	Mean square	F value	Prob>F	
Model	1.66	9	0.18	295.29	0.0001	Significant
A-Concentration of Pb	1.63	1	1.63	2615.80	0.0001	
B-Concentration of Zn	2.620E-004	1	2.620E-004	0.42	0.5411	
C-Inoculation amount	6.210E-003	1	6.210E-003	9.94	0.0197	
Residual	3.747E-003	6	6.244E-004			
Lack of Fit	3.617E-003	5	7.234E-004	5.58	0.3104	Not significant
Pure error	1.296E-004	1	1.296E-004			
Cor total	1.66	15				

DF: degree of freedom.

Table 4 showed the analysis of variance table of the model. The "Pred R-Squared" of 0.9832 is in reasonable agreement with the "Adj R-Squared" of 0.9944.

Table 4: Analysis of variance of the model

Response1	R2	Adj-R2	Pred-R2	Mean	Std. Dev.
Concentration of lead after biosorption	0.9977	0.9944	0.9832	0.96	0.025

Figure 1 illustrates the current lambda=1, and the best lambda=1.04, low C.I. =0.33 and high C.I.=2.88. The data do not require a transformation, as current value of confidence interval it contains is very close to the optimum value. After reviewing all the statistical outputs for design evaluation and three-dimensional plots, the minimum value of standard error relatively low, which indicates the design points and polynomial fitness of the model, as shown in figure 2. And the relationship between the concentration of lead after biosorption is showed in figure 3.

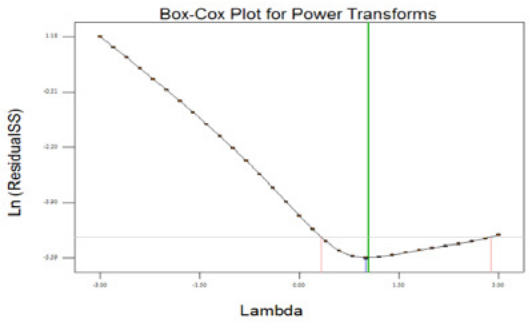

Figure 1: Box-Cox plot for power transforms

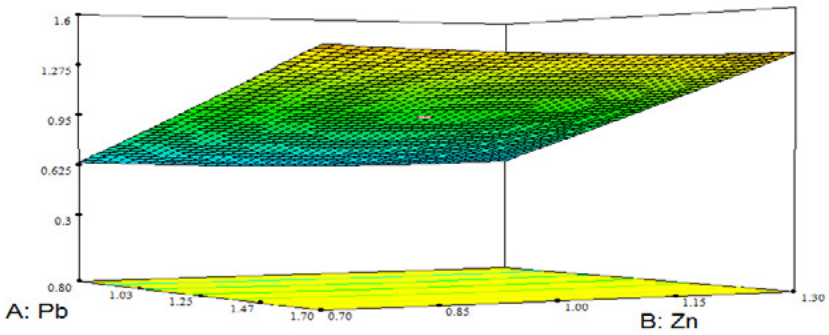

Figure 2: Three-dimensional graph of results

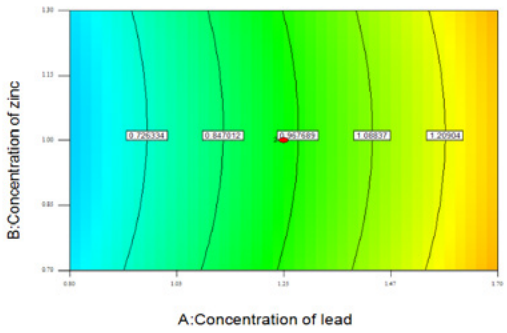

Figure 3: Two-dimensional graph of results

3.2 Effect of variables on the removal of zinc

As shown in Table 5, the variance of the removal of zinc is analyzed. The quadratic regression showed that the model was significant because the value of F-test is less than 0.05 and model F value 146.27 which indicated the significance of the model terms. And Table 6 showed the R square.

The "Pred R-Squared" of 0.9499 is consistent with the "Adj R-Squared" of 0.9667. Figure 4 illustrates the variance of the biosorption of fungi on Zn by model. And the experimental results of the removal of zinc are shown in figure 5. As can be seen, the results showed an approximate linear relationship between X2 and response 2.

Table 5: Analysis of variance (ANOVA) for response surface quadratic model

Sources	Sum of squares	DF	Mean square	F value	Prob>F	
Model	0.24	3	0.079	146.27	□ 0.0001	Significant
A-Concentration of Pb	2.618E-003	1	2.618E-003	2615.80	0.0483	
B-Concentration of Zn	0.23	1	0.23	0.42	□ 0.0001	
C-Inoculation amount	3.047E-003	1	3.047E-003	9.94	0.0375	
Residual	6.504E-003	12	5.420E-004			
Lack of Fit	6.475E-003	11	5.877E-004	5.58	0.1700	Not significant
Pure error	2.847E-004	1	2.847E-005			
Cor total	0.24	15				

Table 6: Analysis of variance of the model

Response1	R^2	Adj-R^2	Pred-R^2	Mean	Std. Dev.
Concentration of zinc after biosorption	0.9734	0.9667	0.9499	0.46	0.023

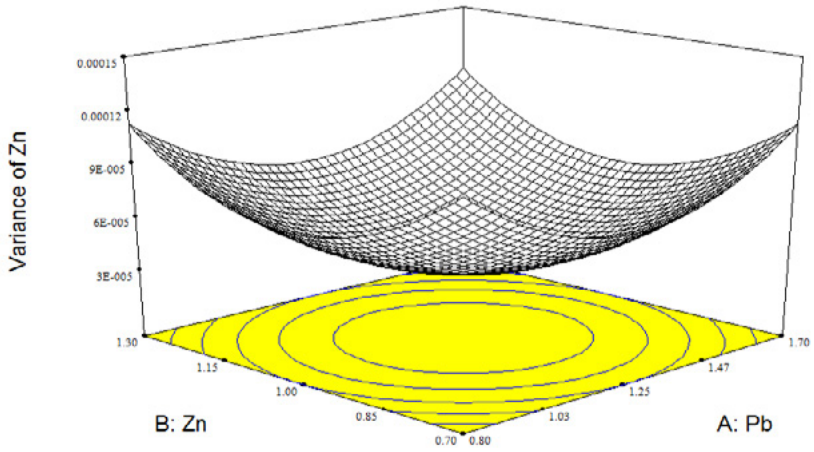

Figure 4: Three-dimensional graph of variance of Zn by model

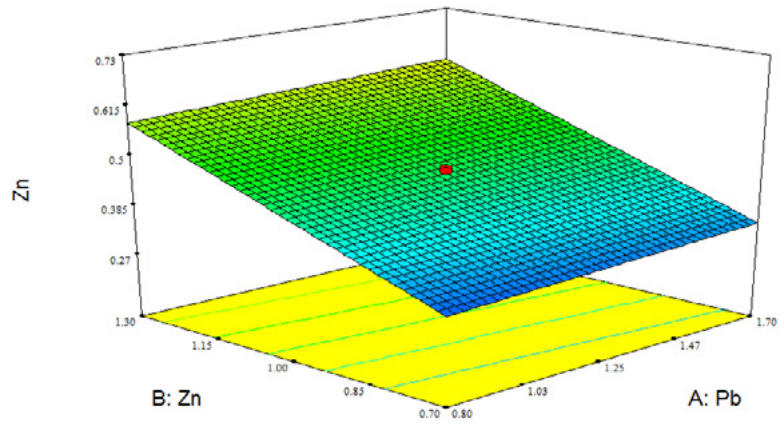

Figure 5: Three-dimensional graph of results

4 Conclusions

This study demonstrates that *Trichoderma reesei* (CCTCC AF 2015005 QM6a) offers a new method of biosorption of the heavy metals i.e. lead and zinc. Response surface method was utilized to establish the model between the heavy metal removal and the concentration of lead and zinc and the fungi that taking effect. Response surface methodology (RSM) is a powerful tool not only can be used for optimization of the process control in biosorption of heavy metal but also for the additional knowledge supplied about the optimization processes in any part of experimental domain. The optimum response 1 (concentration of lead) is 0.8 mg/L, and as for response 2 (concentration of zinc), the optimum concentration is 0.83mg/L,

in the condition of the inoculation amount of fungi is 300 uL. The characteristic of mycelium of *Trichoderma reesei* offers nucleation sites for the biorsorption of heavy metal ions.

5 Acknowledgements

The authors acknowledge the financial supports of National Nature Science Foundation Project of China (No. 51608409), National Science and Technology Support Program of China (2014BAC01B02), the National Key Research and Development Program of China in 13th Five-Year (2016YFC0305101), Yang Fan plan of Guangdong Province (201312C12), Major science and technology project in Zhongshan city, Guangdong province (2017A1021).

6 References

1. Rapoport, A.I., Muter, O.A., Bisorption of hexavalent chromium by yeast. Process Biochemistry. 30(1995), 145–149.
2. Caravelli, A.H., Giannuzzi, L., Zaritzky, N.E., Reduction of hexavalent chromium by Sphaerotilus natans a fifilamentous micro-organism present in activated sludges. Journal of Hazardous Materials. 156(2008), 214–222.
3. Eccles, H., Treatment of metal contaminated waste: why select a biological process? .TIBTECH. 17(1999), 462–465
4. Li, H., Li, Z., Liu, T., Xiao, X., Peng, Z., Deng, L., A novel technology for biosorption and recovery hexavalent chromium in wastewater by biofunctional magnetic beads. Bioresource Technology. 99(2008), 6271–6279.
5. Crisafully, R., Milhome, M.A., Cavalcante, R.M., Silveira, E.R., De Keukeleire, D., Nascimento, R.F., Removal of some polycyclic aromatic hydrocarbons from petrochemical wastewater using low-cost adsorbents of natural origin. Bioresource Technology. 99(2008), 4515 – 4519.
6. Elangovan, R., Philip, L., Chandraraj, K., . Biosorption of chromium species by aquatic weeds: kinetics and mechanism studies. Journal of Hazardous Materials. 152(2008), 100–112.
7. Febrianto, J., Kosasih, A.N., Sunarso, J., Ju, Y.H., Indraswati, N., Ismadji, S., Equilibrium and kinetic studies in adsorption of heavy metals using biosorbent: a summary of recent studies. Journal of Hazardous Materials. 162(2009), 616–645
8. Mohan, D., Rajput, S., Singh, V.K., Steele, P.H., Pittman Jr., C.U., Modeling and evaluation of chromium remediation from water using low cost bio-char, a green adsorbent. Journal of Hazardous Materials. 188(2010), 319–333.
9. Ng, I.S., Tsai, S.W., Ju, Y.M., Yu, S.M., Ho, T.H., Dynamic synergistic effect on Trichoderma reesei cellulases by novel beta-glucosidases from Taiwanese fungi. Bioresource Technology. 102(2011), 6073–6081.
10. Park, D., Yun, Y.S., Ahh, C.K., Park, J.M., Advanced kinetic model of the Cr(VI) removal by biomaterials at various pHs and temperatures. Bioresource Technology. 99(2008), 1141–1147.
11. Ng I S, Wu X, Yang X, et al., Synergistic effect of Trichoderma reesei cellulases on agricultural tea waste for adsorption of heavy metal Cr(VI)[J]. Bioresource Technology. 145(4)(2013):297-301.
12. Dacera, D., Babel, S., Removal of heavy metals from contaminated sewage sludge using Aspergillus Niger fermented raw liquid from pineapple wastes. Bioresour. Technol. 99(2008), 1682-1689.

13. Hu, L., Wan, J., Zeng, G.M., Chen, A.W., Chen, G.Q., Huang, Z., He, K., Cheng, M.,Zhou, C., Xiong, W., Lai, C., Xu, P., Comprehensive evaluation of the cytotoxicity of CdSe/ZnS quantum dots in Phanerochaete chrysosporium by cellular uptake and oxidative stress. Environ. Sci. (2017)Nano. https://doi.org/10.1039/c7en00517b.

14. Design-Expert® Software, Version 6 User's Guide, 2001.

Use of peach shell as lightweight aggregate in pervious concrete

F. Wu[1,2], C. Liu[1,3,4], L.Zhang[3,4], Y. Lu[3,4], Q.L. Yu[2]

[1] Institute of Disaster Management and Reconstruction, Sichuan University-The Hong Kong Polytechnic University, No.1Huanghe Road, Chengdu 610065, China.

[2] Department of the Built Environment, Eindhoven University of Technology, P.O. Box 513, 5600 MB Eindhoven, The Netherlands.

[3] College of Water Resource and Hydropower, Sichuan University, No.24 South Section 1, Yihuan Road, Chengdu 610065, China.

[4] State Key Laboratory of Hydraulics and Mountain River Engineering, Sichuan University, No.24 South Section 1, Yihuan Road, Chengdu 610065, China.

Abstract

Peach shell (PS) is considered as an agricultural waste, which can be used as a lightweight aggregate in concrete due to its porous and lightweight properties. However, few literatures investigated the PS used as an aggregate in pervious concrete (PC). In order to expand the application of the PS in concrete, this study presents the use of PS used as an alternative aggregate in PC. A series of PC mixes were prepared with 0%, 25%, 50%, 75% and 100% replacement of normal weight aggregate (NWA) by PS, while the other parameters were set as constant. The results showed that the replacement of NWA with PS significantly reduced density, compressive strength and splitting tensile strength of PC, while increased the total void ratio and water permeability coefficient. Clogging test results showed that sand and dredged silt had a significant impact on the water permeability coefficient of PC, and the use of the large-grained aggregates in PC had better clogging resistance than the small-grained aggregates. When the PS is used as a coarse aggregate in PC, it cannot be used to fully replace the coarse aggregate. Based on the results of this study, the NWA was replaced by 25% PS, the compressive strength, splitting tensile strength and water permeability coefficient of PC were 7.9MPa, 0.91MPa and 9mm/s, respectively.

Keywords: Pervious concrete, Peach shell, Lightweight aggregate, Permeability, Clogging.

1. Introduction

Demand for concrete has been steadily increasing due to the economic development and increasing population [1]. The exploitation of natural aggregates has led to the scarcity of raw materials, which not only increases the cost of concrete but also destroys the surface landscape. Therefore, in order to achieve the sustainable development of the concrete industry, the utilization of various industrial by-product wastes and agricultural wastes as alternative raw materials for concrete has become one of the research hot issues all over the world [2]. Previous research has shown that some industrial and agricultural wastes can be successfully incorporated into concrete, including rubber, apricot shell, oil palm shell, seashell, plastics, wood and coconut shell, etc. [3-5].

Pervious concrete (PC) is a special type of concrete consisting of cement, a single grade of coarse aggregate,

little or no sand and a small amount of water [6]. Typically, the workability and strength of PC is much lower than that of normal weight concrete due to the lack or only small amount of sand in PC [7], and the permeability coefficient of ordinary PC is between 1.4 mm/s and 12.2 mm/s, the porosity varies from 14% to 35%, and the 28-day compressive strength is usually between 2.8 MPa and 28.0 MPa [8]. Although low-strength PC is not suitable for load-bearing purposes, they can be used in parking lots, drainage pavements and sidewalks, etc. [9].

The main function of the PC is to realize the spontaneous circulation of rainwater for sponge city by penetrating rainwater from the road surface to the underground soil [10]. The studies about previous concrete focused on the permeability coefficient, porosity and clogging performance of PC rather than its strength characteristics [10]. At present, the production of PC usually uses normal weight aggregate (NWA) as a single-grain aggregate, such as crushed granite, limestone and dolomite, etc. Recently, with the rise of the trend towards the use of various types of wastes as aggregates in concrete, some wastes such as recycled aggregate, rubber, seashell and palm oil clinker have also been used in the manufacture of PC [11-13]. Normally, the performance of the PC depends on the replacement ratio and the amount of the wastes. Although the wastes used as a substitute for NWA reduce the strength of PC, they are recycling wastes and reducing the consumption of NWA, which is conducive to the sustainable development of PC. The low-strength PC made of various wastes is adequate for low-strength structures such as sidewalks, parking lots and road shoulders, etc..

Peach is one of the main fruits in China, most of them are used for the products of peach drinks, candied fruit and canned food. The planting area and output of peach in 2016 in China were 742.1 k hm^2 and 13.1 million tons, respectively [14]. Peach shell (PS) is considered as agricultural waste and has no industrial application value. Due to crushed PS is renewable, which has lightweight and porous properties, it can be considered as an alternative aggregate for the manufacture and production of lightweight aggregate concrete (LWAC) [15]. However, there are few limited literatures on the use of such agricultural waste as an alternative aggregate in PC.

In this study, the peach shell (PS) was used to replace the normal weight aggregate (NWA) for producing pervious concrete (PC). NWA of different volume ratios was replaced by PS, while the other parameters were kept constant. The properties investigated included basic physical properties (density, total void ratio and water permeability coefficient), mechanical properties (compressive and splitting tensile strength) and clogging properties.

2. Methodology

2.1 Materials

2.1.1 Cement

Type I 42.5 grade ordinary Portland cement was used as the binder. The Blaine specific surface area and the specific density of the cement are 3532 cm^2/g and 3.14 g/cm^3, respectively. All mixtures were prepared with a cement content of 360 kg/m^3.

2.1.2 Aggregate

In this study, a single-sized normal weight aggregate (NWA) with a 4.75-9.6mm was used and obtained from crushed pebbles. Single-sized peach shell (PS) with 4.75-9.6mm diameter was used as an alternative aggregate, and they were collected from a local orchard. The aggregates used in this study are presented in Figure 1, and the physical properties of aggregates are shown in Table 1. The specific gravity of the NWA was 2.66 g/cm^3 and the bulk density was 1449 kg/m^3. However, the specific gravity and density of the PS

were only 1.33 g/cm^3 and 538 kg/m^3, respectively. The density of PS was significantly lower than that of the NWA due to the presence of the round microscopic pores on the surface and interior of PS. However, the microscopic pore structure also increases the water absorption of PS, resulting in its much higher water absorption than that of the NWA.

Table 1: Physical properties of aggregates.

Physical property	Coarse aggregate	
	NWA	PS
Aggregate size (mm)	4.75-9.6	4.75-9.6
Specific gravity (g/cm^3)	2.66	1.26
Fineness modulus	4.9	5
Bulk density (kg/m^3)	1449	538
Water absorption (24h) (%)	0.5	16.7

Figure 1: a) Normal weight aggregate, b) Crushed peach shell and (c) SEM image of peach shell.

2.1.3 Mix proportions, mixing and casting

The mix proportions of all concrete are summarized in Table 2. For all mixes, cement and water were kept constant. In these pervious concretes, the NWA in the control mix was replaced with crushed PS by mass. The ratio of the PS substitute for the NWA was 25%, 50%, 75% and 100%, respectively. A concrete without PS was also prepared and used for a control purpose.

Table 2: Mix proportion of concretes (kg/m^3).

Mix	Cement	Water	W/C	Coarse aggregate		
				NWA	PS	PS/total Coarse aggregate ratio
Control	360	108	0.3	1550	0	0
PS-25	360	108	0.3	1162.5	135	25%
PS-50	360	108	0.3	775	270	50%
PS-75	360	108	0.3	387.5	405	75%
PS-100	360	108	0.3	0	540	100%

The mixing of all the mixtures was done in the laboratory with an ambient temperature of 23±2℃. Firstly, the NWA, PS and cement were mixed in a circular drum mixer for 2 min. Then 70% of water was added and mixed for 2 min, and the remaining 30% of water was then added and mixed for 3 min.

After that, all mixtures were cast in different sized oiled moulds. 100mm×100mm×100mm cube specimens were used for compressive strength test, splitting tensile strength test and porosity test. The cylindrical specimens with a diameter of 100mm and a height of 200 mm were used for the clogging test and

permeability test. All the mixtures were compacted by a vibrating table. Immediately, after compaction, all specimens along with the mould were covered by the plastic sheathing for preventing moisture evaporation. After 24 h, all specimens were removed from the molds and stored in water until the test age.

Figure 2: The apparatus for permeability test.

2.2.3 Clogging test

Generally, the sediment containing both coarse and fine particles is most significant for reducing the permeability coefficient of pervious concrete [18]. The clogging test was performed in this study to evaluate the clogging performance of peach shell pervious concrete (PSPC). The clogging material used in this study was based on the blended material proposed by Dang et al. [12]. That is, the clogging material was made of 75% dredged silt (0-80μm) and 25% sand (0-4mm), which could be used to simulate field conditions. Before the clogging material was used, they were added to the water and mixed well until a uniform suspension was obtained at a concentration of 1% (Figure 3).

The same device was used for the clogging test and permeability test. The clogging test applied a cyclic test method, and a detailed test process is as follows: Firstly, the initial permeability coefficient was measured by the method of falling head test; Secondly, a suspension of clogging material was prepared at a concentration of 1%; Thirdly, the suspension was poured from the upper surface of the specimen and it slowly permeated the specimen through the pore structures inside the specimen; Fourthly, after the suspension was completely drained, the permeability coefficient of the specimen was determined by falling head test method when the clogging material still presented on the surface of the specimen; Finally, these above steps were repeated for at least four times.

Figure 3: a) Clogging material mixed by sand and dredged silt, b) The suspension of clogging material has a concentration of 1%.

3. Results and discussion

3.1 Density, total void ratio and water permeability coefficient

The density, total void ratio and water permeability coefficient of concretes are shown in Table 3. The results showed that with the content of PS increased, the density of PC significantly decreased while the total void ratio and water permeability coefficient increased. Generally, the typical density of PC varies from 1500 kg/m^3 to 2000 kg/m^3, and the porosity between 15 % and 35 %, and the water permeability coefficient ranges from 1.4 mm/s to 12.2 mm/s [8]. In this study, the density of concrete containing PS varied from 825 kg/m^3 to 1568 kg/m^3, which was lower than the control concrete without any PS due to the density of the PS lower than that of the NWA.

Table 3: Physical properties of concretes.

Mix	Density (kg/m^3)	**Total void ratio** (%)	Water permeability coefficient (mm/s)
Control	1693	26.6	7.9
PS-25	1568	28.4	9.0
PS-50	1424	31.7	9.5
PS-75	1069	35.1	10.3
PS-100	825	37.2	11.2

ACI 522 [19] recommended that the porosity of PCs was usually between 15 % and 35 %. The total void ratio of all PCs varied from 26.6% to 37.2%, and except for PS-75 and PS-100, other mixtures were within the specified range reported by ACI 522. The total void ratio of PC significantly increased with the increasing PS content. When the NWA in the PC was replaced by 100% PS, the PS-100 mix had the highest total void ratio of 37.2%, which was 39.8% higher than that of the control mix. In addition, with the increase of total void ratio, the density decreased. A good linear relationship with a good correlation coefficient (R^2=0.96) between total void ratio and density was presented in Figure 4.

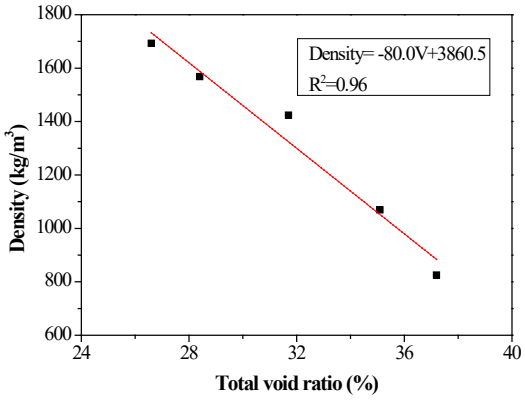

Figure 4: Relationship between total void ratio and density.

Generally, the permeability of PC depends on the connectivity of the internal pores and pore diameter [8]. The water permeability coefficient of PCs varied from 7.9 mm/s to 11.2 mm/s. The water permeability coefficient was lowest without any PS. However, when the NWA was replaced by 100% PS, the water permeability coefficient was increased by 41.8%, compared to the control concrete. The relationship between total void ratio and water permeability coefficient was shown in Figure 5. As expected, the water permeability coefficient of PCs increased as the void ratio increased.

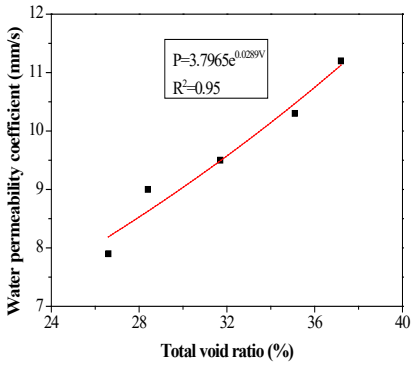

Figure 5: Relationship between total void ratio and water permeability coefficient.

3.2 Compressive and splitting tensile strength

The 28-day compressive strength of all PCs varied from 1.9 MPa to 9.2 MPa, as shown in Table 4. With the PS content increased, the compressive strength significantly decreased. When the NWA was replaced by 100 % PS, the compressive strength reduced by 79.0% compared to the control mix. Güneyisi et al. [8] reported that the strength of PC mainly depends on the bond strength between the aggregate and cement paste. The failure pattern of PC containing PS is presented in Figure 8. The cracks of PC containing PS not only propagated through the interfacial transition zone (ITZ) but also passed through the PS aggregate. The reason for the incorporation of PS to significantly reduce the strength of PCs can be attributed to the following: Firstly, PS is an organic matter, which results in the weak bond in the ITZ [4]. Secondly, the shrinkage of PS also is an important influence on the aggregate-paste binding ability [14]. Thirdly, the strength of PS is much lower than that of the NWA [15], which also contributed to the low compressive strength of PC.

Table 4: Mechanical properties of concretes.

Mix	Compressive strength (MPa)			28-day splitting tensile strength (MPa)
	7-day	14-day	28-day	
Control	5.6	7.8	9.2	1.08
PS-25	4.9	6.7	7.9	0.91
PS-50	2.6	3.8	5.1	0.73
PS-75	1.4	2.5	3.2	0.56
PS-100	1	1.3	1.9	0.28

Figure 6: Failure pattern of PC containing PS.

The relationship between total void ratio and water permeability coefficient and compressive strength are presented in Figure 7 and Figure 8, respectively. It was clear that the compressive strength decreased as the total void ratio and water permeability coefficient increased.

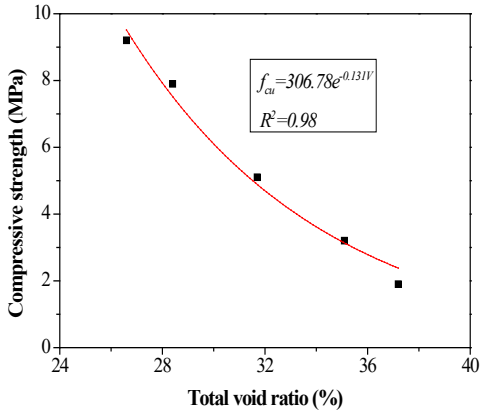

Figure 7: Relationship between total void ratio and compressive strength.

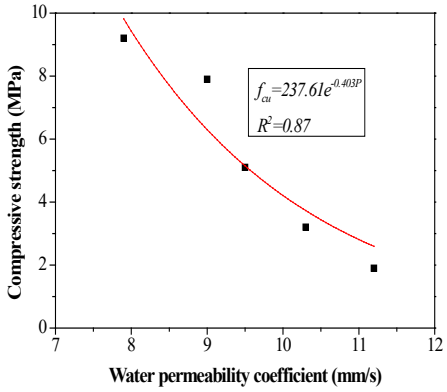

Figure 8: Relationship between water permeability coefficient and compressive strength.

The splitting tensile strength results are also presented in Table 4. The splitting tensile strength decreased as the increase in PS content. The splitting tensile strength of all PCs ranged from 0.28 MPa to 1.08 MPa. Wu et al. [15] reported that PS can be used to produce lightweight aggregate concrete by replacing 100 % NWA. However, the use of 100 % PS instead of NWA for the manufacture of PC is not feasible. When PS is used in PC, the content of PS should not exceed 25%. The relationship between compressive strength and splitting tensile strength is shown in Figure 9. The results showed that the splitting tensile strength increased as the increase of compressive strength.

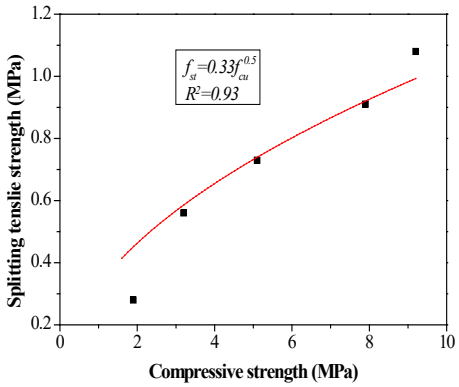

Figure 9: Relationship between compressive strength and splitting tensile strength.

3.3 Clogging test results

The relationship between clogging cycles and water permeability coefficient is shown in Figure 10. The results showed that the water permeability coefficient of PC decreased gradually after each clogging cycle due to the suspension containing clogging material was poured into the upper surface of the PC, which could penetrate into the PC and deposited on the pore wall [12]. After the fourth clogging cycle, the water permeability coefficient of the Control, PS-25, PS-50, PS-75 and PS-100 were 0.2 mm/s, 0.4 mm/s, 0.6 mm/s, 0.9 mm/s and 1.3 mm/s, respectively, which decreased by 97.5%, 95.6%, 93.7%, 91.3% and 88.4%, respectively, compared to the initial value. The results also indicated that dredged silt and sand had a significant impact on the permeability of PC, and the PC with higher porosity had better clogging resistance.

The detailed blocking process may be as follows: firstly, the sand grains entered the large pore structure inside the PC, and then the dredged silt grains filled the remaining voids and increased the blockage of the permeable pores, resulting in the water permeability coefficient decreased rapidly. Dang et al. [12] found that after the first plug cycle, the water permeability coefficient of PC containing 2-4 mm was reduced by 95% of the initial value. In this study, after the first cycle, the water permeability coefficient of the Control, PS-25, PS-50, PS-75 and PS-100 mixes decreased by 50.6 %, 46.7 %, 38.9 %, 28.2 % and 28.6 %, respectively, compared to the initial values.

This may be contributed to the PS and the NWA used in this study have a particle size of 4.75-9.6 mm, which are larger than the particle size of seashell of 2-4 mm, and consequently resulting in a higher porosity of PC. Therefore, the large-grained aggregates are more advantageous than the small-grained aggregates in resisting clogging.

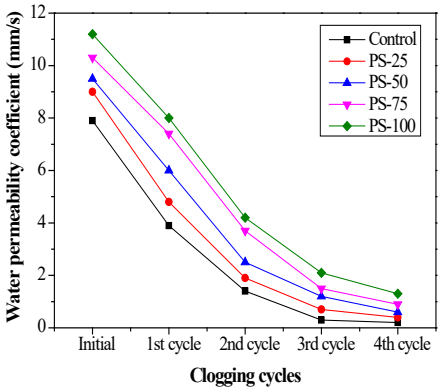

Figure 10: Relationship between clogging cycles and water permeability coefficient.

Changes in the top surface of the PS-50 mix during the clogging test are shown in Figure 11. It is clear that after the second clogging cycle, most of the suspensions containing the clogging material could not penetrate the PS-50 mix and only remained on the upper surface, resulting in the lower water permeability coefficient.

After the fourth clogging cycle, the clogging material was almost fully deposited on the surface of the PS-50 mix, and water could hardly penetrate through the PS-50 mix.

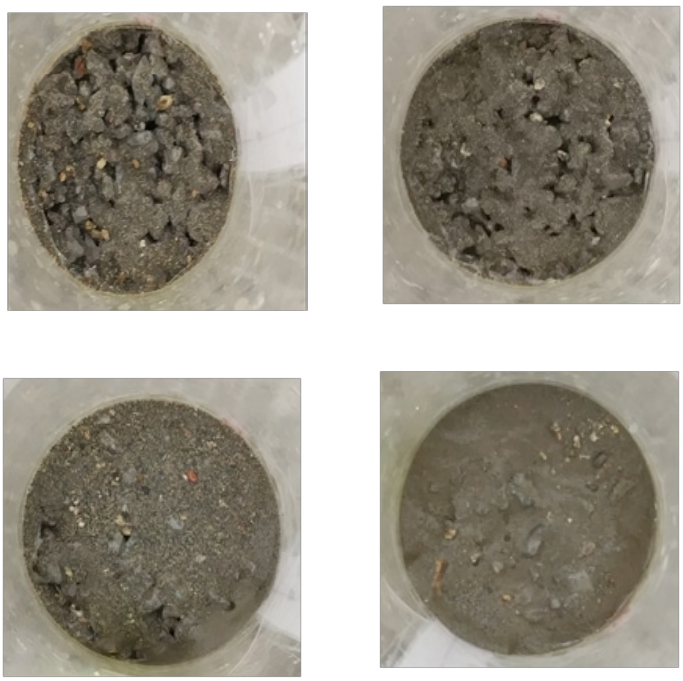

Figure 11: Changes in the top surface of the PS-50 mix during clogging test a) First cycle, b) Second cycle, c) Third cycle and d) Fourth cycle.

4. Conclusions

In this study, the peach shell (PS) was used as a substitute for the normal weight aggregate (NWA) to produce pervious concrete (PC). The physical properties (density, total void ratio and water permeability coefficient), mechanical properties (compressive and splitting tensile strength) and clogging properties of PC were investigated. The following conclusions can be drawn based on the present study:

- The replacement of the NWA with the PS reduces density, compressive strength and splitting tensile strength of PC while increasing the total void ratio and water permeability coefficient. When the NWA is replaced by 100 % PS, the density, compressive strength and splitting tensile strength decrease by 51.3 %, 79.0 % and 74.1 %, respectively. However, the total void ratio and water permeability increases by 39.8 % and 41.8 %, respectively, compared to the control mix.
- The low strength of the PS aggregate results in low mechanical properties of the PC. However, the compressive strength, splitting tensile strength and water permeability coefficient of PS-25 mix are 7.9 MPa, 0.91 MPa and 9 mm/s, respectively. Therefore, it is feasible that the use of PS to produce the PC with suitable mechanical properties by adding less than 25 % PS.
- Clogging materials made of sand and dredged silt have a significant impact on the water permeability coefficient of PC. The large-grained aggregates are more advantageous than the small-grained aggregates in resisting clogging. The water permeability coefficient of PC decreases gradually after each clogging cycle, after the fourth clogging cycle, the water permeability coefficient of the Control, PS-25, PS-50, PS-75 and PS-100 decreased by 97.5 %, 95.6 %, 93.7 %, 91.3 % and 88.4 %, respectively, compared to the initial values.

5. Acknowledgment

This work was funded by the Graduate Student's Research and Innovation Fund of Sichuan University

(Grant No. 2018YJSY091), and the Key Laboratory of Geological Hazards Mitigation for Mountainous Highway and Waterway, Chongqing Municipal Education Commission Chongqing Jiaotong University (Grant No. kfxm2018-01), the China Scholarship Council (CSC) Fund (Grant No. 201806240037) and Eindhoven University of Technology.

6. References

[1] Huiskes, D.M.A., Keulen, A., Yu, Q.L., Brouwers, H.J.H., 2016, Design and performance evaluation of ultra-lightweight geopolymer concrete, Materials & Design. 89, 516-526, DOI: 10.1016/j.matdes.2015.09.167.

[2] Sata, V., Wongsa, A., Chindaprasirt, P., 2013, Properties of pervious geopolymer concrete using recycled aggregates, Constr. Build. Mater. 42, 33-39, DOI: 10.1016/j.conbuildmat.2012.12.046.

[3] Mo, K.H., Alengaram, U.J., Jumaat, M.Z., Yap, S.P., Lee, S.C., 2016, Green concrete partially comprised of farming waste residues: a review, Journal of Cleaner Production. 117,122-138, DOI: 10.1016/j.jclepro.2016.01.022.

[4] Wu, F., Liu, C.W., Zhang, L.W., Lu, Y.H., Ma, Y.J., 2018, Comparative study of carbonized peach shell and carbonized apricot shell to improve the performance of lightweight concrete, Construction and Building Materials. 188,758-771, DOI: 10.1016/j.conbuildmat.2018.08.094.

[5] Wu, F., Liu, C.W., Sun, W., Zhang, L.W., 2018, Mechanical Properties of Bio-based concrete containing blended peach shell and apricot shell waste, Materiali in Tehnologije. 52(5),645-651, DOI: 10.17222/mit.2018.065.

[6] Chindaprasirt, Prinya., Peem, Nuaklong., Yuwadee, Zaetang., Purimpat, Sujumnongtokul., and Vanchai Sata, 2015, Mechanical and thermal properties of recycling lightweight pervious concrete, Arabian Journal for Science and Engineering, 40(2), 443-450, DOI: 10.1007/s13369-014-1563-z.

[7] Dang, Hanh Nguyenab., Nassim, Sebaibia., Mohamed, Boutouila., Lydia, Leleyterb., Fabienne, Baraudb, 2014, A modified method for the design of pervious concrete mix, Constr. Build. Mater. 73, 271-282, DOI: 10.1016/j.conbuildmat.2014.09.088.

[8] Erhan, Güneyisi., Mehmet, Gesoğlu., Qays, Kareem., Su¨leyman, İpek., 2016, Effect of different substitution of natural aggregate by recycled aggregate on performance characteristics of pervious concrete, Materials and Structures, 49, 521-536, DOI:10.1617/s11527-014-0517-y.

[9] Bhutta, M.A.R., Tsuruta, K., Mirza, J., 2012, Evaluation of high-performance porous concrete properties, Constr. Build. Mater. 31, 67-73, DOI: 10.1016/j.conbuildmat.2011.12.024.

[10] Shu, Xiang., Huang, Baoshan., Wu, Hao., Dong, Qiao., Burdette, Edwin G., 2011, Performance comparison of laboratory and field produced pervious concrete mixtures, Construction and Building Materials, 25,3187-3192, DOI: 10.1016/j.conbuildmat.2011.03.002.

[11] Gesog˘lu, M., Güneyisi, E., Khoshnaw, G., İpek S., 2014, Investigating properties of pervious concretes containing waste tire rubbers, Constr. Build. Mater. 63,206-213, DOI: 10.1016/j.conbuildmat.2014.04.046.

[12] Dang, Hanh Nguyen., Mohamed, Boutouil., Nassim, Sebaibi., Fabienne, Baraud., Lydia, Leleyter., 2017, Durability of pervious concrete using crushed seashells, Construction and Building Materials, 135, 137-150, DOI: 10.1016/j.conbuildmat.2016.12.219.

[13] Hussein, Adebayo Ibrahim., Hashim, Abdul Razak.,2016, Effect of palm oil clinker incorporation on properties of pervious concrete, Construction and Building Materials, 115,70-77, DOI: 10.1016/j.

conbuildmat.2016.03.181.

[14]Wu, F., Liu, C., Sun, W., Ma, Y., & Zhang, L, 2019, Effect of peach shell as lightweight aggregate on mechanics and creep properties of concrete, European Journal of Environmental and Civil Engineering, 1-19, DOI: 10.1080/19648189.2018.1515667.

[15]Wu, F., Liu, C., Diao, Z., Feng, B., Sun, W., Li, X., & Zhao, S., 2018, Improvement of mechanical properties in polypropylene-and glass-fibre-reinforced peach shell lightweight concrete, Advances in Materials Science and Engineering, 2018, DOI: 10.1155/2018/6250941.

[16] Montes, F., Valavala, S., Haselbach, L., 2005, A new test method for porosity measurements of Portland cement pervious concrete, Journal of ASTM International, 2(1):13, DOI: 10.1520/JAI12931.

[17] Narayanan, N., Jason, W., Jan, O., 2006, Characterizing enhanced porosity concrete using electrical impedance to predict acoustic and hydraulic performance, Cem Concr Res,36:2074-2085, DOI: 10.1016/j.cemconres.2006.09.001.

[18] Schaefer, V.R. Kevern, J.T., 2011, An Integrated Study of Pervious Concrete Mixture Design for Wearing Course Applications, National Concrete Pavement Technology Center, Iowa State University, Iowa, p. 158.

[19] A. Committee, 2010, Report on pervious concrete (ACI 522R-10), American Concrete Institute.

A concrete composite from biologically based binders and mineral aggregates for constructional 3D-printing

J. Christ[1], H. Koss[1], L.M. Ottosen[1]

[1]Department of Civil Engineering, Technical University of Denmark, Brovej 118, 2400 Kgs. Lyngby

Abstract

The paper presents an alternative binder for structural 3D-printing with composite materials. The binder eases the control of setting times after extrusion through thermoplastic hardening properties. The material could therefore enable the production of thin-walled geometries in large-scale 3D-printing with higher degrees of freedom in respect to overhanging geometries without supporting structures. The proposed composite material is made from mineral aggregates and biological gels, resourced from animal tissue and bone. The used mineral aggregates are not deviating significantly from conventional concrete or mortar.

So far, the research determined a maximum flexural- and compressive strength of 8 MPa and 21 MPa. Furthermore, first material compositions are introduced and respective material properties tested. As a conclusion, the paper presents limitations and potentials of the concrete for the use as structural building material and the use within large-scale 3D-printing.

Keywords: Bio-based concrete, constructional 3D-printing, biopolymers, concrete composite, mineral aggregates

ICSBM 2019
ID 119

1. Introduction

Additive manufacturing and 3D-printing in the construction sector is a rapidly growing field of interest in research and industry [1], [2]. Possible material savings and a higher degree of freedom in shape forming increase both, sustainability in construction and architectural expression [3]. Some of the materials used for constructional three dimensional extrusion processes are steel ([4], [5]) , carbon fibre[6], or polymers ([7], [8], [9]). The main focus however lays on the printing with concrete ([1], [3], [10]), due to proven beneficial properties of cementitious materials, such as durability, inexpensiveness, fire resistance, structural strength and its plasticity during extrusion.

The current focus on cementitious concrete has its drawback regarding its sustainability account. This is due to the high amount of energy used under production, the CO_2-emissions of the chemical process during calcination of limestone and the high transport efforts due to dependency on centralised large-scale production sites. In many cases, the extruded material comprises substantially higher cementitious shares than conventionally casted concretes [11]–[13]. Additionally, extensive admixtures are being used to adapt the composite's performance as intended, enabling rapid viscosity change from liquid to solid during the printing process by thixotropic or chemical procedures. The combination of large limitations in reinforcement integration [3] and low early-age strength of concrete causes buckling and moment failures during printing, and restrain degree-of-freedom to an almost vertical build up.

The here presented research proposes an alternative concrete composite, based on biologically (bio-) based binding materials, for constructional 3D-printing. This concrete is in the following referred to as Biopolymer Concrete (BPC). The novelty of the material is the compound of biopolymers, resourced from animal tissue, bones, fish, shellfish, or algae as binding material in concrete, purposed for additive manufacturing processes. The intention is to completely replace any cementitious share in the composite with the biopolymer- and water- based binders. Sought after properties of the BPC with regards to constructional 3D-pinting are rapid viscosity change due to its thermoplastic hardening. Possibly, higher material savings in comparison to cementitious concrete could be reached by enabling higher resolution prints, i.e. thin-walled and overhanging geometries, through the rapid solidification.

Different sources for the binding material are considered. As a first prove of construction-worthiness of the novel material, the research presented here is conducted with BPC samples made of bone glue, a biologically resourced gel from animal tissue and bones (meat industrial waste products). The samples were tested for compressive- and flexural strength with different binder contents in the composite material. Other properties relating to the construction process, i.e. printability of the concrete, such as hardening and drying time as well as shrinkage, density and thermoplasticity have been tested explicitly or will be discussed based on available information.

2. Methodology

2.1 Materials

The tested BPC composite material was manufactured using bone glue as bio-based binding material, and mineral aggregates. In the following, the individual components, are described and characterized.

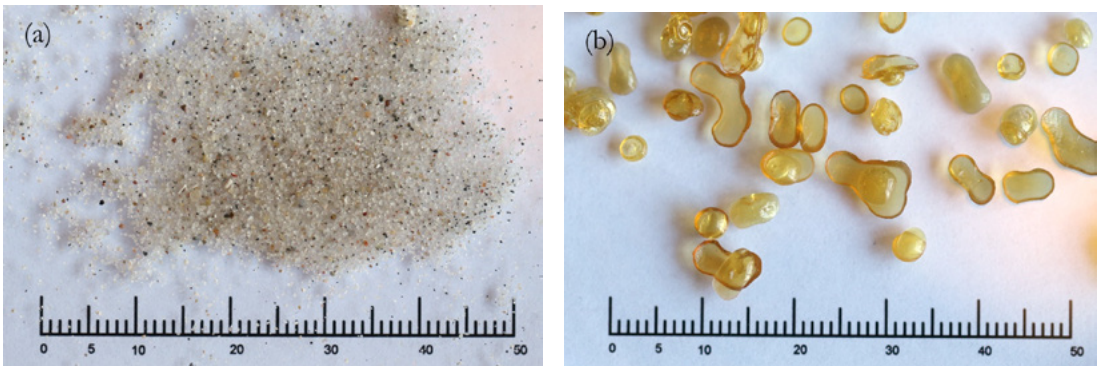

Figure 1: Raw materials used for BPC – (a) Mineral aggregates: Sand with a grain size distribution between 0-2mm, (b) biologically based binder granulate: bone glue – in [mm]

2.1.1 Mineral Aggregates

The used mineral aggregates are limited to sand with a grain size composition of 0-2mm (Figure 1 - a). The used sand is taken from the Great Belt strait in Denmark, part of the Baltic Sea. Due to the maritime origin,

The small grain size was chosen to:

reach a sufficient homogeneity of the composite material for small sample sizes

assure applicability for constructional 3D printing, for which rather small grained aggregates are used (as in [12], [13]) to enable thin extrusion processes and high resolution.

the rounded shape adds to good workability of the fresh concrete mix

2.1.2 Bio-based binding material

Bone glue is used as a biologically based binder to produce test specimen in this paper. The material is commercially available and extracted from industrial waste in food production (animal tissue and bones). It is traditionally used as adhesive for carpentry, woodwork, as well as for restauration and instrument making. Under soaking of water and the influence of heat, covalent bonds of long chained bio-polymers dissolve and a biological gel is separated from the raw biological material by Gelatinization. The adhesive is dried and sold in form of granulate (see Figure 1 – b).

The bone glue was purchased from DICTUM [14], a supplier for woodworking tools and materials. The delivered glue granulate has a grain size of 2-7mm (Figure 1 – b). Covered with water, the granulate dissolves and the gel liquefies. This process is intensified when adding heat to the solution. Both, water content and temperature in particular affect the viscosity of the gel significantly (thermoplasticity) and are hence pivotal to the workability of the composite material. The viscosity decreases significantly when increasing the binder's temperature to 70°C. The raw granulates density is $1.3 \frac{g}{cm^3}$ [1].

2.1.3 Nomenclature

To specify the composition of the tested BPC materials, a coding indicating the different constituents by letters and numbers of mass percent is used. In this study, specific constituents are water **(W)**, bone glue **(BG)** and Great Belt sea sand 0-2mm **(Z1)**. Symbols for less specified groups or more general terms would be glue granulate **(GG)** or binder **(b)**. This system allows to write unspecific (1) and specified (2) balanced equations describing BPC materials:

$$b1 = 44GG + 56W \quad (1)$$

$$BPC1 = 10(44BG56W)90Z1 \quad (2)$$

Equation (2) omits arithmetic operators (+) as used in equation (1). The unspecified glue granulate in equation (1) is in equation (2) replaced with the specific reference to bone glue. In this way, the notation allows defining parent types and sub groups of binders and composites. Finally, a specific sample of any BPC material is identified by a unique number at the end of the material code separated by a dot. The fifth sample made of BPC1 would bear the code:

$$BPC1.5 = 10(44BG56W)90Z1.5 \quad (3)$$

All numeric values and ratios refer to the material's weight and to compositions under mixing. The specified material proportions do not account for hardened samples, since water content decreases during drying.

2.1.4 Mixture

The tested compositions consist of bone glue, water and mineral aggregates. The specifications of the different BPC materials are listed in Table 1. In all cases, a W/GG-ratio of 1.25 has been chosen due to benefits in the workability of the heated mass. This was found during preliminary experiments. Material coding is according to Section 2.1.3.

2.2 Methods

The used methods for mixing, moulding and testing are largely inspired by the standardised procedures for cementitious mortar and concrete as described in EN 196-1 [15]. However, due to thermoplastic properties of the binding material, some adaptions were made. The steps in sample production, testing and property

1 Characterised by weight and volumetric analysis with water bath. A weight scale with an accuracy of 0.01g was used, as well as a single graduated 100ml cylinder to measure the volumetric increase of 50ml of water by adding 20g of binder granulate.

characterisation are in the following described in more detail.

2.2.1 Composite production

The production of the concrete composite, including the process for moulding and drying is compiled in Table 2, with approximate durations of the individual steps.

Table 1: Overview of the used material compositions.

#	Sample	Binder-content	Glue granulate-content	Water-content	Aggregate-content
[-]	[-]	[wt.%]	[wt.%]	[wt.%]	[wt.%]
BPC1	10(44BG56W)90Z	10	4.44	5.56	90
BPC2	15(44BG56W)85Z	15	6.67	8.33	85
BPC3	20(44BG56W)80Z	20	8.89	11.11	80
BPC4	25(44BG56W)75Z	25	11.11	13.89	75

Table 2: In-sum process specifications for the production of bio-based concrete composite samples.

Process #	Process specification	Duration	Notes
1	Soaking of GG in W	>1h	Soaking of glue granulate in water
2	Heating	~1h	Heating of Z and b in oven to 70°C
3	Mixing	2min	Mixing in mortar blender, standardised in EN196-1 [15]
4	Moulding	3min	Moulded on vibration table until solidity is reached
5	Thermoplastic hardening	1 day	1 day left in mould - actual thermoplastic hardening time substantially lower - dependant on geometry, ambient temperature, etc.
6	Demoulding		Demoulding 1day after casting
7	Dry-hardening A	1 day	Dry hardening under room temperature
8	Dry-hardening B	4-48 days	Dry hardening in well ventilated oven at 50°C

1. Soaking of GG in W: Soaking the glue granulate in water for >1 hour, until a homogenous concentration of gel in the GG-W mix could be reached. The granulate increases its volume in reaction with water. The viscosity in this step depends on both, amount of added water and soaking time, and can range from solid to liquid. Frequently, the mix has been stirred with a glass spatula.

2. Heating of constituents: The viscosity of the GG-W mix can be decreased by heating (thermoplasticity). The water addition can be thereby decreased due to temperature control. To avoid sudden cooling and undesired hardening during the mixing process of the binder, aggregates are heated as well. Both materials are heated to 70°C to ensure the plasticity of the mix. Higher temperatures were avoided to prevent damage of the molecular structure.

Mixing of constituents: The heated constituents are mixed with a mortar blender for conventional cementitious material (Mixer specification: Seger – Tonindurtie), standardised in EN196-1 [15]. The mixing vessel is prior tempered to 70°C to prevent premature cooling of the mass. A homogenous material mix could be assumed after 2 minutes of mixing. The mixing and moulding was conducted at room temperature, giving a time limitation for the mixing. Due to cooling, the mass becomes unworkable after a short time (about 5-10min).

Moulding: The composite material is poured into moulds. This is done in a rather rapid fashion to prevent the material from premature stiffening. The moulds were filled on a vibration table to prevent large captivities and larger inhomogeneity inside the sample. The vibration was conducted with 60-80Hz until the material

increased in viscosity (approx. 3min). Prism moulds with dimensions of 40x40x160mm (width/height/length) after EN 196-1 [15], as well as cylinders with a measurement of 50x100mm (diameter/height) were used. Metal surfaces of the moulds needed to be covered with a thin PE-foil to prevent the corrosion caused by the acidic nature of the bio-binder.

1. Thermoplastic hardening: Thermoplastic hardening occurs directly after the binding material is removed from a heat source and placed in a cooler ambient temperature. The material's viscosity increases noticeably throughout mixing and moulding process.

2. Demoulding of the samples was conducted one day after moulding, to support the integrity of the sample by reaching additional strength through the outset of the dry hardening process.

3. Dry hardening: Even if the material shows stiffness after the thermoplastic hardening process, the material still contains water which prevents the biopolymers to form stronger bonds. After all water is evaporated, the material is considered as hardened. The duration of this process is dependent on water content, dimension of the sample, aggregate content and porosity. To accelerate the process for testing, samples were, after one day drying under room temperature, placed in a well ventilated oven (Oven specification: Memmert UF 160) at 50°C. For most samples, an oven drying time of 21 days was chosen.

2.2.2 Structural testing of cylindrical samples

A total of 12 cylindrical samples, 50mm diameter and 100mm height, were casted to determine compressive strengths. For loading tests, an 'Instron-6025' with a capacity of 100kN was used to load the samples, as well as for recording of force and displacement. Circular platens with a diameter of 50mm were used to slender the apparatus' loading surface down to the geometry of the material cylinders. Force was applied with a loading rate of 2400 N/s.

The moulding and drying of the samples left the top and bottom surfaces of the cylinders uneven. The samples were cut with a circular saw to a length of ~90mm before testing and after drying. The sawing was conducted slowly and without any water-cooling of the blade to prevent the material from weakening by water soaking.

2.2.3 Structural testing of prism samples

Prism samples with the size of 40x40x160mm were tested for flexural- and compressive strength according to EN196-1 [15].

For flexural strength, the prism samples were tested in a three-point bending test as standardized with a distance of the supporting rollers of 100mm and a loading rate of 50N/s on an 'Instron-6022' with a loading capacity of 10kN. The specimen was mounted with the from the moulding created even surfaces in contact with the flexure device.

The compressive strength was measured for each of the two fragments obtained from the segmentation when measuring the flexural strength. Above and below, the specimen was loaded on a surface of 40x40mm. The orientation of the samples for compressive strength was in accordance to the flexural tests, described above. Loading was applied at a rate of 2400N/s with an 'Instron-6025' testing machine with a loading capacity of 100kN.

2.2.4 Density-measurements of the composite

Calculated as ratio of individually measured mass (accuracy 0.01g) and volume (accuracy 0.01mm).

2.2.5 Shrinkage

Shrinkages of prism samples were determined by evaluating the differences in length before and after dry hardening, i.e. immediately after demoulding and before testing. Therefore, shrinkage information relates only to the dry-hardening process during this time and not to thermoplastic-hardening.

2.2.6 Dry-hardening times

The binding material develops strength over the thermoplastic- and the dry-hardening period. The duration of the thermoplastic hardening was short and easy controllable by temperature. The duration of the dry-hardening depends on geometry, porosity, ambient temperature and binder or water contents. A total of 12 cylindrical samples of BPC3 have been tested in compression (see Section 2.2.1 and 2.2.2) to evaluate the rapidity of the drying process. The sample production was conducted as indicated in Table 2. The duration of step 8 was varied. Three samples have been tested, respectively after 4, 12, 22 and 48 days of oven drying at 50°C. To keep samples comparable, the W/GG and b-content has not been varied and kept on 1.25 and 20%.

3. Results and discussion

3.1 Results

Examples of BPC are seen in Figure 2.

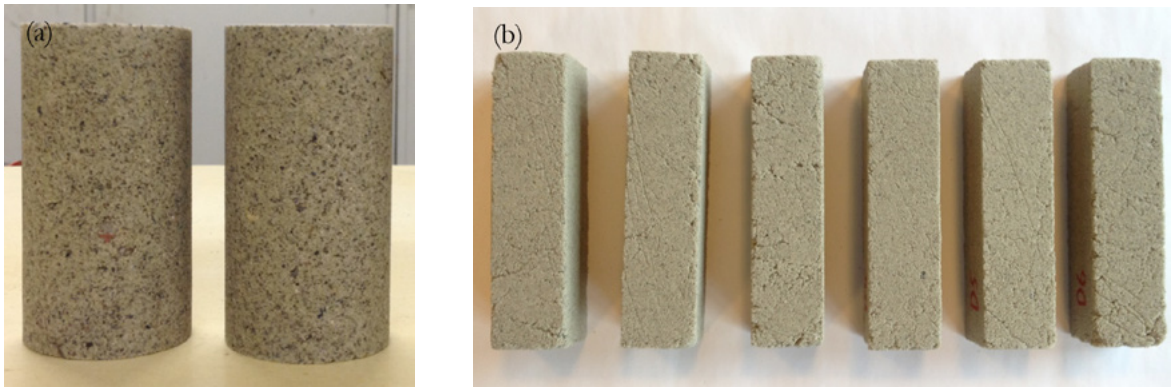

Figure 2: Biopolymer Concrete (BPC) Samples: (a) circular cylinders 100mm high and 50mm in diameter, (b) square prism samples with a length of 160mm and a cross-section of 40x40mm.

3.1.1 Property variations under hardening

The two hardening characteristics, thermoplastic- and dry-hardening, are key-influencer on the materials strength and viscosity. The thermoplastic hardening time already occurs after several minutes after discontinuity of heat exposure, the material's viscosity increases and the composite gains integrity. Due to the obvious relation of the material's temperature to its fluidity, the rapidity of the process is thought to be connected with the composite's geometry, heat capacity, water content, initial- and ambient temperature. The observations of this process proposes therefore, its simple controllability. The subsequent dry hardening can be described as the water loss through evaporation and extends, dependant on the water content, over a longer period of time.

Figure 3 shows the dependency of the compressive strengths on this dry-hardening duration. Illustrated results display that the material strength is increasing for an increase of dry-hardening time, suggesting that the strength of the material is strongly dependant on its water content. Hence, a high water content implies low strength and an advanced drying process a higher strength. The four data points were tested with a respective sample quantity of three, namely samples BPC3.1-12 (Figure 2 – a). The mean of each tested

point in time has been connected by a smoothened line. A substantial increase of compressive strength was observed (until 22 days), where after the graph flattens. The flattening starts between 12 days and 22 days, an exact point in time, however, could not be determined. For the values around the flattening, the graph shows larger variabilities. Contrary, minor variations were observed for short and extensive dry-hardening durations. A bend in the smoothened curve of Figure 3 denotes a characteristic change of drying rapidity.

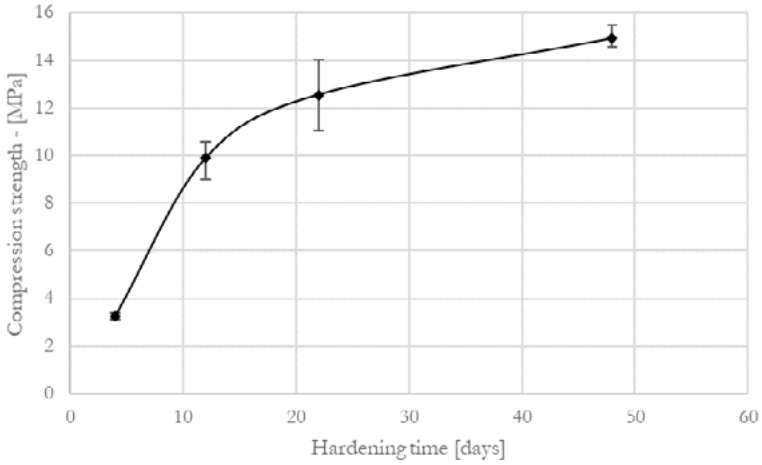

Figure 3: Compressive strength of cylindrical samples BPC3.1-12. over dry hardening times at 50°C (corresponding to step 8 in Table 2). The error bars show maximum and minimum values. The connecting line has been smoothened.

The drying characteristics are expected to be geometry dependent, as well as reliant on initial water content, ambient temperature and humidity. Other than the thermoplastic hardening, dry hardening is expected to not conclude, but rather to approximate asymptotically to an upper bound, which is dependent on the ambient humidity. Therefore, varying water contents through differing binder to aggregate compositions, possibly show divergent hardening times. This, however is up to date not experimentally verified.

3.1.2 Density

Characterizing density and shrinkage is useful to evaluate the material on its suitability for constructional 3D printing by limiting self-weight and shrinkage cracking. For sample batches BPC1, BPC2, BPC3, and BPC4 (cf. Table 1); volume, weight and length have been measured before testing and after drying. Respectively calculated density values can be seen in Figure 4. The mean values range from 1.6g/cm^3 to 1.4g/cm^3 for varying binder contents. Densities generally decrease with a decrease in aggregate shares in the mix.

The material's density is scattered around a value of about 1.5 g/cm^3. The composite is therefore lighter than cementitious mortar, which is here assumed with the typical value of 2.2 g/cm^3. The mixing ratios influences the material's density only marginally for a binder content of 10%-20% (BPC1, BPC2, BPC3). A content of 25%, however, causes a large density loss of 10%. Due to the comparably high density of the used sand (2.6 g/cm^3), low density binder (1.3 g/cm^3), and the continuous change of mixing ratios (10%, 15%, 20%, 25% binder content) throughout the tests, a linear decrease of density could have been expected. Contrary, the non-linear appearing measurements of Figure 4 let suppose, that the pore content for samples with a binder content of over 20% increases substantially, i.e. its density decreases.

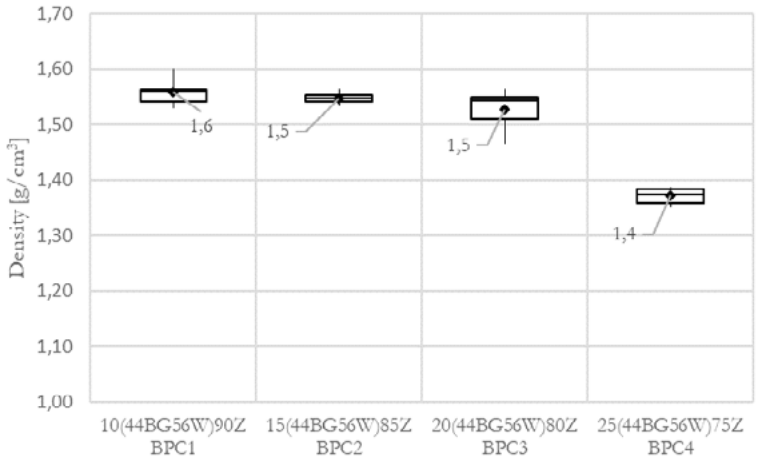

Figure 4: Density of sample batches with varying binder contents. Whiskers show maximum and minimum value of the data set; boxes define upper, middle and lower quartile; the marker shows mean values. Each boxplot is substantiated with a data point quantity of six measurements.

3.1.3 Shrinkage

The densities tendency is reversely reflected by shrinkage ratios in Figure 5. The continuous increase of the data set ranges from 0.3% to 2% and increases for higher binder contents. Therefore, shrinkage appears to be directly interlinked to the materials composition, or rather to the binder's water content. The results suggest that the evaporation of water causes the material to shrink.

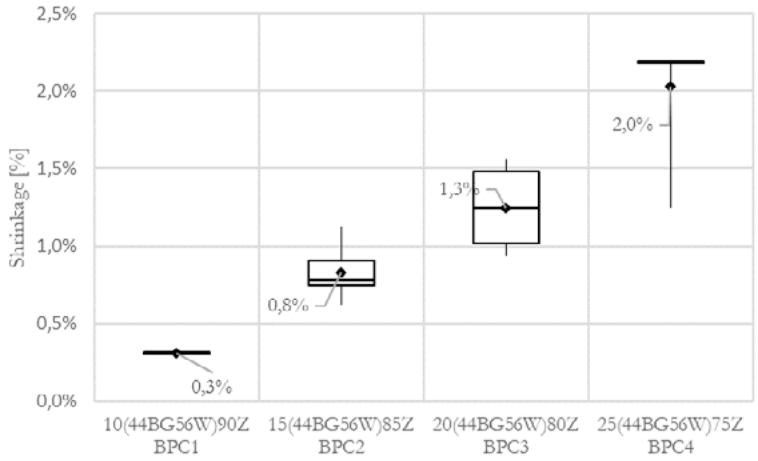

Figure 5: Shrinkage of sample batches with varying binder contents. Whiskers show maximum and minimum value of the data set; boxes define upper, middle and lower quartile; the markers show mean values. Each boxplot is substantiated with a data point quantity of six measurements.

3.1.4 Strength of BPC

The composite's properties are expected to be strongly dependant on the material's composition. Therefore, the dependencies on varying binder-contents were measured to determine performance peaks of flexural and compressive strength. Six prisms (Figure 2-b) for each composition were casted with a binder content of 10%, 15%, 20% and 25% (BPC1-4) and a W/GG-ratio by weight of 1.25. Corresponding mixtures can be found in Table 1, a dry-hardening duration of 21 days was chosen for all samples. Figure 6 and 7 show the obtained results for flexural and compressive strengths.

Flexural strength: As shown in Figure 6, batch BPC2 had the highest flexural strength, i.e. the batch with a binder content of 15%. When lowering the binder content to 10% (Batch BPC1), the flexural strength

was more than halved. Increasing the binder content to 20% and 25%, i.e. BPC3 and BPC4, resulted in a decreased flexural strength, though not as significant as for the prisms with 10% binder.

Compressive Strength: The compressive strength for the prisms are shown in Figure 7. A tendency to a maximum mean compressive strength of batch BPC3 can be identified as a peak performance value. However, the upper error bar for batch BPC3 has a relatively large magnitude and is decisive for an increased mean value, being higher than middle and upper quartile. Therefore, a difference between batch BPC2 and BPC3 can not be concluded. A major drop in strength is located between BPC3 and BPC4.

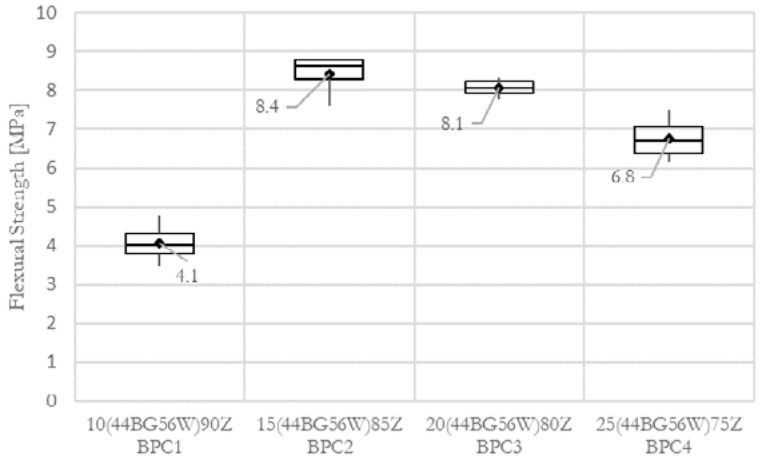

Figure 6: Flexural strength of prism samples with varying binder contents. Whiskers show maximum and minimum value of the data set; boxes define upper, middle and lower quartile; the marker shows mean values.

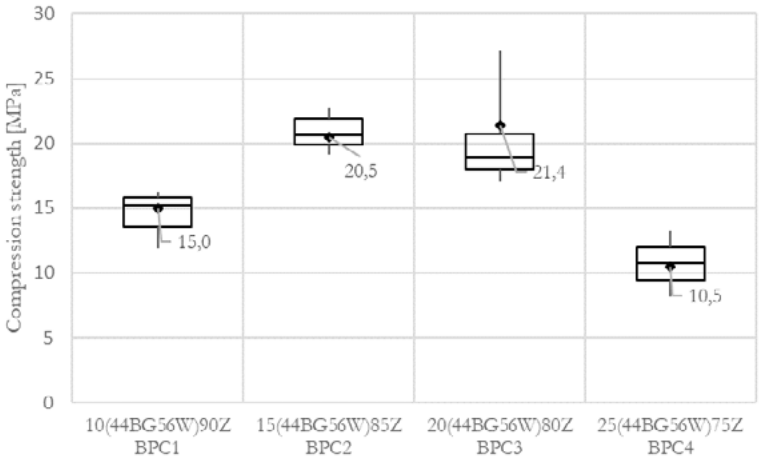

Figure 7: Compressive strength testing of prism samples with varying binder contents. Whiskers show maximum and minimum value of the data set; boxes define upper, middle and lower quartile; markers show mean values.

Both, flexural and compressive strength suggest a performance peak between 15% and 20% binder content. The peaking of strength in this range, and the subsequent decrease for higher binder contents can potentially be explained with: 1) an increase of porosity due to the higher binder content and therefore decrease in density and strength (see Figure 4), or 2) an incomplete or not comparable dry-hardening process between varying binder contents as described in Section 3.1.1.

Even though in similar range, flexural- and compressive strength propose diverging mean performance peaks in the margin of 15%-20%. The boxplots however do show similar order for both stresses in Figure 6 and 7. The correlation of mean flexural- and compressive strength was therefore evaluated to determine

the consequences of an increase of binder content in the mixture. The results are shown in Figure 8. It appears that the two properties react differently on the composition change. A consistent ratio in strength could therefore be excluded. A general observed trend is that higher binder contents cause an increase in relative flexural strength. Contrary, low binder contents lay the performance's focus on the compressive strength. The maximum ratio in Figure 8 has a magnitude of 65% for a binder content of 25% (BPC4). The indicated performance peaks for BPC2 and BPC3 show a strength ratio of around 40%. In all cases, the ratio of flexural- to compressive strength surpasses the performance of conventional cementitious concrete, which is around 10%, as a rule of thumb.

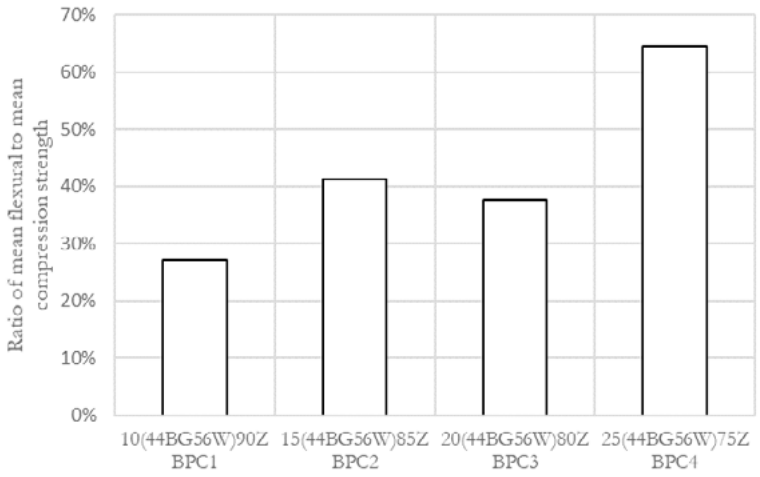

Figure 8: Ratio of flexural strength to compressive strength for varying binder contents. Mean values of measured strengths as in Figure 6 and 7 were used.

3.2 Discussion

The BPC's properties were tested to assess the materials suitability for constructional 3D-printing. In the following, the results are brought into context, i.e. 'suitable'- and 'to be further advanced' properties are listed and compared.

Suitable properties of BPC for constructional 3D-printing:

Printability of BPC: Primary advantage of BPC for constructional 3D-printing is the easy controllable thermoplastic hardening and thickening of the material. The in Section 2.2 and 3.1.1 discussed thermoplasticity shows, that the material increases rapidly in viscosity only by the exposure to room temperature. During an envisaged printing process, the material itself would therefore not only rely on the thixotropic build-up of the composite material, as for 3D-printing with cementitious concrete [16]. By the ability of controlling the thermoplasticity to a high degree, and increasing the early age strength of the matrix, the thinness of layers could be increased and potential early age moment failure of the built up prevented. More slender constructions and higher degree of freedom in terms of overhanging prints, could possibly be realised. This is also supported by the material's low density and high relative flexural strength, as described in Section 3.1.4, which can increase the early age moment resistance and lower the dead load added to the system under construction.

Composite strength: As proposed in Section 3.1.4, BPC shows generally a strength in the order of magnitude of cementitious concrete, though not comparable with high performance printing concretes [12]. One of the biggest challenges of constructional 3D-printing is the integration of reinforcement [3]. The printing process prevents the placing of extensive steel reinforcement and limits the freedom of shape

for cementitious concrete substantially due to the lack of flexural strength in cementitious materials. With a high ratio of flexural- to compressive strength of BPC, as described in Section 3.1.4, the BPC material could deliver a filament that could render building components loaded in flexure and thereby diminish the need for reinforcement.

Structural integrity of prints: Assuming a layer-by-layer 3D-printing process for the constructional use of the material, the integrity of the meso-scale structure is at risk by possibly exceeded shrinkage limits or detachment of layers through lacking interface adhesion [17]. Shrinkage, as evaluated in Section 3.1.3, can be controlled by editing the binder content. Possibly, fibre reinforcement could be added to limit shrinkage cracking. The found shrinkage ratios of 0.3% to 2% is therefore evaluated as suitable for constructional 3D-printing. The bone glue has furthermore been traditionally used for carpentry constructions and instrument making and adheres well to itself. It is therefore expected, that the contact surface of a printed layer bonds well to precedent layers. This, however needs to be experimentally verified in further work.

- *Sustainability:* The substitution of high cement contents and extensive admixtures in constructional 3D-printing filaments with biologically based binders such as bone glue could have a positive impact on the sustainability account of the method. This is due to lower production temperatures of bone glue in comparison to cement, and avoidance of CO_2-emissions under the calcination of limestone.

BPC properties, crucial to be further advanced:

- *Durability:* BPC has, due to its organic compounds and hygroscopic behaviour, a high risk of fast deterioration. During the testing, some of the samples, especially for binder contents over 20%, showed moulding attack.
- *Fire resistance:* The thermoplastic properties of the material are expected to be beneficial for the 3D-printing process but disadvantageous for its fire-resistance. The fireproofing of the material is crucial for further development.
- *Hygroscopic properties:* As described in Section 3.1.1, the water content is decisive for the structural strength of the material. Removing the water contents, hardens the material. The process can also be reversed, i.e. exposure of the hardened material to water softens its strength, which is critical for the use as structural material.

An overview of the above described can be found in Table 4.

Table 4: In sum – advantageous properties in comparison to ongoing advancements

Properties of BPC, suitable for constructional 3D-printing	Properties of BPC, crucial to be advanced
Thermoplasticity	Durability
Flexural- /compressive strength	Fire resistance
Low density	Water resistance
Self-adhesion	
Shrinkage	

4. Conclusions

A composite of a biopolymer binding material (bone glue – a bio-gel produced from the meat industry's waste) in conjunction with mineral aggregates was evaluated on its suitability as a filament for constructional 3D-printing of concrete. The findings show structural strengths in the order of magnitude of conventional concrete, i.e. flexural strength of 8 MPa and compressive strength of 21 MPa, and suggest therefore the

composite's usability as a structural building material. A density of around 1.5 g/cm^3, easy controllable thermoplastic hardening characteristics, and a high moment resistance through high flexural- to compressive strength ratios of up to 65%, propose furthermore the benefit for additive manufacturing processes. Low induced dead loads, early-age material strength and high moment resistance, could diminish the need for reinforcement integration of 3D-printed structures, and enable higher degrees of freedom in terms of overhanging and thin geometries. The results suggest the suitability of bone glue as a binding material for concrete and the use in constructional 3D printing, linked with further research and development work for the composite's durability, fire- and water resistance.

5. Acknowledgment

The presented research work in this paper has been financed by Ingeniør Kaptajn Aage Nielsens Familiefond, grant (00023307) from VILLUM FONDEN (VILLUM Experiment), and DTU's Department for Civil Engineering. We thank our lab-personnel for technical advice and assistance.

6. References

[1] Y. W. D. Tay, B. Panda, S. C. Paul, N. A. Noor Mohamed, M. J. Tan, and K. F. Leong, "3D printing trends in building and construction industry: a review," *Virtual Phys. Prototyp.*, vol. 12, no. 3, pp. 261–276, 2017.

[2] N. Labonnote, A. Rønnquist, B. Manum, and P. Rüther, "Additive construction: State-of-the-art, challenges and opportunities," *Autom. Constr.*, vol. 72, pp. 347–366, 2016.

[3] F. Bos, R. Wolfs, Z. Ahmed, and T. Salet, "Additive manufacturing of concrete in construction: potentials and challenges of 3D concrete printing," *Virtual Phys. Prototyp.*, vol. 11, no. 3, pp. 209–225, 2016.

[4] S. Ren and S. Galjaard, "Topology Optimisation for Steel Structural Design with Additive Manufacturing Shibo," in *Modelling Behavior*, 2015, pp. 35–36.

[5] "MX3D Bridge." [Online]. Available: https://mx3d.com/projects/bridge-2/. [Accessed: 26-Apr-2019].

[6] A. Menges, "BUGA Fibre Pavilion 2019 | Institute for Computational Design and Construction," 2018. [Online]. Available: https://icd.uni-stuttgart.de/?p=22271. [Accessed: 26-Apr-2019].

[7] S. J. Keating, J. C. Leland, L. Cai, and N. Oxman, "Toward site-specific and self-sufficient robotic fabrication on architectural scales," *Sci. Robot.*, vol. 2, no. 5, 2017.

[8] G. Pasquarelli, W. Sharples, C. Sharples, and R. Caillouet, "Additive Manufacturing Revolutionizes Lightweight Gridshells," 2017.

[9] L. Mogas-Soldevila and N. Oxman, "Water-based engineering & fabrication: Large-scale additive manufacturing of biomaterials," *Mater. Res. Soc. Symp. Proc.*, vol. 1800, pp. 46–53, 2015.

[10] I. Perkins and M. Skitmore, "Three-dimensional printing in the construction industry: A review," *Int. J. Constr. Manag.*, vol. 15, no. 1, pp. 1–9, 2015.

[11] D. Marchon, S. Kawashima, H. Bessaies-Bey, S. Mantellato, and S. Ng, "Hydration and rheology control of concrete for digital fabrication: Potential admixtures and cement chemistry," *Cem. Concr. Res.*, vol. 112, no. December 2017, pp. 96–110, 2018.

[12] T. T. Le, S. A. Austin, S. Lim, R. A. Buswell, A. G. F. Gibb, and T. Thorpe, "Mix design and fresh properties for high-performance printing concrete," *Mater. Struct. Constr.*, vol. 45, no. 8, pp. 1221–1232,

2012.

[13] Y. Zhang, Y. Zhang, W. She, L. Yang, G. Liu, and Y. Yang, "Rheological and harden properties of the high-thixotropy 3D printing concrete," *Constr. Build. Mater.*, vol. 201, pp. 278–285, 2019.

[14] "More than Tools | Dictum." [Online]. Available: https://www.dictum.com/en/. [Accessed: 23-Apr-2019].

[15] DS/En 196-1, "Metoder til prøvning af cement – Del 1: Styrkebestemmelse Methods of testing cement – Part 1: Determination of strength," 2016.

[16] R. J. M. Wolfs, F. P. Bos, and T. A. M. Salet, "Early age mechanical behaviour of 3D printed concrete: Numerical modelling and experimental testing," *Cem. Concr. Res.*, vol. 106, no. May 2017, pp. 103–116, 2018.

[17] Y. W. D. Tay, G. H. A. Ting, Y. Qian, B. Panda, L. He, and M. J. Tan, "Time gap effect on bond strength of 3D-printed concrete," *Virtual Phys. Prototyp.*, vol. 14, no. 1, pp. 104–113, 2019.

A silica aerogel synthesized from olivine and its application as a photocatalytic support

Y.X. Chen [1,2], Y. Hendrix [1], K. Schollbach[1], H.J.H Brouwers [1,2]

[1] Department of the Built Environment, Eindhoven University of Technology

P.O. Box 513, 5600 MB Eindhoven, The Netherlands

[2] State Key Laboratory of Silicate Materials for Architectures, Wuhan University of Technology, Wuhan 430070, PR China

Abstract:

Air purification is an important topic for public health and one of the solutions is to apply photocatalysis. It has been shown that the photocatalytic activity increases when the photocatalyst is supported on a silica network with a large surface area like silica aerogels. Silica aerogels are an ultralight and porous inorganic material consisting of 90~99% air voids inside a porous silica network structure. The inter-connected pore structure and the pore size are advantageous for the silica aerogel to function as a catalyst support or absorbent. However, silica aerogel is currently mainly produced with organic silica precursors and via supercritical drying, which is an energy intensive production route. Therefore, it is of interest to lower the production cost and reduce the energy input to produce silica aerogel with a lower CO_2 footprint. In this study, silica aerogel was first synthesized from olivine via ambient pressure drying and was applied as a support to load photocatalytic anatase crystals. The aerogel production steps include sol-gel synthesis, ion-exchange, surface modification and ambient pressure drying. The produced silica aerogel obtained a high specific surface area (694 m^2/g) and pore volume (2.99 cm^3/g), with a uniform pore size distribution and mesoporous structure. Titania was loaded onto the prepared silica aerogel through the precipitation method. Titanium (IV) isopropoxide was used to slowly form titania in a dispersion with the silica aerogel. This method was used to precipitate titania inside the mesopores of the silica aerogel to obtain a great spread of the titania around and inside the aerogel for a high photocatalytic activity. The resulting samples were tested by measuring their conversion efficiency to oxidize nitric oxide under UV-light irradiation, nitrogen physisorption and FTIR. The prepared silica aerogel with titania crystals showed a photocatalytic activity of 99.6%, showing to be a promising photocatalysts for air purification.

Keywords: Silica aerogel, Titanium oxide, Photocatalytic support, NO oxidation

1. Introduction

Silica aerogel is an ultra-light inorganic material that contain above 90% porosity filled with air. Silica aerogel obtain ultra-low density (0.03-0.2 g/cm^3), high specific surface area (500-900 m^2/g) and ultra-high porosity (90-99%). Due to these properties of aerogel, many researchers have synthesized different kinds of silica aerogels and applied them as thermal insulation materials [1, 2], catalytic supports [3, 4], absorbent of pollutants [5] and drug carrier materials [6]. However, the industrial silica aerogels are mostly produced from organic silica sources like tetrathoxysilane (TEOS) and methyltrimethoxysilane (MTMS), through supercritical drying [7]. These processes are energy intensive and obtain a high carbon footprint

[8]. Therefore, a sustainable and low energy consumption method to produce silica aerogel would be a more desirable way to produce silica aerogel.

In the last few years, researchers developed several methods to produce silica aerogel from alternative silica sources, like kaolin [9] and fly ash [10]. However, all these methods include a calcination process that can increase the carbon footprint and energy consumption. Recently a novel nano-silica was produced from olivine at low temperatures (50-90 ^{O}C) [11, 12]. Olivine silica is produced by the dissolution of olivine in acid and shows advantages in terms of lower CO_2 footprint, energy consumption and costs [13]. In this research, olivine silica is prepared at 50 ^{O}C and obtains a silica purity higher than 99% with SSA_{BET} between 100 to 400 m^2/g, indicating a fast reaction with sodium hydroxide solution and a pure water glass formation. Thus, olivine silica has great potential to be a sustainable silica source in the production of silica aerogel while the total energy consumption is lower. In terms of drying procedure, ambient pressure drying was applied in this study due to the lower pressure and temperature that used compared to supercritical drying [7]. This drying method includes a surface modification process that transforms the surface –OH group on silica gel surface to $–CH_3$ group with TMCS and heptane as an agent. Therefore, with a 'spring back' effect the silica gel can re-expand the volume under ambient pressure drying and lower the density and increase the porosity of the final silica aerogel.

Due to the large pore volume and porosity of silica aerogel, it is promising to apply silica aerogel as a catalyst support to load a catalyst like photocatalytic titania. The crystal size of well-prepared anatase crystals can be smaller than the majority of the pore sizes in the silica aerogel (10~20 nm) [14]. Therefore, it is possible to apply the aerogel as a catalyst support to make a great spread of the titania on and inside the aerogel for a high photocatalytic activity. Therefore, in this research, silica aerogel was first synthesized from olivine via ambient pressure drying. Then the as-prepared silica aerogel was applied as a photocatalytic support to load titania and the photocatalytic efficiency was measured. Furthermore Fourier-transform infrared spectroscopy (FTIR) and nitrogen physisorption were used to analyze the microstructure of the resulting silica aerogel-TiO_2 composite.

2. Methodology

2.1 Materials

Olivine used in this research was from Norway supplied by Eurogrit (GL70). Table 1 lists the oxides composition of GL70 measured by X-ray fluorescence (XRF). The loss on ignition and the olivine content are also shown in Table 1.

Table 1: Composition of GL-70 from Norway and olivine silica

Composition	MgO	Fe_2O_3	SiO_2	Cr_2O_3	Al_2O_3	NiO	MnO	CaO	LOI*	Olivine
GL-70	49.3	7.32	41.4	0.31	0.46	0.32	0.09	0.15	0.59	88.9
Olivine nano-silica	0.03	0.02	99.8	-	-	-	-	0.03	-	-

*Loss on ignition

-Not detected

Sodium hydroxide pellets (NaOH, VWR), Ethanol absolute (CH_3CH_2OH, 100%, VWR), n-Heptane (C_7H_{16}, Analytic grade, Biosolve), Ammonia solution ($NH_3 \cdot H_2O$, 5N, Sigma-Aldrich), Trimethychlorosilane (C_3H_9SiCl, ≥99%, Sigma-Aldrich) and Amberlyst 15 hydrogen form (Strongly acidic cation exchange resin, Sigma-Aldrich) were used to prepare silica aerogel from olivine GL-70. Olivine silica was prepared

according to our previous research [15] and its chemical composition is shown in Table 1. Titanium (IV) isopropoxide 97% (Sigma-Aldrich) was used as the precursor to produce the titania monomer. Commercial titania P25 was used as a reference to compare the performance of titania-aerogel composite sample.

2.2 Methods

2.2.1 Preparation of silica aerogel

The primary procedures for the preparation of silica aerogel via ambient pressure drying include network strengthening, solvent exchange and surface modification. For the solvent exchange, different kinds of alcohols and alkanes with low surface tension are believed to be the best options. The surface tension of the pore liquid can be reduced through stepwise solvent exchange and hence prevent capillary pressure from damaging the network of silica aerogel during ambient pressure drying. For the surface modification, the hydroxyl groups of the aerogel can be replaced by non-polar silyl groups through the use of trimethylchlorosilane (TMCS) and n-heptane as solvent. When drying a hydrophobic gel, the skeleton of the silica network is barely influenced by the surface tension of water, thus avoiding the collapse of the pores of the aerogel. Furthermore, the 'spring back' effect further lowers the density of the silica aerogel due to inert $-CH_3$ groups attaching on the surface of the gel. During the full evaporation of the pore liquid, the aerogel can bounce back and increase the volume of the aerogel. The schematic process of the projected silica aerogel production is presented in Fig. 1.

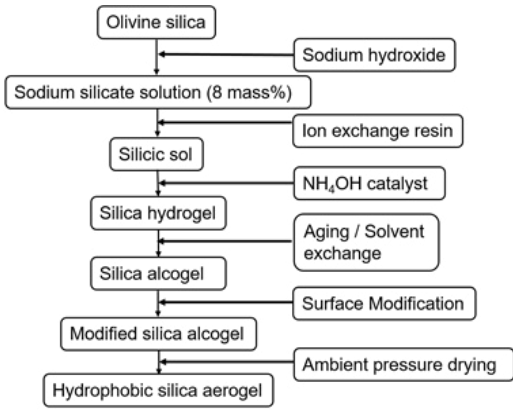

Figure 1: Schematic process of silica aerogel production from olivine silica

2.2.2 Preparation of titania-silica aerogel composite

The silica aerogel was first dried at 500 ℃ overnight to remove the $-CH_3$ groups on the surface of silica. Subsequently, 1 g of silica aerogel was weighed and then milled with a mortar. Then silica aerogel was dispersed in a 500 ml ethanol absolute solution and the pH was adjusted to 3~4 by adding small amounts of sulfuric acid. The molar ratio of titania and silica aerogel was kept at 1:1, which was determined according to our previous study to be a proper amount. Afterwards, 4.16 g TP (Titanium isopropoxide) was added into the solution quickly to avoid any contact with moist air. Then water was slowly added during 12 hours until the water content of the dispersion medium reached 2.5 vol%. After the synthesis of the composite, the resulting sample was filtered and washed 4 times with distilled water. Lastly, the sample was dried overnight at 105 ℃ and then calcined at 300 ℃ for 3 hours.

2.2.3 Characterization methods

The resulting photocatalytic properties of silica aerogel-titania composites were evaluated by testing their photocatalytic conversion of NO under UV-light using the ISO 22197-1 standard for comparative purpose. The setup for these measurements is shown in Fig. 2.

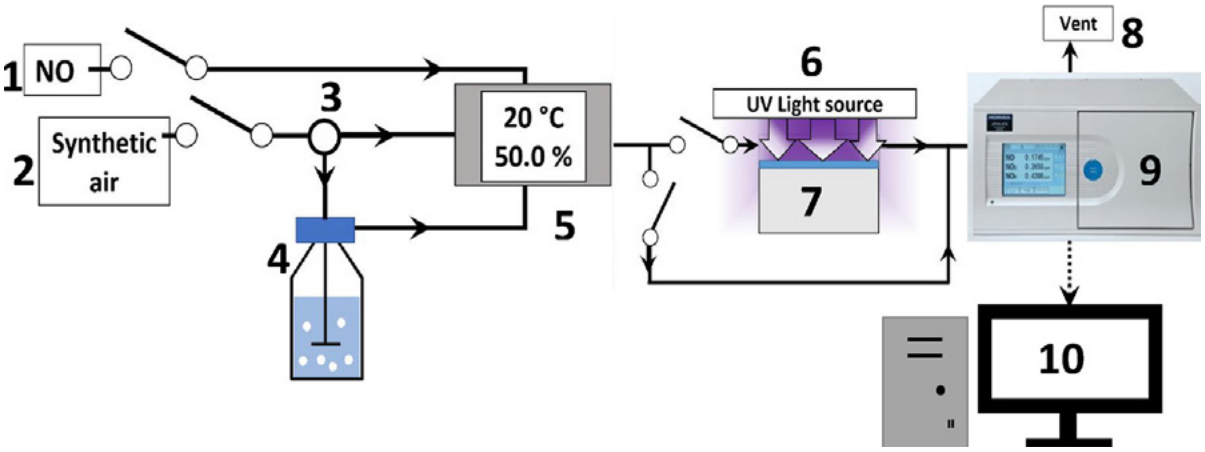

Fig. 2 Schematic view of the PCO measurement setup: 1) NO gas source, 2) synthetic air source, 3) valve, 4) bottle containing water, 5) humidity and temperature sensor, 6) light source, 7) reactor, 8) air vent, 9) NOx detector and 10) computer to control inflow of gasses and data collection. (Permission from [14])

Chemical bonds in the silica aerogel were detected by Fourier-transform infrared spectroscopy (FTIR), which was performed with a Varian 3100 instrument with the wavenumbers ranging from 4000 to 400 cm-1 at a resolution of 2 cm^{-1}. Nitrogen physisorption was performed with a Tristar II equipment at 77 K using liquid nitrogen to determine the specific surface area using the BET theory and pore size distribution using the BJH theory. For microstructure analysis, transmission electron microscopy (TEM) was performed using a Tecnai 20 microscope, operated at 200 kV.

3. Results and discussion

3.1 Properties of olivine silica aerogel

The density and porosity of the prepared silica aerogel is shown in Table 2. All the silica aerogel obtained a porosity beyond 93.6% and density below 0.134 g/cm^3. It can be observed that 48 hours aging slightly increased the particle density of the silica aerogel. The reason behind this is that a longer aging time means a higher degree of poly-condensation between colloidal particles and hence a denser silica gel microstructure. The strength of the silica network increased, and could more easily resist the pressure caused by evaporation of the solvent, but with the sacrifice of an increase in density and decrease in porosity. Also, excessive aging reduces the permeability of the silica gel and make it difficult for the solvent exchange process to work properly. Therefore, a suitable aging time of 36 hours is suggested in this study.

The pH of the silicic acid can also influence the density of the produced silica aerogel by changing the hydrolysis and condensation rates of the silicic sol. When the pH of the silicic sol is 4.5, the silica monomer concentration increases too fast and forms silicate nuclei rather than cross linking silica networks, leading to an increase in density. It is observed that a pH of 5.5 can balance the hydrolysis rate and condensation rates, which means condensation immediately follows hydrolysis of silicate and a uniform nanoporous structure can be formed. The silicate monomer concentration is low and favours to grow and form cross-linking silica particles. Therefore, the strength of the gel would increase and less shrinkage happened, leading to a lower density and higher porosity of silica aerogel. The specific surface area and pore size distribution of the silica aerogel (pH 5.5, A36) is shown in Fig. 3. It can be seen from Fig. 3 (a) that the isotherm of the aerogel shows a typical type IV isotherm with an obvious hysteresis. The hysteresis is caused by the narrow pore size distribution with most of the pores being around 8 nm as shown in Fig. 3 (b). The specific surface area and pore volume of the aerogel is 694 m^2/g and 2.99 cm^3/g, respectively. After calcination at 500 ^{O}C for 4 hours, the SSA of silica aerogel rises to 920 m^2/g and pore volume to 5.30 cm^3/g. The reason behind

this result is that the calcination process makes the aerogel expand its pore size and coarsens the backbone of silica particles. The silica aerogel after heating to 500 ^{O}C has a larger pore size, which is around 18 nm, indicating a different pore structure and silica network. Also, the amount of absorbed nitrogen increases at a high relatively pressure, indicating a greater SSA and bigger pore size as well. These properties are suitable for silica aerogel function as a catalytic support with the aim of a better spread of titania both around and inside the pores of silica aerogel.

Table 2: Particle density and porosity of olivine silica aerogel.

Density (g/cm^3) / Porosity (%)	pH 4.5	pH 5.2	pH 5.5	pH 5.9
A36	0.134/93.6	0.124/94.1	0.0972/95.4	0.110/94.8
A48	0.138/93.8	0.128/94.3	0.105/95.0	0.125/94.0

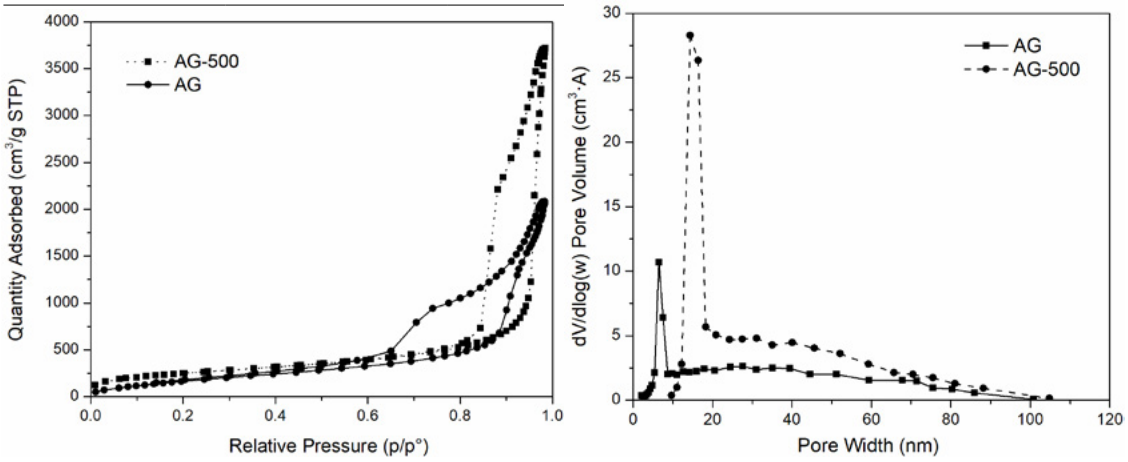

(a) (b)

Figure 3: Physisorption isotherm (a) and pore size distribution (b) of olivine silica aerogel before and after 500 ℃ calcination using BET and BJH methods

3.2 Microstructure of titania-silica aerogel composite

The physisorption isotherm and pore size distribution before and after incorporation of titania are shown in Fig.4. The hysteresis loop of the silica aerogel-titania composite is quite small compared to the pure silica aerogel, indicating a smaller pore size of the composite samples, as shown in Fig. 4 (b). The pore size shrank to 10 nm and pore size distribution is broader than the sole silica aerogel. Moreover, the pore volume decreased significantly, which reduced from 4.99 cm^3/g to 1.77 cm^3/g. Therefore, it can be inferred from the nitrogen physisorption results that titania crystals are inside the pores of silica aerogel which makes the pore volume decrease significantly.

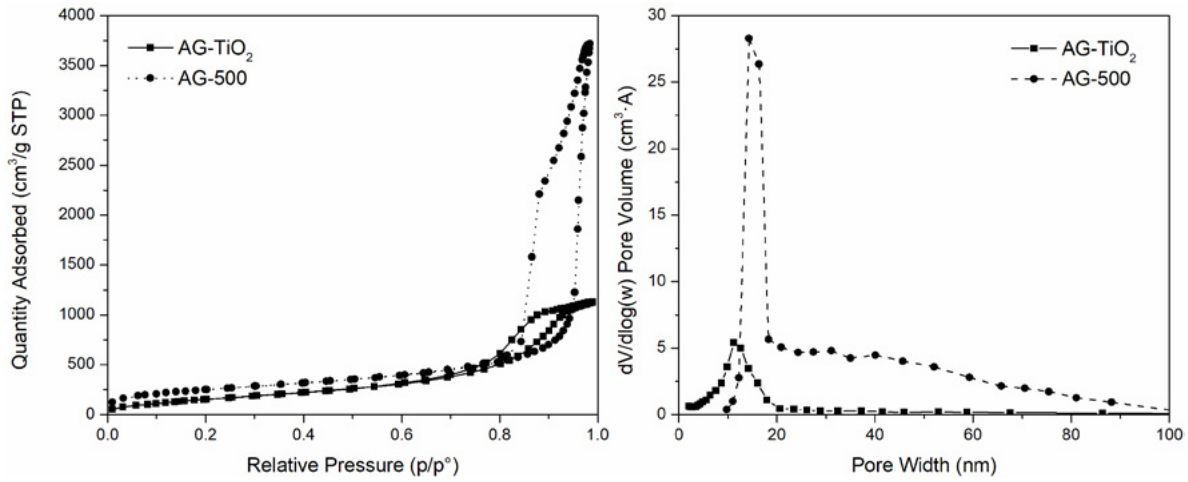

(a) (b)

Figure 4: Physisorption isotherm (a) and pore size distribution (b) of silica aerogel after incorporation of titania

The FTIR spectra (Fig. 5) shows the $–CH_3$ groups are grafted on the surface of the original silica aerogel. After 500 ^{O}C heat treatment, the $–CH_3$ groups disappear and –OH groups are visible, which may be due to the moisture in the atmosphere forming the silanol bond. With the incorporation of titania, the Si-O-Ti bond is visible at 960 cm^{-1}, indicating a good chemical combination between silica aerogel and titania. The reason behind this is that the pH around 3-4 of the reacting solution leads to opposite charge between the aerogel and formed titania. Moreover, the pH value is lowered to 3~4 for the sake of a slower hydrolysis reaction of TP. According to a model proposed from [14], the ratio between the Ti-O-Si bond and Si-O-Si bond is around 0.059, indicating a moderate bonding between these two materials.

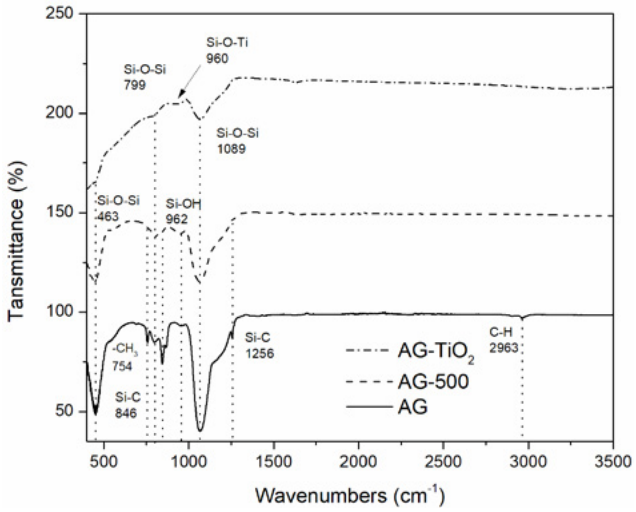

Figure 5: FTIR spectra of silica aerogel and composite sample

3.3 PCO efficiency of the titania-silica composite

The degradation of the NOx gasses is shown in Fig. 6. While the degradation of NO is 99.6%, it is almost the same as that of the coating using P25, the degradation of NOx (which is the combination of NO and the intermediate NO_2) is higher with the silica aerogel composite. The overall conversion on the composite of NOx is 93.6%, while only 57.8% for the reference P25. The high conversion of NO and NOx is due to the titania forming inside and around the silica aerogel, which fills the pores and as a result, some of the titania being spread evenly. This is confirmed by the nitrogen adsorption and FTIR test in

the previous section. Therefore, the silica aerogel-titania composite is a promising photocatalyst and needs further research.

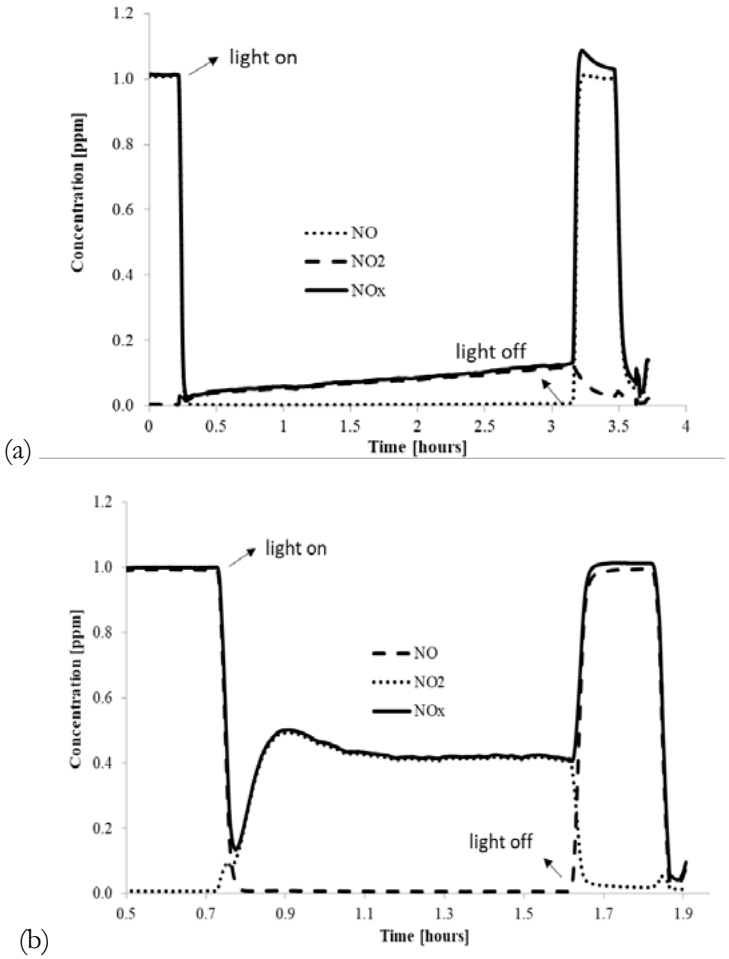

Figure 6: Concentration of NO, NO_2 and NOx in time, showing degradation due to conversion by titania. (a) Silica aerogel-titania composite (b) P25

4. Conclusions

Silica aerogel has been synthesized from olivine via ambient pressure drying at a low temperature. The produced silica aerogel obtained high SSA of 694 m^2/g and 2.99 cm^3/g. Calcination at 500 ^{O}C increased the SSA (920 m^2/g) and pore volume (5.3 cm^3/g) significantly. Titania was loaded into the silica aerogel using a precipitation method. The prepared silica aerogel-titania composite shows a greater conversion efficiency (99.6% for NO and 99.3% for NOx) than the reference sample P25.

5. Acknowledgment

This research was supported by the Department of the Built Environment at Eindhoven University of Technology and China Scholarship Council (201706950053). Ing. A.C.A. Delsing is acknowledged for the experimental support on analytical analysis.

6. Reference

[1] M. Koebel, A. Rigacci, P. Achard, Aerogel-based thermal superinsulation: an overview, J Sol-Gel Sci Techn, 63 (2012) 315-339.

[2] A.M. Papadopoulos, State of the art in thermal insulation materials and aims for future developments,

Energy and Buildings, 37 (2005) 77-86.

[3] J.E. Amonette, J. Matyáš, Functionalized silica aerogels for gas-phase purification, sensing, and catalysis: A review, Microporous and Mesoporous Materials, 250 (2017) 100-119.

[4] H. Maleki, N. Hüsing, Current status, opportunities and challenges in catalytic and photocatalytic applications of aerogels: Environmental protection aspects, Applied Catalysis B: Environmental, 221 (2018) 530-555.

[5] H. Maleki, Recent advances in aerogels for environmental remediation applications: A review, Chem Eng J, 300 (2016) 98-118.

[6] H. Maleki, L. Duraes, C.A. Garcia-Gonzalez, P. Del Gaudio, A. Portugal, M. Mahmoudi, Synthesis and biomedical applications of aerogels: Possibilities and challenges, Advances in colloid and interface science, 236 (2016) 1-27.

[7] M.A. Aegerter, N. Leventis, M.M. Koebel, Aerogel handbooks, Springer, New York, 2011.

[8] J. Fricke, Aerogels-Recent progress in production techniques and novel applications, J Sol-Gel Sci Techn, 13 (1998) 299.

[9] W. Hu, M. Li, W. Chen, N. Zhang, B. Li, M. Wang, Z. Zhao, Preparation of hydrophobic silica aerogel with kaolin dried at ambient pressure, Colloids and Surfaces A: Physicochemical and Engineering Aspects, 501 (2016) 83-91.

[10] F. Shi, J. Liu, K. Song, Z. Wang, Cost-effective synthesis of silica aerogels from fly ash via ambient pressure drying, Journal of Non-Crystalline Solids, 356 (2010) 2241-2246.

[11] A. Lazaro, G. Quercia, H.J.H. Brouwers, J.W. Geus, Synthesis of a Green Nano-Silica Material Using Beneficiated Waste Dunites and Its Application in Concrete, World Journal of Nano Science and Engineering, 03 (2013) 41-51.

[12] A. Lazaro, L. Benac-Vegas, H.J.H. Brouwers, J.W. Geus, J. Bastida, The kinetics of the olivine dissolution under the extreme conditions of nano-silica production, Applied Geochemistry, 52 (2015) 1-15.

[13] A. Lazaro, H.J.H. Brouwers, G. Quercia, J.W. Geus, The properties of amorphous nano-silica synthesized by the dissolution of olivine, Chem Eng J, 211-212 (2012) 112-121.

[14] Y. Hendrix, A. Lazaro, Q.L. Yu, H.J.H. Brouwers, Influence of synthesis conditions on the properties of photocatalytic titania-silica composites, Journal of Photochemistry & Photobiology A: Chemistry, 371 (2019) 25-32.

[15] A. Lazaro, nanosilica production at low temperatures from the dissolution of olivine, Eindhoven University of Technology, Eindhoven, 2013.

The influence of cellulose-based micro and nanomaterials on early-age properties of cement grouts

H. Karimi[1], Q.L. Yu[1], H.J.H. Brouwers[1]

[1] Department of the Built Environment, Eindhoven University of Technology, P.O. Box 513, 5600 MB Eindhoven, the Netherlands.

Abstract

This study investigates the use of different cellulose micro and nanofibers in cement pastes and examines the early-age properties of cement pastes in terms of rheology, shrinkage deformation, and hydration kinetics, compared to two commercially available viscosity-modifying admixtures. The results show that for a constant water to binder ratio, cellulose-based materials are capable of adjusting flowability in terms of yield stress and dynamic viscosity similar to commercially-available viscosity-modifying admixtures. In addition, cellulose-based materials do not affect the hydration kinetics at the studied low dosages. Their effect on volume change depends on their morphology and fineness.

Keywords: cement grout, cellulose nanofiber, cellulose microfiber, shrinkage, hydration.

1. Introduction

Cement grouts are currently being used in a wide variety of applications such as post-tensioning, anchorage sealing, and injection grouting. Different types of chemical admixtures can be added to cement grouts to improve or control their mechanical properties. For example, high range water reducers (HRWRs) are utilized to improve the flowability and viscosity modifying admixtures (VMAs) are applied to control that of cement grouts. Since the incorporation of admixtures into cement grouts increases the production costs, many efforts are made to find new sources and obtain cheaper VMAs. Cellulose is a sustainable material which is the most abundant of all naturally occurring organic compounds, constituting the largest natural resource available to man [1]. Cellulose microfibers (CMF) and cellulose nanofibers (CNF) are capable of modifying the rheology of cement grouts and may be considered as an interesting resource to produce VMA [2,3]. Hence, this study aims to investigate the viscosity-modifying performance and early-age impact of these materials in cement grouts.

Cellulose can be extracted from plants, wood, cotton, hemp, etc. [4]. It can also be synthesized by tunicates, bacteria, and algae [4,5]. Cellulose microfibrils can be mass-produced with the thickness of 2-10 nm and the length of 100-200 nm, while cellulose nanofibers have diameters of down to 15 nm [6,7]. A few chemical and mechanical extraction methods for cellulose-based materials (CMs) in addition to CMs' classification based on the morphology and crystallinity have been introduced [8]. Cellulose-based materials (CMs) can have very different properties including, for instance, tensile strength, elongation at break and Young's modulus depending on their source [9]. Pure crystalline nano-cellulose has exceptional mechanical properties with Young's modulus estimated at 150 GPa and theoretical tensile strength of 7.5-7.7 GPa which is much higher than that of steel wire or aramid fibre [8]. Moreover, nano-cellulose has a good chemical resistance and heat stability allowing high-temperature applications (lower than 200 °C) [10].

Despite a few researches on applying CMs in cement and concrete have been reported [2,3], there is little information on the effect of CMs on the early-age properties, especially as a viscosity modifying admixture (VMA), in cement composites.

Viscosity Modifying Admixtures (VMAs) increase the passing ability and stability of concrete mixtures at lower levels of cementitious materials [11]. They enhance the rheological properties of cement-based materials in the plastic state to reduce the risk of segregation and washout [12]. In other words, VMAs work to mimic the effect of higher fines - substituting polymer interaction or ultra-fine particle interaction to achieve the cohesive effect made by much higher levels of cementitious materials [11]. They are often used as pumping aids since they can lubricate mixtures and decrease the needed pumping pressure [13]. Studies on the changes caused by the incorporation of VMAs in cementitious composites cover a broad scope of topics including, but not limited to: compatibility [14], washout [15], interfering with hydration [14], capillary pore structure [14], excessive air entrainment capacity [16], plastic shrinkage cracking susceptibility [16] and robustness [17,18]. Despite the many advantages of VMAs, they may increase the concrete production cost [19]. Since cellulose is the most abundant natural product on our planet, it could provide a sustainable route to produce VMAs. In order for a CM (CMF or CNF) to be regarded as a useful additive to modify the early-age behaviour of cement grouts, it should be compatible with the other admixtures incorporated, especially the HRWR. Further, to be regarded as a VMA, it should be able to modify the flow behaviour of cement grout. Since CMs absorb part of free water available in the mixtures, they may change autogenous shrinkage behaviour of cement grouts. Also, since some wood-based materials release sugar and deteriorate hydration the effect of CMs on hydration kinetics should be investigated. This study aims to investigate these effects of CMs on the fresh characteristics of cement grouts regarding flowability, shrinkage, and hydration kinetics at early age. The yield stress and viscosity are studied as a function of the shear rate and compared with that of the commercially-available VMAs, either natural, such as diutan gum, or synthetic, such as high-molecular-weight synthetic copolymers.

2. Methodology

2.1 Materials

Ordinary Portland Cement CEM I 52.5 R, provided by ENCI (The Netherlands), in combination with a polycarboxylic ether based high-range water reducer admixture (HRWRA) were used in proportioning cement grouts. Neat cement grout was made without adding VMA and was referred to as the reference mixture (REF) throughout this study. The mixtures were made using two types of CMFs (CMF1 and CMF2), three types of CNFs (CNF1 to CNF3), and two different commercially available VMAs, diutan gum (COM1) and a synthetic copolymer (COM2). The difference between different CMFs and CNFs was in the mechanical energy used in their manufacturing. The dosages of HRWR, cellulose micro and nanofibers, and diutan gum were calculated as their solid ratio by the weight of binder and kept constant at 0.35%, 0.08%, 0.08%, and 0.08%, respectively. CMF and CNF were stabilized in a slurry with a solid content of 1%. The synthetic copolymer was in liquid form and was used at the maximum suggested dosage by the manufacturer, which was 1% of binder.

2.2 Methods

All the mixtures were prepared using a high shear mixer. The mixing procedure started with placing all the mixing water, HRWR, and VMA in the double-wall mixing bowl connected to a bath thermostat and mixing at 800 rpm for 1 min. Then the cement was added to the liquid while mixing at 800 rpm in 30 s. After mixing at the same speed for 30 s, the mixer was stopped and scraped with a spatula for 30 s. The mixer was restarted at 2000 rpm, and the material was mixed for another 2 min. After stopping the mixer for 30 s and scraping the bowl for 30 s again, the mixing was continued at the same speed for 1 min. Fresh

cement grouts were then placed in the rheometer to study the flow behaviour. The rheology of the mixtures was characterized using an Anton Paar 300 rheometer equipped with a water bath unit and Peltier Plate temperature control system. Serrated parallel plate-plate geometry covered with waterproof sandpaper grit 180 with 1 mm spacing was used in the flow curve tests. The temperature was kept steady at 23 °C in all the experiments. All the samples were tested 7 min after cement comes into contact with water. Hydration kinetics were measured by a TAM Air isothermal calorimeter according to the ASTM C1679 [20]. All the samples were mixed externally and transferred into glass ampoules and sealed. The sealed vials were then inserted into isothermal calorimeter and kept there for seven days. Autogenous shrinkage tests were carried out according to the ASTM C1698 [21]. Three replicate specimens were used for each batch. The length of samples was first measured at the time of final setting, and all the measurements were specified by the date of the first contact between cement and water.

3. Results and discussion

3.1 Rheology

The effect of the additives on the flow behaviour of cement grouts is shown in Figure 1. As listed in Table 1, the different flow curves could be well-described with the Bingham model (Equation 1) (R^2>0.985):

$$\sigma = \sigma_D + \eta\dot{\gamma} \quad (1)$$

with σ the shear stress, σ_D the dynamic yield stress, η the viscosity and $\dot{\gamma}$ the shear rate. Neat cement grout curve (REF) has the lowest viscosity and yield stress among all the mixtures. The mixture modified by diutan gum (COM 1) shows high viscosity and yield stress. However, CNF2 is able to increase the viscosity more than the diutan gum at lower yield stress. The synthetic copolymer's effect on the yield stress and viscosity is very similar to CNF 1. Different cellulose-based materials cover a wide variety of rheology modifying effects and are able to mimic the properties of commercially available VMAs, either synthetic (e.g. synthetic copolymer in COM 2), or in natural form (e.g. diutan gum in COM1). Hence, cellulose-based materials can be designed and manufactured to incorporate different viscosity-modifying effects in cement grouts. While they can be designed to increase viscosity even more than diutan gum, at similar dosages (CNF 2 vs. COM 1), they can also be manufactured to change the thickness similar to synthetic commercial copolymers. Although modifying a synthetic copolymer to change its effect on the rheology of cement grouts is somewhat complicated, the structure of cellulose may allow producers to manufacture cellulose based VMAs with a broad range of modifying effects (CNF1 to CNF 3 or CMF1 to CMF2).

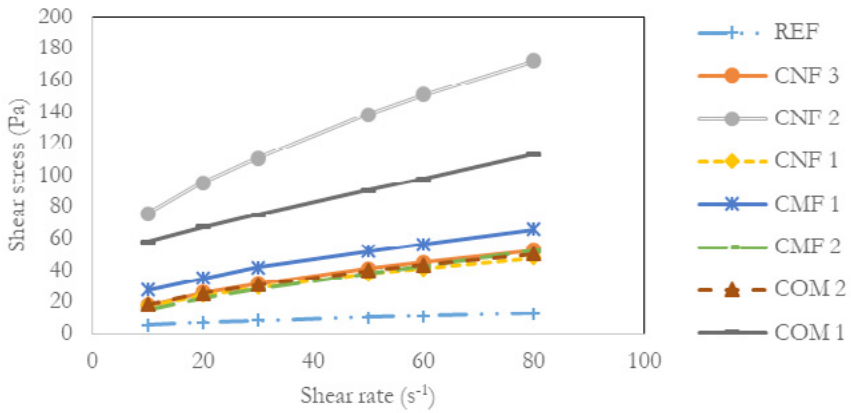

Figure 1: Influence of different cellulose-based materials on the rheology of cement grouts.

Table 1: Parameters of the Bingham flow model

Mixture	σ_D	η	R^2
REF	4.4817	0.1016	0.9873
CMF1	23.9091	0.5355	0.9925
CMF2	11.0521	0.5246	0.9958
CNF1	15.4877	0.4183	0.9873
CNF2	66.9335	1.3653	0.9902
CNF3	15.1874	0.4880	0.9858
COM1	51.1060	0.7800	0.9993
COM2	15.9725	0.4481	0.9878

3.2 Autogenous shrinkage

The effect of different CNFs on the autogenous shrinkage of the cement grouts is shown in Figure 2. The results imply that adding CNF to cement grouts increases the autogenous shrinkage, depending on the structure and morphology of CMs. This effect might be attributed to the fact that the CMs absorb a fraction of free water available in the mixture and decrease water to cement ratio, hence increasing the autogenous shrinkage. It can also be observed that different CMs with different routes (CNF1 to CNF3) may result in different volume changes.

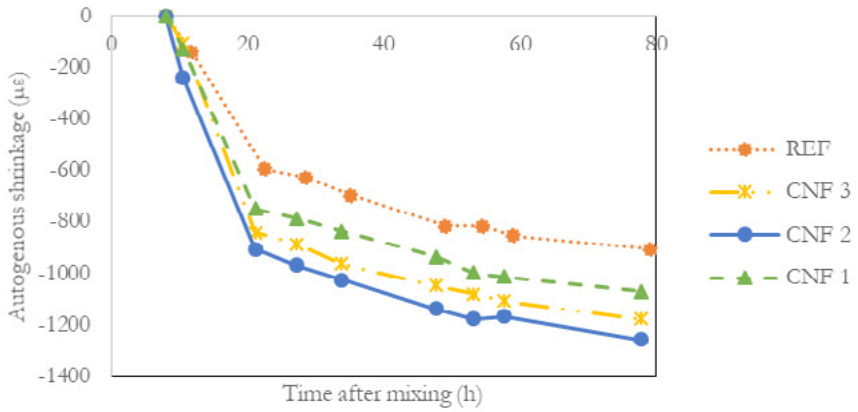

Figure 2. Linear autogenous shrinkage of cement grouts with and without CMs

Figure 3 compares the effect of the size of CM (CNF vs. CMF2) on linear autogenous shrinkage. The dosage of superplasticizer in Figure 3 is twice as much as that in Figure 2. Specimens incorporating CMF2 tend to draw more free water from the mixtures and shrink more than the ones proportioned with CNF at the similar dosages. The difference in water absorption might also be attributed to the differences in morphology of CMFs and CNFs. The mechanical milling process changes morphology and converts cellulose clusters to single fibres, hence altering shrinkage susceptibility.

3.3 Hydration kinetics

The effects of different cellulose nanofibers (CNF) and cellulose microfibers (CMF) are shown in Figure 4. Studies have shown that some wood-based pulp may deteriorate hydration kinetics due to water-soluble sugars [22,23]. However, isothermal calorimetry test results show that using CMs has a negligible effect on the peak height and the time required to reach the early rate peak. Therefore, hydration kinetics is not

affected by the addition of cellulose-based materials at the very low dosages of the admixtures incorporated in this study (0.08 % of cement).

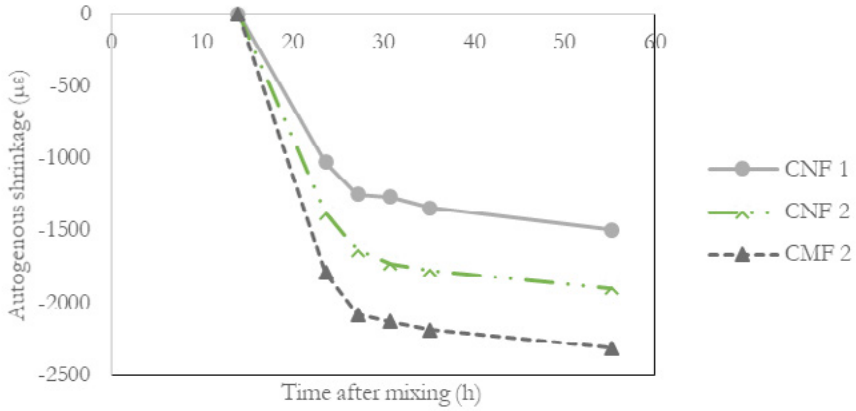

Figure 3. Linear autogenous shrinkage of cement grouts with CMF or CNF

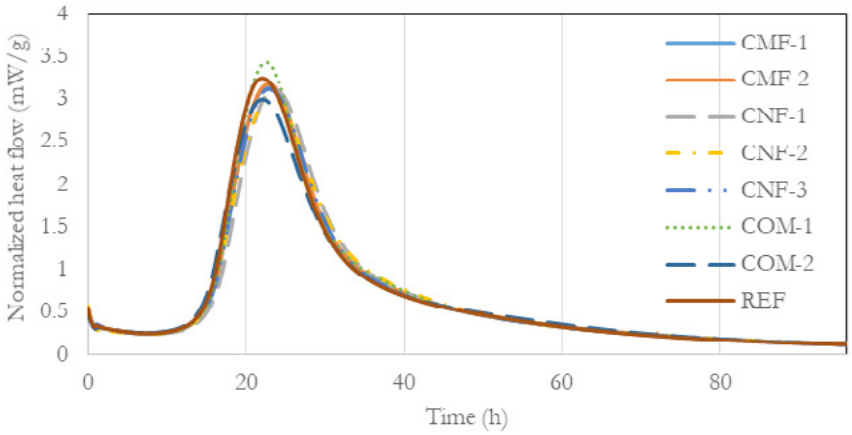

Figure 4: Isothermal calorimetry test results of different CMFs and CNFs

4. Conclusions

In the present research, the effects of two different types of cellulose-based materials (CMs) in micro and nano form on the viscosity of cement grouts and associated hydration and shrinkage are investigated. Two commercially available viscosity modifying admixtures, namely diutan gum and a synthetic copolymer, are used as references. Based on the properties assessed and the results obtained, the following conclusions can be drawn:

- Cellulose based materials, either cellulose microfiber or cellulose nanofiber, modify the rheology of cement grouts, and their modifying capacity is comparable to diutan gum or synthetic copolymers. Depending on their structure, they can adjust viscosity in different levels based on their structure.
- Various types of cellulose-based material affect linear shrinkage deformation differently, based on their morphology and structure.
- Application of CMF or CNF at low dosages (0.08% of cement) does not influence the hydration kinetics.

5. Acknowledgment

This research is a cooperation with Sappi Nederland Services BV. Dr. L. Xu and Dr. M. Jennekens are thanked for initiating the collaboration, and Dr. R. Cardinaels, Ir. R. Claessen, Dr. L. Tufano and Dr. L. Xu are thanked for the fruitful discussions throughout the project.

6. References

[1] N.P. Kutscha, J.R. Gray, TB41: The Potential of Lignin Research, Maine Agric. For. Exp. Stn. Tech. Bull. 41 (1970). http://digitalcommons.library.umaine.edu/aes_techbulletin.

[2] X. Sun, Q. Wu, S. Lee, Y. Qing, Y. Wu, Cellulose Nanofibers as a Modifier for Rheology, Curing and Mechanical Performance of Oil Well Cement, Sci. Rep. 6 (2016) 31654. doi:10.1038/srep31654.

[3] X. Sun, Q. Wu, J. Zhang, Y. Qing, Y. Wu, S. Lee, Rheology, curing temperature and mechanical performance of oil well cement: Combined effect of cellulose nanofibers and graphene nano-platelets, Mater. Des. 114 (2017) 92–101. doi:10.1016/j.matdes.2016.10.050.

[4] J.H. Kim, B.S. Shim, H.S. Kim, Y.J. Lee, S.K. Min, D. Jang, Z. Abas, J. Kim, Review of nanocellulose for sustainable future materials, Int. J. Precis. Eng. Manuf. - Green Technol. 2 (2015) 197–213. doi:10.1007/s40684-015-0024-9.

[5] N. Lavoine, I. Desloges, A. Dufresne, J. Bras, Microfibrillated cellulose - Its barrier properties and applications in cellulosic materials: A review, Carbohydr. Polym. 90 (2012) 735–764. doi:10.1016/j.carbpol.2012.05.026.

[6] X.Y. Jin, C.W. He, X.R. Liu, X.J. Yan, Q.Z. Yu, Effect of Cellulose Crystal Content on the Mechanical Property of Nano-Crystalline Cellulose/Lignin Composite Fibrous Film, Key Eng. Mater. 727 (2017) 527–531. doi:10.4028/www.scientific.net/KEM.727.527.

[7] S. Boufi, I. González, M. Delgado-Aguilar, Q. Tarrès, P. Mutjé, Nanofibrillated cellulose as an additive in papermaking process, in: Cellul. Nanofibre Compos. Prod. Prop. Appl., 2017: pp. 153–173. doi:10.1016/B978-0-08-100957-4.00007-3.

[8] R.J. Moon, A. Martini, J. Nairn, J. Simonsen, J. Youngblood, Cellulose nanomaterials review: structure, properties and nanocomposites, Chem. Soc. Rev. 40 (2011) 3941. doi:10.1039/c0cs00108b.

[9] A.N. Nakagaito, H. Yano, Novel high-strength biocomposites based on microfibrillated cellulose having nano-order-unit web-like network structure, Appl. Phys. A. 80 (2005) 155–159. doi:10.1007/s00339-003-2225-2.

[10] J. George, S. S N, Cellulose nanocrystals: synthesis, functional properties, and applications, Nanotechnol. Sci. Appl. Volume 8 (2015) 45. doi:10.2147/NSA.S64386.

[11] ACI Committee 212, ACI 212.3R-16 Report on Chemical Admixtures for concrte, Farmington Hills, 2016.

[12] ACI Committee 237, Report on Chemical Admixtures for Concrete, 2016.

[13] ACI Committee 237, ACI 237R-07 Self-Consolidating Concrete, American Concrete Institute, Farmington Hills, 2007.

[14] K.H. Khayat, Effects of antiwashout admixtures on properties of hardened concrete, ACI Mater. J. 93 (1996) 134–146. doi:10.14359/1412.

[15] K.H. Khayat, Viscosity-enhancing admixtures for cement-based materials — An overview, Cem. Concr. Compos. 20 (1998) 171–188. doi:10.1016/S0958-9465(98)80006-1.

[16] K.H. Khayat, K. H. Khayat, Workability, Testing, and Performance of Self-Consolidating Concrete, ACI Mater. J. 96 (1999). doi:10.14359/632.

[17] M. Sakata, N., Maruyama, K., and Minami, Basic properties and effects of welan gum on self-consolidating concrete, Prod. Methods Work. Concr. Proc. Conf. RILEM, E&FN Spon. (1996).

[18] O. Berke, N.S., Cornman, C.R., Jeknavorian, A.A., Knight, G.F., Wallevik, The effective use of superplasticizers and viscosity-modifying agents in self-consolidating concrete, First North Am. Conf. Des. Use Self-Consolidating Concr. Chicago, ACBM. (2002) 173–178.

[19] M. Lachemi, K.M.A. Hossain, V. Lambros, N. Bouzoubaâ, Development of Cost-Effective Self-Consolidating Concrete Incorporating Fly Ash, Slag Cement, or Viscosity-Modifying Admixtures, ACI Mater. J. 100 (2003) 419–425. doi:10.14359/12818.

[20] ASTM Committee C09.48, ASTM C1679-14: Standard Practice for Measuring Hydration Kinetics of Hydraulic Cementitious Mixtures Using Isothermal Calorimetry, West Conshohocken, 2014. doi:10.1520/C1679-14.

[21] ASTM Committee C09.68, ASTM C1698 - 09(2014) Standard Test Method for Autogenous Strain of Cement Paste and Mortar, West Conshohocken, 2014. doi:10.1520/C1698-09R14.

[22] K. Bilba, M.A. Arsene, A. Ouensanga, Sugar cane bagasse fibre reinforced cement composites. Part I. Influence of the botanical components of bagasse on the setting of bagasse/cement composite, Cem. Concr. Compos. 25 (2003) 91–96. doi:10.1016/S0958-9465(02)00003-3.

[23] O. Onuaguluchi, N. Banthia, Plant-based natural fibre reinforced cement composites: A review, Cem. Concr. Compos. 68 (2016) 96–108. doi:10.1016/j.cemconcomp.2016.02.014.

The recycling potential of waste wood into wood-wool/cement composite

F. Berger[1], F. Gauvin[1], and H.J.H. Brouwers[1]

[1] Department of the Built Environment, Eindhoven University of Technology, P. O. Box 513, 5600 MB Eindhoven, The Netherlands.

Abstract

Nowadays, the recycling potential of waste wood is still limited and in a resource cascading approach, recycling waste wood in cement composite materials, such as wood wool cement board (WWCB), appears as a promising solution. The quality of the waste wood is the main factor leading to the instability of the final product and can affect the mechanical proprieties or the wood cement compatibility. However, the possibility to recycle waste wood as spruce replacement for WWCB manufacture needs more investigation in order to assess the impact of waste wood on the mechanical performances of the final product but also to characterize the behavior of hazardous substances embodied in a cement matrix. This paper addresses the characterization of two types of waste wood, from pallets and demolition waste and their influence on the manufacturing process, mechanical proprieties and the chemical compatibility when used in WWCB. A comprehensive approach is provided to define the influence of waste wood on the hydration reaction of the cement and the chemical and physical proprieties of the composite are assessed by isothermal calorimetry, leaching measurement and microscopy. Finally, the mechanical proprieties of WWCB are tested for different waste wood content in order to define the best wood/waste wood ratio and thereby confirming the possibility to reuse waste wood in fiber/cement composite for building applications.

Keywords: Circular economy; natural fibers; treated wood; cement composite; leaching; mechanical testing;

ICSBM 2019
ID 141

1. Introduction

Nowadays, waste wood represents an important economic and environmental issue. Recently, studies estimate that 50 million cubic meters of waste wood is generated each year in the European Union [1]. Currently, the recycling potential of waste wood is still low, mainly caused by a lack of sustainable reusing or recycling applications [2,3]. In fact, the main part of waste wood can be treated by different ways (e.g. heat, chemical or mechanical treatment) and this involves a large amount of preservative-treated wood which contains organic and inorganic contaminants [4,5]. Those contaminants represent a real issue in waste management which can conduct to health and environmental issues during the end of life of wood [6]. Waste wood is subject to two different approaches in terms of waste management according to policy targets: It can be reused as materials in the *circular economy* or as energy recovery (e.g. Renewable Energy Directives). However, several environmental assessments show contradictory results about these two options because of the presence of contaminants in wood products [7]. The EU encourages the « resources cascading » approaches in order to promote the circular economy. This dynamic is described in the *Waste Framework Directive* (2008/98/EC) by the European Parliament, which helps to determine the future reuse of waste (Figure 1).

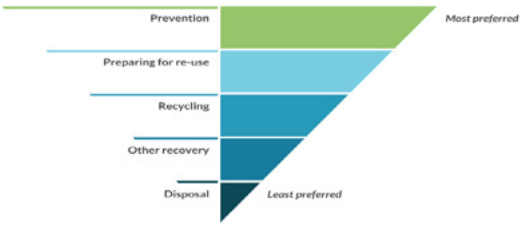

Figure 1: Circular economy diagram showing the different recycling options

In a resource cascading approach, various options are possible. But in order to use wood without losing its value (i.e mechanical properties), this current study focuses on the possibility to find sustainable applications in order to recycle waste wood into wood wool, in order to reinforce wood-cement composites, such as Wood Wool Cement Board (WWCB) (Figure 2). In these applications, the waste wood is turned into fibers and can be used in state-of-the-art materials.

Figure 2: Wood wool cement board (WWCB) manufactured with spruce wool

WWCBs are an example of wood-cement composites. They are made of wood which can be spruce (softwood) or poplar (hardwood), as well as a binder which is commonly ordinary Portland cement (OPC) or white cement (WC). These binders are known to guarantee the mechanical and physical properties of the final product [8]. Since 1940, WWCBs are commonly used in Europe and Asia, thanks to their good resistance to decay and insect but also for their good thermal and acoustical insulating properties and low density (300-500 kg/m^3) [9]. Nowadays, the wood used for the manufacture of WWCB comes from forest harvesting and industrial wood products [2]. Replacing spruce by waste wood can lead to environmental issues because waste wood is mixed with differents type of waste (raw wood, processed wood) and various treatments and contaminations can be found. Moreover, the presence of contaminants can disturb the wood cement compatibility and also limit the potential range of application due to leaching and the toxicity of waste wood [10–14]. Heterogeneity of waste wood is also a critical factor. As shown in several studies, depending on the wood species, its hygroscopic behavior, cement compatibility and effect on cement hydration can be significantly different due to the carbohydrate and saccharides contents in the fibers but also because of the different morphologies of the wood fibers. [15,16].

Countless type of waste wood can be used, but among the potential candidates, the wood from pallets is one the most interesting because it is generally only heat-treated for environmental and recycling reasons leading to a clean wood resource for biomass or reuse applications. Moreover, wood from construction

and demolition wastes is also very interesting because of its great availability. However, several types of treatments are used, as shown by the UK Waste and Resources Action Program. Indeed, 74% of waste wood which comes from construction and building site are treated [17]. During the past 40 years, *Chromated copper arsenate* (CCA), *Penta* and *Creosote* are the three most used preservative treatments for wood products. Furthermore, the use of CCA treatment was the main preservative for housing or decking applications in order to prevent or delay decay caused by fungi or termites, especially in Australia, New Zealand, and the United States [5][11]. Therefore, a huge amount of CCA treated wood still remains in service worldwide and will be concerned with disposal and recycling applications. This fact implies a real recycling potential for these upcoming waste into composite materials.

In this study, the mechanical and chemical properties of the two waste wood samples provided by Nedvang (Pallets and C&D) are studied in order to compare them with conventional spruce wood, used as a reference. The wood-cement compatibility is assessed as well as the leaching behavior of the waste woods by various methods, such as pH measurement, isothermal calorimetry and scanning electron microscopy (SEM). Then, wood fibers are processed and studied (mechanical behavior, microstructure). Thereafter, the mechanical, physical and leaching properties of WWCB manufactured with different percentage of waste wood (every 10% until 100%) are compared to conventional and commercial WWCBs.

2. Methodology

2.1 Materials

In this study, the spruce wood is taken as reference in the form of Excelsior wood wool (or also called *fiber* in this study) and is provided by Knauf insulation (NL). These fibers are conventionally used for the industrial manufacture of WWCB. The studied waste woods are provided by Nedvang (NL) and come from pallets and construction & demolition sites, respectively. The binder applied in the study is CEM I 52.5 R white (PC) provided by ENCI (NL).

2.2 Methods

2.2.1 Scanning electron microscopy

Microstructure analysis of the waste wood fiber is performed by Scanning Electron Microscopy (SEM, Phenom pro-X) with a back-scattering electron detector (5 kV). The waste wood fiber has been coated with a 20 nm gold layer before the microscopy. The moisture content of the waste wood has been limited by drying the material in an oven at 60° C, for 2 h prior to analysis.

2.2.2 Leachates characterization

The leaching of waste wood is studied by using the TCLP extraction methods to obtain the leachate solution. The samples are reduced to a particle size of less than 1 cm. Subsequently, the leachate is prepared according to the TCLP standard, the waste was added to a determined extraction fluid and mixed during 18h at 30 rpm at room temperature. Thereafter, the solution is filtrated through a 0,6 to 0,8 µm glass fiber filter. The leachate obtained is analyzed by inductively coupled plasma mass spectrometry (ICP-MS) in order to measure the concentration of heavy metal and other potential contaminants rejected by the wood.

2.2.3 Isothermal calorimetry

The hydration kinetics is studied by isothermal calorimetry with a TAM Air Isothermal calorimeter set at a constant temperature of 20 °C during 72h. The wood samples and the binder were first well mixed in an ampoule before the water was added. After addition of water, the mixture was mixed for 3 min before being loaded in the calorimeter. The heat evolution rate data were calibrated by subtracting the heat evolution of

ampoules with water as a baseline.

2.2.4 Mechanical properties of the wood fibers

Mechanical properties of wood strands are measured by using an Instron 5967 bench equipped with a 2530-100 N load cell and 2710-111 wedge grip with rubber jaw faces. Tensile tests are conducted in displacement control with a crosshead speed of 5 mm/min. More than 15 samples for each condition are tested. Tensile strength (cN/tex) and Young's modulus (N/tex) are measured as a function of the linear density of the fiber (tex) by measuring the length and the weight of each fiber prior to analysis.

2.2.5 Manufacture of the composites

In order to evaluate the mechanical performances of the composite according to different Waste wood/ spruce wood ratios (called *W/S ratio* in this study), WWCBs are manufactured with 10 different chosen ratios (0.1 to 1), named PW/S0.1 to PW/S1.0 for pallets wood. In this study, the manufacture of the composites is based on the dry method, usually applied in the WWCB production. The final product is placed into a mold 30 x 60 cm and pressed for 24 h, using a mechanical press. Successively, the sample is cured in a plastic sheet for 7 days and then left drying at ambient conditions for another 3 days. In order to achieve the same moisture content before testing, the boards are dried in the oven for 2 h at 50 °C.

2.2.6 Mechanical performances of the composites

The bending strength is measured at 10 days by a three-point flexural test (Instron 5967) on a sample with dimensions of 5 x 20 x 1.5 cm, using a testing speed of 5 mm/min, and a support span of 15 cm. Three samples of each W/S ratio are tested. As reference values, the dimensional stability has to be satisfied, by a maximum thickness of 15 mm and a minimum bending strength of 1.7 MPa, according to the BS EN 12089, *Thermal insulating products for building applications* standard.

2.2.7 Thermal conductivity measurement

Thermal conductivity is measured on WWCB by a heat transfer analyzer *ISOMET 2104*. As a reference, commercial WWCB with a thickness between 15 and 30 mm have a thermal conductivity range of 0.08-0.11 $W.m^{-1}.K^{-1}$ according to the BS EN 12089, *Thermal insulating products for building applications* standard.

3. Results and discussion

3.1 Waste wood characterization

In order to characterize the two streams of wood, microscopy and isothermal calorimetry are performed. These two methods allow controlling the potential compatibility (i.e. mechanical and chemical) between the wood and the cement in WWCB.

The micrographs in Figure 3 shows the surface of spruce (in the form of fiber) and pallet wood (waste strands). These two kinds of wood are closed to each other and depict the same microstructure and surface aspect. Tubular cell walls are visible for both types of wood and the lumens (white arrows) have the same shape and almost the same size, with around 7µm for the pallets wood and 5µm for the spruce. Additional cell walls are visible with the waste wood (black arrows) indicating some heterogeneity. In addition, the pallet wood shows no noticeable signs of contaminants at its surface. Moreover, as compared to the reference, the surface of the waste wood seems to have less wax and lignin. These observations indicate a potential good wood/cement compatibility. The very similar structure also indicates that the manufacture of WWCB with waste wood from pallet would be not problematic because similar pore size means the same water demand and same cement coating during the process.

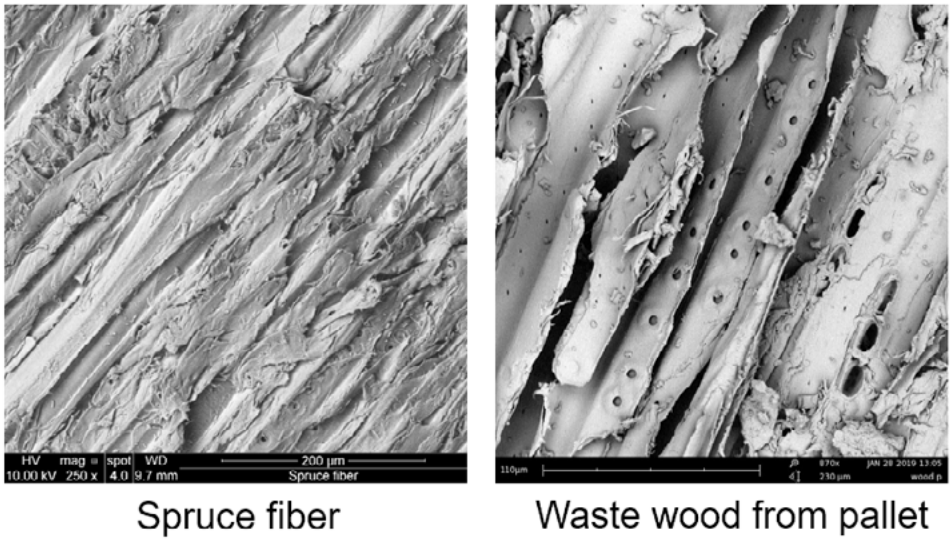

Figure 3: SEM microscopy of waste wood from pallet and spruce fiber, which is used in WWCB manufacture

However, waste wood from construction and demolition (C&D) sites seems more problematic, even if its structure remains quite close to the spruce because its cell walls and its surface show the presence of contaminants (Figure 4). These particles can be heavy metals such as chromium or inorganics substances that have been mixed with the waste woods. These substances can disturb the manufacturing process by delaying the hydration reaction of the cement, reducing the wood cement compatibility or limiting the range of applications due to health and environmental issues involved by the leachates.

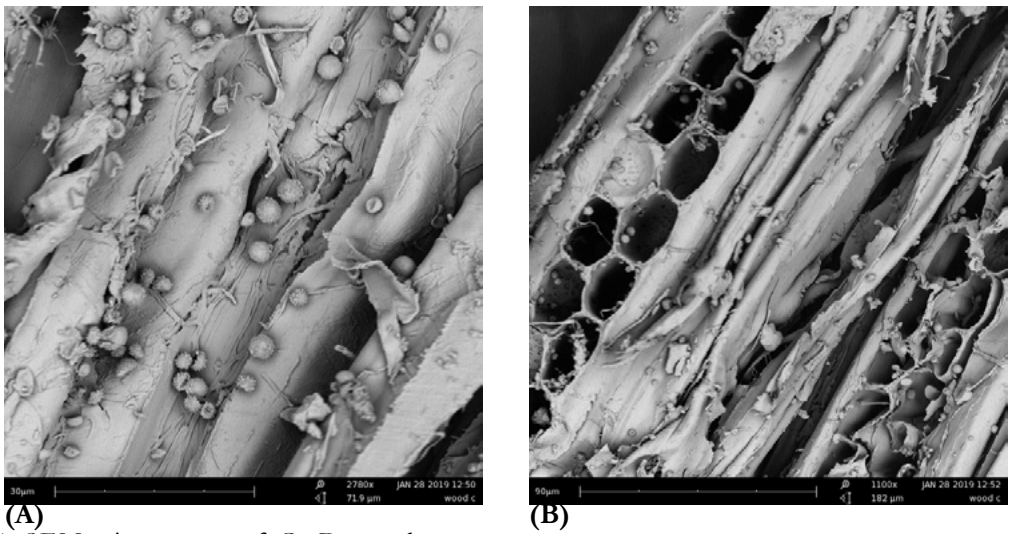

Figure 4: SEM microscopy of C&D wood

3.2 Compatibility with cement

Results of the calorimetry of the three kinds of wood are depicted in Figure 5, showing the chemical compatibility between the wood and the cement.

From the results, the two types of waste wood (building and pallets) are really close to each other. As compared to the reference, the hydration peaks have been delayed by 1.5h due to the presence of the waste wood. A probable hypothesis is that the waste wood is slightly degraded, especially at its surface,

as it can be seen by SEM (i.e. lack of matrix at the surface of the wood). The hemicellulose degradation creates monosaccharides and polysaccharides that are mixed in the cement paste and can delay the cement hydration. However, this retardation is not very important and indicates that both kinds of waste wood have a low sugar content and will not affect the manufacturing process nor the final proprieties of the WWCB. In addition, the maximum released heat is 20% lower in the presence of wood inside the cement paste. This decrease does not have a significant impact on the reaction as it remains low and also it can be explained by the presence of sugars involved by waste woods.

From these results, it appears that both types of waste wood have good chemical compatibility with cement. Moreover, the waste wood from pallets is surprisingly close to the spruce fiber and would be a perfect candidate to replace it due to its similar microstructure. Therefore, in this study, only waste wood from pallets is be turned into fibers and used in WWCB.

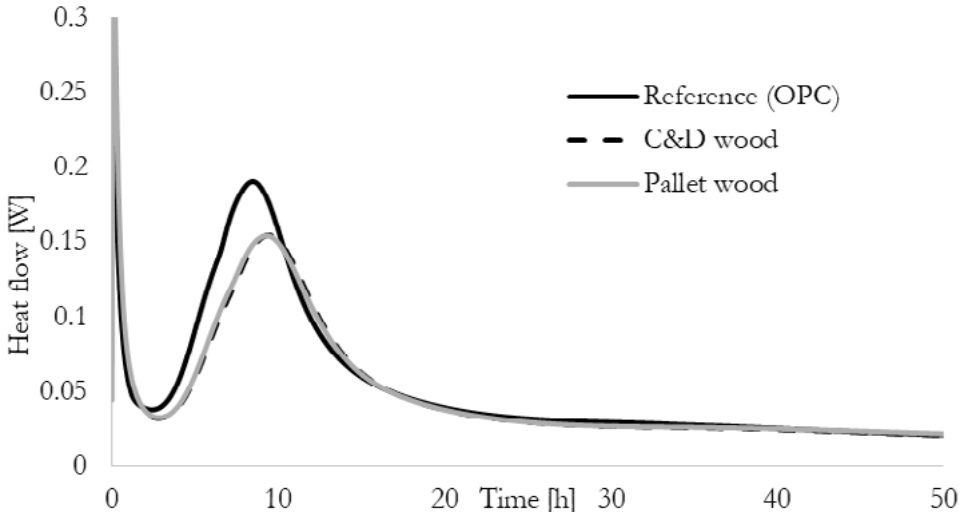

Figure 5: Isothermal calorimetry of the 2 wood streams as compared to the reference (i.e. white cement), showing the effects of the waste woods on the cement hydration

3.3 Pallet wood fiber manufacture

Fibers made of pallets are manufactured in the TU/e BPS laboratory using thin layers of pallet cut with a ribbon saw and then turned into fibers with a wood plane. Figure 6 depicts the process, which resulted in wood wool with very similar aspect than regular wood wool manufactured from spruce (Figure 6-C).

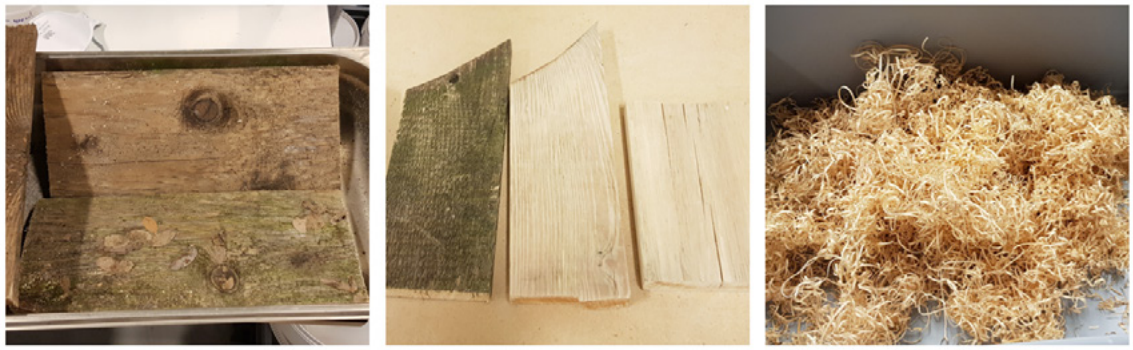

Figure 6: Pallet wood fiber manufacture. A: Pallet is cut into pieces, washed; B: wood is sanded and dried; wood is cut into 10-15 cm fibers.

3.4 Mechanical properties of wood fibers

The tensile test of fibers highlights the variation of the mechanical properties between the pallet wood and the spruce in the form of fibers. These results average 30 tests on each type of wood fibers and are displayed in Figure 7 and Table 1.

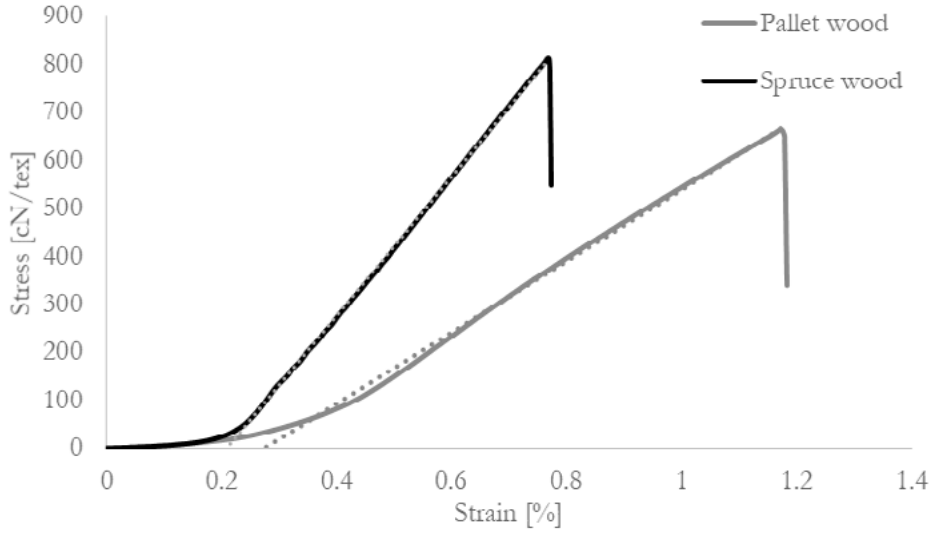

Figure 7: Average stress/strain curve of the two types of fibers

Table 1: Summary of the mean results

Sample	Modulus [cN/tex]	Tensile strain [cN/tex]
Pallet fibers	770	812
Spruce fibers	1332	663

The tensile strength of the pallet fibers is slightly lower than the spruce one, with a decrease of approximately 20%. On the other hand, the modulus of elasticity is almost 50% lower. Many phenomena can affect the mechanical behavior of the fiber (e.g. external degradation, differences in morphology or composition…) but here, SEM characterization has shown that spruce and pallet woods are very similar.

First of all, it is unlikely that the pallet wood is degraded. SEM characterization has shown very clean wood and isothermal calorimetry has shown almost no impact on cement. If the wood would have been degraded, the tensile strength of the fiber would have been critically affected since the degradation would have affected the wood structure. Here, only the modulus of elasticity of the pallet wood is significantly different and this propriety is directly related to the cellulosic fibrils within the structure of the wood. Therefore, the difference between the two types of wood can be explained by an internal degradation of the cellulose but also by the orientation of the cellulose fibrils depending on the cutting axis of the fibers. The first hypothesis is very unlikely, because the isothermal calorimetry shows no real difference between the two types of wood, and degradation of the cellulose would also indicate a major hemicellulose degradation, thereby inducing a critical amount of polysaccharide in the system.

A more probable explanation would be that these differences can be related to the manufacturing process or the morphology of the fibers. The spruce fibers are made thanks to an industrial process, using wood logs whereas the pallet fibers have been made differently because the conventional process is not applicable for a recycled material due to the variation in terms of shape and size. The industrial process is specially

developed to obtain the greatest mechanical proprieties for each fiber, following the cell walls of the wood, with an optimum orientation of the cellulose fibrils.

SEM microscopy of the pallet wood fiber (Figure 8) confirms these observations. It does not show matrix degradation and reinforce the fact that the microstructure of both wood sample is the same (as compared to Figure 4). However, the structure of the wood (following the black arrow in A) is slightly tilted as compared to the cutting direction (in the box), which can explain the low modulus of elasticity. Therefore, the anisotropy of wood causes the differences in Young's modulus. But this significant decrease is not very problematic in the composite strength because WWCBs are tested in flexural mode, and the rigidity of the boards are not a requirement in the existing standards.

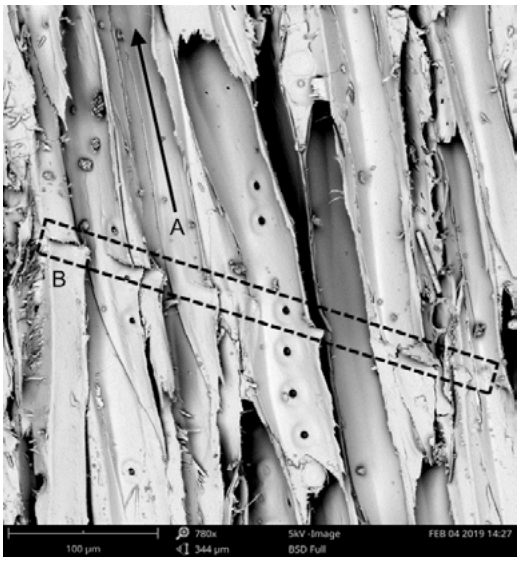

Figure 8: SEM microscopy wood fiber made of pallet. The cell direction is indicated with the black arrow (A). The cutting direction is indicated in B, with scratching marks.

3.5 Mechanical properties of WWCB

Flexural strength of WWCB containing 10 to 100% of pallet wood fibers (as replacement of spruce) are measured, as well as the density of these boards. Results are shown in Figure 9.

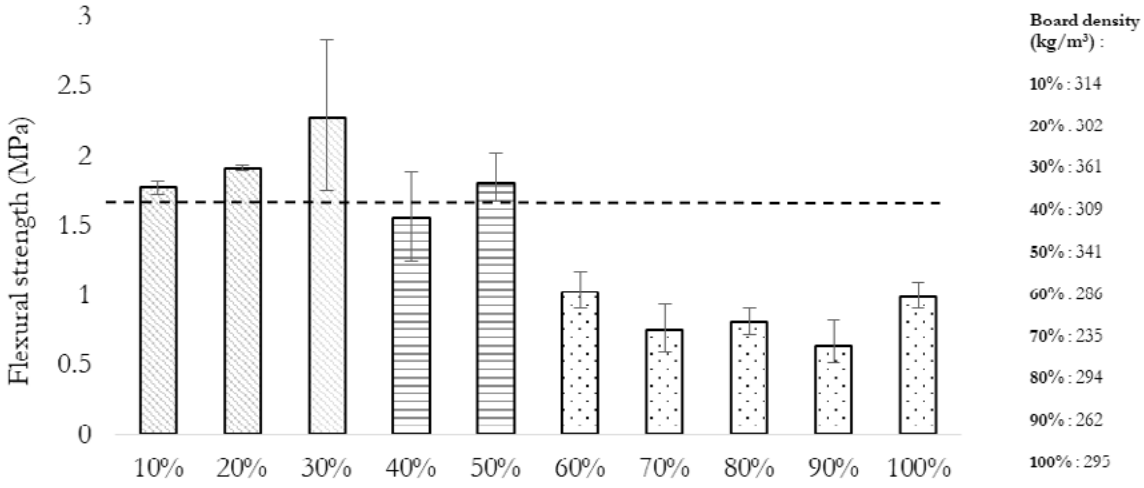

Figure 9: Flexural strength of WWCB containing 10 to 100% of waste wood (mixed with spruce wood). The dashed black line is set at 1.7 MPa, which is the acceptable limit for boards

In average, WWCB made industrially with spruce have a flexural strength of 2 MPa, for low-density range

(300-400 kg/m^3). When waste wood is added to spruce in WWCB, results can be regrouped in three groups.

Between 10 and 30% of waste wood (light grey dashed lines), WWCBs are always above the acceptable limit since all tested specimens have a flexural strength above 1.7 MPa. An important standard deviation is visible for the PW/S0.3 board but only because some specimens have shown extraordinary results (probably because of the good cement/fiber dispersion).

When more than 30% of waste wood is added to spruce (dark grey, horizontal lines), results are acceptable. PW/S0.4 averages a flexural strength of 1.7 MPa and PW/S0.5 is always slightly above the limit. It proves that up to 50% of spruce can be replaced with waste wood, without causing issues.

However, above 50% of waste wood (black dots), the flexural strength of WWCBs significantly decrease, with average values from 1 to 0.6 MPa. Increasing the weight fraction of waste wood also leads to a decrease in the density of the boards. This phenomenon is explained by the expansion of boards after compression during the manufacturing process: Boards with more than 50% of wood are 1 to 2 cm bigger than boards made with more than 50% of spruce wood. As it was explained before, pallet wood fibers are very heterogeneous, and the fiber orientation is not optimal. It means that some fibers have the tendency of being curled as compared to spruce wood fibers which are always straight (see Figure 10).

Figure 10: WWCB made of 100% of waste wood. In the red box, a fiber is curled, explaining the higher porosity of WWCBs containing a high fraction of waste wood

3.6 Thermal properties of WWCB

Thermal conductivity of WWCB containing 10 to 100% of pallet wood fibers (as replacement of spruce) are measured and the average results are shown in Figure 11. The first observation is that the thermal conductivity of all the manufactured boards is way below the acceptable limit (0.11 W.m^{-1}.K^{-1}), which can be explained by the low density of all the boards, due to the selected recipe design.

Moreover, the differences in the thermal conductivity are mostly due to the density difference, as Figure 11 shows some correlation between these two properties. Since the microstructure of the two kinds of wood is very close, only the porosity and the macrostructure of the composite can explain this phenomenon. Besides, it is also noticeable that using a higher fraction of waste wood help to decrease the thermal conductivity because of the higher porosity formed by the curled-fibers in the structure, as shown in Figure 10.

Figure 11: Average thermal conductivity of WWCB as well as the boards' density

3.7 Environmental assessment

Leaching analysis of the waste wood is performed on its leachate and the results are shown in Table 2, showing heavy metal contaminants as well as some alkali and earth alkali. From the EU 2009/894/EC legislation, when recycled wood is used in wood-based materials, some elements such as arsenic, lead or copper should not exceed a limit value, indicated in the table.

Here, leaching values of all elements are far below the limit, which means that the wood can be used freely in WWCB. Moreover, these values are measured prior to manufacture meaning that the concentration of the WWCB leachate would be even lower, due to the complexation of some element with cement.

Table 2: Element concentration (mg/L) in waste wood leachate.

Element concentration (mg/L)	**As**	**Al**	**Ba**	**Cd**	**Co**	**Cr**	**Cu**	**Fe**	**Li**
	0.031	0.200	0.163	-	-	0.022	0.115	0.085	0.021
Limit values from EU 2009/894/EC	25	-	-	50	40	25	40	-	-
Element concentration (mg/L)	**Ni**	**Pb**	**Sr**	**Ti**	**Zn**	**Na**	**K**	**Mg**	**Ca**
	-	0.057	0.218	0.007	0.971	100	50	30	100
Limit values from EU 2009/894/EC	100	90	-	-	-	-	-	-	-

4. Conclusions

In this study, waste wood has been used in order to replace conventional spruce wood in wood wool cement boards (WWCB), composite that can be used for ceilings or walls. Following the experimental results, the following conclusions have been drawn:

- Wood from pallets is an excellent candidate for WWCB because its structure is very similar to the spruce industrially used in the manufacture of these composites. On the other hand, using wood from construction and demolition sites is more challenging, because this wood is more heterogeneous (i.e. more than one type of wood is used in this kind of application) and can be contaminated.
- Waste wood is quite compatible with white cement, which is used in the production of WWCB. Measured by isothermal calorimetry, the effect of waste wood on cement is not significant. Moreover, the environmental assessment made on waste wood shows no traces of contaminants in wood, paving the way for its usage in composites.

- Making wood fibers from waste material is challenging because the conventional industrial process is not designed for waste wood. Yet, in this study, an alternative method has been used, turning successfully pallet wood into fibers, with microstructure and mechanical properties very close to spruce wood. The only noticeable issue is the difficult control of the anisotropy of the wood, leading to fibers not always oriented in the right direction (alongside the cell walls of the wood).
- WWCBs have been made mixing 10 to 100% of waste wood fibers with spruce fibers. Results show that up to 50% of waste wood, boards are above the acceptable limit (1.7 MPa). Above 50% of waste wood, flexural strength and density of the boards decrease significantly. Thermal properties of these boards are always acceptable, with very good values below 0.08 $W.m^{-1}.K^{-1}$.

In conclusion, waste wood from pallet can be a good option to replace spruce in WWCB. So far, its replacement level is successful until 50%. Above this limit, the fiber morphology is too heterogeneous to guarantee a good reinforcement. Better process or another source of wood can be evaluated in the future, as well as another kind of *green* binder, in order to create a more sustainable composite for building applications.

5. Acknowledgment

The authors would like to acknowledge the financial support provided by M2i (Materials innovation institute). For the material support, the authors would like to acknowledge Nedvang (The Netherlands), Knauf Insulation (The Netherlands) and ENCI (the Netherlands).

6. References

[1] F.C. Bergeron, Energy and climate impact assessment of waste wood recovery in Switzerland, Biomass and Bioenergy. 94 (2016) 245–257. doi:10.1016/J.BIOMBIOE.2016.09.009.

[2] M.H. Ramage, H. Burridge, M. Busse-Wicher, G. Fereday, T. Reynolds, D.U. Shah, G. Wu, L. Yu, P. Fleming, D. Densley-Tingley, J. Allwood, P. Dupree, P.F. Linden, O. Scherman, The wood from the trees: The use of timber in construction, Renew. Sustain. Energy Rev. 68 (2017) 333–359. doi:10.1016/J.RSER.2016.09.107.

[3] M. Humar, J. Jermer, R. Peek, Regulations in the European Union with Emphasis on Germany, Sweden and Slovenia, Environ. Impacts Treat. Wood. (2006) 37–57. doi:10.1201/9781420006216.ch3.

[4] E.-H. Pommer, Wood, Preservation, in: Ullmann's Encycl. Ind. Chem., Wiley-VCH Verlag GmbH & Co. KGaA, Weinheim, Germany, 2000. doi:10.1002/14356007.a28_357.

[5] C.C. Felton, R.C. Groot, The recycling potential of preservative-treated wood., For. Prod. J. 46 (1996) 37–46.

[6] M.I. Shahidul, M.L. Malcolm, M.S.J. Hashmi, M.H. Alhaji, Waste Resources Recycling in Achieving Economic and Environmental Sustainability: Review on Wood Waste Industry, Ref. Modul. Mater. Sci. Mater. Eng. (2018). doi:10.1016/B978-0-12-803581-8.11275-5.

[7] G. Faraca, D. Tonini, T.F. Astrup, Dynamic accounting of greenhouse gas emissions from cascading utilisation of wood waste, Sci. Total Environ. 651 (2019) 2689–2700. doi:10.1016/J.SCITOTENV.2018.10.136.

[8] K. Kochova, K. Schollbach, H.J.H. Brouwers, Use of alternative fibres in Wood Wool cement boards and their influence on cement hydration, in: 19th Int. Conf. Build. Mater., Ibausil, 2015: pp. 2–1375. https://pure.tue.nl/ws/files/3889104/935776505712757.pdf.

[9] F.C. Jorge, C. Pereira, J.M.F. Ferreira, Wood-cement composites: A review, Holz Als Roh - Und Werkst. 62 (2004) 370–377. doi:10.1007/s00107-004-0501-2.

[10] J.A. Hingston, C.D. Collins, R.J. Murphy, J.N. Lester, Leaching of chromated copper arsenate wood preservatives: A review, Environ. Pollut. 111 (2001) 53–66. doi:10.1016/S0269-7491(00)00030-0.

[11] A. Mohajerani, J. Vajna, R. Ellcock, Chromated copper arsenate timber: A review of products, leachate studies and recycling, J. Clean. Prod. 179 (2018) 292–307. doi:10.1016/j.jclepro.2018.01.111.

[12] R.W. Wolfe, A. Gjinolli, Cement-Bonded Wood Composites as an Engineering Material, (1997) 84–91. https://www.fpl.fs.fed.us/documnts/pdf1997/wolfe97a.pdf (accessed February 20, 2019).

[13] T. Townsend, T. Tolaymat, H. Solo-Gabriele, B. Dubey, K. Stook, L. Wadanambi, Leaching of CCA-treated wood: implications for waste disposal, J. Hazard. Mater. 114 (2004) 75–91. doi:10.1016/J.JHAZMAT.2004.06.025.

[14] A. Quiroga, V. Marzocchi, I. Rintoul, Influence of wood treatments on mechanical properties of wood-cement composites and of Populus Euroamericana wood fibers, Compos. Part B Eng. 84 (2016) 25–32. doi:10.1016/j.compositesb.2015.08.069.

[15] K. Kochova, K. Schollbach, F. Gauvin, H.J.H. Brouwers, Effect of saccharides on the hydration of ordinary Portland cement, Constr. Build. Mater. 150 (2017) 268–275. doi:10.1016/j.conbuildmat.2017.05.149.

[16] G.C.H. Doudart De La Grée, Q.L. Yu, H.J.H. Brouwers, THE EFFECT OF GLUCOSE ON THE HYDRATION KINETICS OF ORDINARY PORTLAND CEMENT, in: First Int. Conf. Bio-Based Build. Mater., Clermont-Ferrand, 2015: pp. 126–132.

[17] Composition of wood waste from construction & demolition (C & D) sites, (2009).

[18] & C. Schmidt, R., Marsh, R., Balatinecz, J. J., Increased wood-cement compatibility of chromate-treated wood, 44 (1994) 5–9.

Mechanical properties and shrinkages of coir fibers reinforced light-weight aggregate concrete

X.X. Zhang, F. Gauvin, H.J.H. Brouwers

Department of the Built Environment, Eindhoven University of Technology, P. O. Box 513, 5600 MB Eindhoven, the Netherlands.

Abstract

Natural fibers (NFs) from agricultural wastes have been increasingly used as reinforcements in cement-based materials to replace synthetic fibers thanks to their advantages, for instant, low cost, light weight and considerably mechanical properties. The present research aims to investigate the effects of different contents of saturated coir fibers on the mechanical properties and drying and autogenous shrinkages of cement-based lightweight aggregate concrete (LWAC). The concrete is designed by adopting the modified Andreasen and Andersen (A&A) particle packing model to achieve a more compacted matrix. LWAs made of waste glass are applied to develop a greener concrete. Three dosages of coir fibers, 0.5%, 1.5%, and 3%, are added by weight of the concrete. The results show that the compressive strength, flexural strength and toughness of LWAC are enhanced with added coir fibers. A low content of coir fibers such as 0.5% is benefit for achieving favourable compressive and flexural strength of concrete meanwhile higher contents of coir fibers such as 1.5% and 3% is in favour of obtaining good flexural toughness. The drying shrinkage of LWAC is slightly increased by adding coir fibers, while the autogenous shrinkage decreases significantly. Concrete with 3 wt.% coir fibers exhibits an expansion deformation, which indicates the internal curing effects of saturated coir fibers.

Keywords: Coir fibers, reinforcement, shrinkage, internal curing

ICSBM 2019
ID 147

1. Introduction

Due to the requirement for high-rise, long-span or functional buildings, lightweight aggregate concrete (LWAC) has attracted increasing attention because of its unique advantages, for example, lower density, larger specific strength and superior thermal insulation [1–8]. However, LWAC also has drawbacks such as low flexural strength and poor fracture toughness which have restricted its wider applications [9–11]. These defects could be usually compensated by adding fibers such as steel or synthetic fibers [12,13]. Nevertheless, even though these fibers are found to positively influence the properties of LWAC, some correlatively negative effects should be addressed. For example, both the steel and synthetic fibers have both high material and energy consumption, and can lead to a substantial environmental footprint in their production processes [14]. Moreover, synthetic fibers can cause health risks (e.g. skin irritations or respiratory diseases) during the manufacturing and bring environmental burden due to difficulty in disposing [15]. Additionally, the cost of some fibers like carbon fibers is not economical [16]. Moreover, steel fibers significantly increase the density of LWAC, especially when their fraction exceeds 1vol.% [17].

Unlike artificial fibers, natural fibers (NFs) are eco-friendly, renewable, recyclable and disposable [18,19], and have other advantages such as their low cost, light weight and good mechanical properties [20–22]. Brittle

materials reinforced with natural fibers exhibit equivalent mechanical performance as with synthetic fibers [23–25]. Thus, NFs are a good candidate to replace synthetic fibers to reinforce concrete with economic and environment benefits. Furthermore, due to the compatibility of NFs and LWAC, both have relatively light-weight and low mechanical properties, therefore, NFs are especially suitable for reinforcing LWAC. Among the various available NFs, coir fibers extracted from the waste coconut husks is abundant, with approximately 500,000 tons of coir fibers produced annually worldwide [26]. As compared to the most used NFs such as flax or bamboo, coir fibers possess a comparable specific tensile strength and have a higher toughness and flexibility [27]. Moreover, coir fibers can preserve good mechanical properties under aggressive conditions [28]. Some studies have been carried out to investigate the reinforcing effect of various contents and lengths of coir fibers on the mechanical performance of concrete. The results show that coir fibers significantly enhance the flexural strength, toughness and impact resistance of concrete [29,30] and their optimum content ranges from 1% - 3 wt.% (about 2% - 12 vol.%) with length of 2 - 5 cm, respectively [31,32].

However, because coir fibers are hydrophilic and thus their high moisture absorption can cause competitive water absorption with cement, thereby consequently affecting the available water amount for cement hydration [33,34]. Saturated fibers can be used to take advantage of this feature, thus extra water can be entrained in cement system for internal curing [35]. Nevertheless, only several presented studies are related to the internal curing effect of macro saturated fibers [35,36]. Accordingly, the objective of this study is to investigate the reinforcement effects of saturated coir fibers in concrete. The concrete is designed by adopting the modified Andreasen and Andersen (A&A) particle packing model to achieve a more compacted matrix and LWAs made of waste glass are applied to develop a greener concrete. The influence of saturated coir fibers with various contents on the mechanical properties and drying and autogenous shrinkages of cement composites are analysed. In addition, the internal curing effect of saturated coir fibers are investigated.

2. Methodology

2.1 Materials

The cement used is Ordinary Portland Cement (OPC) CEM I 52.5 R, supplied by Heidelberg Cement (The Netherlands). The chemical compositions and particle size distributions (PSDs) of cement are determined by X-ray fluorescence (XRF) and laser particle size analyzer (LPSA), shown in Table 1 and Figure 1, respectively.

The lightweight aggregates presented in Figure 2 are produced from recycled glass, supplied by Liaver Company (Germany). The chemical compositions and particle size distributions of LWAs are provided by the supplier, listed in Table 1 and Fig. 1. The physical properties of LWAs are presented in Table 2, obtained from the research of Yu et al. [37]. These LWAs have encapsulated cellular structures inside but a closed external shell outside, resulting in their low water absorption. The SEM graphs of LWAs microstructure are shown in Figure 3.

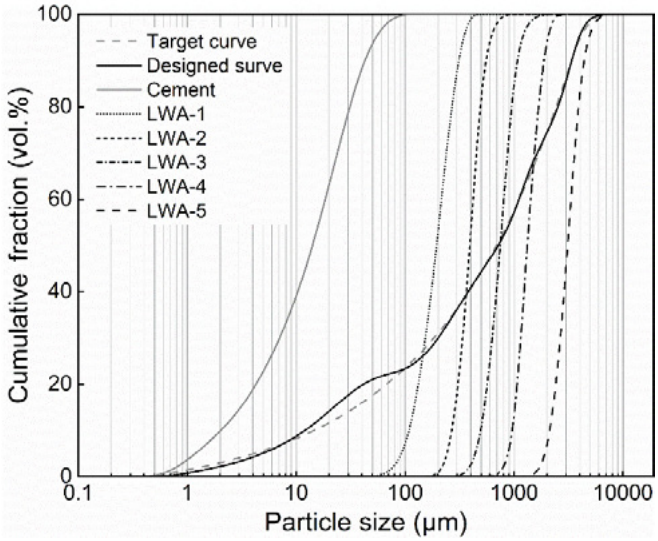

Figure 1: Particle size distributions (PSD) of the raw materials, the target curve and the resulting integral grading curve of the mixture.

Table 1. Chemical compositions of the cement and LWAs

Substances	Cement (mass %)	LWAs (mass %)
CaO	64.60	64.68 ± 2
SiO_2	20.08	71 ± 2
Al_2O_3	4.98	2 ± 0.3
Fe_2O_3	3.24	0.5 ± 0.2
K_2O	0.53	1 ± 0.2
Na_2O	0.27	13 ± 1
SO_3	3.13	-
MgO	1.98	2 ± 1
TiO_2	0.30	-
Mn_3O_4	0.10	-
P_2O_5	0.74	-
Cl^-	0.05	<0.01

Figure 2: Appearance of lightweight aggregates (LWAs): expanded waste glass

Coir fibers are provided by the Wageningen University & Research (The Netherland), shown in Figure 4. The chemical compositions of CFs are analyzed by a high performance anion exchange chromatography (HPAEC), given in Table 3. The bulk density is measured as the mass of coir fibers divided by their total bulk volume, and the specific density is tested by a Helium pycnometer (AccuPyc II 1340 Micromeritics). The bulk density and specific density of coir fibers are shown in Table 4.

Table 2. Physical properties of LWAs [37]

Materials size range	Bulk density	Specific density	Crushing resistance
(mm)	(kg/m^3)	(kg/m^3)	(N/mm^2)
LWA-1: 0.1-0.3	450	810	>3.5
LWA-2: 0.25-0.5	300	540	>2.9
LWA-3: 0.5-1.0	350	450	>2.6
LWA-4: 1.0-2.0	220	350	>2.4
LWA-5: 2.0-4.0	190	310	>2.2

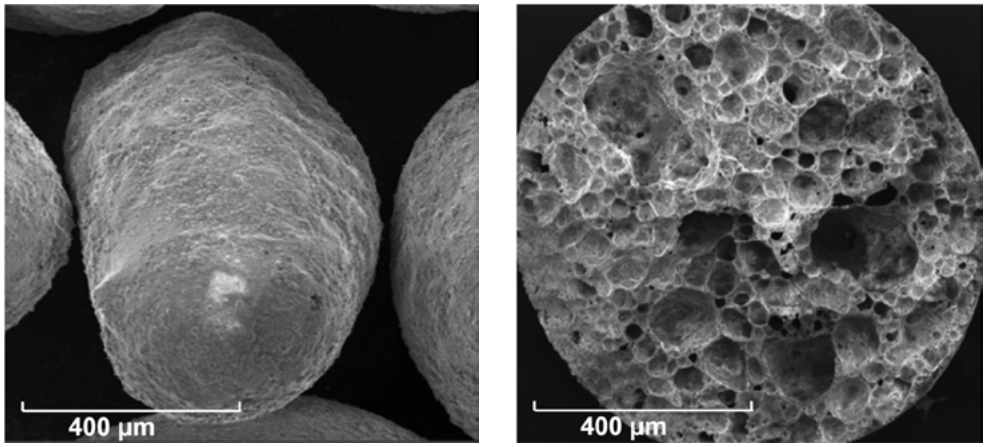

Figure 3: Microstructure of LWAs

Figure 4: Appearance of coir fibers

Table 3. Chemical compositions of coir fibers

Substances	Coir fibers (mass %)
Cellulose	36.6 ± 0.15
Hemicellulose	37.0 ± 0.15
Lignin	22.2 ± 0.05
Ash	1.9 ± 0.04
Extractive	5.7 ± 0.05

Table 4. Physical properties of coir fibers

Density (kg/m³)	Coir fibers
Bulk density	69.8
Specific density	1539.6

2.2 Methods

2.2.1 Mixture design and mixing procedures

The mix proportions of LWAC are presented in Table 5. The mixtures of the LWAC are designed by applying the modified Andreasen and Andersen (A&A) packing model to optimize the granular packing of all solid materials [38]:

$$P(D) = \frac{D^q - D_{min}^q}{D_{max}^q - D_{min}^q} \quad (1)$$

where P(D) is the fraction of total solid materials with particle sizes lower than D (μm). D_{min} and D_{max} are the smallest and largest particle sizes (μm), which are 0.4 and 4000 μm, respectively. q is the distribution modulus, and a larger q results in a coarser mixture. In order to achieve a targeted strength as well as a low density of LWAC, a relatively large q is chosen as 0.35 for all mixtures. The PSDs of the target curve and the resulting integral grading curve (designed curve) of the mixture are shown in Figure 1.

Table 5. Mix proportions of LWAC (unit: kg/m3)

No.	C	LWA-1	LWA-2	LWA-3	LWA-4	LWA-5	W	SP	Coir fibers (wt.%)
F0 (Ref)	526.7	85.1	32.3	41.2	43.9	60.9	210.7	0.8	0.0%
F0.5	524.1	84.6	32.1	41.0	43.7	60.6	209.6	1.0	0.5%
F1.5	518.8	83.8	31.8	40.6	43.3	60.0	207.5	2.3	1.5%
F1.5-Ca	518.8	83.8	31.8	40.6	43.3	60.0	207.5	2.3	1.5%
F1.5-Si	518.8	83.8	31.8	40.6	43.3	60.0	207.5	2.3	1.5%
F3	510.9	82.5	31.3	40.0	42.6	59.1	204.4	4.1	3.0%

To avoid segregating without deteriorating the workability of the mixes, a water/cement ratio is fixed at 0.4. The dosages of coir fibers are 0.5%, 1.5%, and 3%, respectively, by weight of the concrete (including cement and LWAs). Meanwhile, a polycarboxylic ether based superplasticizer (SP) is adopted to adjust the workability of concrete, and all slumps of concrete are controlled under about 140 mm. According to the adopted fiber contents, the amounts of SP are 0.2%, 0.45%, 0.8% by weight of the cement to remedy the workability loss caused by adding fibers. For the reference mixture without fibers, the SP amount is used as 0.15%.

The mixing procedures are carried out as descripted below. Cement and LWAs are firstly put in a mixer for dry mixing about 1 min. Then around 75% water is gradually added and mixed with the cement and LWAs for about 2 min, meanwhile coir fibers are consistently fed. Subsequently, the remaining water mixed with SP is added and mixed for an additional 2 min. The fresh concrete are poured into the molds and vibrated for about 1 min with a vibration table, then its surface is covered with a plastic film. After the first 24 h, the samples are demolded and cured in a climate chamber at a temperature of 20 °C and a relative humidity of 95%, following EN 12390-2:2000.

2.2.2 Compressive properties

The compressive strength is measured under load control by an Automax 5 Automatic tester, following EN 196-1. The loading speed used is 2400 N/s. Samples with a dimension of 40 x 40 x 40 mm³ are tested at the

ages of 3, 7 and 28 days. In total, six samples are measured at each age to obtain the average compressive strength.

2.2.3 Flexural properties

The flexural properties are measured under three-points bending combined with displacement control with an Instron 5967 universal testing machine, following the EN 196-1. The span support adopted is 100mm and the mid-span deflection rate applied is 0.5 mm/min. Samples with a dimension of 160 x 40 x 40 mm^3 are tested at the ages of 3, 7 and 28 days. At least three samples are measured at each age for calculating the average flexural strength.

The flexural strength can be determined from the ultimate load:

$$\sigma = \frac{3FL}{2bh^2} \quad (3)$$

where F is the ultimate concentrated load, L is the span length; b and h are the width and height of samples.

The flexural toughness, expressing the energy absorption capacity of a material, can be calculated from the area under the load-deflection curves:

$$T_f = \int_0^{\delta_u} F(\delta) d\delta \quad (4)$$

where δu is the maximum deflection, generally about 10 mm in this study.

2.2.4 Drying and autogenous shrinkage

Both the drying and autogenous shrinkage tests are conducted on samples of 160 x 40 x 40 mm^3. After 24 h sealed curing, the specimens are demolded for shrinkage tests and additionally, the specimens for autogenous shrinkage test are immediately sealed with a hydrophobic plastic film to avoid moisture loss. The zero-time of measurement is defined as the demolding time for both shrinkages. The initial length of all samples is straightway measured by a dial gauge, then the followed length is measured once per working day until 28 days and three times a week until 56 days. Totally, three specimens are tested to obtain the average values of the two shrinkages.

3. Results and discussion

3.1 Compressive strength

The compressive strength of LWAC is shown in Figure 5. The compressive strength of LWAC slightly increases by adding coir fibers, while decreases with the increased coir fiber content. The 28-day compressive strength of the reference sample is 19.0 MPa and those of mixtures with 0.5% and 1.5% coir fibers are 21.6 MPa and 19.8 MPa, respectively, corresponding to an approximately 14%, and 5% increase. This is because of the bridging effect of coir fibers. Coir fibers retard the cracks propagation and bridge the matrix from rupture under compression, thus a larger force are required for concrete failure [39]. However, when the coir content further increases to 3%, no improvement is observed in compressive strength. The explanations seem to be related to the mixing procedure, the porous structure of fibers and the introduced ITZs between fibers and matrix. More fibers tend to cause fiber agglomeration during mixing thus has a negative effect on the compaction and homogeneity of mixture [40], leading to reduced bonding between fibers and matrix, and increased flaws in the mixture. In addition, due to the cellular structure of coir fibers, a higher fiber content leads to larger porosity in the mixture. Moreover, more weak ITZs are introduced which are easily subject to failure. Finally, the combined action from these factors deteriorates the compressive strength of the mixture.

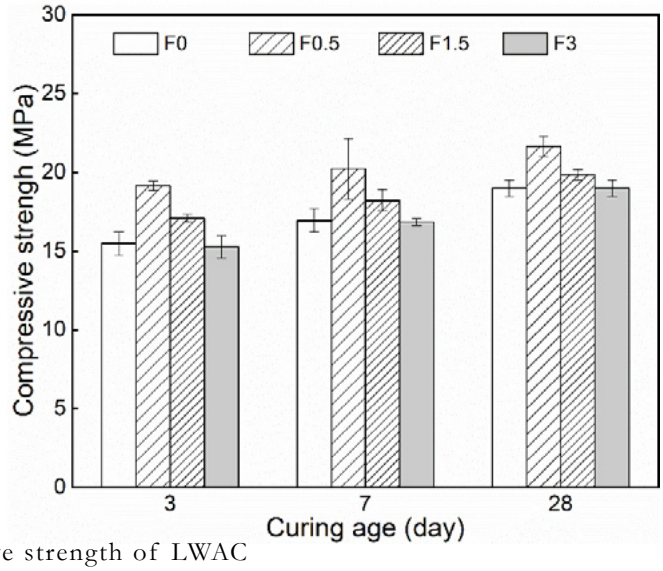

Figure 5: Compressive strength of LWAC

3.1 Flexural properties

The load–deflection curves are shown in Figure 6. The initial cracking strength significantly increases with improved fiber contents. After the initial cracking, a sharp drop in loads in all samples can be seen because of the reduced load-bearing capacities. Usually, a lower drop of loads occurs in the samples with a higher fiber content, while in the reference samples, the stress drops to zero directly. This is because of more active fibers, allowing improved tolerance to stress, thus higher residual strengths can be observed [41].

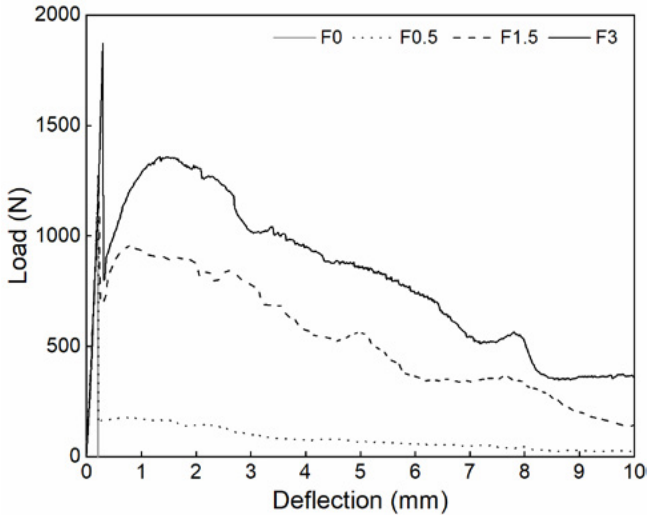

Figure 6: Average load–deflection curve of LWAC

The flexural strength of LWAC is shown in Figure 7. The flexural strength of LWAC significantly increases with an increased fiber content. The highest 28-day flexural strength of samples with 3% fibers is about 4 MPa, indicating an increase of about 70% as compared to the reference samples (2.6 MPa). The main explanation can be that a load applied can be transferred to coir fibers which are more tolerant to tension than cement matrix [42], and more fibers can bear a higher tensile stress for cement resulting in a higher flexural strength. The flexural strength of the samples with 1.5% fibers shows a negligible improvement compared to 0.5% fibers, since fibers can introduce additional defects into the matrix.

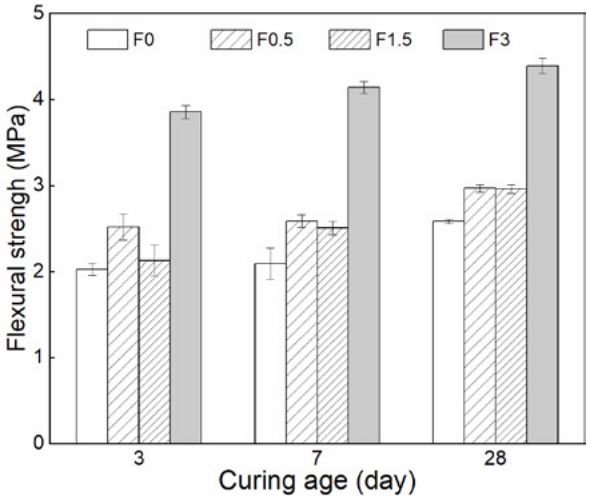

Figure 7: Flexural strength of LWAC

The flexural toughness of each mixtures is shown in Figure 8. The toughness is obviously enhanced by increasing the amount of fibers. The toughness of the sample with 3% fibers shows about 8 times increase than the reference sample. This is because the cracks extending acquires stretching, debonding and breaking of fibers [41,43], during which generates a considerable energy loss, contributing to increased fracture toughness.

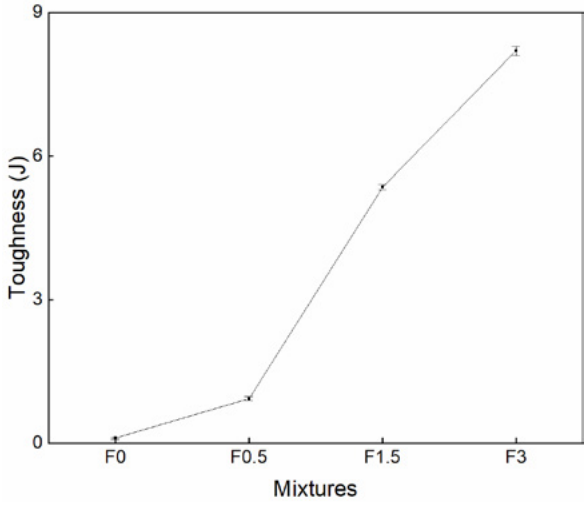

Figure 8: Flexural toughness curve of LWAC

3.2 Drying and autogenous shrinkages

Figure 9 shows the drying shrinkage development of concrete with coir fibers within 56 days. The drying shrinkage increases rapidly within the first two weeks, after which the growth of the shrinkage slows down since less water loss occurs in the later age. Moreover, the drying shrinkage notably rises by the increased fiber content. This behaviour can be firstly explained by the increased water introduced by more coir fibers in the system, which results in a higher amount of evaporated water loss, thus causing larger desiccative deformation. Another explanation is that coir fibers enlarge the porosity in the matrix and increase the connectivity of pores [44,45], which accelerates the drying process and consequently increases the drying shrinkage.

Figure 10 shows the autogenous shrinkage development in coir fibers reinforced concrete within 56 days. Most of the autogenous shrinkage is developed within the first week and then its intensity appears to

reduce because of subdued cement hydration. Coir fibers seem to result in a reduction in the autogenous shrinkage, and the increasing amount of fibers significantly decreases the autogenous shrinkage. This performance is due to the higher quantity of coir fibers contributing to sufficient internal curing water, which compensates for cement internal self-desiccation caused by chemical hydration [46] . As a result, a lower capillary pressure is induced, and thus less autogenous shrinkage is observable. Another reason is that fibers can sustain tensile strain and restrain cracking introduced by drying, and thus decrease the autogenous shrinkage of concrete. When the fiber content is set to 3%, the concrete exhibits a rapid expansion during the first day and continues showing a slight expansion during the whole period, therefore, the autogenous shrinkage of concrete is completely eliminated. This expansion is mostly because of the higher crystallization stress resulting from the increasing level of the oversaturated portlandite in solution caused by fiber leachates [47,48], which can entirely overwhelm the effect of self-desiccation resulting in almost no autogenous shrinkage. Therefore, when plenty of coir fibers are used, sufficient water can be introduced for internal curing in the cementitious matrix.

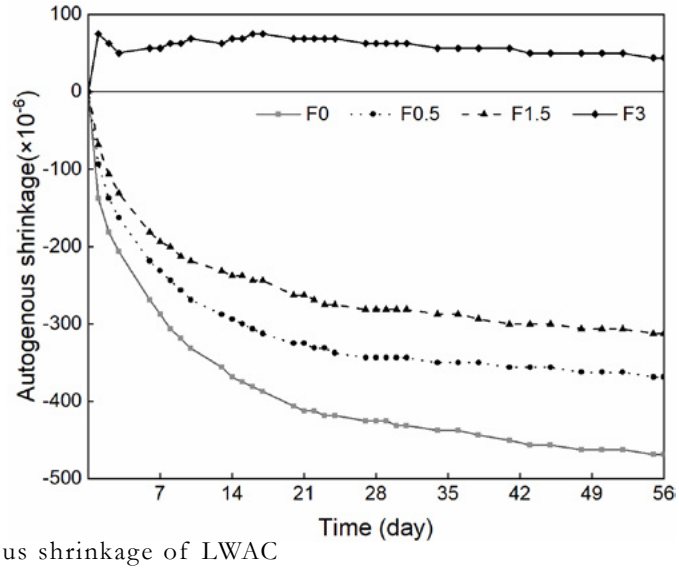

Figure 10: Autogenous shrinkage of LWAC

4. Conclusions

This paper presents the influences of coir fibers on the mechanical properties and shrinkages of cement-based LWAC. Based on the results obtained, the following conclusions can be drawn:

- The compressive strength of LWAC increases slightly by adding fibers but shows no improvement when the fiber fraction increases up to 3 %. This is caused by the porous structure of fibers and the more weak interfaces introduced by fibers.
- Both flexural strength and toughness increase significantly by increasing the fiber contents. It is resulting from the bridging effect of fibers, and more fibers in composite requires larger force and energy to develop cracks and to debond and break fibers.
- The drying shrinkage of concrete increases by increasing the coir fiber content. This is because of the extra water introduced by saturated fibers and improved connectivity of pores caused by porous fibers, resulting in accelerated drying process.
- The autogenous shrinkage markedly decreases as increasing fiber dosage. It is due to sufficient preserved water in fibers, providing internal curing for cement.
- When a sufficient content of coir fibers (i.e. in this study: 3 wt.%) is applied, fibers can be used for

internal curing.

5. Acknowledgment

This research was carried out under the fund of China Scholarship Council and Eindhoven University of Technology.

6. Reference

[1] M. Davraz, M. Koru, A.E. Akdağ, The effect of physical properties on thermal conductivity of lightweight aggregate, Procedia Earth Planet. Sci. 15 (2015) 85–92.

[2] H. Uysal, R. Demirboga, R. Şahin, R. Gül, The effects of different cement dosages, slumps, and pumice aggregate ratios on the thermal conductivity and density of concrete, Cem. Concr. Res. 34 (2004) 845–848.

[3] M.E. Dilli, H.N. Atahan, C. Şengül, A comparison of strength and elastic properties between conventional and lightweight structural concretes designed with expanded clay aggregates, Constr. Build. Mater. 101 (2015) 260–267.

[4] H.K. Kim, J.H. Jeon, H.K. Lee, Workability, and mechanical, acoustic and thermal properties of lightweight aggregate concrete with a high volume of entrained air, Constr. Build. Mater. 29 (2012) 193–200.

[5] O. Sengul, S. Azizi, F. Karaosmanoglu, M.A. Tasdemir, Effect of expanded perlite on the mechanical properties and thermal conductivity of lightweight concrete, Energy Build. 43 (2011) 671–676.

[6] O. Ünal, T. Uyguno□ lu, A. Yildiz, Investigation of properties of low-strength lightweight concrete for thermal insulation, Build. Environ. 42 (2007) 584–590.

[7] C. Tasdemir, O. Sengul, M.A. Tasdemir, A comparative study on the thermal conductivities and mechanical properties of lightweight concretes, Energy Build. 151 (2017) 469–475.

[8] R. Demirbo□ a, Thermal conductivity and compressive strength of concrete incorporation with mineral admixtures, Build. Environ. 42 (2007) 2467–2471.

[9] M.H. Zhang, L. Li, P. Paramasivam, Flexural toughness and impact resistance of steel-fibre-reinforced lightweight concrete, Mag. Concr. Res. 56 (2004) 251–262.

[10] G. Zi, S. Kim, J. Choi, S. Hino, K. Yamaguchi, Influence of fiber reinforcement on strength and toughness of all-lightweight concrete, Constr. Build. Mater. 69 (2014) 381–389.

[11] M. Chen, D. Law, M. Zhao, M. Zhao, J. Li, An experimental study on strength and toughness of steel fiber reinforced expanded-shale lightweight concrete, Constr. Build. Mater. 183 (2018) 493–501.

[12] J. Li, J. Niu, C. Wan, X. Liu, Z. Jin, Comparison of flexural property between high performance polypropylene fiber reinforced lightweight aggregate concrete and steel fiber reinforced lightweight aggregate concrete, Constr. Build. Mater. 157 (2017) 729–736.

[13] B. Chen, J. Liu, Contribution of hybrid fibers on the properties of the high-strength lightweight concrete having good workability, Cem. Concr. Res. 35 (2005) 913–917.

[14] M.A. Aziz, P. Paramasivam, S.L. Lee, Prospects for natural fibre reinforced concretes in construction, Int. J. Cem. Compos. Light. Concr. 3 (1981) 123–132.

[15] A.I. Al-mosawi, Natural Fiber as a substitute to Synthetic Fiber in Polymer Composites: A review, Res. J. Eng. Sci. 2(3) (2013) 46–53.

[16] S. Das, Life cycle assessment of carbon fiber-reinforced polymer composites, Int. J. Life Cycle Assess. 16 (2011) 268–282.

[17] S. Guler, The effect of polyamide fibers on the strength and toughness properties of structural lightweight aggregate concrete, Constr. Build. Mater. 173 (2018) 394–402.

[18] A.K. Mohanty, M. Misra, G. Hinrichsen, Biofibres, biodegradable polymers and biocomposites: An overview, Macromol. Mater. Eng. 276–277 (2000) 1–24.

[19] R. Dungani, M. Karina, Subyakto, A. Sulaeman, D. Hermawan, A. Hadiyane, Agricultural waste fibers towards sustainability and advanced utilization: A review, Asian J. Plant Sci. 15 (2016) 42–55.

[20] L.Y. Mwaikambo, Review of the history, properties and application of plant fibres, African J. Sci. Technol. 7 (2006) 120–133.

[21] A. Kicińska-Jakubowska, E. Bogacz, M. Zimniewska, Review of natural fibers. Part I-vegetable fibers, J. Nat. Fibers. 9 (2012) 150–167.

[22] R. wood Chang Hong, A Review on natural fibre-based Composites-Part I: structure, processing and properties of vegetable fibres, J. Nat. Fibers. 1 (2004) 37–41.

[23] S. Mukhopadhyay, S. Khatana, A review on the use of fibers in reinforced cementitious concrete, J. Ind. Text. 45 (2015) 239–264.

[24] C.A. Juarez, G. Fajardo, S. Monroy, A. Duran-Herrera, P. Valdez, C. Magniont, Comparative study between natural and PVA fibers to reduce plastic shrinkage cracking in cement-based composite, Constr. Build. Mater. 91 (2015) 164–170.

[25] P. Wambua, J. Ivens, I. Verpoest, Natural fibres: Can they replace glass in fibre reinforced plastics?, Compos. Sci. Technol. 63 (2003) 1259–1264.

[26] http://www.naturalfibres2009.org/en/fibres/coir.html, (n.d.).

[27] A. Komuraiah, N.S. Kumar, B.D. Prasad, Chemical composition of natural fibers and its influence on their mechanical properties, Mech. Compos. Mater. 50 (2014) 359–376.

[28] T.H. Nam, S. Ogihara, N.H. Tung, S. Kobayashi, Effect of alkali treatment on interfacial and mechanical properties of coir fiber reinforced poly(butylene succinate) biodegradable composites, Compos. Part B Eng. 42 (2011) 1648–1656.

[29] C. Hwang, V. Tran, J. Hong, Y. Hsieh, Effects of short coconut fiber on the mechanical properties , plastic cracking behavior , and impact resistance of cementitious composites, Constr. Build. Mater. 127 (2016) 984–992.

[30] M. Ali, A. Liu, H. Sou, N. Chouw, Mechanical and dynamic properties of coconut fibre reinforced concrete, Constr. Build. Mater. 30 (2012) 814–825.

[31] Z. Li, L. Wang, X. Wang, Flexural characteristics of coir fiber reinforced cementitious composites, Fibers Polym. 7 (2006) 286–294.

[32] V.M. John, M.A. Cincotto, C. Sjöström, V. Agopyan, C.T.A. Oliveira, Durability of slag mortar

reinforced with coconut fibre, Cem. Concr. Compos. 27 (2005) 565–574.

[33] B. Taallah, A. Guettala, The mechanical and physical properties of compressed earth block stabilized with lime and filled with untreated and alkali-treated date palm fibers, Constr. Build. Mater. 104 (2016) 52–62.

[34] V. Caprai, F. Gauvin, K. Schollbach, H.J.H. Brouwers, Influence of the spruce strands hygroscopic behaviour on the performances of wood-cement composites, Constr. Build. Mater. 166 (2018) 522–530.

[35] P. Jongvisuttisun, J. Leisen, K.E. Kurtis, Key mechanisms controlling internal curing performance of natural fibers, Cem. Concr. Res. 107 (2018) 206–220.

[36] V. Zanjani Zadeh, C.P. Bobko, Nano-mechanical properties of internally cured kenaf fiber reinforced concrete using nanoindentation, Cem. Concr. Compos. 52 (2014) 9–17.

[37] Q.L. Yu, P. Spiesz, H.J.H. Brouwers, Ultra-lightweight concrete: Conceptual design and performance evaluation, Cem. Concr. Compos. 61 (2015) 18–28.

[38] H.J.H. Brouwers, Packing fraction of particles with lognormal size distribution, 052211 (2014) 1–12.

[39] S. Yin, R. Tuladhar, F. Shi, M. Combe, T. Collister, N. Sivakugan, Use of macro plastic fibres in concrete : A review, Constr. Build. Mater. 93 (2015) 180–188.

[40] A.M. Brandt, Fibre reinforced cement-based (FRC) composites after over 40 years of development in building and civil engineering, Compos. Struct. 86 (2008) 3–9.

[41] H. Unwerstty, Models of fiber debonding and pullout in brittle composites with friction, Mechamcs Mater. 9 (1990) 139–163.

[42] C.X. Qian, P. Stroeven, Development of hybrid polypropylene-steel fibre-reinforced concrete, Cem. Concr. Res. 30 (2000) 63–69.

[43] C. Marotzke, L. Qiao, Interfacial crack propagation arising in siger-fiber pull-out tests, Compos. Sci. Technol. 57 (1997) 887–897.

[44] L.C. Roma, L.S. Martello, H. Savastano, Evaluation of mechanical, physical and thermal performance of cement-based tiles reinforced with vegetable fibers, Constr. Build. Mater. 22 (2008) 668–674.

[45] F. de A. Silva, R.D.T. Filho, J. de A.M. Filho, E. de M.R. Fairbairn, Physical and mechanical properties of durable sisal fiber-cement composites, Constr. Build. Mater. 24 (2010) 777–785.

[46] D.P. Bentz, O.M. Jensen, Mitigation strategies for autogenous shrinkage cracking, Cem. Concr. Compos. 26 (2004) 677–685.

[47] O.M. Jensen, P.F. Hansen, Water-entrained cement-based materials II. Experimental observation, Cem. Concr. Res. 32 (2002) 973–978.

[48] O.M. Jensen, P.F. Hansen, Water-entrained cement-based materials I. Principles and theoretical background, Cem. Concr. Res. 31 (2001) 647–654.

Super-hydrophobic magnesium oxychloride cement (MOC): from structural control to self-cleaning property evaluation

Z.Y. Qu[1,2*], F.Z. Wang[1], Q.L. Yu[2], H.J.H. Brouwers[1,2]

1State Key Laboratory of Silicate Materials for Architectures, Wuhan University of Technology, Wuhan 430070, PR China

2Department of the Built Environment, Eindhoven University of Technology, P.O. Box 513, 5600 MB Eindhoven,

Abstract

We report our study on designing a super hydrophobic magnesium oxychloride cement (MOC), applying a facile method involving immersion in a fluoroalkylsilane (FAS) -ethanol solution. We evaluate the super hydrophobicity and self-cleaning property of the new material and correlate them with the structural characteristics of the raw materials. The phase compositions, microstructure, compressive strength, water resistance and wetting behaviour are studied in detail by using X-Ray diffraction (XRD), scanning electron microscopy (SEM), a water contact angle measurement instrument, and mechanical testing. We observe a very high water contact angle of the as-prepared MOC up to about 152±1°, and we explain the derivation of water contact angle with the Cassie-Baxter model. The experiments using rolling off dust on the super hydrophobic surface present excellent self-cleaning ability. Moreover, the super hydrophobic surface presents excellent UV-durability, indicating a promising potential for outdoor application..

Keywords: Magnesium oxychloride cement, super hydrophobic, UV-durable, water-resistance, self-cleaning.

ICSBM 2019
ID 149

1. Introduction

Magnesium oxychloride cement (MOC) is a promising material thanks to its excellent materials properties such as fast setting, high mechanical strength, good resistance to abrasion and fire [1–5]. The behavior of MOC is mainly regulated by the composition and microstructure of the hydration products, produced through neutralization-hydrolysis-crystallization process in the ternary system of MgO–MgCl2–H2O [2,6]. Mg(OH)2·MgCl2·8H2O, or widely recognized as Phase 5 (P5), has been commonly recognized as the most desirable reaction product in MOC-based composites, as it is believed that the Phase 5 crystals can provide the best mechanical properties [3,5,6].

However, when exposed to water, Phase 5 will be easily decomposed to Mg(OH)2 that leads to a poor water resistance, which seriously restricts its outdoor applications. Preventing the water penetration by generating super-hydrophobic surfaces has already led to various new hybrid materials with astonishing properties [10–12]. A surface can be described as super hydrophobic if the contact angle (CA) of water on this surface is larger than 150° [13,14]. The best known example of super hydrophobic surface is the lotus leaf, on which water easily rolls off, leaving little or no residue and carrying away surface contamination, showing excellent self-cleaning properties [10,15]. Scanning electron microscopy (SEM) analysis shows that the surface of lotus leaves possesses protruding nubs of 20–40 μm apart each covered with a smaller

scale rough of epicuticular wax crystalloids [12]. This wax only consists of –C–H and –C–O group, which are the origin of the super hydrophobicity and self-cleaning property of the lotus leaf. Since Tsujii et al. first fabricated biomimetic surfaces in the mid-1990s, numerous smart and efficient methods for attaining rough surfaces to prepare super hydrophobic surface have been reported [12,16–18]. In summary, there are two main kinds of surface microstructures to prepare super hydrophobic surface: one is the hierarchical micro- and nanostructure like the lotus leaf and the other one is the unitary micro-line structure like the ramee leaf [19–22].

Considering the complexity of the preparation of micro-, nano-, and lotus-type micro-/ nanocomposite structures, unitary micro-line structure provides a facile solution to prepare super hydrophobic surfaces [13,23]. Ogawa et al. prepared super hydrophobic film-coated nano-fibrous membranes based on the inspiration of self-cleaning silver ragwort leaves [23]. After the modification with fluoroalkylsilane (FAS), the surface of the nano-fibrous membrane presented super hydrophobicity with the highest water contact angle of 162° and the lowest water-roll angle of 2° [23]. Li et al. reported a simple solution-immersion method to fabricate a super hydrophobic surface on a cellulose-based material (i.e. cotton fabric or paper) [24]. The surface morphology of the fabric provided ideal roughness for trapping the air to build a super hydrophobic surface [24]. Jiang et al. prepared $Cu(OH)_2$ nano-needle arrays presenting little contact-angle hysteresis, even under certain hydrostatic pressures, by a facile chemical-base deposition method [25]. The average length of the needles is 5 μm and the average diameter of the nano-needle is 300 nm [25]. The above results also inspired us to prepare super-hydrophobic and self-cleaning surface by taking advantages of the native needle structure of MOC. Until now, research about construction of superhydrophobic surface on MOC is still limited.

We aim to propose a novel and facile method for the fabrication of super hydrophobic surface on MOC by applying the unique needle-like structure Phase 5 of MOC. The compressive strength and water resistance of the MOC samples are studied. The phase composition and microstructural properties were determined by using X-ray diffraction (XRD) and scanning electron microscopy (SEM). The water-repellence ability was evaluated by performing the water contact angle and water sliding angle tests. As UV-durability property is crucial for practical outdoor use, which mainly depends on the surface chemical composition and surface structures, UV-durability of the as prepared surface was also examined. The results show that the designed super MOC surface possesses a super hydrophobic property, together with an excellent water-repellence and self-cleaning ability.

2. Methodology

2.1 Materials

We use the following raw materials to prepare the MOC cement paste: light-burnt magnesia powder (MgO), magnesium chloride hexahydrate (MgCl2·6H2O), and tap water. Triethoxy-1H,1H,2H,2H-tridecafluoro-n-octylsilane (FAS) and Ethanol is used to prepare a FAS-ethanol solution. The MOC samples are prepared by mixing MgO and the MgCl2·6H2O solution (see Table 1). Based on the mixed recipe, the samples are designated as MOC-510 (Mixture 1), MOC-68 (Mixture 2) and MOC-610 (Mixture 3). The samples are prepared following EN 196-1 [26] and cast in cubic moulds with dimensions of 40 × 40 × 40 mm^3 to determine the compressive strength. For the preparation of superhydrophobic MOC, after 48 hours' curing in the air, the MOC products are then placed in a FAS ethanol solution (5%) for 24 hours at room temperature and then dried for 1 hour.

2.2 Methods

The XRD analysis is performed by using a Bruker D8 advance powder X-ray diffractometer with a Cu tube

(20 kV, 30 mA) with a scanning range from 5° to 65° (2θ), applying a step 0.02° and 0.2 s/step measuring time. A contact angle meter DataPhysics SCA20 (DataPhysics Germany) is used to measure the static water contact angle and sliding angle with 10 µl water drop at the ambient temperature. The morphologies of the MOC are observed using a field emission scanning electron microscopy (FESEM) of Quanta 450 (FEI USA). The UV durability test under different environmental conditions is performed in a homemade set-up. MOC boards with the dimension of 20 cm × 10 cm× 5 cm are prepared for the UV durability test which fit the size of our reactor. The UVA light intensity E is kept constant at 14 W/m2 which is close to outdoor conditions during the summer [27].

3. Results and discussion

The XRD patterns of the MOCs show that the mineralogical phases consist of major Phase 5, minor $Mg(OH)_2$ and unreacted MgO and $MgCO_3$ (Fig. 1). As the Phase 5 is the most favourable crystalline phase [3,6], the molar ratio of $MgO/MgCl_2$ is desired to be higher than 5 and the molar ratio of $H2O/ MgCl_2$ is in the range of 6-15. The $MgCO_3$ is from the carbonation during the preparation process. It can be found that MOC-510 exhibits the weakest characteristic peaks of unreacted MgO in the paste matrices, because of the lower molar ratio of $MgO/MgCl_2$.

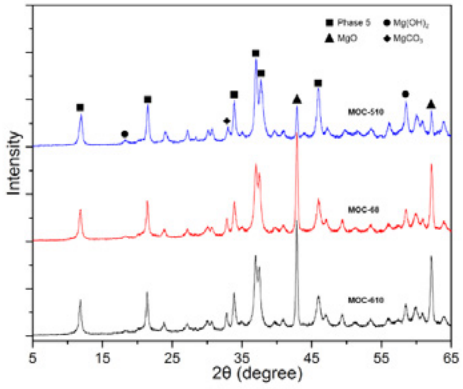

Fig. 1. XRD patterns of the MOCs at 28 days.

The SEM images (Fig. 2) show that all the samples present a composite structure consisting of needle-like Phase 5 and gel-like Phase 5.

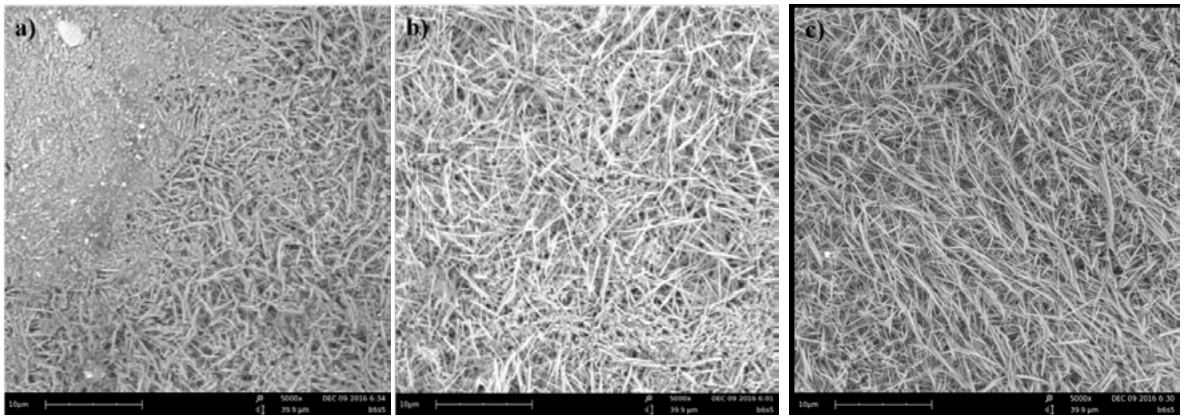

Fig. 2. SEM images of paste matrices of: (a) MOC-510, (b) MOC-68, (c) MOC-610.

It can be seen that MOC-510 presents more gel-like Phase 5 compared to the other two samples. This can be attributed to the smaller amount of MgO in the reaction system. As stated in [3] and [6], MgO could act as a role of reaction seeds, which in turn increase the reaction sites in the MOC hydrated process. So

less MgO seeds would increase the possibility of group growth of the MOC, which leads to more gel-like Phase 5. MOC-610 exhibits more needle-like Phase 5 than MOC-68 as shown in Fig. 2b and Fig. 2c, which is attributed to the lower MgCl2 concentration in MOC-610.

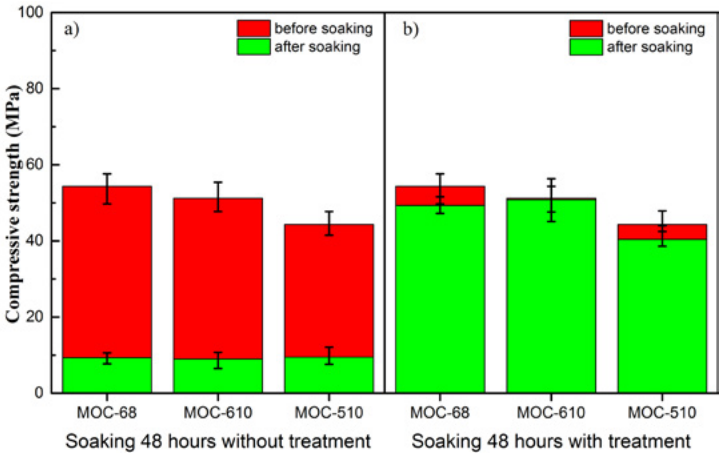

Fig. 3. Comparison between compressive strength of the MOCs before and after 48 hours' soaking: a) without FAS treatment and b) with FAS treatment.

The water resistance improvement of MOC after super hydrophobic modification can be seen from the compressive strength changes after soaking the samples for 48 hours (see Fig. 3). The retention of compressive strengths of unmodified MOC-68, MOC-610 and MOC-510 are only 17.1%, 17.6% and 21.4%, respectively, caused by the decomposition of the hydration products into Mg(OH)2 [6][30]. It should be noted that the compressive strength retention of MOC-510 is higher than the other two samples, attributed to its more gel-like Phase 5. Owing to the super hydrophobicity, all of the MOC samples have a much higher compressive strength retention than the unmodified samples. The compressive strength retentions of MOC 68, MOC-610 and MOC-510 after soaking 48 hours are 91.3%, 99% and 91.2%, respectively, indicating the hydrophobic treatment is highly effective to improve the water resistance of MOC.

All unmodified MOC samples present high hydrophilic property and the water drop penetrate inside the MOC sample very quickly and no water contact angles were able to be tested. After FAS modification, as shown in Fig. 4a, the MOC-510 has a water contact angle about 130°, indicating a hydrophobic property [12,13]. After the increase of the MgO content, the CA of the MOC-610 increased to about 152°, indicating that the MOC surface becomes super hydrophobic. On the contrary, the water repellence of MOC-68 decreases and the CA decreases to about 143° after decreasing the amount of MgO. The change of the surface microstructures (Fig. 2(a–c)) was responsible for the increase of CA. This can be explained by the ideal Young equation [27,31,32] and the Cassie-Baxter equation [33,34]. A rougher surface will lead to a larger contact angle and more hydrophobic behaviour [33,34]. When gel-like Phase 5 is generated among the needle-like structure, it will fill in the interspace that in turn decreases the air amount for air trapping. This can be used to explain the decrease of super hydrophobic ability from MOC-610 to MOC-510 as the amount gel-like Phase 5 increases.

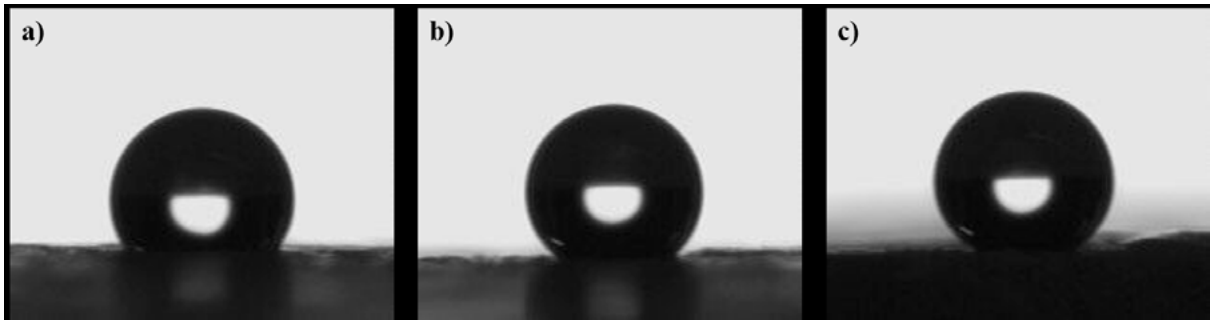

Fig. 4. Water contact angle of: (a) the MOC-510, 130°±1°. (b) the MOC-68, 143°±1°. (c) the MOC-610, 152±1°.

Barthlott et al. reported that water droplets can roll off from the lotus leaves and remove the dust particles [35]. As MOC products are often used for a decorative purpose (e.g. decoration boards), it will be very meaningful for MOC possessing the self-cleaning ability. Fig. 5a shows the results of rolling water on the super hydrophobic MOC surface (MOC-610). UV-resistivity is crucial for practical outdoor applications, which mainly depends on the surface chemical composition and surface structures [36–38]. The static contact angle and sliding angle as a function of UV-irradiation time are presented in Fig. 5c. It is shown that after 7 days' UV irradiation, the surface still exhibits a contact angle of 152.1° and a sliding angle of 8° at 25℃ and 50% humidity and a contact angle of 152.8° and a sliding angle of 9° at higher temperature. Even under a higher humidity, the MOC surface presents a contact angle of 152.3° and a sliding angle of 8 °, suggesting a superior UV-durability. This can be attributed to both the properties of the MOC and the low surface energy of FAS.

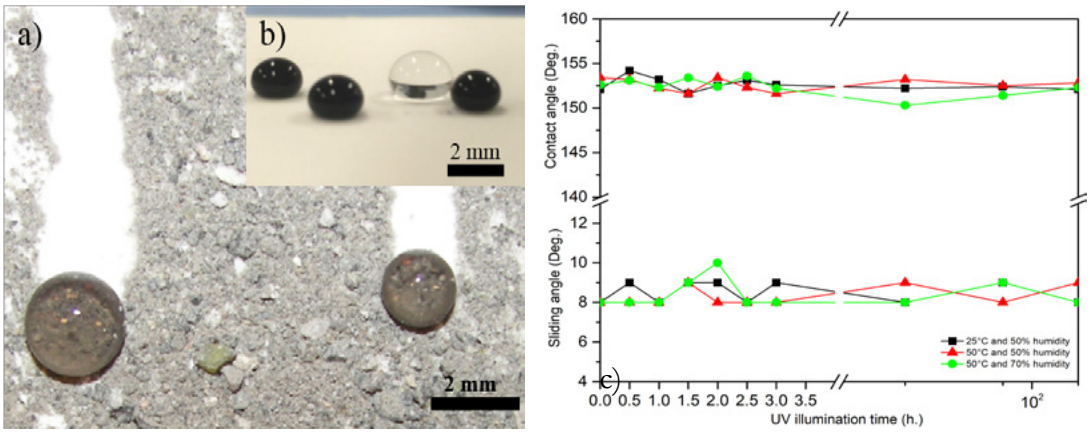

Fig. 5. Assessment of the hydrophobicity and self-cleaning ability by: (a) the rolling of particles, and (b) blue ink and water drops on the sample surface; and (c) Contact angle and sliding angle of MOC-68 samples over UV-irradiation time under different environmental conditions.

4. Conclusions

A super hydrophobic MOC surface with excellent self-cleaning ability is fabricated applying a facile solution immersion method with FAS. The influences of the molar ratio on the microstructures, compressive strength, water resistance and hydrophobic performance are investigated. The self-cleaning ability and UV-durability are characterized. Through the control of the MgO/MgCl2 and H2O/MgCl2 molar ratios, MOC samples with different microstructures are acquired. From the XRD and SEM results, it can be concluded that MOC-510 exhibits a higher amount of gel-like Phase 5 and MOC-610 presents a higher amount of nano-needle like Phase 5. The hydrophobic treatment improves the water resistance of the MOC samples. The compressive strength retentions after 48 hours' water soaking of MOC-510, MOC-68 and MOC-610 are only 17.1%, 17.6% and 21.4%, respectively, before the modification by FAS. However,

the compressive strength retentions increase to 91.3%, 99% and 91.2%, respectively, after the hydrophobic treatment. Owing to the large amount of nano-needle like Phase 5 structures, MOC-610 is found to be the optimum recipe for the super hydrophobic surface fabrication, having a water contact angle of 152°±1°. The prepared super hydrophobic surface presents an excellent self-cleaning ability. Moreover, the super hydrophobic MOC surface is highly durable under UV irradiation.

5. Acknowledgment

The authors would like to acknowledge the financial support by STW-foundation and the EPSRC-NSFC Joint Research Project (No. 51461135005) for funding this research. Mrs. A.C.A. Delsing in the lab of Building Physics and Services at Eindhoven University of Technology is acknowledged for providing experimental support on the SEM analysis.

6. References

[1] B. Xu, H. Ma, C. Hu, S. Yang, Z. Li, Influence of curing regimes on mechanical properties of magnesium oxychloride cement-based composites, Constr. Build. Mater. 102 (2016) 613–619.

[2] D. Dehua, Z. Chuanmei, The formation mechanism of the hydrate phases in magnesium oxychloride cement, Cem. Concr. Res. 29 (1999) 1365–1371.

[3] Z. Li, C.K. Chau, Influence of molar ratios on properties of magnesium oxychloride cement, Cem. Concr. Res. 37 (2007) 866–870.

[4] Z. Liu, M. Balonis, J. Huang, A. Sha, G. Sant, The influence of composition and temperature on hydrated phase assemblages in magnesium oxychloride cements, J. Am. Ceram. Soc. 100 (2017) 3246–3261.

[5] Z. Liu, S. Wang, J. Huang, Z. Wei, B. Guan, J. Fang, Experimental investigation on the properties and microstructure of magnesium oxychloride cement prepared with caustic magnesite and dolomite, Constr. Build. Mater. 85 (2015) 247–255.

[6] Y. Li, Z. Li, H. Pei, H. Yu, The influence of FeSO4 and KH2PO4 on the performance of magnesium oxychloride cement, Constr. Build. Mater. 102 (2016) 233–238.

[7] C.K. Chau, J. Chan, Z. Li, Influences of fly ash on magnesium oxychloride mortar, Cem. Concr. Compos. 31 (2009) 250–254.

[8] D. Deng, The mechanism for soluble phosphates to improve the water resistance of magnesium oxychloride cement, Cem. Concr. Res. 33 (2003) 1311–1317.

[9] C. Li, H. Yu, Influence of fly ash and silica fume on water-resistant property of magnesium oxychloride cement, J. Wuhan Univ. Technol. Sci. Ed. 25 (2010) 721–724.

[10] S. Grumbein, D. Minev, M. Tallawi, K. Boettcher, F. Prade, F. Pfeiffer, C.U. Grosse, O. Lieleg, Hydrophobic Properties of Biofilm-Enriched Hybrid Mortar, Adv. Mater. 28 (2016) 8138–8143.

[11] P.A. Levkin, F. Svec, J.M.J. Fréchet, Porous polymer coatings: a versatile approach to superhydrophobic surfaces, Adv. Funct. Mater. 19 (2009) 1993–1998.

[12] Z. Guo, W. Liu, B.-L. Su, Superhydrophobic surfaces: from natural to biomimetic to functional, J. Colloid Interface Sci. 353 (2011) 335–355.

[13] L. Jiang, Y. Zhao, J. Zhai, A lotus-leaf-like superhydrophobic surface: a porous microsphere/nanofiber composite film prepared by electrohydrodynamics, Angew. Chemie. 116 (2004) 4438–4441.

[14] H.Y. Erbil, A.L. Demirel, Y. Avcı, O. Mert, Transformation of a simple plastic into a superhydrophobic surface, Science (80-.). 299 (2003) 1377–1380.

[15] A.V. Rao, M.M. Kulkarni, S.D. Bhagat, Transport of liquids using superhydrophobic aerogels, J. Colloid Interface Sci. 285 (2005) 413–418.

[16] E. Celia, T. Darmanin, E.T. de Givenchy, S. Amigoni, F. Guittard, Recent advances in designing superhydrophobic surfaces, J. Colloid Interface Sci. 402 (2013) 1–18.

[17] M. Horgnies, J.J. Chen, Superhydrophobic concrete surfaces with integrated microtexture, Cem. Concr. Compos. 52 (2014) 81–90.

[18] I. Flores-Vivian, V. Hejazi, M.I. Kozhukhova, M. Nosonovsky, K. Sobolev, Self-assembling particle-siloxane coatings for superhydrophobic concrete, ACS Appl. Mater. Interfaces. 5 (2013) 13284–13294.

[19] Z. Guo, W. Liu, Biomimic from the superhydrophobic plant leaves in nature: Binary structure and unitary structure, Plant Sci. 172 (2007) 1103–1112.

[20] M. Nosonovsky, B. Bhushan, Biomimetic superhydrophobic surfaces: multiscale approach, Nano Lett. 7 (2007) 2633–2637.

[21] J.-Y. Shiu, C.-W. Kuo, P. Chen, C.-Y. Mou, Fabrication of tunable superhydrophobic surfaces by nanosphere lithography, Chem. Mater. 16 (2004) 561–564.

[22] J.B. Boreyko, C.-H. Chen, Self-propelled dropwise condensate on superhydrophobic surfaces, Phys. Rev. Lett. 103 (2009) 184501.

[23] T. Ogawa, B. Ding, Y. Sone, S. Shiratori, Super-hydrophobic surfaces of layer-by-layer structured film-coated electrospun nanofibrous membranes, Nanotechnology. 18 (2007) 165607.

[24] S. Li, S. Zhang, X. Wang, Fabrication of superhydrophobic cellulose-based materials through a solution-immersion process, Langmuir. 24 (2008) 5585–5590.

[25] X. Yao, Q. Chen, L. Xu, Q. Li, Y. Song, X. Gao, D. Quéré, L. Jiang, Bioinspired ribbed nanoneedles with robust superhydrophobicity, Adv. Funct. Mater. 20 (2010) 656–662.

[26] T.S. EN, 196-1, Methods Test. Cem. 1 (2006).

[27] X. Zhang, F. Shi, J. Niu, Y. Jiang, Z. Wang, Superhydrophobic surfaces: from structural control to functional application, J. Mater. Chem. 18 (2008) 621–633.

[28] D. Dehua, Z. Chuanmei, The effect of aluminate minerals on the phases in magnesium oxychloride cement, Cem. Concr. Res. 26 (1996) 1203–1211.

[29] Y. Li, H. Yu, L. Zheng, J. Wen, C. Wu, Y. Tan, Compressive strength of fly ash magnesium oxychloride cement containing granite wastes, Constr. Build. Mater. 38 (2013) 1–7.

[30] J.J. Beaudoin, V.S. Ramachandran, Strength development in magnesium oxychloride and other cements, Cem. Concr. Res. 5 (1975) 617–630.

[31] W. Li, A. Amirfazli, Hierarchical structures for natural superhydrophobic surfaces, Soft Matter. 4 (2008) 462–466.

[32] F. Dong, M. Zhang, W.-W. Tang, Y. Wang, Formation and mechanism of superhydrophobic/hydrophobic surfaces made from amphiphiles through droplet-mediated evaporation-induced self-assembly,

J. Phys. Chem. B. 119 (2015) 5321–5327.

[33] A. Marmur, Wetting on hydrophobic rough surfaces: to be heterogeneous or not to be?, Langmuir. 19 (2003) 8343–8348.

[34] A. Marmur, The lotus effect: superhydrophobicity and metastability, Langmuir. 20 (2004) 3517–3519.

[35] C. Neinhuis, W. Barthlott, Characterization and distribution of water-repellent, self-cleaning plant surfaces, Ann. Bot. 79 (1997) 667–677.

[36] N. Wang, D. Xiong, Y. Deng, Y. Shi, K. Wang, Mechanically robust superhydrophobic steel surface with anti-icing, UV-durability, and corrosion resistance properties, ACS Appl. Mater. Interfaces. 7 (2015) 6260–6272.

[37] M. Manca, A. Cannavale, L. De Marco, A.S. Arico, R. Cingolani, G. Gigli, Durable superhydrophobic and antireflective surfaces by trimethylsilanized silica nanoparticles-based sol− gel processing, Langmuir. 25 (2009) 6357–6362.

[38] T. Verho, C. Bower, P. Andrew, S. Franssila, O. Ikkala, R.H.A. Ras, Mechanically durable superhydrophobic surfaces, Adv. Mater. 23 (2011) 673–678.

[39] M. Miwa, A. Nakajima, A. Fujishima, K. Hashimoto, T. Watanabe, Effects of the surface roughness on sliding angles of water droplets on superhydrophobic surfaces, Langmuir. 16 (2000) 5754–5760.

[40] R. Fürstner, W. Barthlott, C. Neinhuis, P. Walzel, Wetting and self-cleaning properties of artificial superhydrophobic surfaces, Langmuir. 21 (2005) 956–961.

Durability of photocatalytic mortars

A.M. Kaja[1], H.J.H. Brouwers[1], Q.L. Yu[1]

[1]Department of the Built Environment, Eindhoven, University of Technology Eindhoven, 5600 MB, the Netherlands.

Abstract

Photocatalytic technology attracts great attention due to the increasing need to improve air quality, especially in highly polluted urban areas. Concrete is found to be an excellent substrate for photocatalytic processes due to its high availability and exposure of large surfaces to solar irradiation. The presence of semiconductors in the concrete surface layer induces the oxidation of air pollutants. For example, NO and NO_2 can be photocatalytically oxidized to nitrates, which are later removed from the concrete surface with rainwater. Among the available semiconductors, titania is the most commonly used. TiO_2 nanoparticles can be either coated on the concrete surface or intermixed with cement in concrete surface layer. Simple coating, however, does not result in sufficient durability. On the other hand, even if titania is intermixed with cement, some durability aspects like carbonation cannot be avoided. This study aims to evaluate the impact of carbonation on the photocatalytic efficiency of white cement-based photocatalytic mortars doped with three types of titania photocatalysts (Aeroxide TiO_2 P25, KRONOclean 7000 carbon doped titania, and one home-synthesized composite photocatalyst consisting of 85% of SiO_2 and 15% of TiO_2). The study revealed that the oxidation of the pollutants by photocatalytic mortars dramatically depends on the type of photocatalyst. Silica-titania composite exhibits equally high performance as P25 providing the alternative route for the costs reduction during the manufacture of photocatalytic concrete. Upon carbonation, a drastic decrease of photocatalytic efficiency occurs regardless of the type of photocatalysts used. This effect is intensified when photocatalyst forms agglomerates. The selectivity of the photocatalytic reaction is also lowered after carbonation.

Keywords: Photocatalytic mortar, carbonation, photocatalytic efficiency, selectivity.

Self-cleaning and air purification performance of Portland cement paste with low dosage of nanodispersed TiO_2 coatings

Z. Wang[1, 2 *], F. Gauvin[2], P. Feng[1], H.J.H. Brouwers[2], Q.L. Yu[2]

[1] School of Materials Science and Engineering, Southeast University, Nanjing 211189, China, Email: z.wang3@tue.nl

[2] Department of the Built Environment, Eindhoven University of Technology, P.O. Box 513, 5600 MB Eindhoven, The Netherlands

ICSBM 2019
ID 159

Abstract

In this study, a stable and nano dispersed anatase TiO_2 hydrosol was synthesized by hydrolysis of titanium isopropoxide at low temperatures. The self-cleaning and depollution performance of Portland cement paste at early age with TiO_2 hydrosols were investigated with different dosages. According to the results, the average hydraulic diameter of TiO_2 particles in aqueous solution was about 19 nm and the zeta potential was higher than +30 mV, which indicating this nanodispersed TiO_2 hydrosol can be easily dispersed in water evenly without producing agglomeration. The self-cleaning and air purification properties of TiO_2 hydrosols coated cement paste were evaluated by the photodegradation of Rhodamine B (RB) and NO_X under the UV light over different irradiating time after 7 days of hydration. The RB colour change rates of cement samples coated TiO_2 hydrosol tested by spectrometer was more than 90% after 2640 min UV irradiation, which was 1.5 times as higher than that of cement paste coated with P25 at the same dosage and test conditions. The NO conversion (>97%) of TiO_2 hydrosol coatings and P25 coatings were similar at the lower dosage, while the TiO_2 hydrosol coatings presented better NO conversion effect than P25 at higher surface concentration. These differences may relate to the better dispersion and greater specific surface area of TiO_2 nano particles in the form of hydrosols. Due to the high self-cleaning, air purification and solar reflectance of TiO_2 hydrosol coatings on the surface of Portland cement paste, the nano dispersed TiO_2 hydrosols provide a low cost, low-energy consumption, high efficient and convenient choice to form the protective and self-cleaning layer on the surface of concrete structures.

Keywords: Nano dispersed TiO_2 hydrosol, Air purification performance, Self-cleaning coatings, Portland cementitious materials

1. Introduction

Cementitious materials in buildings are directly and continuously exposed to many atmospheric and organic pollutants, microorganisms under different weather conditions. Colour, the main index of aesthetic properties of buildings, has to give a pleasant appearance that should give to the public an adequate perception of the quality and maintenance. The main cause of colour change on the surface of cementitious materials is the reduction in initial solar reflectivity, mainly from atmospheric aerosol pollutants such as nitrogen oxides, carbon-based materials and volatile organic compounds [1,2]. Titanium-based photocatalysis has proven to be a promising technology for the efficient degradation of a range of organic compounds and some

inorganic compounds (NO_x and SO_2), in busy canyon streets, road tunnels, urban environments, etc [3]. In addition, the combination of TiO_2 and cement-based products have some synergistic advantages because the reaction product can be adsorbed on the surface and then washed away by rain [4]. Furthermore, when TiO_2 is activated by solar photons, holes diffuse to the surface and react with water molecules adsorbed on the surface to generate hydroxyl radicals, thereby increasing the number of hydroxyl groups on the surface of TiO_2 during irradiation [5]. Therefore, during irradiation, the contact angle of the surface of TiO_2 with water molecules is gradually close to zero. This phenomenon is called light-induced super-hydrophilicity, which present as the self-cleaning performance of the TiO_2 coated surfaces. Thus, TiO_2 could be used to increase the life cycle of cement-based materials while it could also substantially decrease the concentration of some air pollutants and enhance the self-cleaning property.

In most of the studies [6–9], the commercially available nano TiO_2 powder (Degussa P-25) was studied either as concrete coatings to improve its photocatalytic activity. The inherent agglomeration and very poor dispersity of nano TiO_2 powders in aqueous system caused by the calcination in synthetic process maybe the biggest holdback in making photocatalytic and self-cleaning cement-based materials. The nanodispersed TiO_2 hydrosols are usually synthesized by the sol–gel process of titanium alkoxide precursors [10–12], where the solvent is water, in large excess with respect to the alkoxide [13–19]. The acids are used as peptizator and produce a colloidal suspension containing TiO_2 particles with size ranges from 15 to 100 nm. This route is a cheap and low-energy consumption method to obtain anatase and well-dispersed nano TiO_2 particles. Moreover, the good dispersity of nano TiO_2 particles in coatings is the critical point of self-cleaning and photocatalytic performances, because the photodegrading reactions between pollutants and coatings occur on the surface of TiO_2 particles and the stable dispersion of nano TiO_2 particles in coatings can provide more reaction areas because of the greater specific surface areas [20]. In nano dispersed TiO_2 hydrosol can be considered as the water was divided by the nano TiO_2 particles evenly. According to the definition of specific surface area, which is the surface area of an object per unit volume (or per mass), the surface area of TiO_2 particles (for example the particle size is 10 nm and mass content is 1% of hydrosol) in 1 g hydrosol is more than 1×10^5 m^2/g. Compared with the specific surface area of the P25 powders (about $50g/m^2$), the specific surface area of nano TiO_2 in hydrosol is super huge that indicates the surge of surface energy, and the surface characteristics of the system, such as adsorption, double-layer effect, and chemical reaction performance become more prominent.

In this study, the self-cleaning and photocatalytic performance of cement paste with anatase and well dispersed TiO_2 hydrosols coatings synthesized at low temperatures were studied at 7 days age. The commercial nano powder P25 suspension was selected as the reference coating. The self-cleaning properties and photocatalytic performance enhancement of TiO_2 hydrosol was also discussed via optical analysis.

2. Materials and experimental

2.1 Materials

Titanium tetra-isopropoxide (TTIP, 97.0%) was purchased from Sigma-Aldrich. Acetic acid glacial (99.6%), absolute ethanol (99.9%), were purchased from VWR Chemicals. Deionized water (18.2 MΩ.cm) was used throughout the preparation process of TiO_2 hydrosol. The method anatase TiO_2 hydrosols was referred from literatures [21][14], and the different synthesis temperatures were carried out. The synthesis was as follows: TTIP was dissolved in absolute ethanol with the TTIP/ethanol molar ratio of 2.44, and then the solution was stirred for 30 min at different temperatures (50 °C and 40 °C). Then, the obtained solution was added dropwise of the speed 0.01 mL/s into a mixture containing acetic acid and deionized water with the molar ratio of 0.175. After that, the suspension was continually stirred for 48 h at 50 °C or 40 °C, and then aged for at least 72 h at room temperature to produce a translucent sol.

In preparing cement paste, CEM I 52.5R cement and tap water were used and the water to cement ratio was 0.4. The samples were wet-mixed for four minutes before moulded in 40 mm× 40 mm× 40 mm moulds and 100 mm× 200 mm× 5 mm, and then the samples were covered with plastic sheets. After 1 day curing (20 °C/60% RH), the samples were demoulded and cured in ambient until test ages.

2.2 Methods

2.2.1 Particle size and zeta potential

The particle size distribution and zeta potential of TiO_2 hydrosol were tested by the Zetasizer NanoSeries (Malvern Panalytical) at 25 °C. In these tests, the initial hydrosol was diluted 100 times in distilled water. The TiO_2 hydrosol samples were tested three times by Zetasizer Nano Series by using a process called Dynamic Light scattering (DLS). The Zetasizer Nano Series calculated the zeta potential by determining the electrophoretic mobility and then applying the Herny equation.

2.2.2 XRD pattern analysis

The phase composition of TiO_2 hydrosol dried at 105 °C were investigated by comparing X-ray diffraction (XRD) pattern (Bruker D4 PHASER, Philips, The Netherlands) with a Co tube (40 kV, 40mA). A typical run was made with a step size of 0.02°/min and a dwell time of 0.5s.

2.2.3 UV-VIS absorbance and UV-VIS-NIR reflectance

The UV-VIS absorbance spectrum of TiO_2 hydrosol and P25 suspension samples was measured by the UV-VIS-NIR spectrophotometer (Perkin Elmer Lambda 750), the tested range was 250 nm to 800 nm, 1 nm per second. For the reflectance test of cement paste coated with different coatings, the TiO_2 hydrosol and P25 suspension coatings with the solid content of 1.54% were applied on the surface of paste samples after 28 days hydration. Due to the Beer–Lambert law, the samples content should lower than 0.01M and the absorbance should below 1.0, in this test the P25 suspension sample was diluted down to 0.02 % and the TiO_2 hydrosol sample was diluted down to 1.0 % by distilled water.

2.2.4 Self-cleaning performance

The self-cleaning performance of the cubic coated cement paste was evaluated by colorimetric analysis of the degradation of the organic dye Rhodamine B (RB). Before tests, the paste top surfaces were polished by SiC sand papers to obtain relative smooth surface with the roughness in the range of 10 to 14 micrometres. Each surface area of paste samples was stained by painting 600 uL of 0.1 mM RB aqueous solution. Then the samples were kept overnight in dark box at room temperature for drying. For each coated sample, 9 points were considered for the colorimetric tests and each point was tested for 4 times. The samples were exposed to a UV lamp (10±0.05 W/m^2) to simulate UV light in natural conditions, monitoring the discoloration of the stains.

The reflected colour measurements were taken directly on the surface of each points on each sample at different illumination with a spectrometer USB4000 Oceanoptics, which optimized for the 380- 780 nm wavelength range and analysed mathematically to yield colorimetric quantities like xyz, RGB or L*a*b*. In this study, the percentage of discoloration (R_t) was expressed with the coordinate of the dominant colour of dye a*, value of the CIE Lab colour space for RB [22,23][24], according to Eq. (1).

$$R_t(\%) = \frac{a_0^* - a_t^*}{a_0^*} \times 100 \quad (1)$$

Where, a_0^* the value of a* at time 0 before irradiation, a_t^* its value after t minutes irradiation.

2.2.5 Air purification performance

The air purification experiments [8,9,25,26] of coated cement paste were carried out in a homemade reactor designed in accordance with standard ISO 22197-1. The experimental setup consisted of a planar reactor cell, an UVA light source, a chemiluminescent NO_x analyser, and a gas supply. The main operating conditions of the system were as follows: the wavelength of UV light resource was 300-400 nm, the irradiance flux on the surface of cement paste samples was 10 ± 0.05 W/m^2, the pollutant source concentration was 1.0 ppm, the NO flow and air flow were 60 mL/min and 2.94 L/min, and the total gas flow was 3.0 L/min, the relative humidity in the reactor was 50 ± 1%. The concentration of TiO_2 particles in two coatings were 1.54 g/m^2 and 3.08 g/m^2. Before the test the top surfaces of cement paste panels were pre-prepared by the same method as shown in Section 2.2.4. The amount of NO_x converted in the reactor is calculated following:

$$NO_X Conversion(\%) = \frac{[C_{NO_X}]_{in} - [C_{NO_X}]_{out}}{[C_{NO_X}]_{in}} \times 100 \quad (2)$$

Where $[C_{NOx}]_{in}$ is the initial concentration [ppm], measured by taking the average value of the first 5 min of the experiment, before turning on the light. The outlet concentration $[C_{NOx}]_{out}$ is measured by taking the average value of the last 5 min of the irradiation period [ppm].

The amount of NO converted in the PCO reactor is calculated following:

$$NOConversion(\%) = \frac{[C_{NO}]_{in} - [C_{NO}]_{out}}{[C_{NO}]_{in}} \times 100 \quad (3)$$

Where $[C_{NO}]_{in}$ is the initial concentration [ppm], measured by taking the average value of the first 5 min of the experiment, before turning on the light. The outlet concentration $[C_{NO}]_{out}$ is measured by taking the average value of the last 5 min of the irradiation period [ppm].

ICSBM 2019
ID 159

3. Results and discussions

3.1 Effects of synthesis temperatures on the dispersity of TiO_2 hydrosols

The average particle size and Zeta potential values were showed in the Table 1. The average particle size (of intensity) of TiO_2 hydrosol samples at 40 °C and 50 °C was 19 nm and 38 nm respectively. The zeta potential of TiO_2 hydrosol synthesized at 40 °C and 50 °C were 43 mV and 39 mV, which meant that the dispersion of hydrosols in distilled water was stable. These results indicated that the synthesis temperature had a great influence on the particle size of TiO_2 in hydrosols, while the influence on the zeta potential of TiO_2 hydrosols was limited.

Table 1 The average particle size and zeta potential of TiO_2 hydrosols

Synthesis temperatures	Size±SD (d. nm)	%Intensity	Z-average ±SD (d. nm)	Polydispersity Index	Zeta potential	Conductivity (mS/cm)
50 □	38±16	100	35±13	0.14	39	0.12
40 □	19±6	100	17±6	0.11	43	0.11

3.2 Crystal form of TiO_2 hydrosols

The diffraction angle 2θ of (101) crystal plane of anatase TiO_2 crystal was 29.4°, the (004) crystal plane was 44.2° and the (200) (105) and (204) crystal planes were 56.4°, 63.5° and 74.3°. As it can be seen in Figure 1, the TiO_2 particles in hydrosol synthesized at 40 °C and 50 °C showed all the typical diffraction peaks of anatase TiO_2 that indicating the synthesized TiO_2 particles in TiO_2 hydrosol was pure anatase TiO_2 crystal. Since the TiO_2 hydrosol synthesized at lower temperature presented smaller particle size, dispersity and same crystal form, the following charactering tests were focused on the comparison between TiO_2 hydrosol synthesized at 40 °C and P25 suspension.

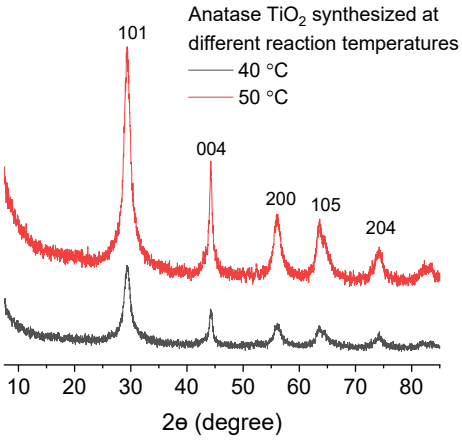

Figure 1 XRD pattern of TiO_2 hydrosols dried at 105 °C

3.3 UV-VIS absorbance of TiO_2 hydrosol

The visual observation of colour changes, as well as UV-VIS absorbance of both TiO_2 hydrosol and P25 suspension are shown in Figure 2. As it can be seen from Figure 2, TiO_2 hydrosol was transparent, while the P25 suspension sample with the same mass content was pure white and non-transparent. In the Figure 2, the light absorbance of TiO_2 hydrosol in the 250-300 nm range is higher than P25 suspension. In general, the P25 powder was made of 20% rutile crystal and 80% anatase crystals, and in theory, the absorption band edge was near 380 nm for anatase and 300 nm for rutile [27]. As seen from Figure 2, the absorbance of light at 400 to 800 nm of P25 suspension is the result of the light scattering phenomenon caused by the big particles of P25 in aqueous solution. As a result, the nano particles in TiO_2 hydrosol were more stable than in P25 suspension.

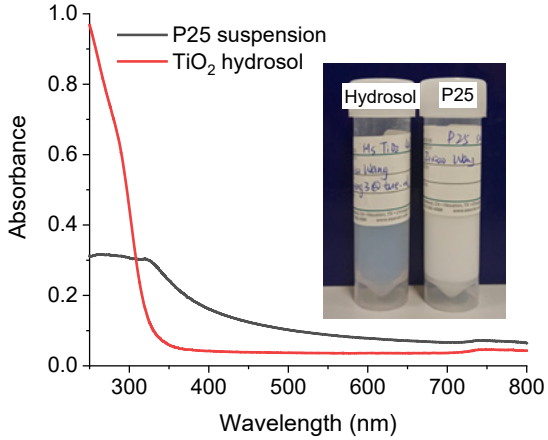

Figure 2 The UV-VIS absorbance spectrums of TiO_2 hydrosol and P25 suspension

3.4 Self-cleaning performance

In Figure 3, the percentage of colour change for RB of cement paste at 7 days age with coatings is presented. The colour change of blank cement sample was around zero after 24 h irradiation, which meant the blank cement at early age present barely no self-cleaning performance. The R_t values of cement paste coated TiO_2 hydrosol with the dosage of 0.77, 1.54 and 3.08 g/m^2 after 24 h irradiation were 85.88%, 91.71% and 94.65% respectively, while the R_t of cement paste coated P25 with the dosage of 1.54 g/m^2 after 24

h irradiation was only 64.88%. In the TiO_2 hydrosol coated samples, the colour change of RB trended to stable after two hours irradiation, while it needed at least 6 hours irradiation to obtain a stable colour change in the P25 coated sample. These results indicated that the self-cleaning performance of cement paste coated 1.54 g/m² TiO_2 as the form of hydrosol coatings is much better than that of P25 suspension coatings.

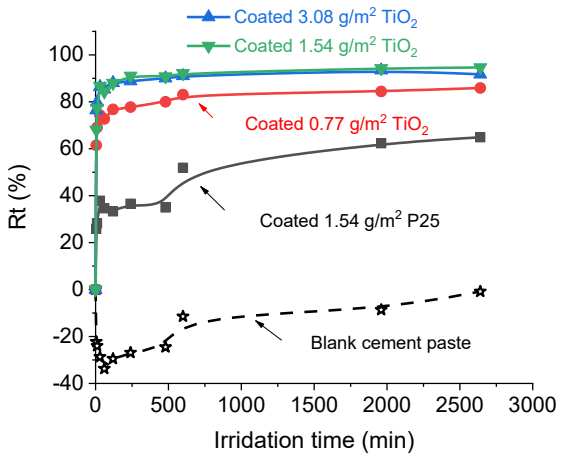

Figure3 Percentage of colour change for RB of cement paste with different coatings after 7 days hydration

3.5 NO_x degradation performance

Figure 4 shows the degradation process of NO_x of cement paste panels at 7 days age. Table 2 presents the conservation values of NO and NO_x of panels. In overall, the cement coated with these two coatings presented very high conversation of NO and NO_x regardless the coating dosage. However, the conversations of NO and NO_x increased along with the dosage of TiO_2 hydrosol coated panels, while the conversations of NO and NO_x decreased with the dosage of P25 coated panels. These results might relate to the poor dispersity and high agglomeration of TiO_2 nano particles in P25 suspension coating with higher dosages. To verify this speculate, the reflectance analysis of cement paste with and without coatings were carried out, this results are discussed in Section 3.6.

Table 2 The conversion rate of NO and NO_x of cement panels with two coatings

Coatings	Dosage (g/m²)	Conversion rate (%)	
		NO	NO_x
TiO_2 hydrosol	3.08	98.88	96.14
	1.54	97.36	93.85
P25 suspension	3.08	87.92	86.01
	1.54	97.66	94.97

3.6 Reflectance of cement paste with coatings

Figure 5 presents the reflectance spectra in the range of 200 nm to 2500 nm of cement paste samples at 28 days age. From Figure 5, it can be seen that after being coated by TiO_2, the reflectance of cement paste samples is significantly increased, especially in the range of VIS (400 to 800nm), NIR (800 to 1000 nm) and SWIR (1000 to 2500nm). These results indicate that the cement paste could also obtain certain solar reflectance from the TiO_2 hydrosol coatings, especially in the range of SWIR. The high reflectance of cement paste coated with P25 suspension in the range of visible light also revealed that the P25 coating was whiter than TiO_2 hydrosol coating, which means that the significant agglomeration of nano TiO_2 particles

in P25 coating. These results supported speculates mentioned in the Section 3.5, showing that the greater agglomeration of TiO_2 particles in P25 suspension was the main reason of the relatively poor performance of air purification in higher surface concentration of coating. Moreover, the better dispersity led to the higher specific surface area of TiO_2 in TiO_2 hydrosol coating, which means that the greater inaction surface areas between TiO_2 and pollutant molecules and better self-cleaning and air purification performance of cement paste with TiO_2 hydrosol coating.

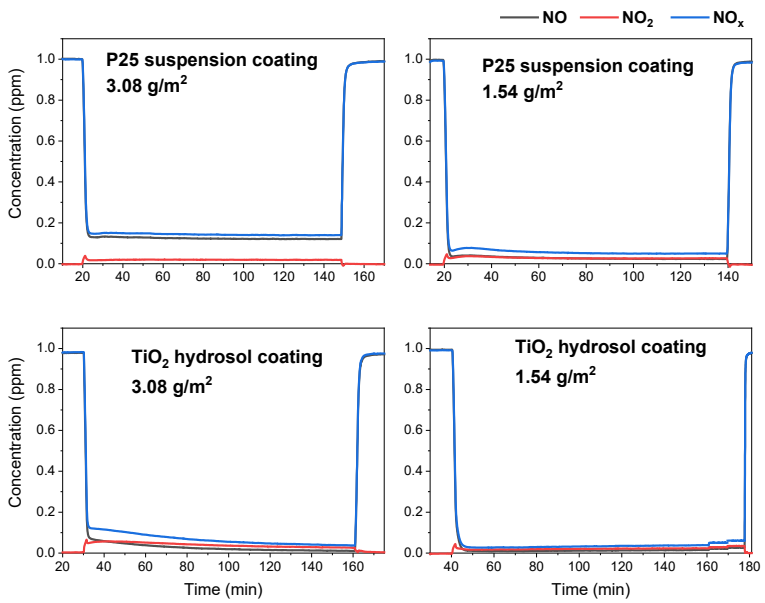

+

Figure4 NO, NO_2 and NO_x concentration graphs of cement panel samples coated TiO_2 hydrosol and P25 suspension coatings

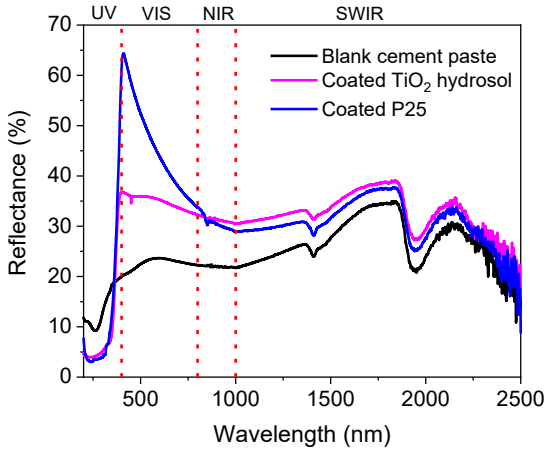

Figure 5 Reflectance of cement paste with different TiO_2 coatings

4. Conclusions

1. In this work, the nano dispersed anatase TiO_2 hydrosol was synthesized by an easy and lower energy consumption method. As compared to the P25 powder suspension, the TiO_2 hydrosol presented much better dispersity and stability in aqueous solution according to the results of particles size, zeta potential test and analysis of UV absorbance.

2. The self-cleaning performance of cement paste sample coated by TiO_2 hydrosol after 24 hour UV irradiation was increased with the surface concentration of TiO_2 hydrosol, and the self-cleaning performance of TiO_2 hydrosol with a surface concentration of 1.54 g/m^2 was 91.71% which was 1.41 times more efficient than P25 coating. The NO and NO_x conversion rates of these two coatings with the surface concentration of 1.54 g/m^2 were higher than 95%.

3. The poor dispersity and high agglomeration of TiO_2 particle in P25 suspension coating led the worse air purification ability of cement panel with higher surface concentration of coating. And the higher reflectance of cement paste with P25 coating in the range of visible light indicated the whiter colour of the coating, which proofed the greater agglomeration of TiO_2 particles in P25 coating. The high self-cleaning and air purification performance of cement paste with TiO_2 hydrosol coating was because of the high dispersity and greater specific surface areas of nano particles in coating.

5. Acknowledgments

The authors appreciate the financial supports from the National Natural Science Foundation of China under the contract No. U170620242, the China Scholarship Council (No. 201806090146) and Eindhoven University of Technology (TU/e). The authors gratefully acknowledge M.Sc. Bin Meng (Building Performance group of TU/e) for his help in processing data of self-cleaning performance characterization, and Prof. Albert Schenning and M.Sc. Xinglong Pan (Stimuli-responsive Functional Materials & Devices group of TU/e) for their supports and advices in the discussion of the spectrum analysis.

6. References

[1] P. Berdahl, H. Akbari, L.S. Rose, Aging of reflective roofs: soot deposition, Appl. Opt. 41 (2002) 2355. doi:10.1364/AO.41.002355.

[2] M. Sleiman, T.W. Kirchstetter, P. Berdahl, H.E. Gilbert, S. Quelen, L. Marlot, C. V. Preble, S. Chen, A. Montalbano, O. Rosseler, H. Akbari, R. Levinson, H. Destaillats, Soiling of building envelope surfaces and its effect on solar reflectance - Part II: Development of an accelerated aging method for roofing materials, Sol. Energy Mater. Sol. Cells. 122 (2014) 271–281. doi:10.1016/j.solmat.2013.11.028.

[3] J. Chen, C. sun Poon, Photocatalytic construction and building materials: From fundamentals to applications, Build. Environ. 44 (2009) 1899–1906. doi:10.1016/j.buildenv.2009.01.002.

[4] E. Boonen, A. Beeldens, Photocatalytic roads: From lab tests to real scale applications, Eur. Transp. Res. Rev. 5 (2013) 79–89. doi:10.1007/s12544-012-0085-6.

[5] R. Wang, K. Hashimoto, A. Fujishima, M. Chikuni, E. Kojima, A. Kitamura, M. Shimohigoshi, T. Watanabe, Photogeneration of highly amphiphilic TiO2surfaces, Adv. Mater. 10 (1998) 135–138. doi:10.1002/(SICI)1521-4095(199801)10:2<135::AID-ADMA135>3.0.CO;2-M.

[6] Y. Hendrix, A. Lazaro, Q.L. Yu, H.J.H. Brouwers, Influence of synthesis conditions on the properties of photocatalytic titania-silica composites, J. Photochem. Photobiol. A Chem. 371 (2019) 25–32. doi:10.1016/j.jphotochem.2018.10.040.

[7] C. Giosuè, Q.L. Yu, M.L. Ruello, F. Tittarelli, H.J.H. Brouwers, Effect of pore structure on the performance of photocatalytic lightweight lime-based finishing mortar, Constr. Build. Mater. 171 (2018) 232–242. doi:10.1016/j.conbuildmat.2018.03.106.

[8] S. Lorencik, Q.L. Yu, H.J.H. Brouwers, Design and performance evaluation of the functional coating for air purification under indoor conditions, Appl. Catal. B Environ. 168–169 (2015) 77–86. doi:10.1016/j.

apcatb.2014.12.012.

[9] E. Luévano-Hipólito, A. Martínez-De La Cruz, E. López-Cuellar, Q.L. Yu, H.J.H. Brouwers, Synthesis, characterization and photocatalytic activity of WO_3/TiO_2 for NO removal under UV and visible light irradiation, Mater. Chem. Phys. 148 (2014) 208–213. doi:10.1016/j.matchemphys.2014.07.034.

[10] Y. Wang, Y. He, Q. Lai, M. Fan, Review of the progress in preparing nano TiO_2: An important environmental engineering material, J. Environ. Sci. (China). 26 (2014) 2139–2177. doi:10.1016/j.jes.2014.09.023.

[11] M. Malekshahi Byranvand, A.N. Kharat, L. Fatholahi, Z. Malekshahi Beiranvand, A review on synthesis of nano-TiO_2 via different methods, J. Nanostructures. 3 (2013) 1–9. http://jns.kashanu.ac.ir/article_5436_20d28461e8600e7c915eab3d24924117.pdf.

[12] R. Vijayalakshmi, V. Rajendran, Synthesis and characterization of nano-TiO_2 via different methods, Arch. Appl. Sci. Res. 4 (2012) 1183–1190. doi:10.11648/j.nano.20140201.11.

[13] O.B. Pavlova-Verevkina, S.N. Chvalun, E.D. Politova, V. V. Nazarov, L.A. Ozerina, A.N. Ozerin, Study of the stable nanocrystalline TiO_2 hydrosol and its fractions, J. Sol-Gel Sci. Technol. 35 (2005) 91–97. doi:10.1007/s10971-005-1311-7.

[14] P. Alphonse, A. Varghese, C. Tendero, Stable hydrosols for TiO_2 coatings, J. Sol-Gel Sci. Technol. 56 (2010) 250–263. doi:10.1007/s10971-010-2301-y.

[15] E. Burunkaya, M. Akarsu, H. Erdem Çamurlu, Ö. Kesmez, Z. Yeşil, M. Asiltürk, E. Arpaç, Production of stable hydrosols of crystalline TiO_2 nanoparticles synthesized at relatively low temperatures in diverse media, Appl. Surf. Sci. 265 (2013) 317–323. doi:10.1016/j.apsusc.2012.11.003.

[16] X. Ding, S. Pan, C. Lu, H. Guan, X. Yu, Y. Tong, Hydrophobic photocatalytic composite coatings based on nano-TiO_2 hydrosol and aminopropyl terminated polydimethylsiloxane prepared by a facile approach, Mater. Lett. 228 (2018) 5–8. doi:10.1016/j.matlet.2018.05.103.

[17] J.X. Yu, R.A. Chi, J. Guo, Desorption and photodegradation of methylene blue from modified sugarcane bagasse surface by acid TiO_2 hydrosol, Appl. Surf. Sci. 258 (2012) 4085–4090. doi:10.1016/j.apsusc.2011.12.106.

[18] E. Ghenne, F. Dumont, C. Buess-Herman, Stability of TiO_2 hydrosols synthesized by hydrolysis of titanium tetraethoxide, Colloids Surfaces A Physicochem. Eng. Asp. 131 (1998) 63–67.

[19] M.M. Soderzhinova, D. V. Tarasova, F.K. Chibirova, Aging of titania hydrosols prepared via ultrasonic processing, Inorg. Mater. 52 (2016) 470–475. doi:10.1134/S0020168516050162.

[20] S. Singh, T. Shi, R. Duffin, C. Albrecht, D. van Berlo, D. Höhr, B. Fubini, G. Martra, I. Fenoglio, P.J.A. Borm, R.P.F. Schins, Endocytosis, oxidative stress and IL-8 expression in human lung epithelial cells upon treatment with fine and ultrafine TiO_2: Role of the specific surface area and of surface methylation of the particles, Toxicol. Appl. Pharmacol. 222 (2007) 141–151. doi:10.1016/j.taap.2007.05.001.

[21] L. Yang, A. Hakki, F. Wang, D.E. Macphee, Photocatalyst efficiencies in concrete technology: The effect of photocatalyst placement, Appl. Catal. B Environ. 222 (2018) 200–208. doi:10.1016/j.apcatb.2017.10.013.

[22] M.V. Diamanti, R. Paolini, M. Rossini, A.B. Aslan, M. Zinzi, T. Poli, M.P. Pedeferri, Long term self-cleaning and photocatalytic performance of anatase added mortars exposed to the urban environment, Constr. Build. Mater. 96 (2015) 270–278. doi:10.1016/j.conbuildmat.2015.08.028.

[23] M. V. Diamanti, B. Del Curto, M. Ormellese, M.P. Pedeferri, Photocatalytic and self-cleaning activity of colored mortars containing TiO_2, Constr. Build. Mater. 46 (2013) 167–174. doi:10.1016/j.conbuildmat.2013.04.038.

[24] E. Jimenez-Relinque, J.R. Rodriguez-Garcia, A. Castillo, M. Castellote, Characteristics and efficiency of photocatalytic cementitious materials: Type of binder, roughness and microstructure, Cem. Concr. Res. 71 (2015) 124–131. doi:10.1016/j.cemconres.2015.02.003.

[25] E. Luévano-Hipólito, A.M. la Cruz, Q.L. Yu, H.J.H. Brouwers, Precipitation synthesis of WO_3 for NOx removal using PEG as template, Ceram. Int. 40 (2014) 12123–12128. doi:10.1016/j.ceramint.2014.04.052.

[26] F. Gauvin, V. Caprai, Q.L. Yu, H.J.H. Brouwers, Effect of the morphology and pore structure of porous building materials on photocatalytic oxidation of air pollutants, Appl. Catal. B Environ. 227 (2018) 123–131. doi:10.1016/j.apcatb.2018.01.029.

[27] E. Jimenez-Relinque, I. Llorente, M. Castellote, TiO_2 cement-based materials: Understanding optical properties and electronic band structure of complex matrices, Catal. Today. 287 (2017) 203–209. doi:10.1016/j.cattod.2016.11.015.

Innovative production technologies and applications in the field of Wood Cement Products

E.J.B. van Elten,

Eltomation BV, Barneveld, The Netherlands

Abstract

This paper describes the further development of advanced production technologies for the manufacture of various types of Wood Cement Boards and the wide range of applications of these boards.

Due to the increasing awareness for healthy and comfortable living conditions with reduced energy costs, the demand for various types of Wood Cement Boards has grown significantly over the last years. In Western Europe this growth is furthermore supported by the increasing need for "acoustic performance" in public buildings and private homes. As a result, the demand for automated production lines for these acoustic and energy-saving boards has also increased.

Eltomation BV, The Netherlands, being a major player in the supply of turnkey Wood-Cement Board Plants, has further developed its advanced production technologies to meet this increasing demand. Although the basis for acoustic Wood Wool Cement Boards lies within Western Europe, an increasing demand for these acoustic and energy-saving boards is being developed in countries such as Russia. In addition, special solutions are being developed to meet the high demand for Affordable & Sustainable Housing in various regions of Africa and elsewhere. This paper provides a general overview of the various Wood Cement Boards on the market and the new technologies being developed to meet the increasing demand for thermal insulation, fire-resistance, acoustic performance and sustainability.

Keywords: Wood Wool Cement Boards, Advanced Production Technology, Energy Saving & Acoustic Applications.

1. Introduction

Eltomation BV of Barneveld, The Netherlands, is specialized in the development and supply of turn-key plants and equipment for the production of various Wood Cement Boards. The family-owned company, active in this specific field for over 60 years, is regarded as a specialist in the production technologies for these Wood-based Mineral Bonded Boards.

The main product produced in these plants is the so-called low-density Wood Wool Cement Board (WWCB). Other Wood-Cement Products include the medium-density Wood Strand Cement Boards (WSCB - EltoBoard) and the Prefab Large WWC Wall Elements. Where the above listed products are based on using long wood wool (excelsior) as raw material, another product for which Eltomation has provided plant solutions is the so-called Cement Bonded Particle Board (CBPB), which high-density (fire-retardant) product is based on using small wood particles as raw material.

Our European clients include renowned producers such as Knauf Insulation (their WWCB products being known under the brand name Heraklith) with multiple plants throughout Europe, Troldtekt A/S – Denmark,

Fibrolith Dämmstoffe GmbH – Germany (part of Soprema Group), Celenit S.p.A – Italy, Träullit AB – Sweden and others. Annual production volume of WWCB is in the range of 16-18 Million square meters, serving mainly the (fire-retardant) acoustic ceiling market. This demand is still rapidly increasing.

During the last decade an increased interest for durable, environmentally friendly and energy-saving building materials has come from the new Russian and Chinese markets. During these recent years a total of 7 additional full-size Wood Wool Cement Board Plants have been supplied to clients in Russia and China for serving the local markets with these fire-resistant, energy-saving products. In addition, these new Russian WWCB Plants also produce large quantities of fine-fibre acoustic ceiling panels for export to the large ready market in Western Europe.

2. Overview of main Wood Cement Products

In general the following Wood Cement Boards (and Large Elements) are considered to be the main Wood-Cement Board products which are on the market today:

1. Wood Wool Cement Board (WWCB);

2. Large WWC Wall Elements;

3. Wood Strand Cement Board (WSCB/ EltoBoard);

4. Wood Residue Cement Board (WRCB);

5. Cement Bonded Particle Board (CBPB).

This paper will mainly deal with the production technology for the first three mentioned product types. Each of these 3 product types require small diameter logs (mostly soft wood species such as pine, spruce, poplar, eucalyptus, etc.) as raw material, to enable the production of long and thin wood wool or wood strands. WRCB and CBPB are not made from wood wool but from wood chips, respectively small wood particles, thereby having different properties and applications.

3. Properties of Wood Wool Cement Board

Of the above described main Wood Cement Products, Wood Wool Cement Board (WWCB) is by far the most common product with a significant annual production volume. To ensure its excellent properties in view of thermal insulation and sound absorption, WWCB is produced at a low density of only approx. 350-460 kg/m^3. These densities are subject to the board thickness and specific application.

The main features of WWCB are:

- Excellent acoustic performance
- High fire resistance (both as B1 and A2 class)
- Wet and dry rot resistance
- Freeze-thaw resistance
- Termite and vermin resistance
- High thermal insulation (energy-saving)

For increased thermal insulation, WWCB can optionally be produced as a (2 or) 3 layer sandwich board with a core of EPS/Polystyrene, Rockwool or PU-foam. This product is referred to as "Composite WWCB". A

main application of such Composite WWCB panel is e.g. acoustic ceilings in open parking garages, where the floor of the apartments or store above the parking house not only needs the required fire-safety, but also a high thermal insulation.

Figure 1 - Standard (white cement) WWC Board

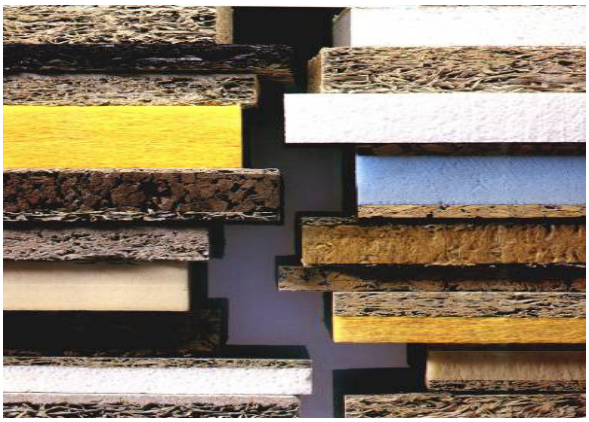

Figure 2 – Various types of Composite WWCB

4. Applications of Wood Wool Cement Board

Standard applications of WWCB include:

- Acoustic ceiling applications (being the vast majority of the market demand);
- Reinforced Roofing boards (mainly applied in Scandinavia, where heavy snow-loads apply);
- In addition, specialty applications include:
- Insulation board for external walls (and floors), referred to as "permanent shuttering" board;
- General board for insulation / renovation / fire protection purposes.

Figure 3 - Acoustic ceiling panels in public building

Figure 4 - Reinforced Roofing Boards

Figure 5 - Permanent Shuttering Boards

Figure 6 – WWCB for renovation projects

Nowadays there is a fast growing application of WWCB in Decorative & Acoustic Applications on walls in offices, bars & restaurants, stores, theatres, etc., mainly due to the good acoustic performances and nice and modern appearance. These boards are typically applied in various decorative shapes or patterns and/ or as a mix of various matching colours. Major players in this field are the companies BAUX from Sweden and Troldtekt, Denmark.

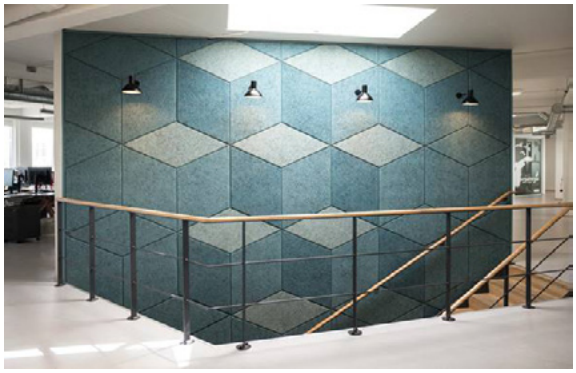

Figure 7 – Decorative WWCB (Troldtekt)

Figure 8 – Decorative WWCB (Träullit/BAUX, Sweden)

5. Production Technology for WWCB

The modern WWCB Plants supplied to the market nowadays combine the need for high-capacity production and minimal labour requirement with consistent high-quality boards. A high percentage of the output will find its way to the acoustic ceiling market. These boards require not only the needed fire-resistance (in either standard B1 or special non-combustible A2 Class) but also have a high standard for visible appearance. This has resulted in an increasing market for special ceiling panels, produced with fine wood wool of minimal width, such as 1,5 mm or only 1,0 mm in width (where standard WWCB is commonly produced with a wood wool width of 2,5 mm or 3,0 mm) and using white cement as binder.

The high-speed production of the fine-fibre wood wool is realized by means of a special-developed Rotating Wood Wool Machine (the so-called "Eltomatic CVS-16"). Such Eltomatic replaces a series of up to 8 of the previously known reciprocating crankshaft driven wood wool planing machines, which are no longer used in modern WWCB production plants due to safety and CE regulations. In the last decades over 30 modern Eltomatics have been installed in WWCB plants worldwide, either as part of a new turn-key plant or simply replacing the old wood wool machines as part of a modernisation (in combination with safety-issues and labour savings).

Where the vast majority of the WWCB Plants use standard Portland Cement as a binder (increasingly white cement replacing the previously common grey cement), a few lines are based on using Magnesite as binder

(where these boards are mainly applied indoors), however the majority is based on having cement as binder. Optionally, these acoustic boards are profiled/bevelled and/or spray-painted in the desired colour.

WWC-Boards are typically produced as 60 cm (optionally 2') in width and having a range in length from 240 – 300 cm (optionally 8'- 10'). Thicknesses of solid WWCB range from 15 to 100 mm, where the majority will be in the 15-35 mm range. For applications with a higher thermal insulation (or further increased fire-resistance), the WWCB panel can be combined with a layer/core of insulating material, such as EPS/XPS, rockwool or PU-foam. These so-called (2- or 3-layer) Composite WWCB Panels are nowadays produced at a thickness of up to 250 mm, subject to application and required R-value. Where in the old days the Composite sheet was added to the fresh WWCB in the main production line, this procedure is nowadays mainly done by gluing such Composite Sheet to a ready WWCB Panel in the Finishing Area.

For acoustic ceiling panels, boards are usually cut into 120 cm length (standard for the European market), where the standard in the USA is mainly based on 60 x 60 cm (or 2'x 2'). Nowadays WWCB is produced in accordance with EN 13168 (replacing the former DIN 1101).

After forming of the fresh mixture, the boards initially cure for 24 hours (up to 48 hours) in the moulds, before being demoulded. The demoulded boards are automatically stacked onto pallets for further curing in the Second Setting Area for say 10-15 days. As a final step all boards pass through an automatic Board Dryer to bring the moisture content of each board down to the desired approx. 12% (ATRO), which provides the required long-term stability of the board. As a final step each board may pass through a Board Thickness Calibrator, before (optionally) being spray-painted in the desired colour. An increasing volume is produced as a "natural-look" panel (non-painted), based on having white cement as a binder.

The capacity of a standard WWCB Plant is nowadays up to 4.100 m^2 boards per shift (based on 25 mm board thickness) with a production line speed of the main line of up to 20 m/min. (resulting in average one board being produced per 7 seconds). Each WWCB Producer determines whether he wishes the line to be operational on either a 1, 2 or even 3 shifts per day. Modern WWCB Plants are able to produce up to 3 Million square meters of boards on an annual basis.

With the integration of modern electronic control systems, the lines are not only more automated but also provide a more accurate formed board in view of even distribution, weight and visual appearance. Only a handful of supervisors are required to operate such line, supported when needed by direct on-line support from the Eltomation office in Barneveld, Holland.

Figures 7, 8 - Eltomatic Rotating Wood Wool Machine Figure 9 – Double Forming Station at WWCB Plant (cap.: 3.000 kg/hr.)

6. Wood Strand Cement Board (WSCB – EltoBoard)

The production of medium-density Wood Strand Cement Board (WSCB – EltoBoard) is accomplished on

a standard WWCB Plant to which a special hydraulic EltoBoard Press has been added at the end of the line. The Press will receive a full stack of filled moulds and will compress the fresh wood-cement mat to a much higher density. To ensure and maintain sufficient pressure during initial curing, the pressed stack of full moulds is secured in a so-called Press Package, consisting of a heavy-duty Top- and Bottom Frame, secured by Tension Arms. The Package is secured under pressure during the initial 24 hours of curing, where after the Press Package is again opened in the same EltoBoard Press, to allow further processing, such as demoulding, further curing, final trimming, etc.

This extra procedure results is a medium density board with structural strength (bending strength of up to approx. 20 MPa). Board dimensions are typically 60 cm wide and 240-300 cm long. Board thicknesses range from 8 to 25 mm.

Producing these medium-density Wood Cement Boards on such WWCB Plant, provides a big advantage to the End-user, by now having the flexibility to produce both low-density WWCB and medium-density Wood Strand Cement Boards on one plant, allowing a wider range of products from one plant location.

Wood Strand Cement Board is commercially being produced in Russia (OOO Building Innovations) and Japan (Takemura Co.).

Figure 10 - WSCB Plant with EltoBoard Press

Figure 11 - WSCB applied in walls, floors and roof (Takemura, Japan)

7. Large WWC Wall Element Building System - introduction

During the last decade, a new revolutionary prefab building system has been developed by the company Träullit AB in Sweden, being one of Eltomation's long-term clients.

Utilising the excellent properties of WWCB in view of thermal insulation, weather-, fire, insect- and rot-resistance, the company decided to produce WWCB in much larger dimensions (referred to as "Large WWC Elements"), enabling fast and efficient prefab construction of homes, schools, offices, etc. These large wall elements are made out of uniform (although light-weight) WWC with dimensions of up to 6 m (optionally 20') in length, 2,7 - 3 m (approx. 9'- 10') in wall height and up to 40 -50 cm (approx. 1' - 4" to 1' - 8") thickness, subject to the local climatic conditions.

In addition to the excellent thermal insulation (U = 0,19 W/m^2 ºC at 40 cm wall thickness), these elements also provide a high thermal storage capacity (250 kJ/m^2 ºC), which contributes to excellent living conditions in these homes.

Figure 16 – Collage of Large Element System: Production, Installation and a Finished Large Element House.

8. Construction with Large WWC Wall Elements

Due to the low weight of the wall elements, a truck/trailer can be loaded with up to 12-16 Elements (subject to wall thickness), allowing for very efficient transport. The elements are loaded into open containers, or onto special drop-off frames, which are commonly used in the concrete element business, so the full load can be dropped-off at the building site (and when possible an empty container/rack is picked- up for return to the plant).

Figures 17, 18 - Ready Elements are loaded into open containers, or onto special drop-off frames

Elements are lifted from the transport frame by a small crane (by making use of the two hoisting straps embedded in each Element). A small team of 3 workers can in this way place all Elements of a typical medium-size one-story house in one day.

Figures 19, 20, 21 - Ready Elements are efficiently placed on the ready concrete slab

For one- and two-story housing, as commonly applied in Sweden, the Large Wall Element System receives its load-bearing properties by means of the reinforced concrete beams, which are freshly poured on-site, by filling up the U-shaped cavities between 2 lined-up Elements. In addition to these vertical "pillars", each Element is provided with a horizontal running U-shaped groove ("Ring-beam") at the crest of each Element. Both the vertical cavities and horizontal U-shaped groove are reinforced with steel bars and are cast on-site. The large wall element itself has a compression resistance of 27 kN per running metre. A possible bending down of the concrete beam is prevented by the large wall element that works together with the concrete ring beam. However, the architects designing these houses are used to put the load-bearing property of the Element to zero, so purely calculating the concrete ring-beam and vertical supports to carry the full load.

Figure 22 - Open Ring-beam

Figure 23 - Pouring of concrete

Figure 24 - Anchors in ring beam for floor support

Some of the main technical properties of the Large WWC Wall Element are listed in the Table A below, based on the standard 40 cm wall thickness, as applied in most projects executed in Sweden.

Table A – Main Technical Specifications of the Large WWC Element.

Träullit Large Wall Element, Thickness 400 mm Technical Data	
U-value	0,19 W/m² K
Fire rating	REI360 (6 hours)
Heat storage capacity	250 kJ/m² °C
Critical RH (preliminary tests)	90 %
Air permeability	20 m³/mhPa
Load carrying strength	27 kN per running metre of wall
Density	Approx. 360 kg/m³

Although the listed thermal insulation of U=0,19 (R=5,2 m²K/W) is sufficient for most projects, such as houses, schools, etc. in Sweden, certain applications (such as a so-called "Artic House Project") may require an even higher thermal insulation. For such projects it will be possible to make the Elements of a thickness of 50 cm and even up to 60 cm. Such 60 cm thick wall will provide for a R-value of up to 10.

From the Table A above, one can see the excellent Heat Storage Capacity (250 kJ/m² °C) of this material, which may be one of the most important features for a comfortable living condition in the house. The heat of the day is stored in the walls, to be only gradually be released during the night. Another figure, which comes to mind is the very high fire-rating of REI 360. Extensive tests have been performed at the SP

Technical Research Institute in Sweden, where a test Element was made subject to flames of 1200 degrees centigrade on one side during an extended period of 360 minutes (6 hours) under load. During this period the temperature on the other side of the element only came to 45 degrees Celsius and the overall Element remained intact. After the 6 hours testing period was successfully reached, the load was steadily increased up to 67 kN/m, which caused initial cracks in the test element.

The various pictures displayed in this paper show the construction of houses, schools, etc. in Sweden, where the Elements are shipped to the building site as cut-to-size Element, however without any base stucco, which is applied only once all Elements are put in place. Also openings for electrical fittings are afterwards milled into the wall. Eltomation's new fully-automated Large Element Line is provided with a CNC Centre, which not only provides the proper sizing of each Element (including cut-outs for window openings, etc.), but will also provide all such openings for cables and piping in the plant, allowing certain components and fittings to be pre-mounted in the factory. As a final step the client may choose to already apply a base stucco in the plant and mount window-frames, where possible.

These additional steps will contribute to a higher efficiency in providing the Elements on full pre-fab basis, thereby further reducing labour on the building site and an overall quicker delivery of the finished house.

Figures 25, 26 - two-story villa under construction (Träullit, Sweden)

Figures 27, 28, 29, 30 – Construction of a highly insulated day-care centre in Sweden, utilising Large Elements for the outer walls and Reinforced Roofing Boards for the roof (Träullit, Sweden)

Figures 31, 32, 32 – Affordable & Sustainable Housing for Africa (and other regions worldwide)

9. Production Line for Large WWC Wall Elements

During the first years of production of the large WWC wall elements, Träullit, Sweden has further optimised its product using semi-automated production facilities, such as for forming, demoulding, storage, cutting/ finishing, etc. In order to meet the demand for a fully-automated production of these Large Elements at considerably higher plant capacity, Eltomation has in recent years developed a production line for the fully-automated production of such large elements at high capacity and reduced labour requirements.

Figures 33, 34 - Impression fully- automated Large Element Line

The first such fully-automated Large Element Line, was supplied to a client in Yixing, Jiangsu Province, PR of China. Plant capacities of such Large Element Line are up to 24-30 Elements per shift (subject to wall thickness), allowing construction of up to 1500 housing units per year. Contracts for the supply of similar Large Elements Lines to clients in Western Europe and Russia are expected to be secured during 2019.

Typical dimensions for these large elements are 6 m length x 2,8 m wall height. The wall thickness will standard be based on 30 - 50 cm, subject to the climatic conditions. Per each plant location and intended range of applications, the maximum wall thickness will be optimised (say up to 30 cm for a potential project in central Africa and up to 50 cm for a project in Northern Europe. Also the maximum wall height will be optimised to the local market demand (typically ranging from 2,7 to 3,0 m). To secure a flexible production range, the Large Element Line can produce various wall thicknesses, which can be secured by laying in a dummy-bottom plate in the large form. For example by adding a 15 cm dummy bottom in a 40 cm high form, also Elements of 25 cm thickness can be produced on the same line.

The fresh mat of material is formed continuously in the slow-moving large forms, which pass underneath the Double Forming Station in an uninterrupted flow. Each Element is formed in 2 subsequent layers (say of 20 cm thickness each, allowing the line to have hoisting straps or reinforcements to be inserted in between the 2 fresh layers of wood-cement mixture material. The continuous mat is hereafter cut into the desired (6 m) lengths by the separating saw, which moves at the same speed of the forms, while making the cut between 2 forms. The individual full forms are stacked for initial curing of the fresh mixture in the forms for approx. 48 hours. After this curing period the cured Element is released form the Form by means of a hydraulic Turing Table, where after each form is returned to the Forming Line. The Element is transferred to a CNC Milling & Cutting Station to be processed to the proper dimensions, including creating openings for window frames, electrical conduits, etc. As a final step the Producer may insert the window frames and apply a base stucco/plaster to both sides of the ready Elements. These steps contribute to an efficient Prefab Building technology, greatly reducing the on-site activities and virtually eliminating on-site construction waste. This all results in a very fast construction time, which benefits not only the contractor but also the new home owner.

Figure 35 - Finished Element from CNC operation

Figure 36 – Elements ready for shipment

The capacity of the Large Wall Element Line is designed to be approx. 500 m^3 of finished product per day (based on a 3 shift production). For typical 40 cm thick Wall Elements, this results in a capacity of up to 23 Elements per shift (subject to complexity), allowing a capacity of Elements for up to 1500 housing units per year. For the market for Affordable & Sustainable Housing Units for countries in e.g. Africa, based on a typical 25-30 cm wall thickness and say 55-60 m^2 single story housing unit, such Large Element Line may have an output of Wall Elements for up to 2500 housing units per year. Such Large Element Line may be supported by a Wood Wool Cement Board (WWCB) Plant, for the production of all partitioning walls (typically 100 mm thickness), Reinforced Roofing Boards (typically 75 mm thickness) and optional acoustic ceiling panels. Such combined Large Element Line and WWCB Plant will allow all such main building materials to come from one plant location, utilising the local available small diameter plantation wood. Other interesting markets for the prefab Large Elements are currently being developed, such as for Sound

Barriers along highways and railroad tracks.

10. Durability and Sustainability

WWCB, WSCB and Large WWC Elements are produced from only natural materials, such as FSC-certified small diameter Spruce (optionally Pine or Poplar), mixed with Portland Cement. To this mixture water and a small percentage of salt-solution is added for the proper binding.

Both scientific tests, initiated by customers of Eltomation, as well as open air application of WWCB have shown that WWCB is unaffected by over 70 years of open air exposure to the elements (even in countries with a high number of freeze-thaw cycles, such as Sweden). This property is further improved when the WWCB is stuccoed as is customary done for applications where the material is exposed to the elements.

At the end of the life cycle the WWC material can be fully recycled. The leading WWCB producer Troldtekt has already obtained a Cradle-to-Cradle Silver Certificate for its WWCB production process. Currently test are being conducted to have the trimming waste from production be ground to form basic ingredients for new cement production. In this respect, WWCB is one of the few building products with a neutral Life Cycle Analyses (LCA). WWCB meets the most stringent international environmental norms and certifications, such as the Danish Indoor Climate Labelling, the Finnish M1 Low-Emission Classification, UK's 'Allergy Friendly Product Award' and Healthy Indoor Climate Certificate.

11. Conclusion

Although Wood Wool Cement Boards (WWCB) have been on the European market for some 100 years, it has seen a sharp increase in sales and applications over the last decade, with annual production volumes growing towards the 20 Million square meters annually. Reasons for this re-birth of WWCB are the steadily increasing volumes for decorative acoustic ceiling panels with fine-fiber boards, produced with white cement. Leading countries in this field are Denmark, Germany and Holland. One specific sector seeing an increased demand is the Agro-sector where special lightweight WWCB is applied in (pig) stables to act as a filter for the clean air flow through the ceiling in such stables. Producers in Austria and Germany also benefit from the market increase for fire-resistant applications in (indoor) parking garages, where new European fire-safety norms apply. In addition, new markets for fully-automated WWCB Plants have been developed in countries such as Russia and China, where consumers, architects and builders have discovered the benefits of this sustainable and energy-saving product in a wide range of applications. As a result of the above, Eltomation BV, The Netherlands has further developed its range of semi-automatic and fully-automatic plants for the production of various types of Wood Cement Products, to meet this market demand. In general, the Wood Cement Products described in this paper, although being a niche product in the huge building materials market, still has a bright future ahead.

12. Acknowledgement

The author wishes to express his gratitude to the management of Träullit AB, Sweden and Troldtekt A/S, Denmark for the technical support provided and the courtesy of making use of the technical data in Table A and some of the pictures used in this paper. Additional pictures of WWCB applications are courtesy of Träullit / BAUX, Sweden and Celenit, Italy.

13. References

1. G. J. (Gerry) van Elten, Eltomation BV, The Netherlands. 2004. History, present and future of Wood Cement Products. 9th International Inorganic Bonded Composite Materials Conference. Vancouver, Canada, 2004. Proceedings published by IIBCC.

2. E. J. (Bert) van Elten, Eltomation BV, The Netherlands. 2010. New Developments in the field of

Wood Cement Products, applications and production technologies. 12th International Inorganic Bonded Composite Materials Conference. Aalborg, Denmark, 2010. Proceedings published by IIBCC.